Ultrasonic studies in gallium arsenide and mercury telluride

Cottam, Ronald Ian

ULTRASONIC STUDIES IN GALLIUM ARSENIDE AND MERCURY TELLURIDE

A thesis by

RONALD IAN COTTAM
B.Sc. (Dunelm)

in candidature for the degree of
Doctor of Philospphy
at The University of Durham
October 1973

Department of Applied Physics and Electronics
Science Laboratories, South Road, Durham City.

R. J. Cottam

24/10/1973

ABSTRACT

Ultrasonic velocities and attenuation in GaAs and HgTe have been measured between 2 K and room temperature in the frequency range 40 to 750 MHz. An experimental evaluation has been made of the pulse-superposition technique used for measuring the ultrasonic velocities, and particular attention has been paid to determination of the uncertainties involved.

A correlation has been found between the ultrasonic pure mode elastic constant combinations of GaAs, HgTe and other III-V and II-VI zinc-blende structure compounds and the group IV elements. The elastic constant temperature dependences are well represented by a phenomenological model based on the Debye phonon frequency spectrum; differences between the model and experimental temperature dependences for the two compounds are compared.

The ultrasonic attenuation in GaAs is dominated by damping due to ultrasonic phonon-thermal phonon interactions. The results are interpreted on the basis of the Woodruff and Ehrenreich model and the detailed nature of the phonon-coupling Grüneisen parameter is examined.

Two main mechanisms contribute to the low-temperature attenuation in HgTe: phonon-phonon damping and dislocation-resonance damping. A large attenuation peak below liquid nitrogen temperature is explained in terms of thermal unpinning of dislocations.

CONTENTS

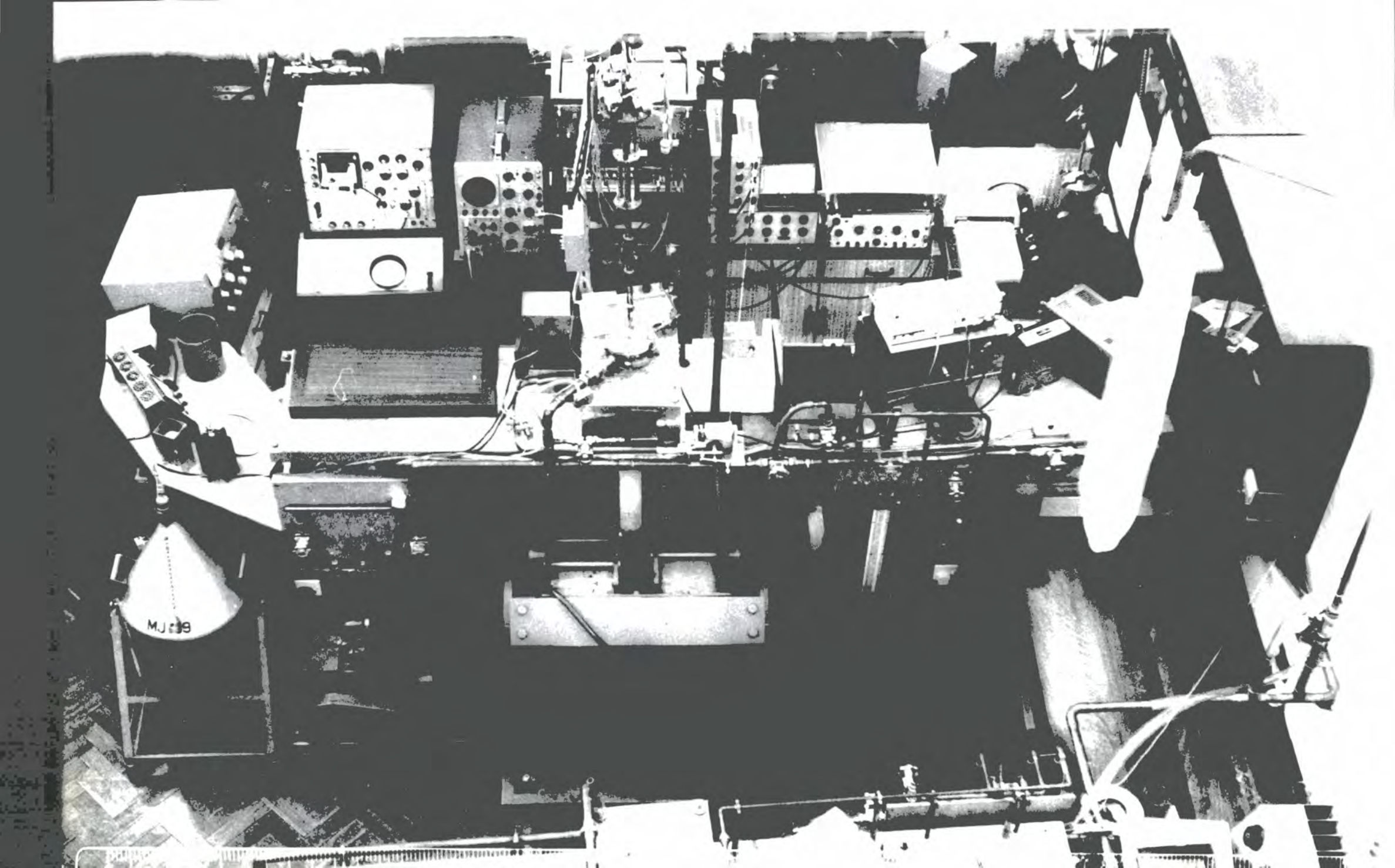

1. A PREFACE

This experimental investigation is submitted as the thesis requirement for the degree of Doctor of Philosophy in the Faculty of Science of the University of Durham, England.

In the model analyses of physical phenomena observable in solids one concept occurs repeatedly; that of material elasticity or anelasticity. Many phenomenological theories have been evaluated through their correct prediction of elastic and anelastic behaviour, and the range of properties and phenomena which are observable and measurable in solids through mechanical investigations is enormous, covering interactions in all of the five classical divisions of physics (thermodynamics, electromagnetics, optics, acoustics and mechanics). Unfortunately there is no unified theory linking the macroscopic elastic and anelastic properties of solids with microscopic models: the problem is very complicated and derivation from fundamental principles is not possible using present techniques of computation. One major difficulty is that of comparing the predictions of approximation models with experimentally determined values. Very often the macroscopic/microscopic correlation requires extreme accuracy of determination of the elastic constants, and sufficiently precise measurements are only available for a very small number of materials. The mechanical damping due to anelasticity is similarly difficult to measure accurately, and often it exhibits very complicated behaviour as a function of controlling factors such as temperature.

In this thesis I wish to present the results of a comprehensive study of the elastic constants and high frequency (ultrasonic) mechanical wave attenuation of two materials which while having the same crystal structure are unlike in many other respects. The prime objective has been to make measurements with a high enough accuracy for quantitative comparison with present elastic constant and attenuation models. Gallium arsenide (GaAs) is a diatomic semiconducting compound of members of groups III and V of the periodic table. Great interest has been shown over a number of years in its electrical properties and a range of gallium arsenide electronic and optical devices is available (Gunn oscillators, solid state lasers, solid state lamps, etc.) However, comparatively little information is available on the mechanical behaviour of GaAs. Mercury Telluride (HgTe) is a less well known semimetallic II-VI compound whose only practical importance has been in alloys with other II-VI materials: extensive work has been done on the application of cadmium-mercury telluride to infrared detection and lasers.

The experimental study falls into three sections: first a critique of the experimental techniques involved (Chapter 5); second the measurement of the elastic constants of the two compounds as a function of temperature from liquid helium to room temperatures (Chapters 6 and 7); third the measurement of the ultrasonic wave attenuation in the materials as a function of temperature and wave frequency (Chapters 8 and 9). The main theme of the work

is the correlation between the elastic and anelastic properties of GaAs and HgTe (Chapter 10) and the use of this correlation to understand not only the mechanical behaviour of these two compounds but also more general features appertaining to a wider range of solids.

The stated aim of a thesis presented in this university is that the author should make a valuable original contribution to the field of study. It has been said that in many theses there is work which is both valuable and original, but unfortunately the valuable is not original and the original not valuable (L.P. Bouckaert): I trust that this is not found to be the case in the present instance. On reflection it seems that little of the credit for this work falls on my shoulders. Primarily my thanks go to Dr. George Saunders, without whose energetic encouragement this thesis would not exist. I can express my gratitude to him in no better way than to say simply, Thank you.

The experiments have been carried out using facilities which are provided in the Department of Applied Physics and Electronics in the University of Durham by Professor D.A. Wright, to whom I am indebted. I am grateful for work carried out by the technical staff headed by Frank Spence, particularly Ron Waite whose cheerful assistance has now helped yet another research project towards its completion. I must express my appreciation of discussions with the members of George Saunders' research group, especially Mike Farley and Colin Maynell who built up the ultrasonic pulse-superposition equipment used here.

Finally I should like to thank John Wilson for extensive advice and assistance in the evaporation of CdS films and Carol Pennington for extensive assistance with the artwork in this thesis. The work has been supported by a grant from the Science Research Council.

CHAPTER 2

"CRYSTALLINE AND BAND STRUCTURES OF GALLIUM ARSENIDE AND MERCURY TELLURIDE"

2.1(a) THE ZINC BLENDE STRUCTURE

The III-V and II-VI compounds form a link between the archetypal elemental semiconductors of Group IV in the periodic table and the extreme I-VII binary compounds.

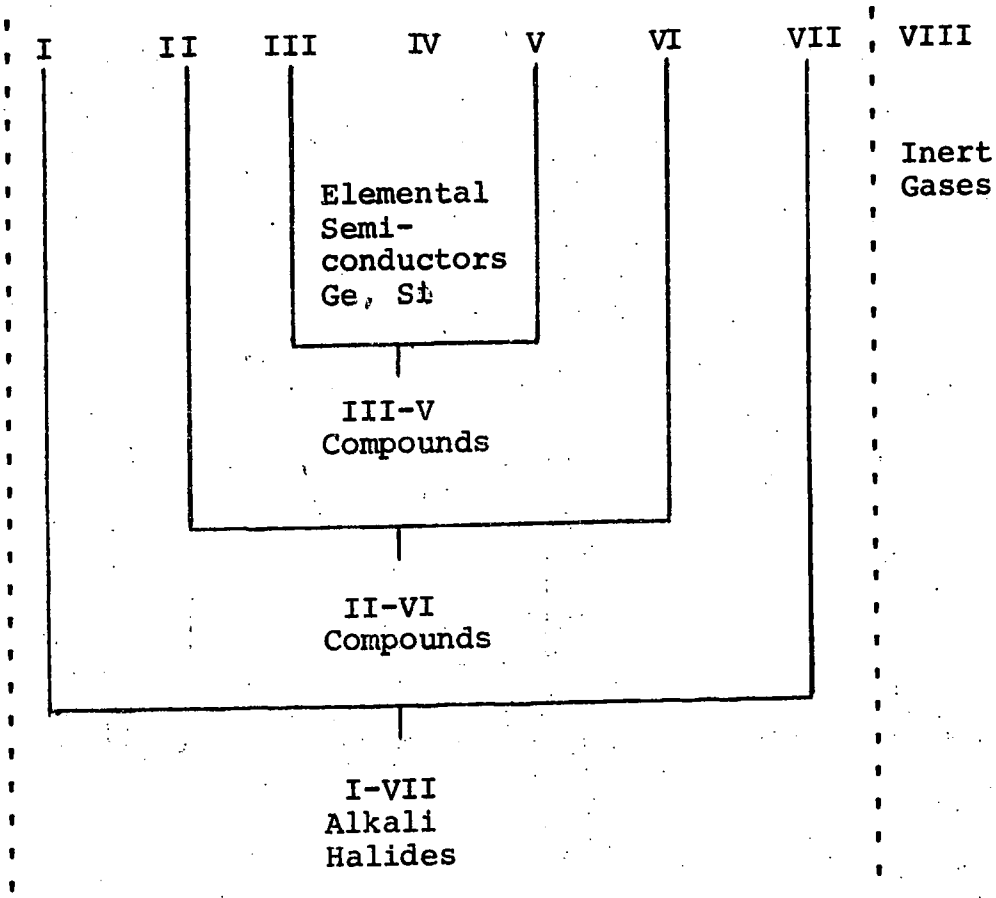

Table 2.A lists the group IV elements and the III-V, II-VI and I-VII compounds. The group IV semiconductors

TABLE 2.A

The group IV elements, the III-V, II-VI and I-VII compounds and their crystal forms.

IV	III-V	II-VI	I-VII
.C(diamond) D	.BN z	.ZnS z	LiF H
Si D	BP z	.ZnSe z	LiCl H
Ge D	.BAs z	.ZnTe z	LiI H
α-Sn D	AlP z	.CdS z	LiBr H
Pb	AlAs z	.CdSe z	NaF H
β-Sn	AlSb z	.CdTe z	NaCl H
.C(graphite)	GaP z	.HgS z	NaI H
	GaAs z	HgSe z	NaBr H
	GaSb z	HgTe z	KF H
	InP z	.ZnS	KCl H
	InAs z	.ZnSe	KI H
	InSb z	.ZnTe	KBr H
	AlN	.CdS	RbF H
	GaN	.CdSe	RbCl H
	.BN	.CdTe	RbI H
	.BAs	.HgS	RbBr H
	AlBi		CsF H
	GaBi		CsCl
	InBi		CsI
	InN		CsBr

D - diamond structure
z - zinc-blende structure
H - halite structure
. - polymorphic forms.

take the diamond form, many of the III-V and II-VI compounds occur with the zinc-blende structure and the majority of the I-VII compounds take the halite form. All three crystal types have the face-centred Bravais lattice with a basis of two atoms. Figure 2.1 shows the atomic arrangements.

Gallium arsenide (GaAs) and mercury telluride (HgTe) both have the zinc-blende cubic structure: that most characteristic of their respective compound groups. Unlike many of the group members, neither gallium arsenide nor mercury telluride is polymorphic under normal conditions.

The zinc-blende crystal structure itself (space group $F\bar{4}3m$) consists of two interpenetrating face centred cubic sub-lattices, one of type A atoms and one of type B. Each sub-lattice is defined by basic translational vectors $\frac{a}{2}$ [110], $\frac{a}{2}$ [011], $\frac{a}{2}$ [101] and displaced by a vector $\frac{a}{4}$ [111] with respect to the other (Figure 2.2). Type A atomic sites in the conventional unit cell are 000, $0\frac{1}{2}\frac{1}{2}$, $\frac{1}{2}0\frac{1}{2}$, $\frac{1}{2}\frac{1}{2}0$, and type B sites are $\frac{1}{4}\frac{1}{4}\frac{1}{4}$, $\frac{1}{4}\frac{3}{4}\frac{3}{4}$, $\frac{3}{4}\frac{1}{4}\frac{3}{4}$, $\frac{3}{4}\frac{3}{4}\frac{1}{4}$. Consequently there are four A atoms and four B atoms in this unit cell: the rhombohedral unit cell contains two atoms. Both atom types have similar environments, each having as nearest neighbours four atoms of the opposite type at the corners of a regular tetrahedron and at distances of $\frac{1}{4}\sqrt{3}$ a. The next nearest are twelve atoms of the same type $\frac{1}{2}\sqrt{2}$ a away.

A consequence of the $\frac{a}{4}$ [111] shift between the two sub-lattices is the lack of a centre of symmetry; along the [111] direction planes of A and B atoms alternate

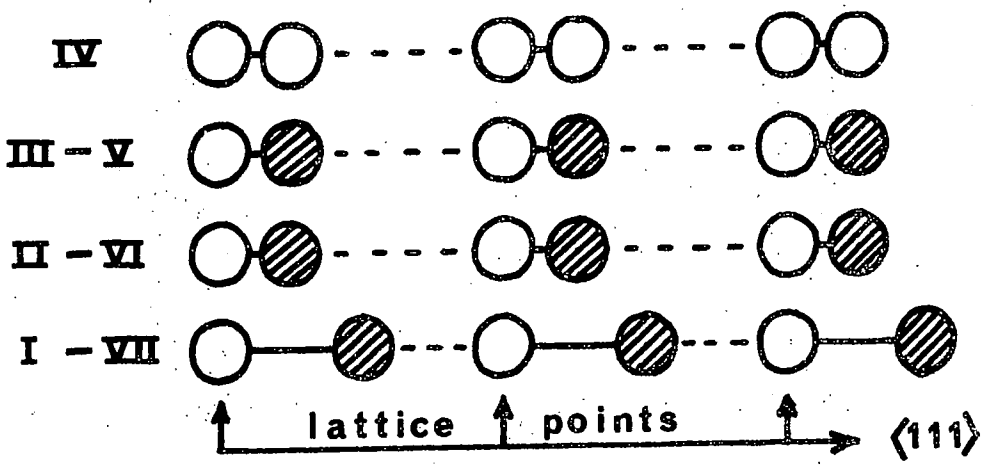

Atomic Arrangements in the sequence IV , III – V, II – VI , I – VII.

FIGURE 2.1

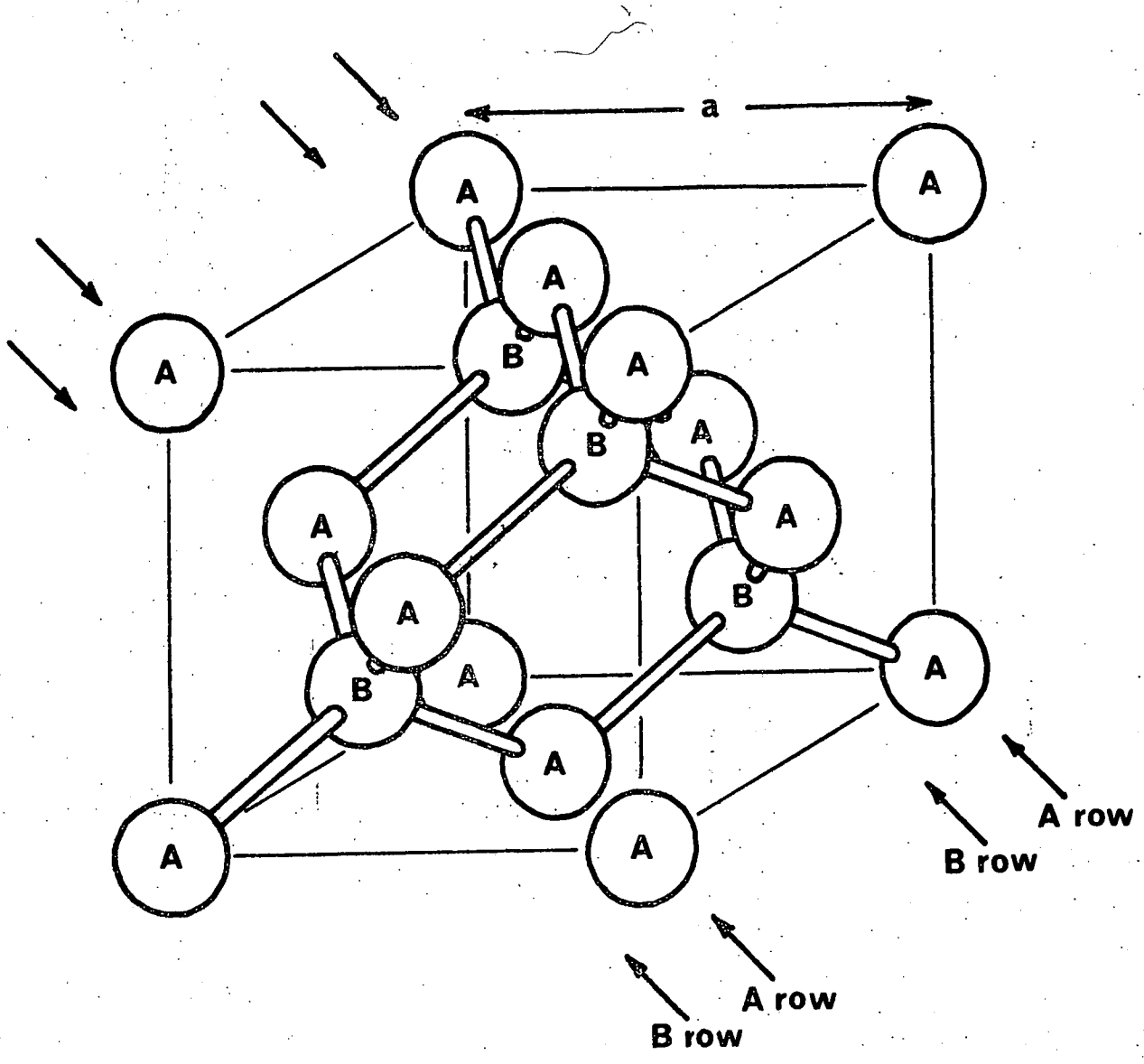

The Zinc Blende Unit Cell

FIGURE 2.2

(Figure 2.1). A more extensive view of the atomic arrangement appears in Figure 2.3. In the diamond structure there is only one kind of atom and in the halite the shift is $\frac{a}{2}[111]$: both have a centre of symmetry. Opposed (hkl) and $(\bar{h}\bar{k}\bar{l})$ faces and opposed [hkl] and $[\bar{h}\bar{k}\bar{l}]$ directions can have different physical and chemical properties in non-centrosymmetric crystals. For example, diffracted X-ray intensities are not the same from (hkl) and $(\bar{h}\bar{k}\bar{l})$ faces: the difference has been observed in gallium arsenide by White and Roth (1959) and in mercury telluride by Warekois et al (1962). Differences in the etching characteristics of the (111) and $(\bar{1}\bar{1}\bar{1})$ surfaces of gallium arsenide (Abrahams and Buiocchi, 1965) and mercury telluride (Warekois et al, 1962) have also been observed.

As the zinc-blende structure has a face-centred cubic Bravais lattice, the Brillouin zone is the tetrakaidekahedron illustrated in Figure 2.4, with eight regular hexagonal faces and six square faces. The standard notation is used (Bouckaert et al, 1936); ΓX, ΓL and ΓK are the 4-fold, 3-fold and binary directions respectively.

2.1(b) BINDING AND IONICITY

Partial ionic bonding in semiconducting compounds has been inferred from bonding theory, carrier mobility, piezoelectric and infrared measurements. We can define an effective interatomic charge transfer e* whose magnitude

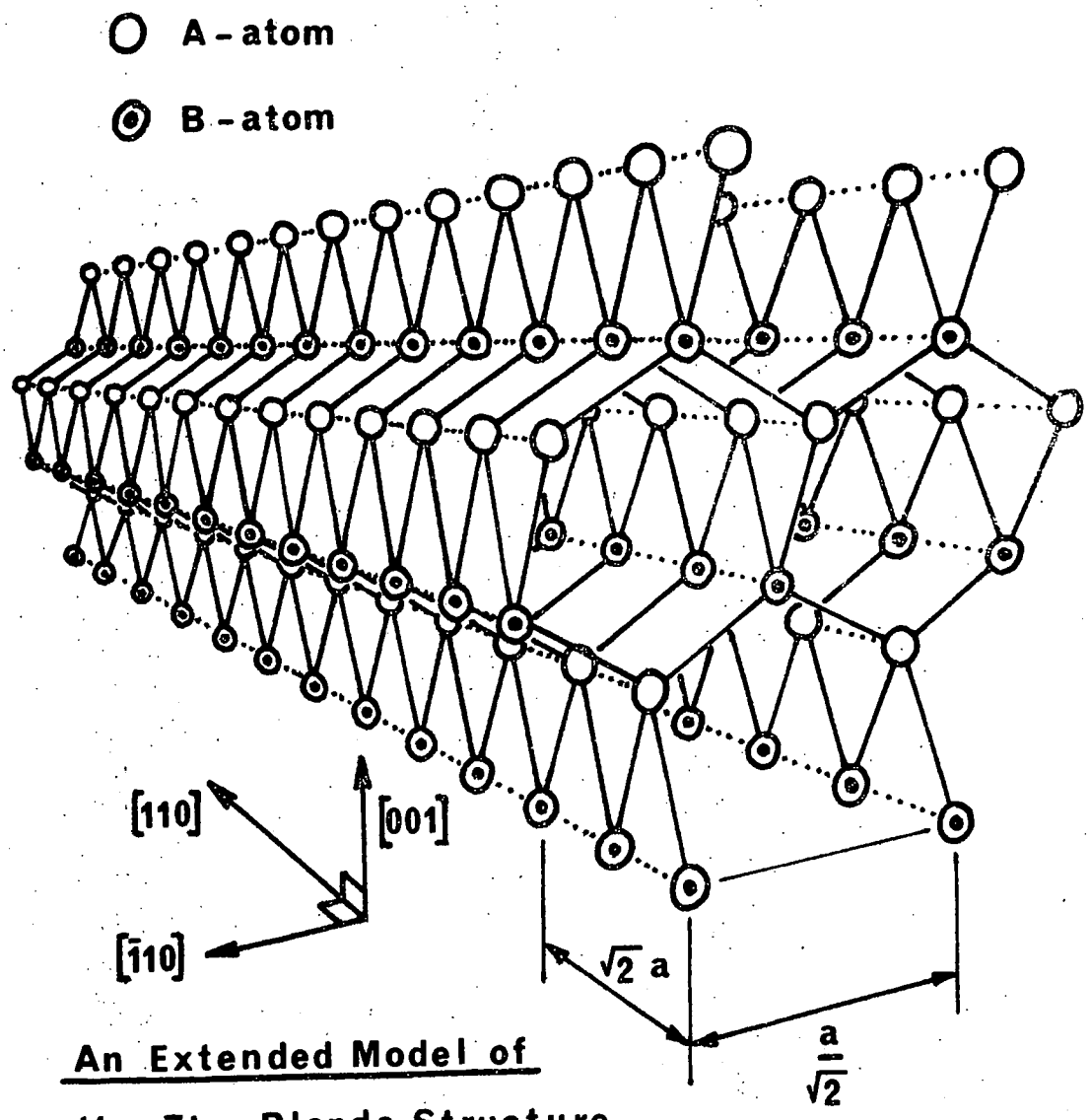

An Extended Model of the Zinc Blende Structure

FIGURE 2.3

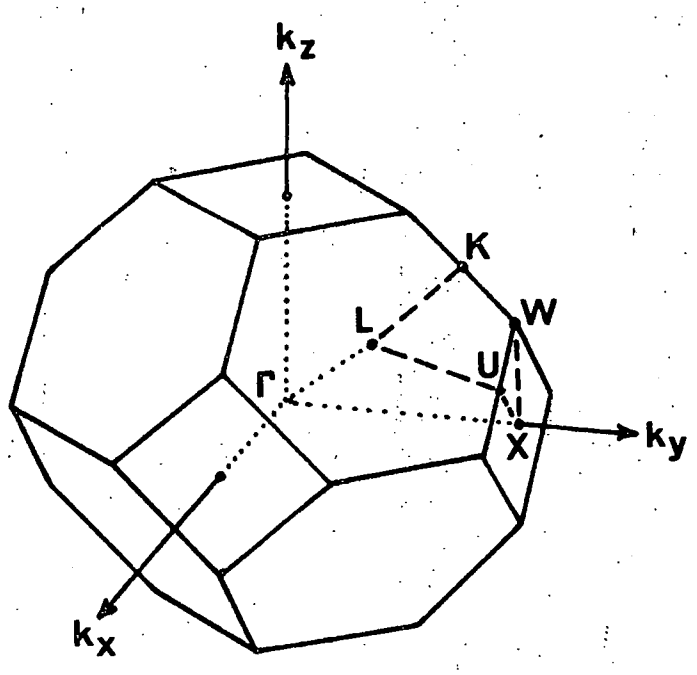

The First Zinc Blende Brillouin Zone

FIGURE 2.4

and sign characterise the bond; positive, zero and negative values indicating 'ionic', 'neutral' and 'covalent' bonding respectively. Transfer of electrons from the Group V atom to the Group III in the III-V compounds, for example, implies a negative value for e*. If we consider the transfer of whole electrons only, the range of permitted values of e* through the sequence IV ⟶ I-VII is

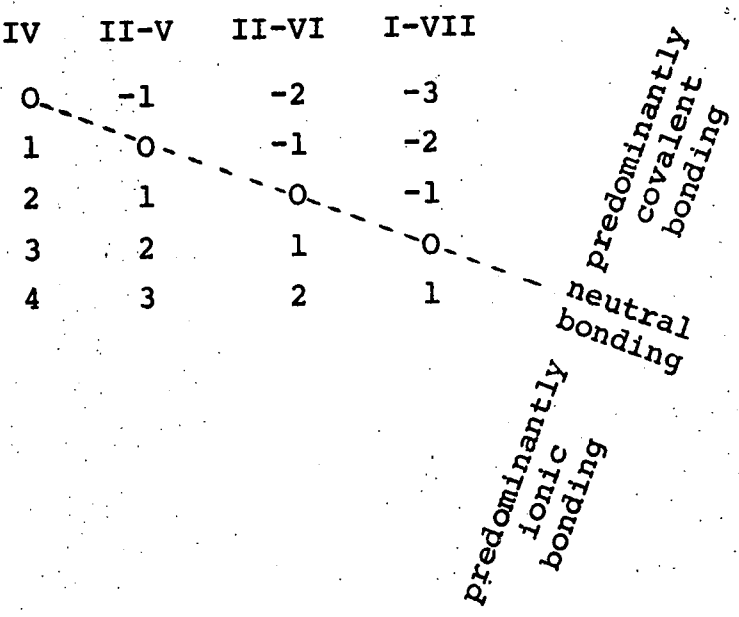

A comparison of bonding ionicities may be made through the crystalline ionicity

$$\lambda = \lambda_o + \frac{e^*}{c} \qquad (2.1)$$

where λ_o is the atomic ionicity and c is the coordination number; e^*/c is the displaced charge per bond (Suchet, 1965). Values of λ from zero to unity cover the range from purely covalent to entirely ionic bonding. Figure 2.5 shows the crystalline ionicities in the IV ⟶ I-VII sequence. A general trend towards higher ionicity can be seen throughout the sequence.

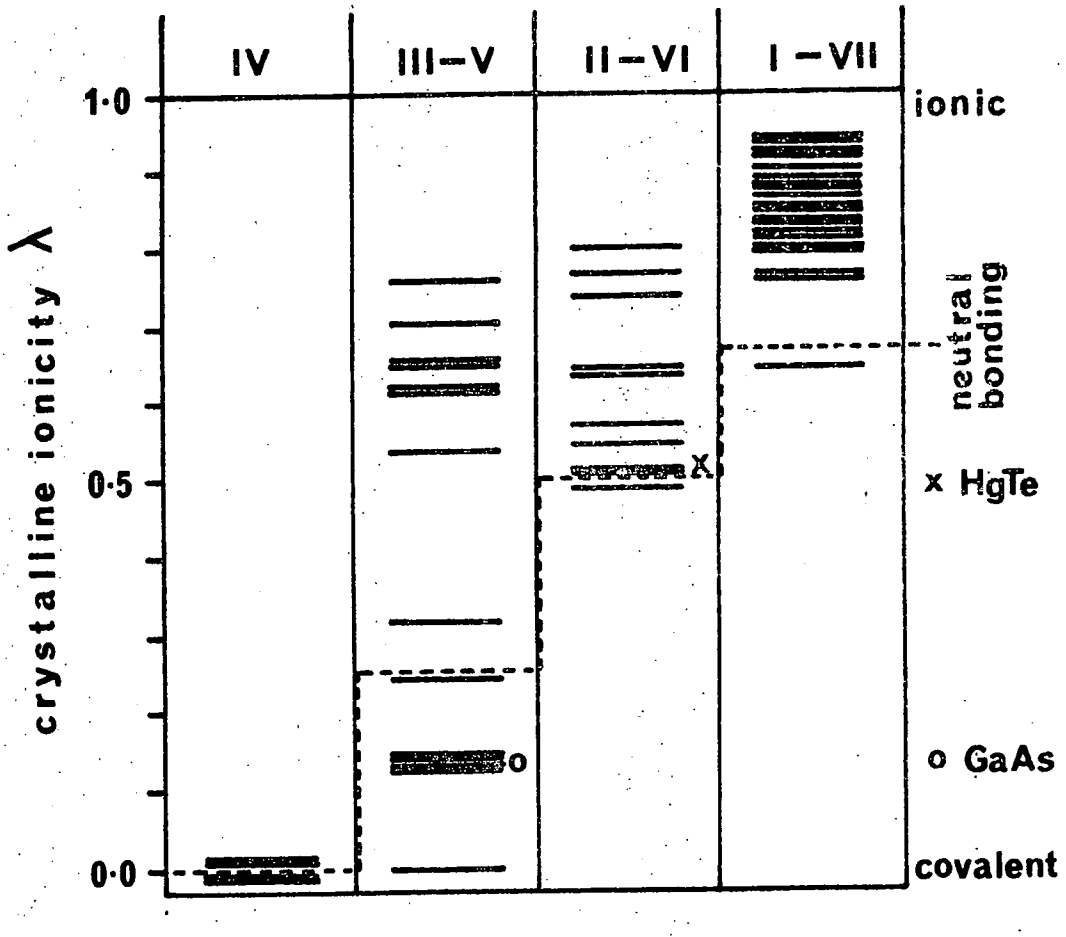

Crystalline Ionicity in the IV → I–VII Series

FIGURE 2.5

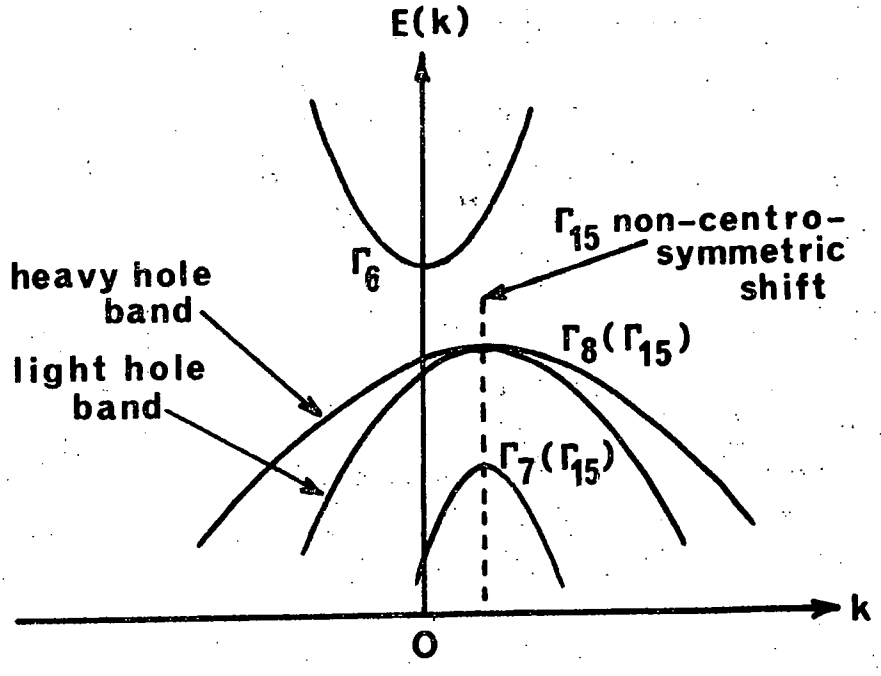

Spin-Orbit Splitting of the Zinc Blende

Γ_{15} Electron Band

FIGURE 2.6

Table 2.B lists charge transfer values reported for gallium arsenide. Agreement between the values from different measurement techniques is very good, indicating a correct value for the effective charge transfer of close to -0.5e : the bonding in gallium arsenide is intermediate between the covalent and neutral types. The direction of transfer does appear to violate the electronegativity principle, but it is quite in accordance with covalency theory (Pauling, 1960). No estimates of the ionicity of gallium arsenide from elastic constant data appear in the literature.

Few experimental evaluations of e* in mercury telluride have been made (Table 2.C). No indication of the sign of the charge transfer can be found from the techniques used: this accounts for the ambiguity in the λ values quoted. Even so, mercury telluride is more nearly neutral than either covalent or ionic.

Both gallium arsenide and mercury telluride fit into the trend of increasing ionicity through the IV $\longrightarrow$ I-VII sequence.

2.2 ELECTRON BAND STRUCTURE

In many respects the electronic band structures of the Group IV semiconductors and the III-V, II-VI and I-VII compounds are similar. In general, the energy gaps between the valence and conduction bands widen on moving horizontally across the periodic table from Group IV to I-VII.

TABLE 2B

Effective Charge Transfer in Gallium Arsenide

Reference	Measurement Technique	e*/e	λ
Attard et al 1969	X-ray Diffraction	-0.52±0.05	0.12
Attard 1968	X-ray Diffraction	-0.46	0.13
Zerbst and Boroffka 1963	Piezoelectric	-0.51	0.12
Hilsum 1966	Optical	0.48†	0.13
Hambleton et al 1961	Optical	0.46†	0.13
Hass and Henvis 1962	Optical	0.51†	0.12

† Optical experiments give the magnitude of e* only; it has been assumed negative in the calculation of λ.

TABLE 2C

Effective Charge Transfer in Mercury Telluride

Reference	Measurement Technique	e*/e	λ
Dickey and Mavroides 1964	Optical	0.6	0.65 0.45
Alper and Saunders 1967	Elastic Constants	0.65±0.05	0.66 0.44
Suchet 1965	Optical	0	0.5
Wolff and Broder 1959	Cleavage	0	0.5

Table 2C

The zinc blende structure may be envisaged as a perturbed homopolar crystal, and its band structure calculated to a reasonable approximation by perturbation theory from the known $E(\underline{k})$ of the Group IV crystals (Herman, 1955). There is a tendency towards a direct minimum in the band gap at k=0 (Cardona and Pollack, 1966), the band gap decreasing with increasing atomic number. With the exception of indium bismuth, all the known III-V compounds are semiconductors: so too are the II-VI compounds, save for the two members of highest molecular weight, namely mercury selenide and telluride, which are semimetals with overlapping valence and conduction bands.

Spin-orbit interaction causes splitting of particular degeneracies in the bands. Especially important is that of the 3-fold $\underline{k}$=0 state Γ_{15} into a 2-fold Γ_8 state and a lower Γ_7. Figure 2.6 provides a general scheme for the band-edges in zinc-blende materials; there is one conduction band and three valence bands, the lowest of which (Γ_7) is usually called the split-off band. The split-off band energy is so far below the Fermi level that carriers in it play no significant part in most physical properties. However, heavy and light hole effects are usually apparent: both the Γ_8 bands are important. The absence of a centre of symmetry causes a shift of the Γ_{15} band maxima from $\underline{k}$=0. This is rarely important in the III-V and II-VI compounds as the shift is small (Hopfield, 1961; Mahan and Hopfield, 1964), but in materials in which the conduction band and valence band edges are close, such as

indium antimonide, α-tin, mercury selenide and mercury telluride, it is a significant feature.

2.2(a) GALLIUM ARSENIDE

The band structure of gallium arsenide fits well into this general scheme. The two-fold degeneracy of the valence band occurs in the close vicinity of the [000] position; the heavy-hole band has slight maxima sited just away from the Brillouin zone centre Γ in the <111> directions (Braunstein and Kane, 1962); the energy surfaces in the light-hole band are nearly spherical. The principal conduction band minimum is at $\underline{k}=0$, about 1.5 eV above the top valence band edge. The transport properties of electrones in gallium arsenide (Wolfe et al, 1970) are in agreement with the assumption that the principal [000] conduction band edge is parabolic.

There is a surrounding set of secondary minima some 0.36 eV above the principal conduction band minimum. This particular feature allows the development of a hot electron population in gallium arsenide, of great technological importance as the source of the Gunn effect. These minima have long been thought to lie in the <100> directions (Figure 2.7). A third set of minima has been reported higher up in the <111> directions (Ehrenreich, 1960). The results of recent investigations (for example Balslev, 1968, and Collins et al, 1970) suggest a reversal of this picture, with the <111> conduction band minima about 0.4 eV above the principal minimum and the

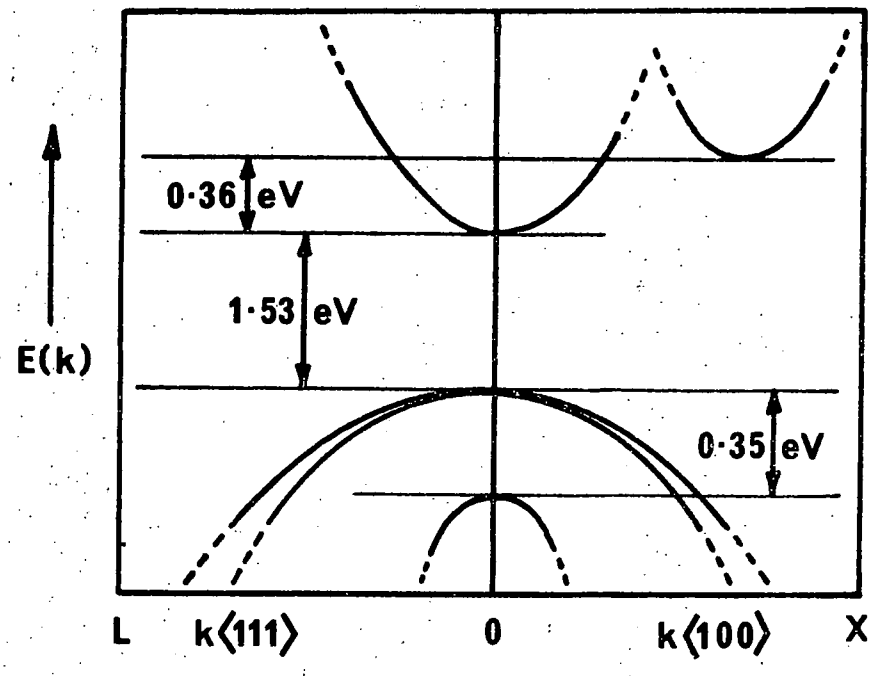

A Simplified Band Structure for Gallium Arsenide

FIGURE 2.7

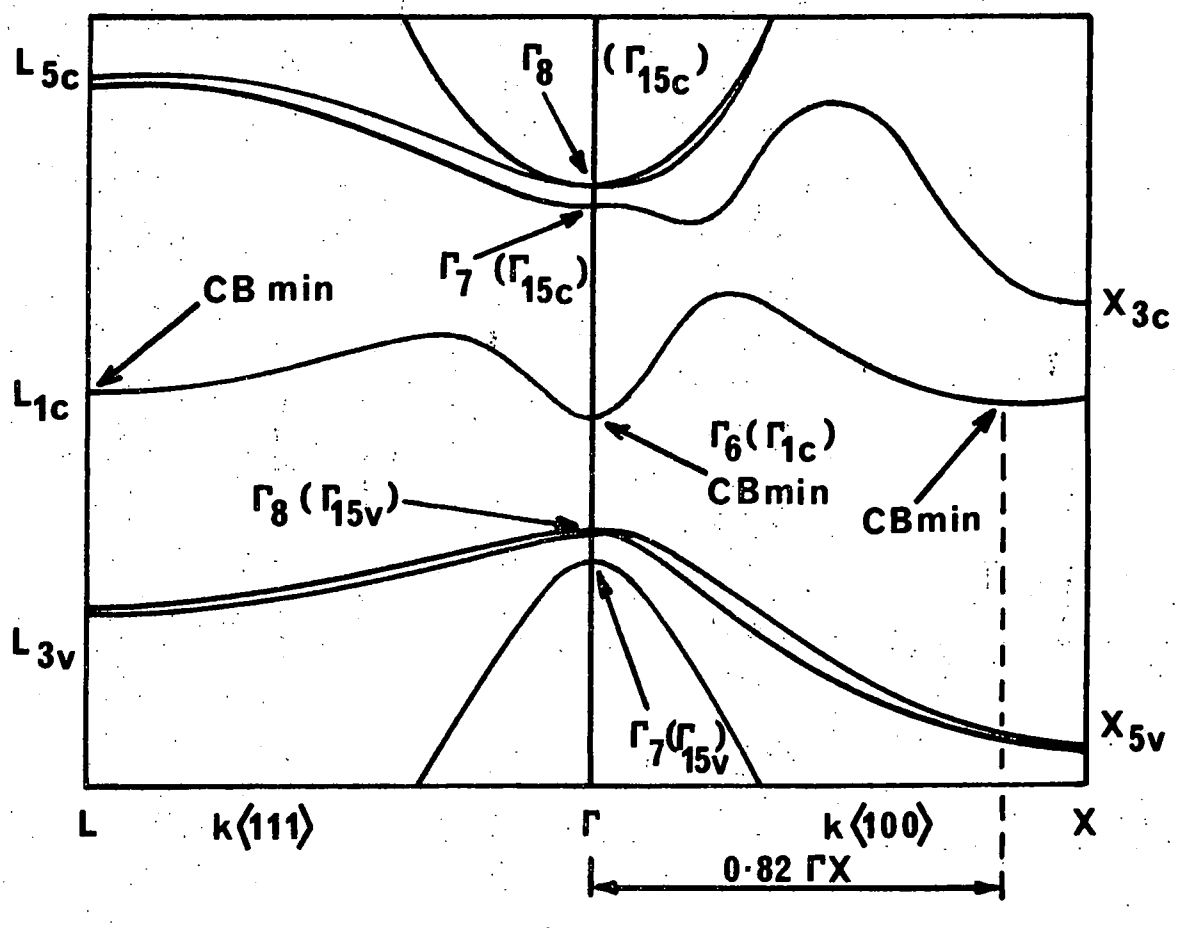

The Band Structure of Gallium Arsenide Including Spin-Orbit Splitting

FIGURE 2.8

<100> ones 0.8 eV above. Figure 2.8 shows the band scheme calculated from the self-consistent orthogonalised-plane-wave model of Collins et al (1970). The conduction band minima are indicated.

2.2(b) MERCURY TELLURIDE

Despite extensive published measurements of the galvanomagnetic, thermoelectric, thermomagnetic and optical properties of mercury telluride, some doubt still exists as to a correct model for the band structure. However, there is now unanimity of opinion on the semi-metallic nature of the compound. Groves and Paul (1963) have suggested an inverted band scheme for grey tin: Harman et al (1964) extended this approach to mercury telluride, on the basis of Kane's model for the band structure of indium antimonide (1957). The main features appear in Figure 2.9. The conduction band is separated from a nearly mirror image valence band by about 0.14 eV. Relatively high carrier concentrations at low temperatures evidence the presence of another valence band, that marked Γ_8 in Figure 2.9. Current carriers are present only in the conduction band and this second valence band. The model is consistent with the general systematics of III-V and II-VI compounds of the zinc-blende structure: the heavy hole band of the III-V compounds (Figure 2.6) is now degenerate with the conduction band at $\underline{k} = 0$.

Rodot and Rodot (1959) have found that the conduction band is isotropic, with its lowest edge at the

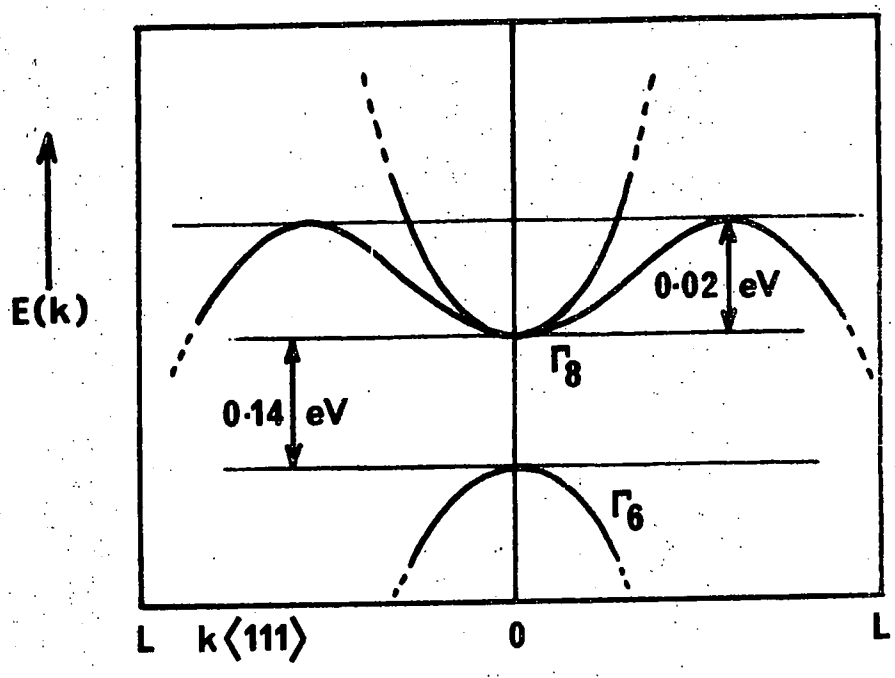

A Proposed Band Structure for Mercury Telluride

FIGURE 2.9

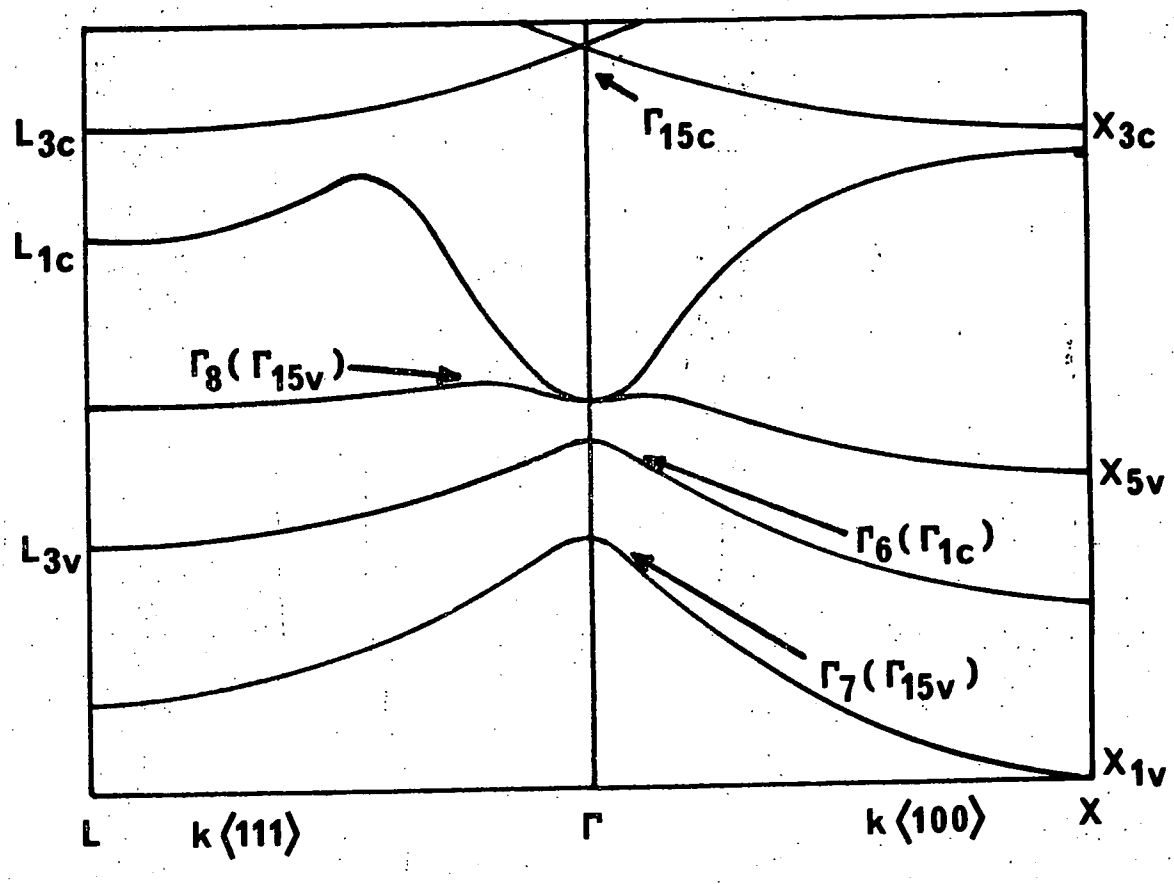

The Band Structure of Mercury Telluride Including Spin-Orbit Splitting

FIGURE 2.10

[000] position. Variation of the electronic effective mass with doping level (Szymanska et al, 1965) demonstrates that the conduction band is non-parbolic.

If the Fermi level is adjusted through doping to be close to the bottom of the conduction band, two sets of electrons and one set of holes should be involved in transport processes. Many unsuccessful attempts have been made to fit experimental data for mercury telluride using only two carrier sets as a simplification (see, for example, Ivanov-Omskii et al, 1965). Yamamoto and Fukuroi (1966) conclude from Shubnikov-de Haas measurements that mercury telluride is characterised by two distinct conduction bands involving electrons of different masses, in agreement with the Harman model. Kolosov and Sharavskii (1966), however, find that to fit the thermomagnetic effects two hole sets and one electron set are required.

The majority of the available evidence favours the inverted band model: this will be adopted. Figure 2.10 shows a more complete model derived from band structure calculations. Electrons occupy two concentric spheres in the Brillouin zone, centred at Γ. Eight hole pockets, aligned in the <111> directions, closely surround the electron spheres (Figure 2.11).

2.3 PHONON DISPERSION CURVES

Phonon dispersion curves of energy E against wave-vector $\underline{q}$ bear a strong resemblance to electron E - $\underline{k}$

E_f just below ⟨111⟩ valence band maxima

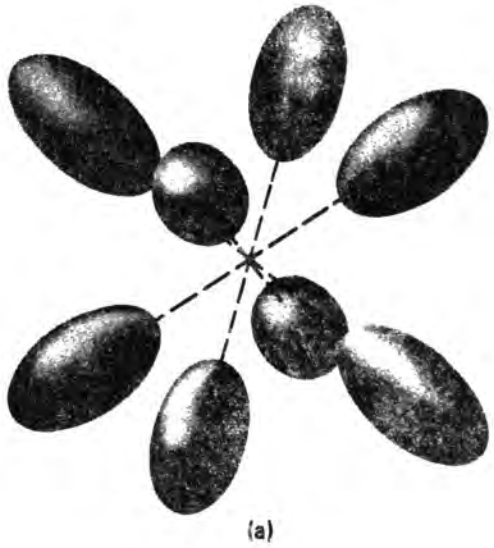

(a)

E_f just below ⟨110⟩ valence band maxima

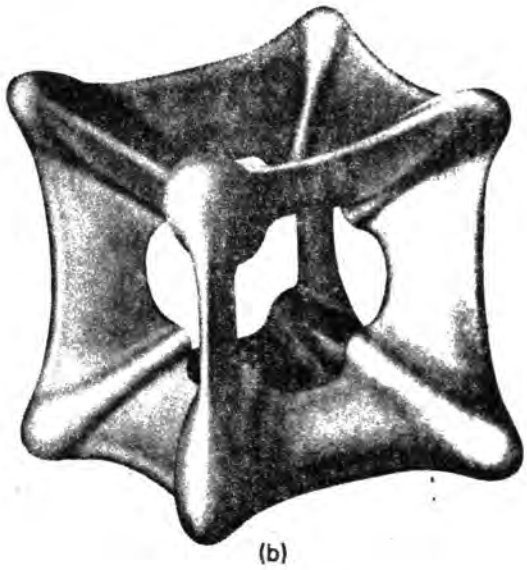

(b)

E_f just below conduction band minimum

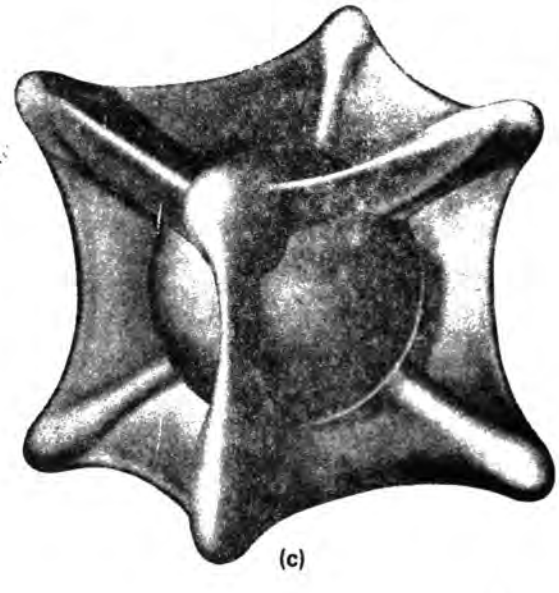

(c)

(after Whitsett & Nelson)

The Hole Fermi Surface of Mercury Telluride

FIGURE 2.11

diagrams: they lie within the same Brillouin zone and exhibit gaps between successive bands. Each band constitutes three branches, analagously to spin-orbit splitting in electron bands. In particular directions two of the branches can be degenerate, for example in the <111> directions of the zinc-blende structure where there is a single longitudinal acoustic mode and two degenerate transverse modes of equal velocity. At any temperature there is a finite probability of all levels being occupied, unlike the electron levels.

The lowest phonon band contains acoustic frequencies up to about 10^{12} Hz. Ultrasonic frequencies fall within the bottom 1% of this range, so their phase velocities may be taken to define the slope of the E - $\underline{q}$ diagram at the origin.

For gallium arsenide the phonon dispersion curves have been constructed by Dolling and Waugh (1964) from neutron spectrometry (Figure 2.12). Calculated phonon dispersions (Banerjee and Varshni, 1968) based on the 'rigid ion' model are in satisfactory agreement. Contributions to the crystal forces are taken in two parts; short-range forces, up to the second nearest neighbours, and long-range Coulombic forces. The latter are written in terms of effective ionic charge, and from the analysis a value of 0.567 is derived for e*, which compares well with the ionicities quoted in Table 2.B (the corresponding λ is 0.11, assuming e* negative).

Figure 2.13 shows the phonon frequency distribution

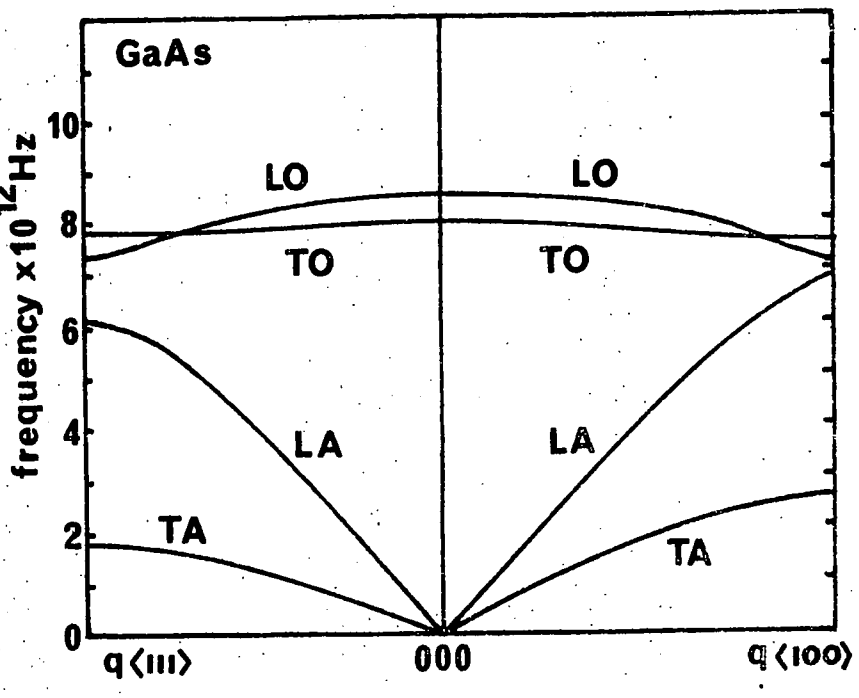

The Phonon Dispersion Curves for Gallium Arsenide

FIGURE 2.12

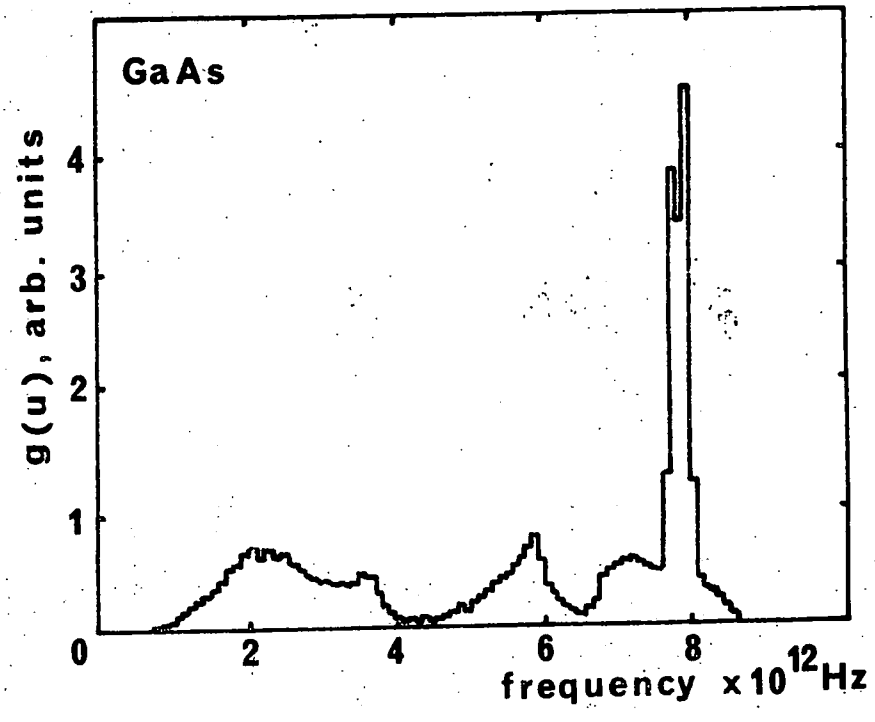

The Phonon Frequency Dispersion Function for Gallium Arsenide

FIGURE 2.13

function obtained by Banerjee and Varshni for gallium arsenide. The shape is similar to that of the function presented by Dolling and Cowley (1966) in a more complicated analysis.

No theoretical or experimental evaluations of phonon dispersion curves for mercury telluride appear in the literature.

CHAPTER 3

"PREPARATION AND EXAMINATION OF SINGLE CRYSTAL SAMPLE"

3.1 ULTRASONIC SAMPLE REQUIREMENTS

Ultrasonic responses of crystals may be evaluated by injecting ultrasonic waves and observing their subsequent behaviour. For simplicity the waves are usually confined to a single axis of propagation between two opposite plane parallel reflecting boundaries (Figure 3.1). Sidewalls must be remote from the region of propagation to prevent the interference of stray reflections; to avoid requirement of samples of infinite cross section a parallel beam of ultrasonic waves is desirable. Beam divergence may be caused by lack of face parallelism, flatness or 'finish' (Figure 3.2). The lower the attenuation of ultrasonic waves in a crystal and the higher the wave frequency, the more critical the flatness and parallelicity of the crystal faces becomes. Typically, the faces may be lapped flat and parallel to between 10^{-4} and 10^{-6} radians. A comprehensive treatment of non-parallel effects is given by Truell et al (1969), and a discussion appropriate to the present case appears in Chapter 5 of this thesis.

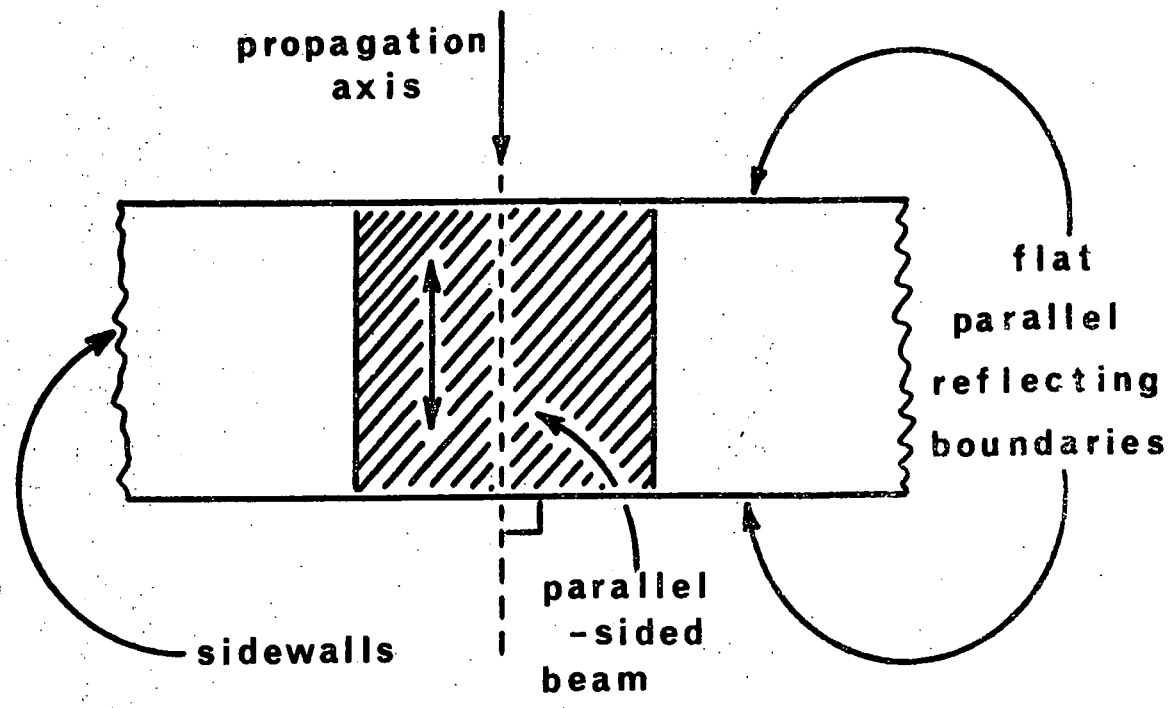

The Simple Ultrasonic Configuration

FIGURE 3.1

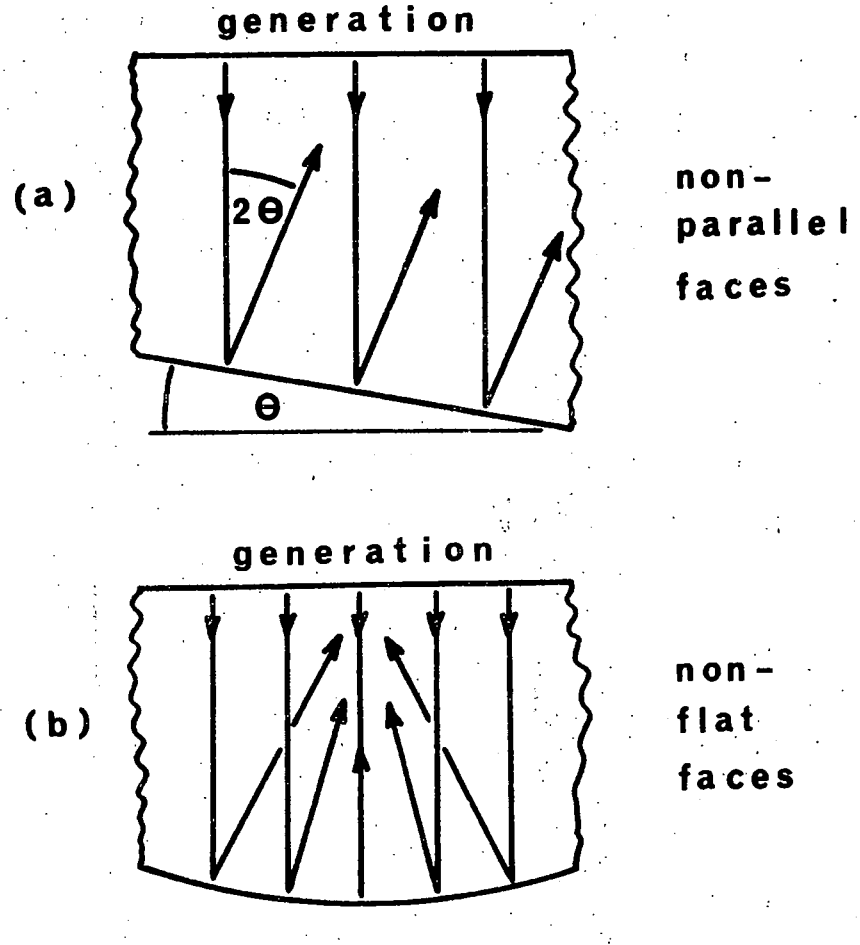

Ultrasonic Beam Divergence
following Reflection

FIGURE 3.2

In the pulse-echo technique adopted in this work, pulses of ultrasonic waves of 0.5 μs length are injected into the crystals from a transducer on one parallel face (Figure 3.3). The echoes returning to the transducer are monitored, and the velocity and decay-rate of the ultrasonic waves are deduced. Velocities are characteristically about 10^5 cm sec^{-1}, and therefore the pulses are of the order of 10^{-1} cm in length. Resolution of successive echoes demands that the crystal be much longer than this: in practice a length of 1 cm is ideal.

Two further beam-spreading mechanisms are diffraction and energy-flux deviation. Diffraction may be reduced by making the ultrasonic beam width very much greater than the wavelength; widths of a substantial fraction of a centimetre are required in the frequency range of 10 MHz to 750 MHz covered in this work, demanding crystals of about 1 cm across (Figure 3.4). In a general crystallographic direction the ultrasonic energy flux vector does not lie along the propagation direction (see Figure 3.5). This phenomenon is described more fully in Chapter 4. Deviations from the chosen propagation directions in gallium arsenide and mercury telluride have been shown to be small; 1 cm wide crystals are adequate.

Analysis of the ultrasonic data is facilitated by careful choice of the propagation directions: the parallel faces must be orientated so that they are perpendicular to the chosen directions. In crystals of anisotropies associated with the zinc-blende structure, orientation to within 1^o of a chosen direction reduces errors in the measurement of

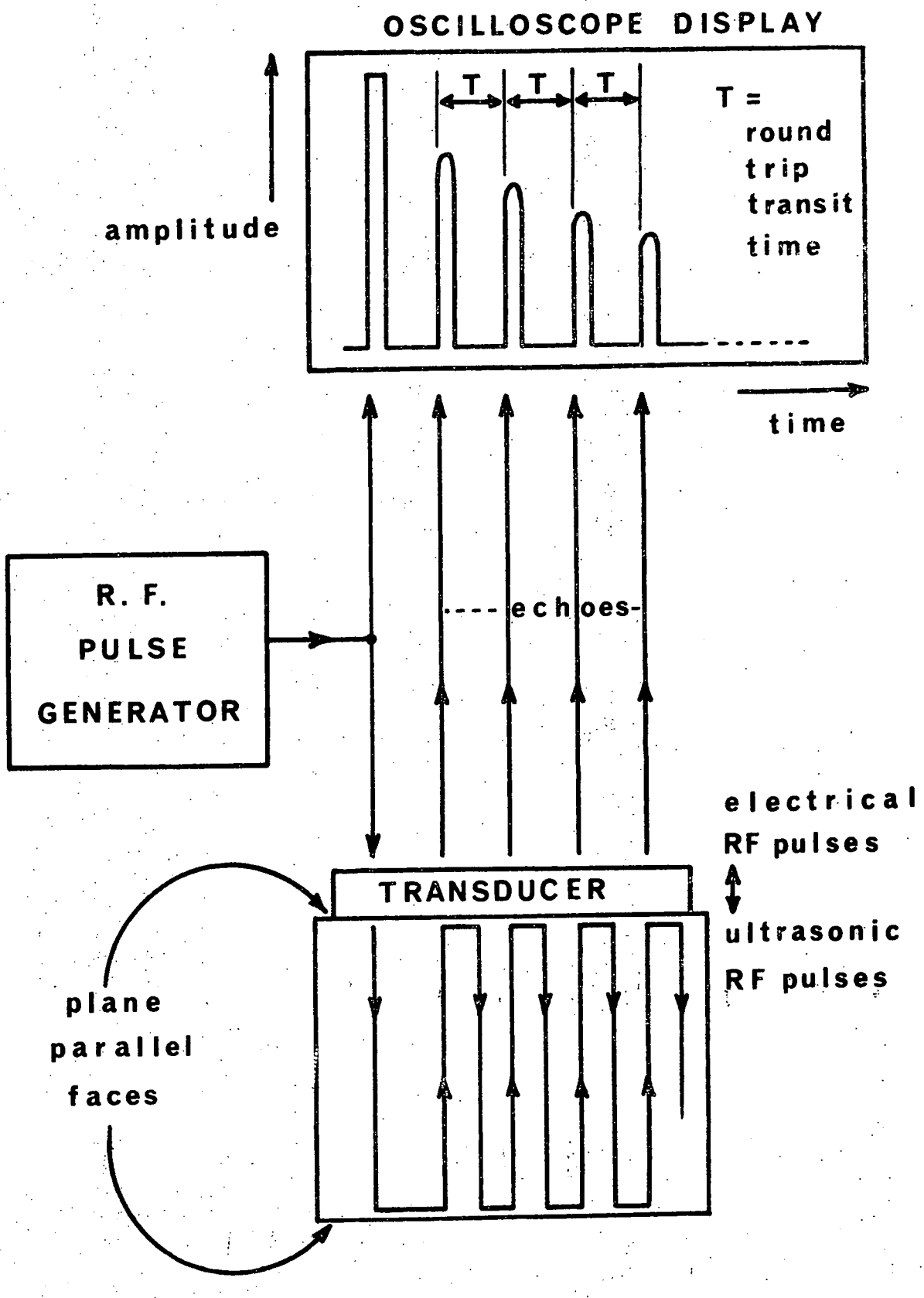

A Schematic of the Simple Pulse-Echo Ultrasonic Method

FIGURE 3.3

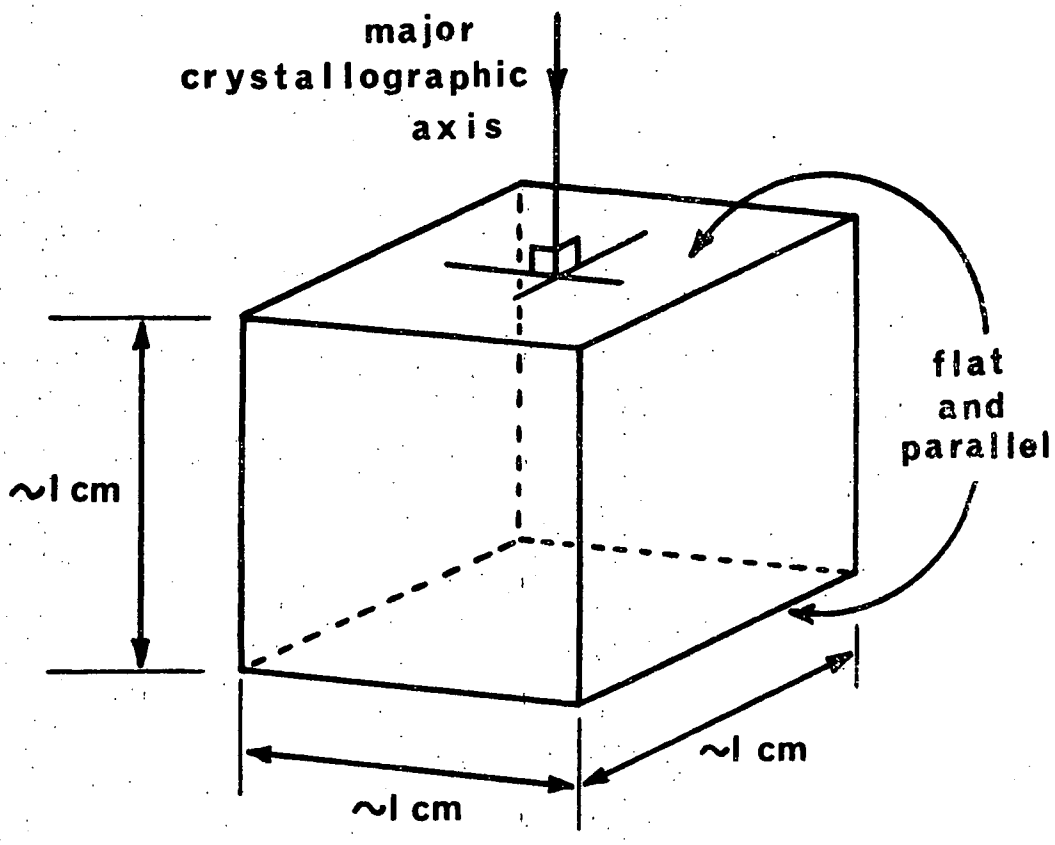

Ultrasonic Single Crystal Sample Requirements

FIGURE 3.4

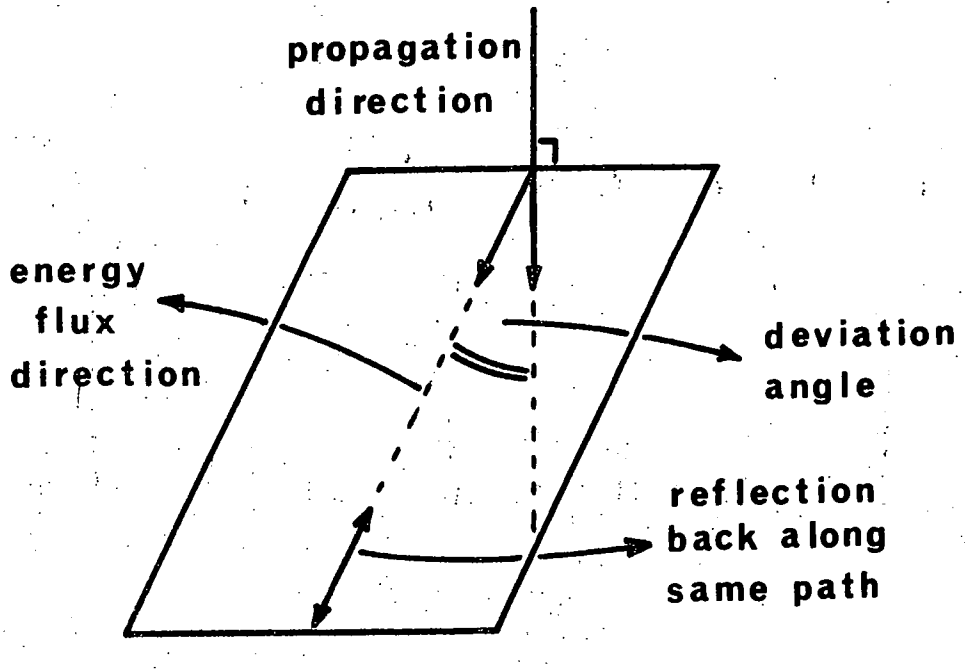

Energy Flux Deviation for Propagation in a General Direction in a Crystal

FIGURE 3.5

velocities, for example, below about 0.03% (Truell et al, 1969).

3.2.(a) CRYSTAL SOURCE AND CHARACTERISATION

Large single crystals of undoped boat-grown n-type gallium arsenide were kindly supplied by Dr. G.D. Pitt of Standard Telecommunication Laboratories (STL), in the form of 1 cm cubes, with faces aligned perpendicular to chosen crystallographic axes to within $\frac{1}{2}^{o}$.

It is convenient to characterise different crystals of a semiconductor by their electrical properties. For gallium arsenide Wolfe et al (1970) have shown that at 77 K the electron mobility may be related to the total ionised impurity density, (Nd + Na), where Nd is the density of donor ions and Na that of acceptor ions (Figure 3.6): at this temperature the mobility is dominated by ionised impurity scattering. Figure 3.7 shows the Hall mobilities measured over a wide temperature range by Stillman et al (1970) for three gallium arsenide samples of differing electron concentrations. At 300 K the controlling factor is polar mode scattering, but variation in mobility with carrier concentration is still that given by the change in ionised impurity scattering: the relation of Wolfe et al should still hold at 300 K. Comparison of the total ionic impurity concentrations (Nd + Na) and the excess electron concentrations n, equivalent to (Nd - Na) assuming donation or acceptance of a single carrier by each ion, gives an indication of the relative purity of the crystals (Harman, 1967).

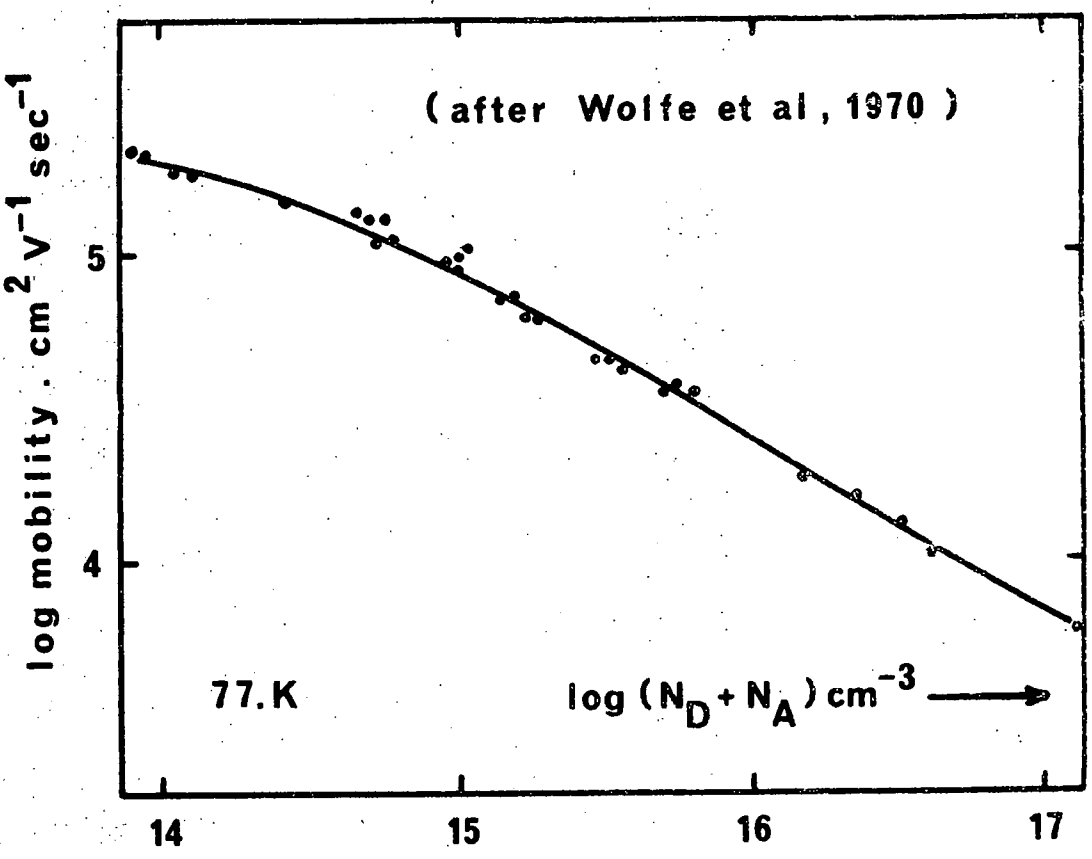

Mobility in n-GaAs: a Function of Total Ionised Impurity Density, ($N_D + N_A$)

FIGURE 3.6

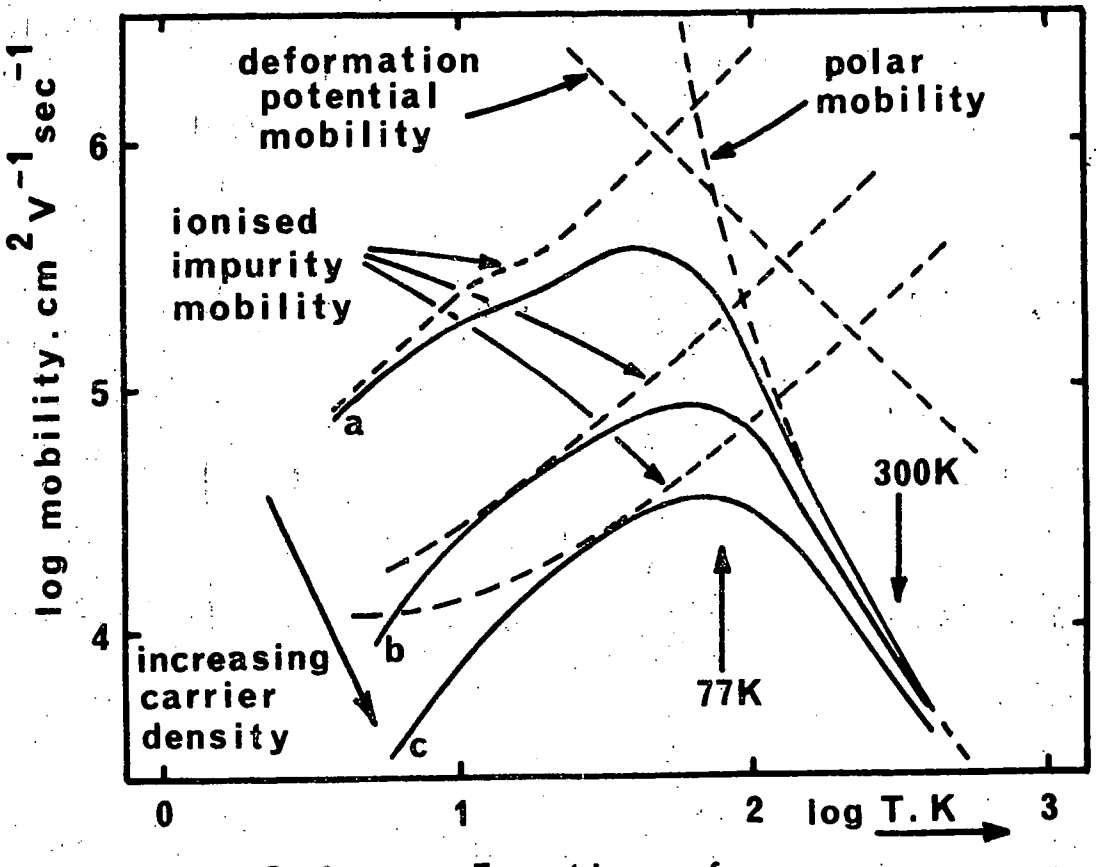

Mobility in n-GaAs: a Function of Temperature, for $n = 2{\cdot}7 \times 10^{13}$ (a), $7{\cdot}7 \times 10^{14}$ (b) and $3{\cdot}1 \times 10^{15}$ (c) cm^{-3} (after Stillman)

FIGURE 3.7

Figure 3.8 shows the mobilities of a large number of samples of gallium arsenide grown by a variety of methods (Bridgman, Czochralski, zone-melting, epitaxial techniques, etc.). Values are representative of those appearing in the literature up to 1973. The higher the mobility for a given excess electron concentration, the higher is the proportion Nd of (Nd + Na). The electrical parameters of the crystals supplied by STL to this laboratory were as follows.

At 300 K:

Excess electron concentration $\eta = 1.30 \times 10^{16}$ cm^{-3}

mobility $\mu = 4700$ cm^2 V^{-1} sec^{-1}

resistivity $\rho = 0.01$ ohm cm

These crystals appear to be of a quality comparable with those from other sources; they fit into the centre of the trend towards lower mobility with increasing carrier concentration.

3.2(b) HEAT TREATMENT

One necessary step in the fabrication of cadmium sulphide transducers on gallium arsenide is heat treatment at 500°C for 5 minutes (Section 5.1(f)). It is well known that n-type gallium arsenide becomes p-type or less n-type as a result of heat treatment. Copper from the heat-treatment container (Edmond, 1960) or the cleaning reagents used is considered to be responsible. While annealing out of growth defects (Blanc et al, 1964) would lead to an improvement of the crystals, the in-diffusion of contaminating impurities should be avoided if possible.

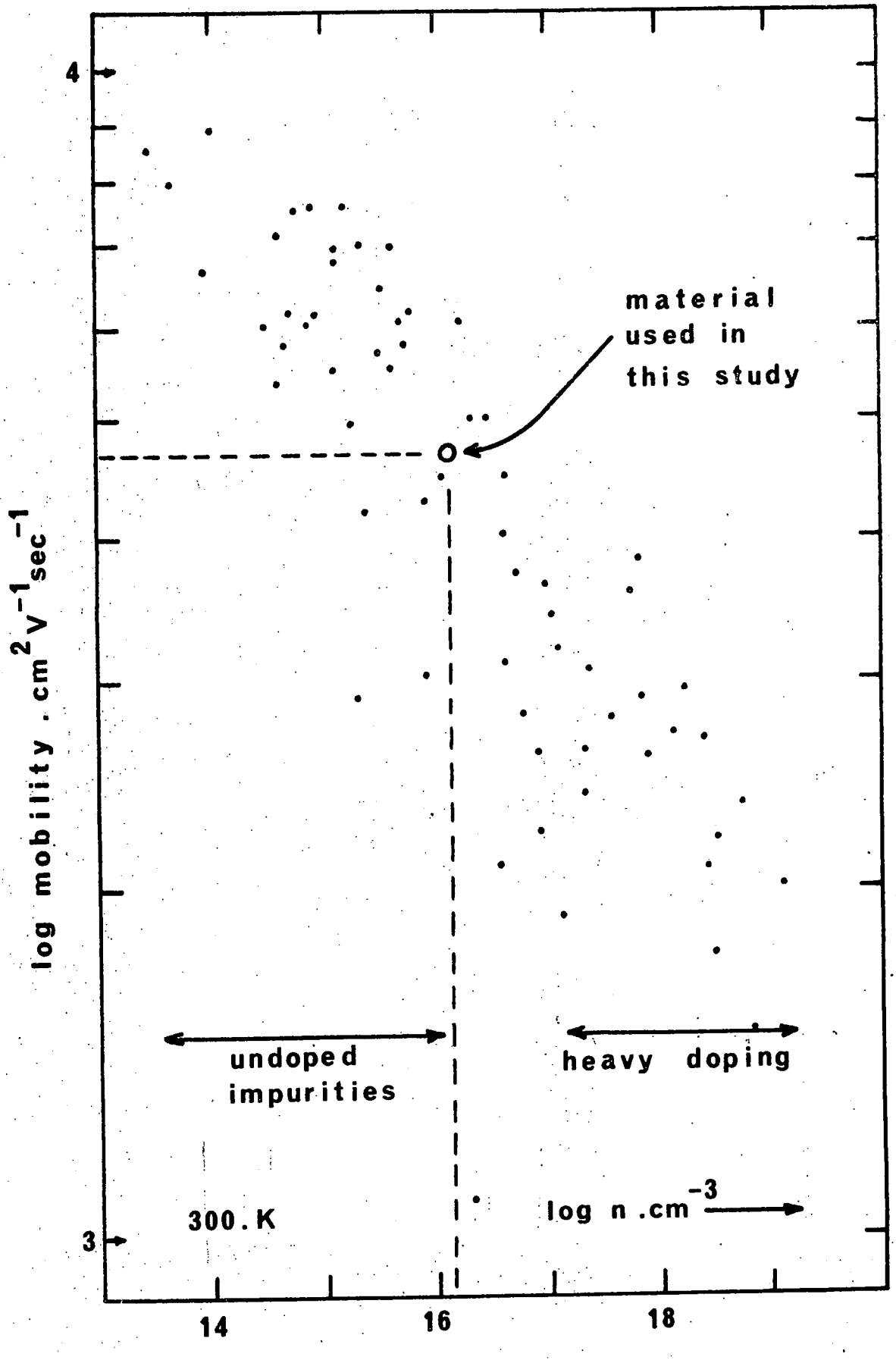

Mobility in n-GaAs : a Function of Excess Electron Concentration, n.

FIGURE 3.8

The effects of heat-treatment on gallium arsenide, and especially undoped boat-grown gallium arsenide, have been extensively studied optically by Hwang (1968). Photoluminescence is strongly dependent on defect concentration: changes in intensity after heat-treatment may be related directly to defects caused by the in-diffusion of impurities, and thus to changes in carrier density. Figure 3.9 shows changes in the electron concentration of n-type gallium arsenide of initial concentration $3x10^{18}$ cm^{-3} electrons as a function of annealing time (after Hwang, 1969.a). For the temperature (500°C) and 'annealing time' (5 minutes) used in this work, we should expect the change in electron concentration to be less than $1x10^{16}$ cm^{-3}. The initial electron concentration in the crystals used in this work was $1.30x10^{16}$ cm^{-3}, two orders of magnitude below that described in Figure 3.9. The variation in electron concentration decrease with initial electron concentration is shown in Figure 3.10 (after Hwang, 1969.b). The decrease for crystals of $1.30x10^{16}$ cm^{-3} is at least one order of magnitude below that for crystals of $3x10^{18}$ cm^{-3}: changes in concentration during the heat treatment employed in this work should be less than $1x10^{15}$ cm^{-3}, or 8% of the initial electron concentration.

3.2(c) X-RAY EXAMINATION AND ETCHING BEHAVIOUR

The three high symmetry axes ([100], [111] and [110]) of the zinc-blende structure were chosen for ultrasonic studies (see Chapter 4). Figure 3.11 shows Laue back-reflection X-ray photographs of gallium arsenide taken along these directions. To establish the degree of surface damage caused by mechanical polishing of the crystal faces,

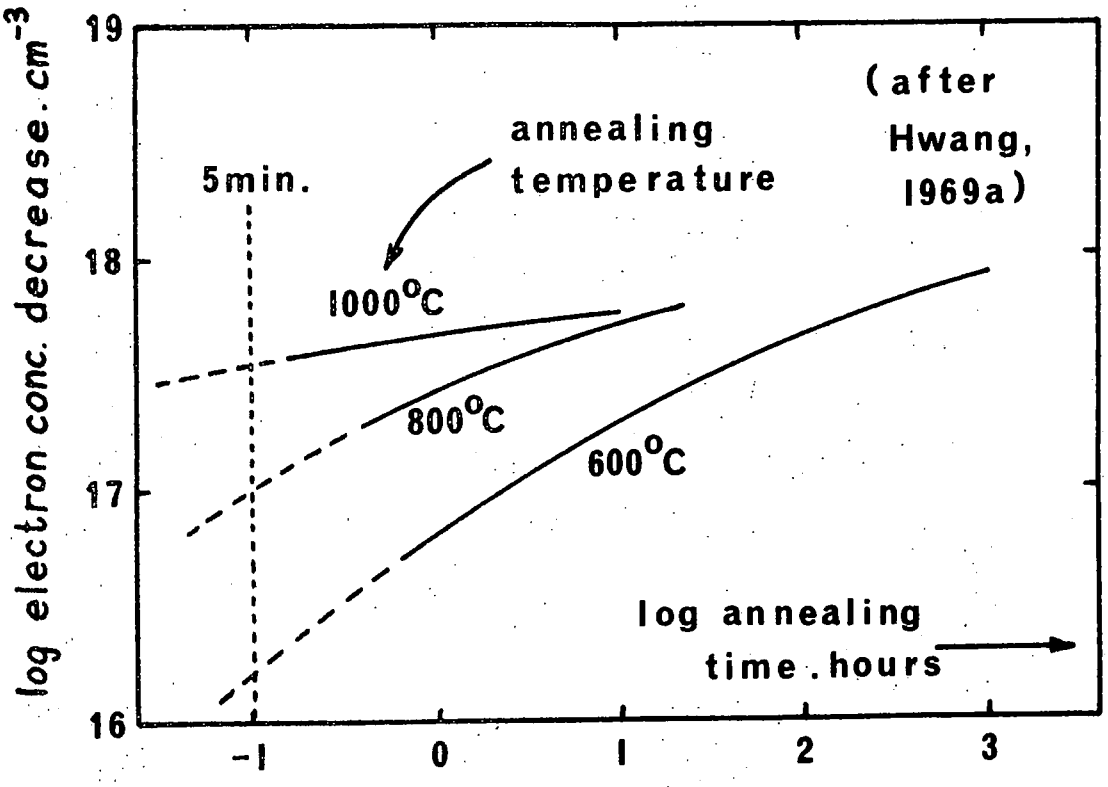

Decrease in Electron Concentration of n-GaAs: a function of Annealing Time for Initial $n = 3 \times 10^{18} cm^{-3}$

FIGURE 3.9

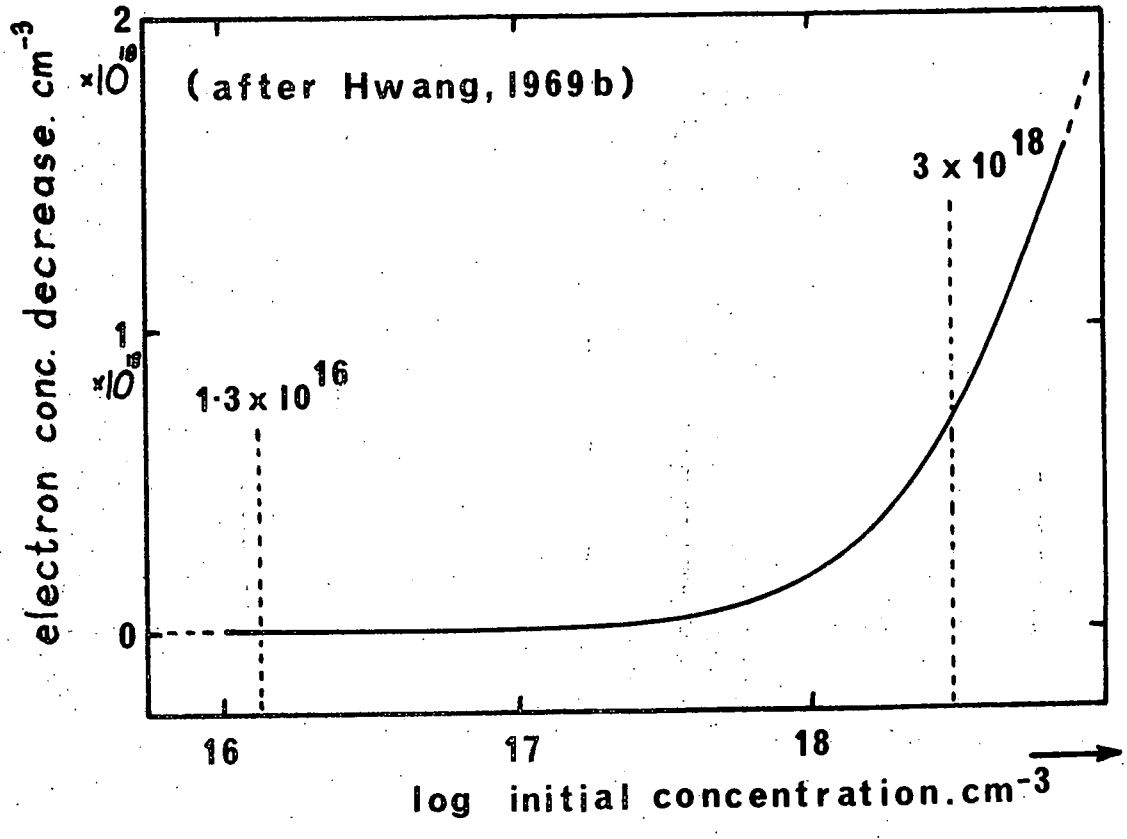

Decrease in electron concentration of n-GaAs after a three hour anneal at 800°C.

FIGURE.3.10

[100] axis : 4-fold symmetry

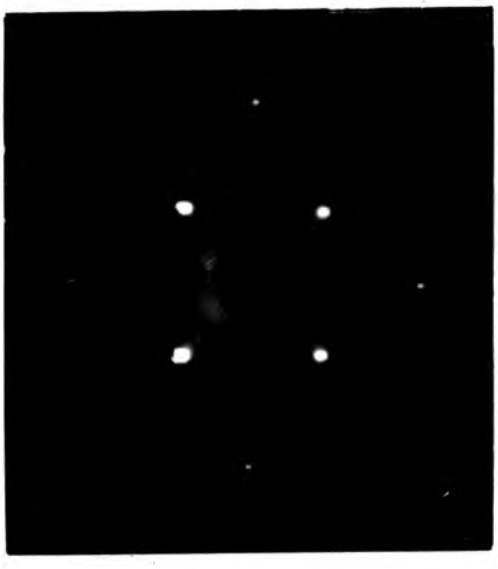

etched surface

[111] axis : 3-fold symmetry

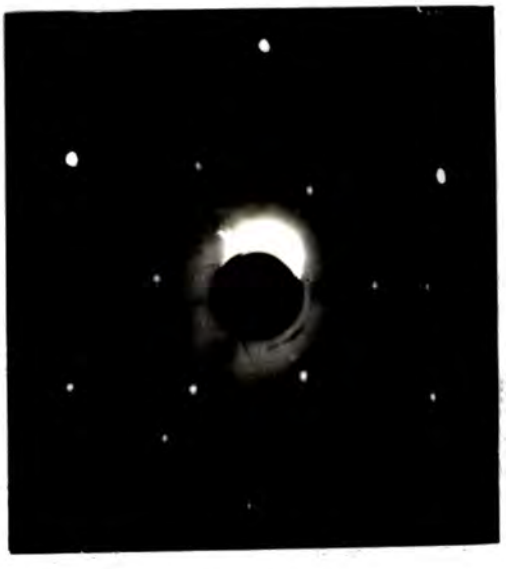

etched surface

[110] axis : 2m symmetry

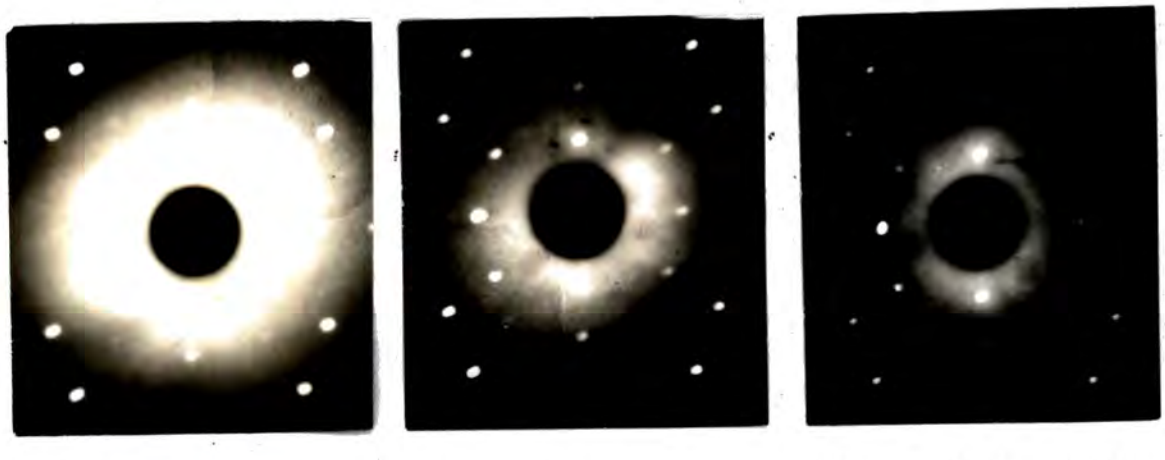

polished surface 5μ etched surface 10μ etched surface

The X-ray back reflection characteristics of gallium arsenide.

FIGURE 3.11

photographs were taken along the [110] direction after mechanical polishing with 6 micron diamond paste and also after a subsequent chemical polishing with an etch of bromine in methanol. The rate of removal of material by this etch is dependent on the bromine concentration, 0.35% by volume of bromine giving a removal rate of 1 micron per minute (Hill and Holt, 1968). Etching was carried out to a depth first of 5 microns, then 10 microns, without unmounting the crystal to ensure that the same part of the surface was examined in each case. In all three photographs (see Figure 3.11) X-ray exposure time, development and printing were kept the same. The Laué photograph obtained from the mechanically-polished surface exhibits extensive spot-spreading, characteristic of highly strained material, and a strong background of random scattering, due principally to direct reflections from the 6 micron surface scratches. Much of the background disappears after etching away a 5 micron layer, but spot-spreading is still evident, although smaller. A further 5 micron etch exposes relatively unstrained material, as evidenced by the small spot-size: excessive strain caused by mechanical polishing apparently extends little further into the crystal than the surface damage itself. Figure 3.12a shows a photograph of a chemically polished (111) face.

The Ga {111} faces of gallium arsenide may be distinguished from the As {111} by use of the A-B etch of Abrahams and Buiocchi (1965), of composition 2ml H_2O, 8 mg $AgNO_3$, 1g CrO_3 and 1 ml HF. Figures 3.12b and 12c show etch pits formed on the Ga {111} and As {111} faces respectively. The pits on the Ga {111} faces are much more

(a) ×400

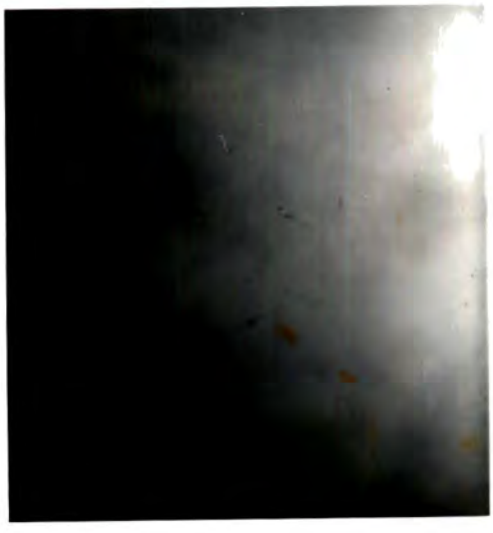

(b) ×400

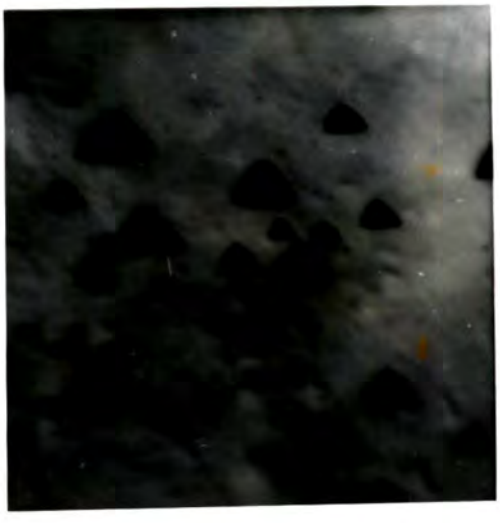

(c) ×1000

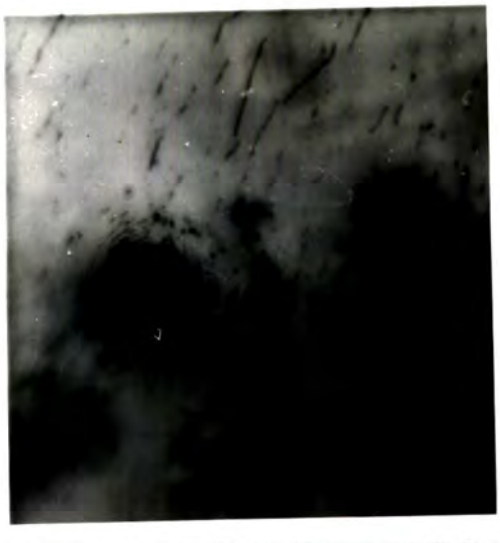

(d) ×1000

The etching characteristics of gallium arsenide:

(a) A chemically polished (111) face
(b) Triangular pits on a Ga(111) face
(c) Round pits with tails on an As(111) face
(d) Triangular pits of mixed sizes on a Ga(111) face in a region of high strain.

FIGURE 3.12

triangular than those of Abrahams and Buiocchi (1965). The circular pits on the As {111} faces have slight tails which point in the same direction as one of the points of the triangular pits on the opposite face. Figure 12d shows pits in a region of high strain, near the edge of a crystal, where groups of pits of widely differing sizes appear.

From comparison with similarly magnified photographs of a stage micrometer, the etch pit density is estimated to be about 10^4 cm^{-2} in the bulk of the crystals.

3.3(a) CRYSTAL GROWTH

Large single crystals of mercury telluride have been grown in this laboratory by T. Alper, using a vertical Bridgman technique, from either stoichiometric or from off-stoichiometric, tellurium-rich melts. Full details of the technique appear in his Ph.D. Thesis (Durham 1968): a brief summary follows.

Stoichiometry play an important part in determining the properties of compounds, particularly those containing volatile components: excess atoms of one component act like foreign impurity atoms. It is most useful to prepare stoichiometric crystals for physical studies. The complete liquidus curve for mercury telluride has been obtained by Delves and Lewis (1963) and by Strauss and Brebrick (1965). The compound melting point is 670°C ± 1 deg C (Delves and Lewis, 1963), higher than that of either component, as is usual for the II-VI binary systems. Figure 3.13 shows a schematic of the mercury telluride phase diagram, around the stoichiometric composition (Delves, 1965). The growth

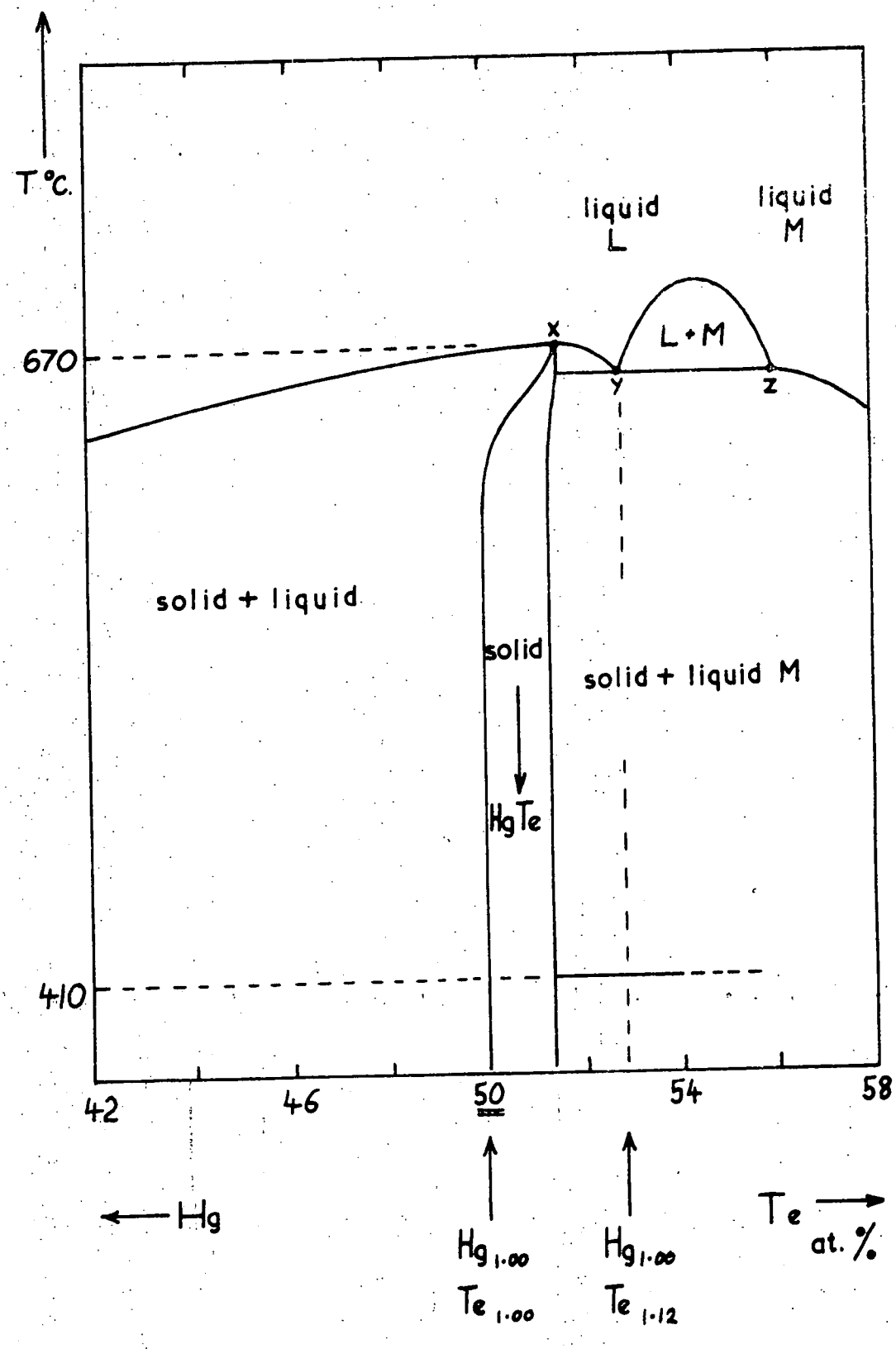

A schematic phase diagram for the mercury-tellurium system, close to the stoichiometric composition.

FIGURE 3.13

of single crystals from stoichiometric or near-stoichiometric melts yields erratic results (Giriat, 1964; Harman, 1967). Delves (1965) suggests that growth of fixed composition crystals may be achieved from the monotectic point labelled Y in Figure 3.13, where the solid is in equilibrium with the two immiscible liquids L and M, the latter containing excess tellurium. Crystals have been grown by Alper (1968) from both stoichiometric and off-stoichiometric melts, using the furnace detailed in Figure 3.14 (Furnace (1)). The furnace is in two sections as shown, to enable a high temperature gradient to be attained. Adjustment of the variable resistance at the centre of the windings enabled the temperature distribution of Figure 3.15a to be achieved. The component elements were sealed into an evacuated quartz growth tube of 24 mm bore (Figure 3.15b), pointed at the lower end to aid crystal nucleation (tip angle of 70^{o}), and placed in a stainless steel bomb to guard against the effects of any explosion: the vapour pressure of mercury at $700^{o}C$ is approximately 70 atmospheres (Brebrick and Strauss, 1965). The component mixture was heated up to $700^{o}C$ over three days, then the Eurotherm power was wound slowly down to lower the overall temperature profice and sweep the freezing temperature through the liquid mixture. Alper found that to grow large single crystals a temperature gradient at the melting point of greater than 5 deg C per cm and a rate of temperature profile fall of less than 2 deg C per hour were necessary. No preferred orientation was found.

Dislocation densities in both stoichiometrically and off-stoichiometrically grown crystals were found to be about 10^{7} per cm^{2}. In this work further mercury telluride

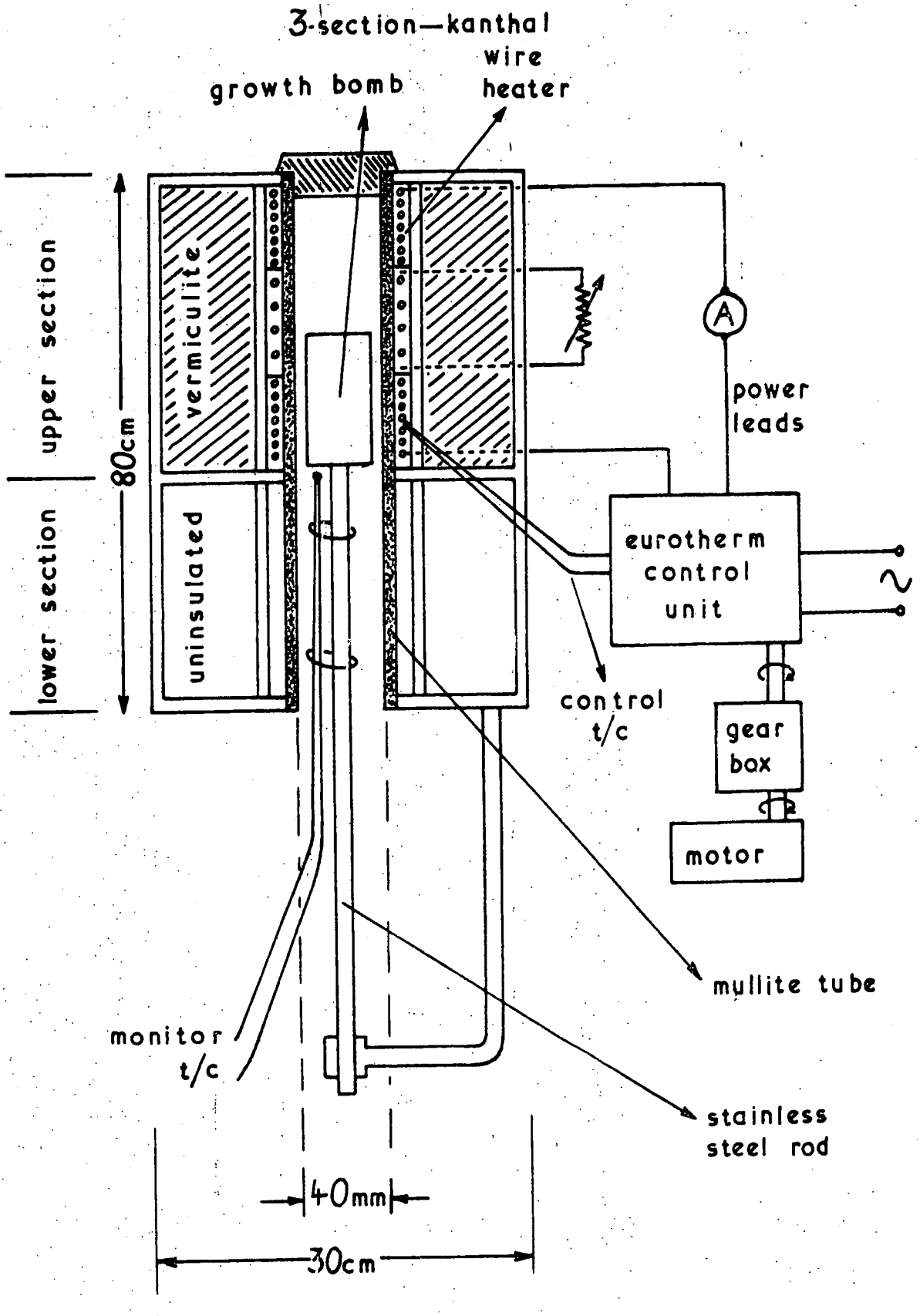

Crystal growth furnace number 1.

FIGURE 3.14

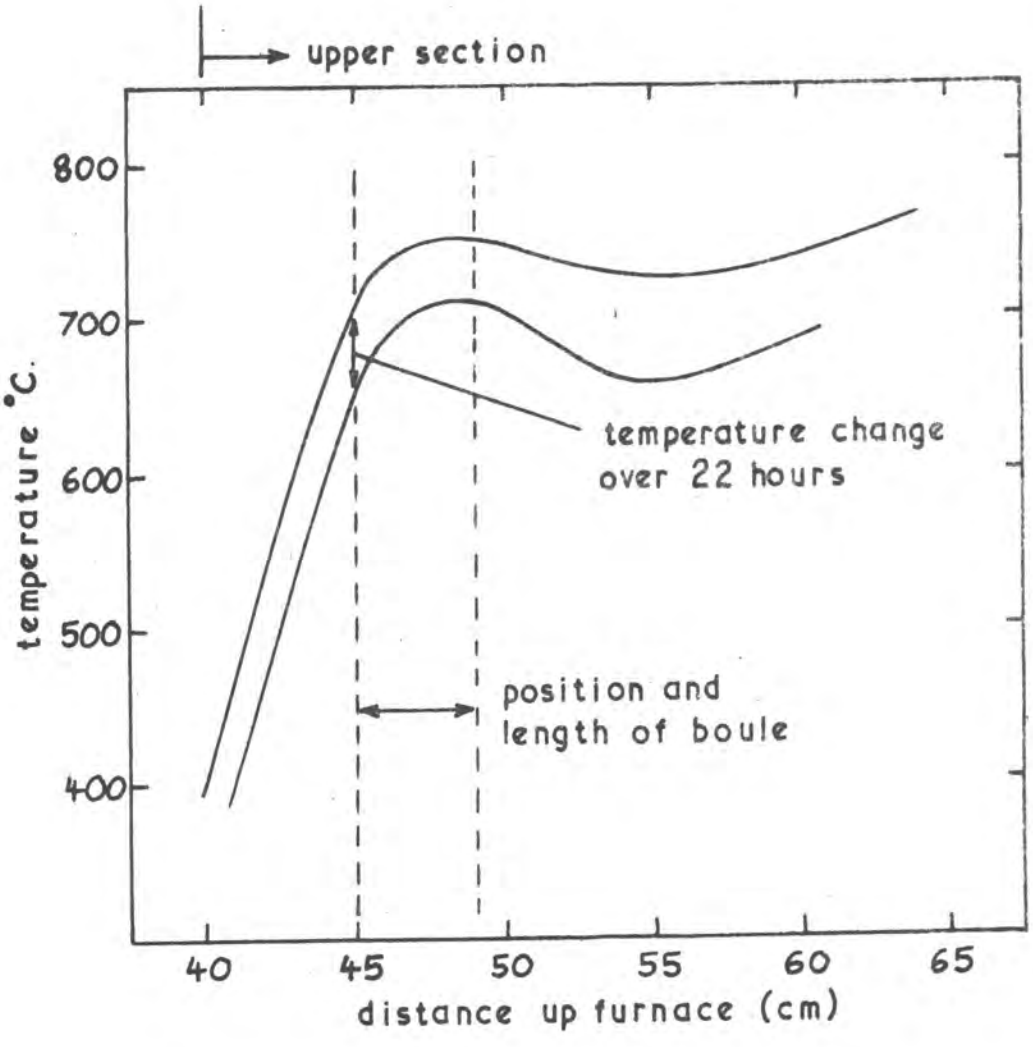

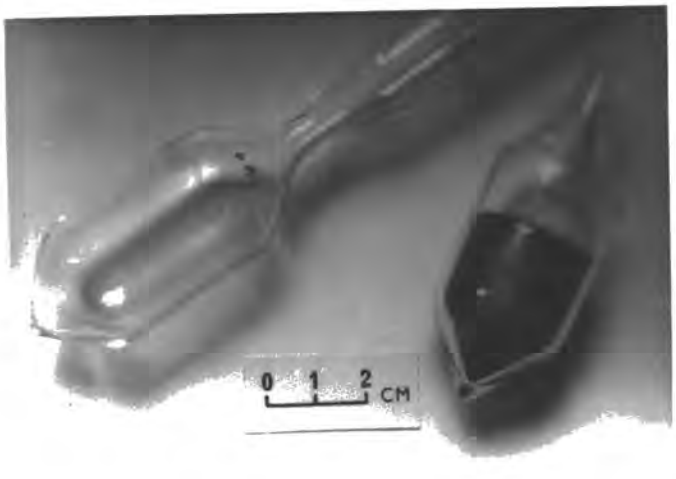

Crystal growth furnace number 1 : temperature profiles, a growth tube and a stoichiometrically grown HgTe sample.

FIGURE 3.15

crystals were grown in an unsuccessful attempt to reduce this figure. The furnace used was that employed in the growth of single crystals of arsenic in the laboratory (Jeavons and Saunders, 1968). A schematic diagram appears in Figure 3.16 (Furnace (2)). The heater-winding is four-sectional, to enable precise control of the temperature profile (Figure 3.17a) The mullite furnace tube is provided with a stainless steel liner to smooth out temperature undulations between heater turns. 'Gouy' modulation is applied to a switching galvanometer controller: the galvanometer pointer is pulsed from a multi-vibrator square-wave generator by about 5 deg C about the mean temperature. Switching of the power to the furnace occurs each time the pointer passes the set temperature, and proportional control ensues (Jewell, 1967). Inclusion of the stainless steel liner necessitates a reduction in the growth-tube diameter: 16 mm bore quartz tubing was used (Figure 3.17b). The 70^{o} tip angle of Alper's tubes was retained.

Cleanliness of the growth tube is of prime importance if crystal contamination is to be avoided. The stages of tube cleaning were as follows:-

1. A general overnight soaking in chromic acid.
2. Surface etching in concentrated (48%) hydrofluoric acid for 1 hour.
3. Baking at 10^{-4} mm of mercury to dry and outgas.

Mercury (99.9999% purity) and tellurium (99.999% purity) were supplied by Koch-Light & Co Ltd. Calculated amounts, totalling about 70 gm and corresponding to either $Hg_{1.00}Te_{1.00}$ or $Hg_{1.00}Te_{1.12}$, were tipped into the growth

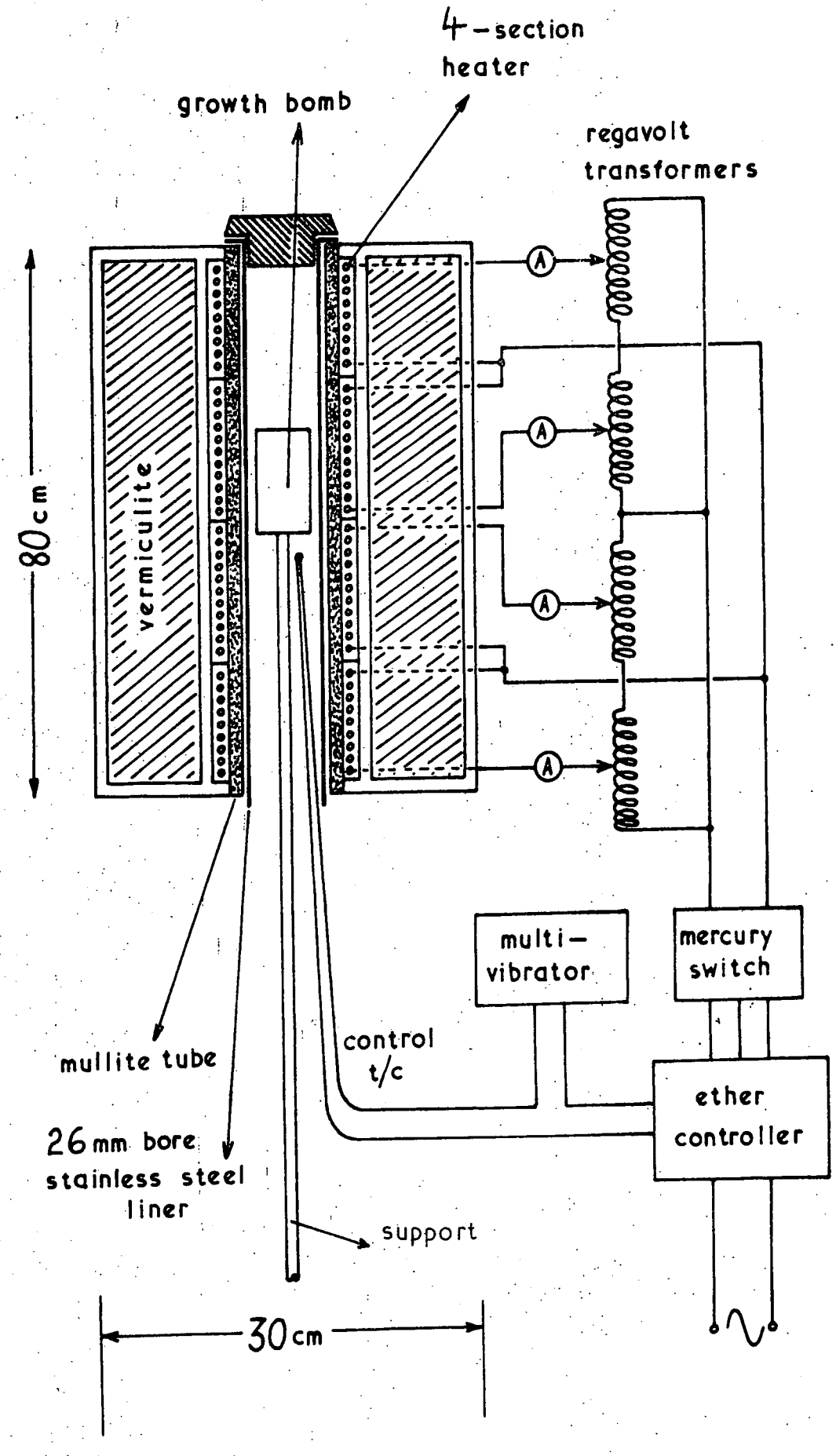

Crystal growth furnace number 2.

FIGURE 3.16

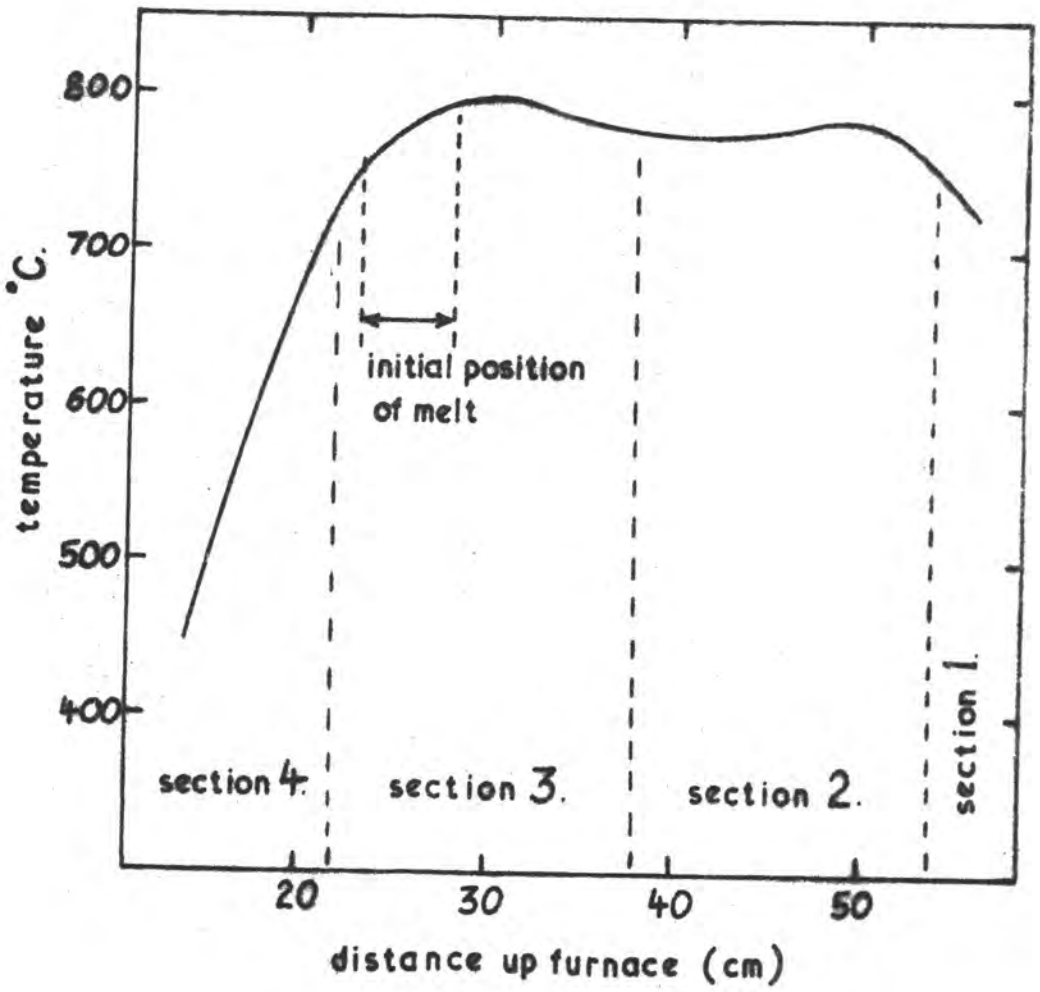

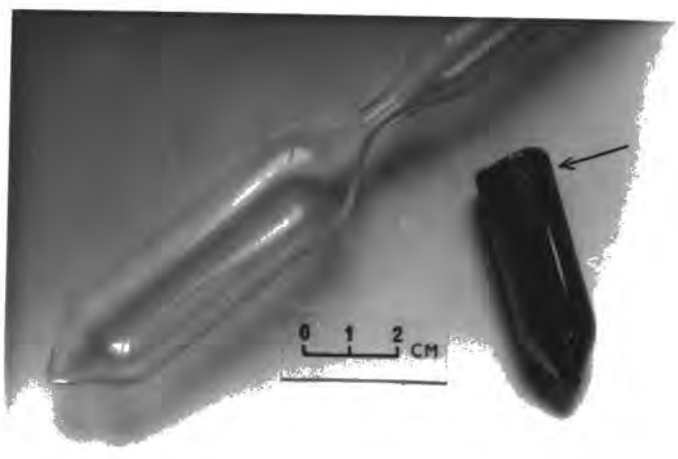

Crystal growth furnace number 2 : the temperature profile, a growth tube, an off-stoichiometrically-grown sample of HgTe : the abrupt line (arrowed) divides the stoichiometric and Te-rich solids.

FIGURE 3.17

tube, which was then evacuated to 10^{-4} torr for several hours and sealed at the constriction using an oxygen-gas flame. The charged tube inside its stainless steel bomb was located at the position shown in Figure 3.17a and the temperature gradually increased over three days. Balance of the variable parameters of this furnace proved difficult, but once completed a temperature stability of 0.1 deg C was achieved. The growth tube was wound down through the temperature gradient at 0.6 mm per hour. A crystal 16 mm in diameter and more than 3 cm long can be grown in about seven days. In spite of all these detailed experimental improvements the crystals grown still contained about 10^7 dislocations per cm^2.

3.3(b) HEAT TREATMENT AND CHARACTERISATION

The composition of mercury telluride samples grown by the Bridgman technique is not stoichiometric, owing to the loss of mercury vapour from the melt. Such samples are p-type, with an acceptor concentration of between 10^{17} cm^{-3} and 10^{19} cm^{-3} (Yamamoto, 1968). Brebrick and Strauss (1965) have suggested a homogeneity range of 0.6 ± 0.2 atomic % for as-grown mercury telluride: the electrical properties have been found to exhibit large variations with the technique of preparation (Giriat, 1964; Harman, 1967), evidencing an appreciable solidus field. We should expect crystals grown from stoichiometric and off-stoichiometric melts to have different electrical characteristics. Dahake (1967) has shown this to be the case. It is suggested by Quilliet et al (1962) that non-annealed samples contain micro-heterogeneities, perhaps mercury precipitates. Surface

precipitates of mercury were found on crystals grown in this work, even on those grown from a tellurium-rich melt. Internal and surface precipitates rather than evaporation from the melt could be the prime cause of mercury loss from the bulk crystal: even crystals grown from mercury-rich melts can show mercury defficiency.

Annealed crystals of mercury telluride exhibit much more uniform electrical properties (Giriat, 1964; Brebrick and Strauss, 1965). The table below shows the properties of two annealed crystals of mercury telluride, one from a stoichiometric and one from an off-stoichiometric melt (after Alper, 1968).

Annealed HgTe	Electrical Conductivity $\Omega^{-1}cm^{-1}$	Hall Coefficient $Rh.cm^3C^{-1}$	Hall Mobility $\mu h.cm^2V^{-1}_{sec^{-1}}$	Carrier Density $cm^{-3}x10^{17}$	Seebeck Coefficient $\mu V.deg\ K^{-1}$
Crystal from stoichiometric melt	420	-25	10600	2.9	-136
Crystal from off-stoich. melt	440	-25	10800	2.9	-136

Brebrick and Strauss (1965) concluded from electrical measurements that the homogeneity range of annealed mercury telluride is 0.01 atom %, much smaller than that of as-grown material: annealing of the samples grown in this work was undertaken. The three controlling parameters are temperature, mercury pressure and annealing time. At a fixed sample temperature

n-type samples are obtained for the higher pressures, p-type samples for the lower pressures, and intrinsic samples at an intermediate pressure (Quilliet et al, 1962). In the suggested annealing process two reactions take place. Firstly micro-heterogeneous precipitates dissolve (Quilliet et al, 1962), and secondly mercury atoms go into the mercury telluride from the surrounding vapour, ultimately making the compound stoichiometric (Giriat, 1964). If the annealing is carried beyond this point excess mercury appears in the compound, increasing the electron population and changing the crystal character from p-type to n-type. The optimum conditions for conversion to intrinsic material were found by Giriat (1964) to be a temperature of 300°C, a mercury pressure corresponding to its saturated vapour pressure at 300°C, and an annealing time of 100 hours: these were adopted by Alper and in this work. Annealing was carried out in a sealed, necked pyrex tube, with mercury on one side of the neck and the samples on the other.

Mercury telluride has not been subjected to the same commerical exploitation as gallium arsenide: far less effort has been put into its growth, and the same high level of crystalline perfection has not beenachieved. Figure 3.18 shows values of electron mobility currently available in the literature for annealed samples of mercury telluride. Quilliet et al (1962) postulate that the highest mobilities may be associated with the purest samples: on this basis great variation in sample purity is apparent in the figure. The electron mobilities of crystals grown in furnace (1) by Alper are indicated: they appear to be of 'average' purity.

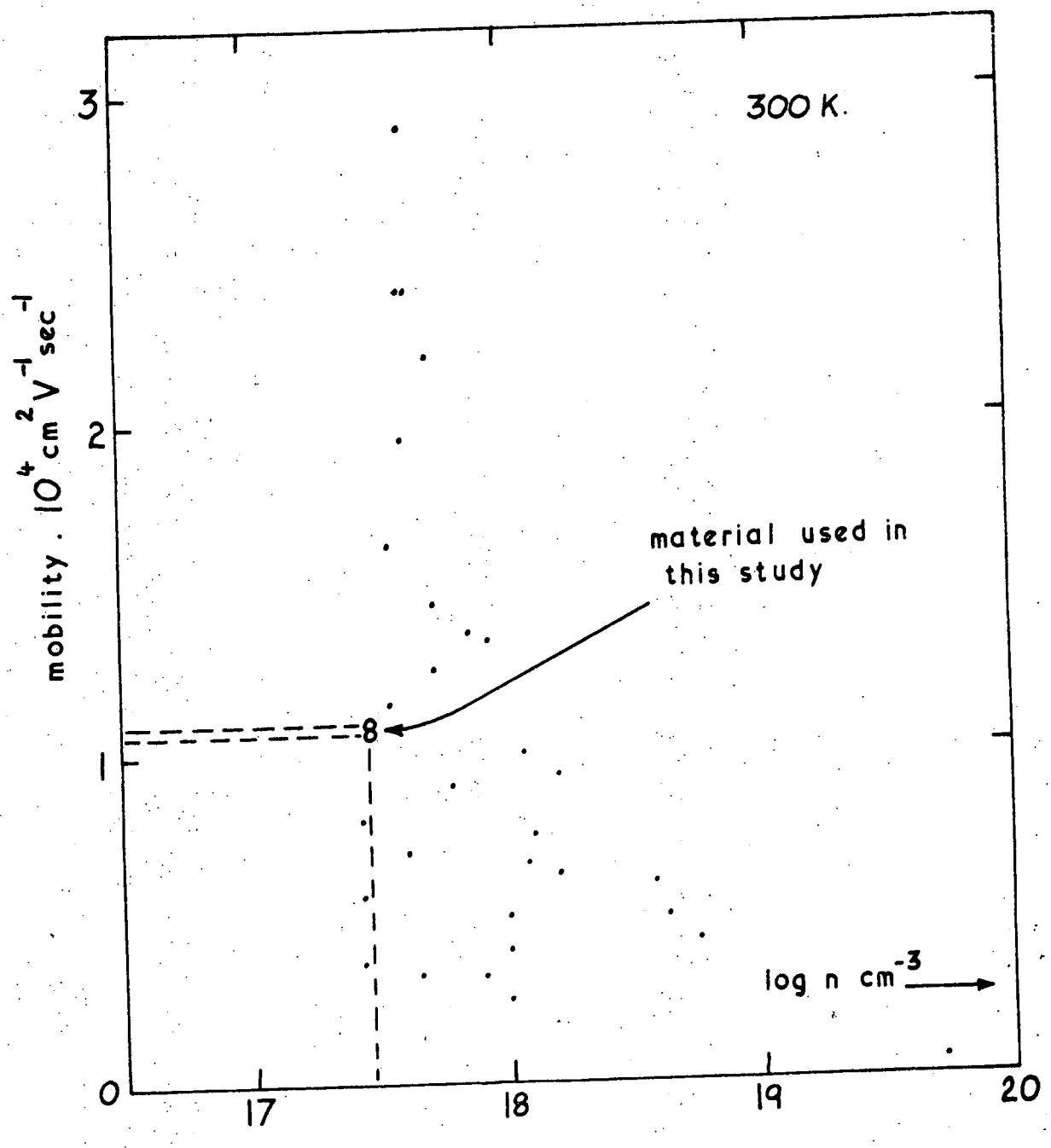

Mobilities of a wide range of crystalls of HgTe.

FIGURE 3.18

It is difficult to attain exceptionally high growth standards in crystals of this size. The conductivities of crystals grown in furnace (2) have been measured, using indium-amalgam contacts. They lie near to 150$\Omega^{-1}cm^{-1}$, suggesting a purity comparable with that of the furnace (1) crystals.

3.3(c) X-RAY EXAMINATION AND ETCHING BEHAVIOUR

Mercury telluride exhibits axial X-ray reflection characteristics similar to those of gallium arsenide; differences arise solely from the lattice parameters and atomic scattering factors.

{111} surfaces of mercury telluride were chemically polished with an etch of 6 HNO_3:1 HCl:1 H_2O (Warekois et al, 1962) (see Figure 3.19a), then etched with 1 HNO_3:1 HCl:2 H_2O to reveal pits on the Hg {111} faces but not on the Te {111} faces (Alper, 1968). Figure 3.19b shows a view of an etched Hg{111} face; pits cover the whole surface with a density of about 10^7 cm^{-2}. In some regions groups of larger pits delineate low angle grain boundaries (see Figure 3.19c). Regularly shaped pits do not form on the Te {111} faces (see Figure 3.19d).

3.4 SAMPLE PREPATATION

Orientation of the gallium arsenide and cutting to within $\frac{1}{2}^{o}$ of the chosen directions was done by STL. The mercury telluride crystals were aligned by Laue back-reflection X-ray techniques to within $\frac{1}{2}^{o}$ of the chosen axes, and the faces were cut by spark erosion (by T. Alper) or by

(a) x 400

(b) x 400

(c) x 400

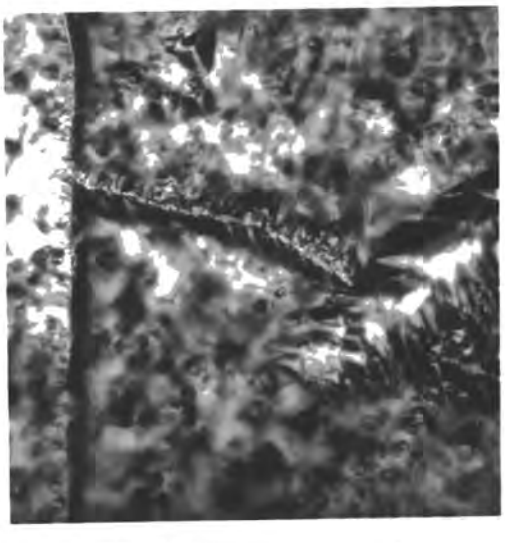

(d) x 400

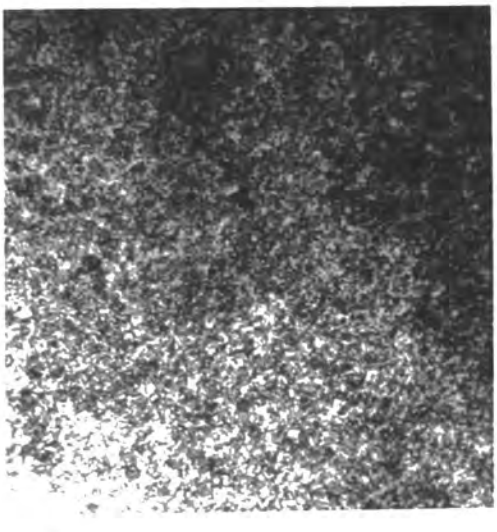

The etching characteristics of mercury telluride:

(a) a chemically polished (111) face
(b) triangular pits on a Hg(111) face
(c) low-angle grain boundaries
(d) lack of regular pits on a Te(111) face.

FIGURE 3.19

diamond wheel (in this work). Any difference in results between the two cutting techniques was eliminated during the subsequent polishing.

Crystals were lapped and polished with a Logitech PM2 precision polishing machine. A crystal face is swept from side to side across a rotating lap, while rotating itself in the plane of the lap. The lap must be softer than the crystal in order to polish away the crystal rather than the lap, and an abrasive/lubricant mixture is spread between the two. The crystal face experiences a combination of all possible rotational and translational motions in the plane of the lap, and a flat polished face results. The crystal is held onto the perforated surface of a vacuum chuck by suction. This was found to provide insufficient grip for crystals of greater than 5 mm length: a surrounding layer of Durofix glue helped to maintain adhesion. The perforated face of the vacuum chuck is set parallel to the lap surface with the help of an optical flat, and a crystal is attached and glued in position. The opposite crystal face is lapped and polished, and its flatness checked with the optical flat: the flat is laid on the polished surface and the fringes from overhead light observed. Straight fringes imply a flat surface, curved ones a correspondingly curved one. This test depends on the presence of dust particles between the two surfaces: if both are flat, parallel and clean a single colour will be observed without fringes. This occurred with one of the mercury telluride crystals. Mating was so good that in trying to remove the optical flat the crystal was broken! Surfaces flat to within one wavelength of sodium

light (5000 Å) were repeatedly attained. The crystal is removed and mounted with its newly polished face on the reference face of the vacuum chuck. Care must be exercised to eliminate all dirt and glue from between the crystal and the chuck, as it is at this stage that the final parallelism is defined. The opposite crystal face is then polished and checked for flatness. In theory the crystal now has a pair of flat, parallel faces. Flatness has already been checked; parallelism may be checked to about 1 part in 10^4 (written 10^{-4}) by measurements of the inter-facial distance over the surfaces. After some problems, parallelisms better than these were achieved.

Details of the polishing method were the same for both gallium arsenide and mercury telluride:

Lap material	lead/tin solder
Lap rotation speed	36 r.p.m.
Crystal sweep length	1 cm
Abrasive material	diamond
Abrasive size sequence	6μ, 1μ, ¼μ
Flatness achieved	<5000 Å
Parallelicity achieved	$<10^{-4}$

For gallium arsenide it was particularly important to chamfer the edges of the surface to be polished, to avoid edge chipping and subsequent scratching of the polished surface by loose chips.

It is always possible for the crystal face normal to deviate from the pre-aligned crystallographic axis during polishing. Alignment was checked after polishing by the laser technique detailed in Figure 3.20. The crystal is

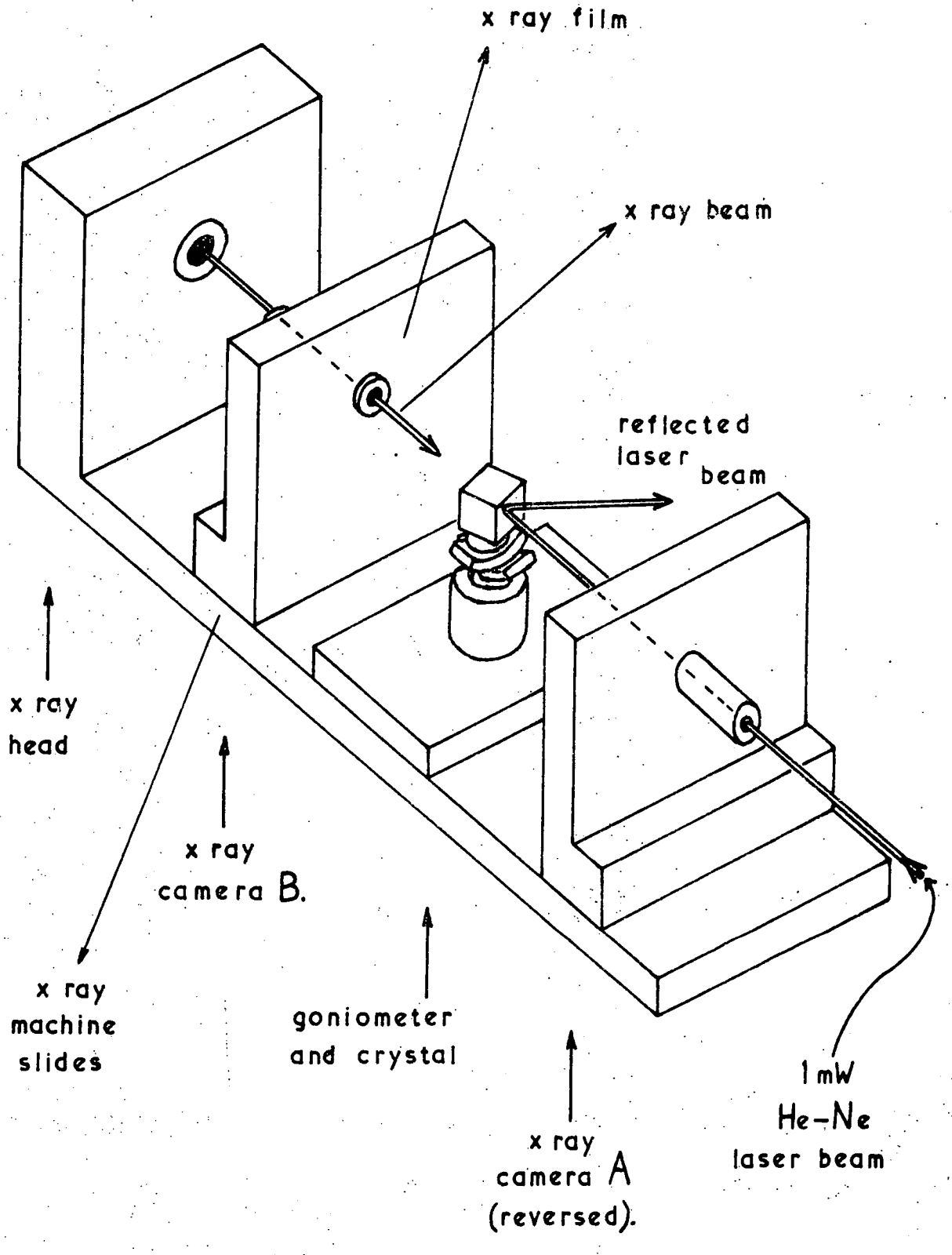

The laser-alignment of crystals for X-ray axial-alignment checks.

FIGURE 3.20

mounted on a goniometer and the laser set up so that its beam is collimated by X-ray camera A and shines on one of the polished crystal surfaces. The goniometer is adjusted so that the laser beam shines straight back down its own path: the crystal face is now perpendicular not only to the laser beam, but also to the X-ray beam axis, to within $\frac{1}{4}^{o}$. A Laue back-reflection photograph taken using X-ray camera B may be compared with a Greninger chart to ascertain the axial deviation from the face normal. This was found to be less than $\frac{1}{2}^{o}$ for all the polished crystals.

CHAPTER 4

"THE PROPAGATION OF ULTRASONIC WAVES IN CRYSTALS"

4.1 THE ELASTIC MODULI

All bodies are deformed under the action of external forces. If the stress and the resulting deformation are uniquely related and the correspondence is not a function of time, then the body is said to be elastic. However, most solids exhibit such a time dependence, and the resulting anelasticity gives rise to energy losses from a mechanical wave propagating through the solid. Phenomena which affect the elastic properties of a body will similarly affect the anelastic properties, and vice versa, but effects of anelasticity on the elastic properties are usually small.

The subject of elastic wave propagation in anisotropic media has been covered in detail by many workers, particularly Musgrave (1954 a,b: 1957), Waterman (1959), Brugger (1965), and Neighbours and Schacher (1967), and

an excellent review is given by Truell, Elbaum and Chick (1969).

(a) STRESS, STRAIN AND HOOKE'S LAW

An elastic solid is one in which the stress σ is proportional to the strain

$$\sigma = C\varepsilon \tag{4.1.a}$$

This is Hooke's law: C is the elastic stiffness constant. The inverse relation is

$$\varepsilon = S\sigma \tag{4.1.b}$$

where S is the elastic compliance. In a three dimensional solid the stress and strain are second rank tensors and the proportionality constant C is a fourth rank tensor

$$\sigma_{ij} = C_{ijk\ell}\, \varepsilon_{k\ell} \tag{4.2}$$

The stress σ_{ij} represents the force per unit area in the i direction on the plane normal to the j direction. Deformation of a body resulting in a point displacement from (X_1, X_2, X_3) to $(X_1 + U_1, X_2 + U_2, X_3 + U_3)$ is defined as a strain of (Nye, 1957)

$$\varepsilon_{ij} = \frac{1}{2}\left(\frac{\partial U_i}{\partial X_j} + \frac{\partial U_j}{\partial X_i}\right) \tag{4.3}$$

The strain ε_{ij} represents the fractional change in length of a line parallel to the X_i direction for $i = j$, or twice the change in angle between lines initially along the X_i and X_j directions for $i \neq j$.

In the most general form of Hooke's Law (equation (4.2)) the elastic tensor $C_{ijk\ell}$ has 81 components. Because both the stress and strain are symmetric ($\sigma_{ij} = \sigma_{ji}$, $\varepsilon_{ij} = \varepsilon_{ji}$), it follows that

$$C_{ijk\ell} = C_{kij\ell} = C_{ik\ell j} = C_{ki\ell j} \tag{4.4}$$

which reduces the number of independent elastic components to 36. A further condition that the elastic potential is a function of thermodynamic state alone gives

$$C_{ijk\ell} = C_{j\ell ik} \tag{4.5}$$

leaving a total of 21 independent coefficients.

Following these reductions in the number of independent components of the tensor $C_{ijk\ell}$, a condensed matrix notation may be used unambiguously for the elastic coefficients (or constants):

Tensor notation	11	22	33	23,32	13,31	12,21
Matrix notation	1	2	3	4	5	6

For example, the elastic constant C_{1112} is written as C_{16}, and C_{2332} as C_{44}.

Under the conditions of an ultrasonic measurement the entropy is effectively constant, and the adiabatic elastic constants are obtained. The difference between the adiabatic constants $C^{\sigma}_{ijk\ell}$ and the isothermal constants $C^{\theta}_{ijk\ell}$ is given by (Nye, 1957)

$$C^{\sigma}_{ijk\ell} - C^{\theta}_{ijk\ell} = \psi_{ij}\, \psi_{k\ell}\, T/C_v \tag{4.6}$$

where ψ_{ij}, $\psi_{k\ell}$ are the temperature coefficients of stress at constant strain, T is the temperature and C_v the specific heat at constant volume. The difference between the adiabatic and isothermal elastic constants is usually no greater than 1%.

(b) THE EFFECT OF CRYSTAL SYMMETRY

The elastic properties of crystals are always

centrosymmetric: the velocity of propagation of an elastic wave mode depends on the direction of propagation but not on the sense of this direction. Consequently all the crystalline point groups belonging to the same Laue group have common arrays of elastic constants.

The least symmetrical crystals, those in the triclinic system, have 21 independent elastic constants. Increase in crystal symmetry brings a reduction in the number of independent constants: all the five cubic point groups have the same C_{ij} matrix in which the number of independent coefficients is reduced from 21 to 3, namely C_{11}, C_{12} and C_{44}:

$$\begin{aligned} C_{11} &= C_{22} = C_{33}, \\ C_{12} &= C_{21} = C_{13} = C_{31} = C_{23} = C_{32} \\ C_{44} &= C_{55} = C_{66} \end{aligned} \tag{4.7}$$

The cubic elastic constant matrix is

$$\begin{pmatrix} C_{11} & C_{12} & C_{12} & 0 & 0 & 0 \\ C_{12} & C_{11} & C_{12} & 0 & 0 & 0 \\ C_{12} & C_{12} & C_{11} & 0 & 0 & 0 \\ 0 & 0 & 0 & C_{44} & 0 & 0 \\ 0 & 0 & 0 & 0 & C_{44} & 0 \\ 0 & 0 & 0 & 0 & 0 & C_{44} \end{pmatrix}$$

(c) THE EQUATION OF MOTION OF AN ELASTIC BODY

The equation of motion (Newton's second law) may be derived by equating the summation of components of forces on opposite sides of an elemental parallelopiped of

the body to the acceleration components for the medium of density :

$$\frac{\partial \sigma_{ij}}{\partial X_j} = \rho \frac{\partial^2 U}{\partial t^2} , \quad (i = 1,2,3)$$

or $$\sigma_{ij,j} = \rho \ddot{U}_i \tag{4.8}$$

where $\underline{U}$ (U_1, U_2, U_3) is the displacement vector, $\underline{X}$ (X_1, X_2, X_3) the position vector and the comma notation ,j indicates differentiation with respect to X_j. If this is substituted in equation (4.2),

$$C_{ijk\ell} \varepsilon_{k\ell,j} = \rho \ddot{U}_i \tag{4.9}$$

where $$\varepsilon_{k\ell,j} = \frac{1}{2} (U_{\ell,k\ell} + U_{k,\ell j}) \tag{4.10}$$

Solutions are required in the form of a plane wave of the type

$$U_\ell = U_{o\ell} e^{i(\omega t - \underline{k}.\underline{x})}, \quad (\ell = 1,2,3) \tag{4.11}$$

Here $\underline{k}$ (k_1, k_2, k_3) is the propagation vector, normal to planes of constant phase as is the unit vector $\underline{n}$:

$$\underline{k} = \left(\frac{\omega}{V}\right) \underline{n} = \left(\frac{2\pi}{\lambda}\right) \underline{n} \tag{4.12}$$

where ω, V and λ are the angular frequency, phase velocity and wavelength, respectively. The displacement vector $\underline{U}$ in general need not be parallel to $\underline{k}$.

By differentiation of equation (4.11),

$$U_{\ell,kj} = -n_k n_j U_{o\ell} \left(\frac{\omega^2}{V^2}\right) e^{i(\omega t - \underline{k}.\underline{x})} \tag{4.13}$$

and $$\ddot{U}_\ell = U_{o\ell} \omega^2 e^{i(\omega t - \underline{k}.\underline{x})} \tag{4.14}$$

Substituting for ε and $\ddot{U}$ in equation (4.9) we find

$$C_{ijk\ell} U_{o\ell} n_k n_j = \rho V^2 U_{oi}, \quad (i = 1,2,3) \tag{4.15}$$

For equation (4.15) to have solutions the determinant of coefficients of the displacement components U_{01}, U_{02}, U_{03} must be zero:

$$\begin{vmatrix} (L_{11}-\rho V^2) & L_{12} & L_{13} \\ L_{12} & (L_{22}-\rho V^2) & L_{23} \\ L_{13} & L_{23} & (L_{33}-\rho V^2) \end{vmatrix} = 0 \qquad (4.16)$$

where

$$\begin{aligned}
L_{11} &= n_1^2 C_{11} + n_2^2 C_{66} + n_3^2 C_{55} + 2n_2n_3 C_{56} \\
&\quad +2n_3 n_1 C_{15} + 2n_1n_2 C_{16}, \\
L_{12} &= n_1^2 C_{16} + n_2^2 C_{26} + n_3^2 C_{45} + n_2n_3 (C_{46} + C_{25}) \\
&\quad +n_3n_1 (C_{14}+C_{56}) + n_1n_2 (C_{12}+C_{66}), \\
L_{13} &= n_1^2 C_{15} + n_2^2 C_{46} + n_3^2 C_{35} + n_2n_3 (C_{45}+C_{36}) \\
&\quad +n_3n_1 (C_{13}+C_{55}) + n_1n_2 (C_{14}+C_{56}), \qquad (4.17) \\
L_{22} &= n_1^2 C_{66} + n_2^2 C_{22} + n_3^2 C_{44} + 2n_2n_3 C_{24} \\
&\quad +2n_3n_1 C_{46} + 2n_1n_2 C_{26}, \\
L_{23} &= n_1^2 C_{56} + n_2^2 C_{24} + n_3^2 C_{34} + n_2n_3 (C_{44}+C_{23}) \\
&\quad +n_3n_1 (C_{36}+C_{45}) + n_1n_2 (C_{25} + C_{46}), \\
L_{33} &= n_1^2 C_{55} + n_2^2 C_{44} + n_3^2 C_{33} + 2n_2n_3 C_{34} \\
&\quad +2n_3n_1 C_{35} + 2n_1n_2 C_{45},
\end{aligned}$$

and n_1, n_2, n_3 are the direction cosines.

Equation (4.16) is cubic in ρV^2: solutions will be in the form of three independent waves of different velocities. In a general direction the wave will be neither purely longitudinal (for which $\underline{U} \wedge \underline{n} = 0$) nor purely transverse (for which $\underline{U}.\underline{n} = 0$). The analysis of ultrasonic data is easiest for propagation along pure mode directions: these are chosen whenever possible.

(d) SOLUTIONS FOR CRYSTALS OF CUBIC SYMMETRY

For a cubic crystal the elastic constant equalities (4.7) hold, and for a general propagation direction with direction cosines (n_1, n_2, n_3) the determinental equation (4.16) becomes

$$\begin{vmatrix} (C_{11}-C_{44})n_1^2+C_{44}-\rho V^2 & n_1n_2(C_{12}+C_{44}) & n_1n_3(C_{12}+C_{44}) \\ n_1n_2(C_{12}+C_{44}) & n_2^2(C_{11}-C_{44})+C_{44}-\rho V^2 & n_2n_3(C_{12}+C_{44}) \\ n_1n_3(C_{12}+C_{44}) & n_2n_3(C_{12}+C_{44}) & n_3^2(C_{11}-C_{44})+C_{44}-\rho V^2 \end{vmatrix} = 0 \qquad (4.18)$$

Pure mode solutions for all three wave conditions are obtained for propagation in the crystallographic directions [100], [110] and [111]. Table 4.A lists the relations between the mode velocities and elastic constants for these three directions. It should be noticed that it is possible to obtain all three elastic constants C_{11}, C_{12} and C_{44} from measurement of the velocities of the three independent wave modes in the [110] direction (this is not necessarily true for a crystal without a centre of symmetry: a discussion is given in Section 4.3(a).

TABLE 4.A

Propagation and polarisation vectors for pure mode propagation in cubic crystals. The relations between the measured propagation velocities V and the elastic moduli C_{ij} is given.

Propagation Direction	Particle Displacement Vector	ρV^2 =
[100]	[100]	C_{11}
[100]	in (100) plane	C_{44}
[110]	[110]	$\frac{1}{2}(C_{11}+C_{12}+2C_{44})$
[110]	[001]	C_{44}
[110]	$[1\bar{1}0]$	$\frac{1}{2}(C_{11}-C_{12})$
[111]	[111]	$\frac{1}{3}(C_{11}+2C_{12}+4C_{44})$
[111]	in (111) plane	$\frac{1}{3}(C_{11}-C_{12}+C_{44})$

(e) THE ULTRASONIC ENERGY FLUX VECTOR

Brugger (1965) has shown that for a pure longitudinal wave mode the energy flux vector is always parallel to the propagation direction. The same result holds for a pure transverse wave propagated along a direction exhibiting twofold, fourfold or sixfold rotational symmetry or normal to a reflection plane. However, in general the energy flux can deviate from the propagation direction (see Figure 3.5), and in particular this is true for propagation along a threefold axis, the only case relevant to measurements made in this study. In the threefold direction degenerate pure shear waves of arbitrary polarisation may propagate. As the plane of the particle vibration is rotated about the axis through an angle π, the energy flux vector rotates about the axis in the opposite sense through an angle 2π, generating a cone for possible directions for the energy flow (Waterman, 1959).

Love (1944) has given the L-th energy flux component in terms of stress and particle displacement velocity for each wave mode (g) as

$$P_i^g = -\sigma_{ij} \dot{U}_j^g \qquad (4.19)$$

Differentiating equation (4.11), which may be written as

$$\underline{U} = p^g \underline{U}_o e^{i(\omega t - \underline{k}.\underline{x})}$$

and substituting, we find

$$P_i^g = -\frac{(p^g \omega)^2}{2V_g} C_{ijk\ell} u_{oj}^g u_{ok}^g n_\ell^g \qquad (4.20)$$

where p^g is the elastic displacement amplitude and V_g, n_1 are the mode velocity and cosine of the angle between the propagation direction and the X_1 coordinate axis, respectively u_{oi} are direction cosines of the displacement vector.

4.2 ANELASTICITY AND ATTENUATION

One of the earliest models for a solid to include anelastic effects was that suggested by Voigt (1892) (see Figure 4.1(a)). This suffered from the omission of instantaneous strain on application of a stress, a phenomenon exhibited by most solids. Zener (1947) has modified Voigt's model to include this effect (Figure 4.1(b)) in the Standard Linear Solid Model. Here Hooke's law is written in terms of time derivatives of the stress and strain up to first order

$$\sigma = \tau\dot{\sigma} = C_1\varepsilon + \tau C_o\dot{\varepsilon} \qquad (4.21)$$

where C_o is the true or unrelaxed modulus, C_1 is the time dependent or relaxed modulus and τ is the stress relation time. A similar analysis to that represented in Section 4.1(c) for a purely elastic solid now yields solutions of the form

$$\sigma = \sigma.e^{-\alpha x}\, e^{i(\omega t-kx)} \qquad (4.22)$$

which defines an attenuated travelling wave, with α the attenuation coefficient. Substituting back this gives expressions for the attenuation as a function of distance and for the velocity of

$$\alpha = \frac{1}{2\tau V}\,\frac{\delta C_o}{C_o}\left(\frac{\omega^2\tau^2}{1+\omega^2\tau^2}\right) \qquad (4.23)$$

and

$$V = \frac{C_o}{\rho}\left[1 - \frac{\delta C_o}{2C_o}\left(\frac{1}{1+\omega^2\tau^2}\right)\left(1 - \frac{2\omega^2\tau^2}{1+\omega^2\tau^2}\right)\right] \qquad (4.24)$$

where δC_o is the relative difference between the unrelated and relaxed moduli. The frequency dependence of α and V are shown in Figure 4.2.

Voigt solid

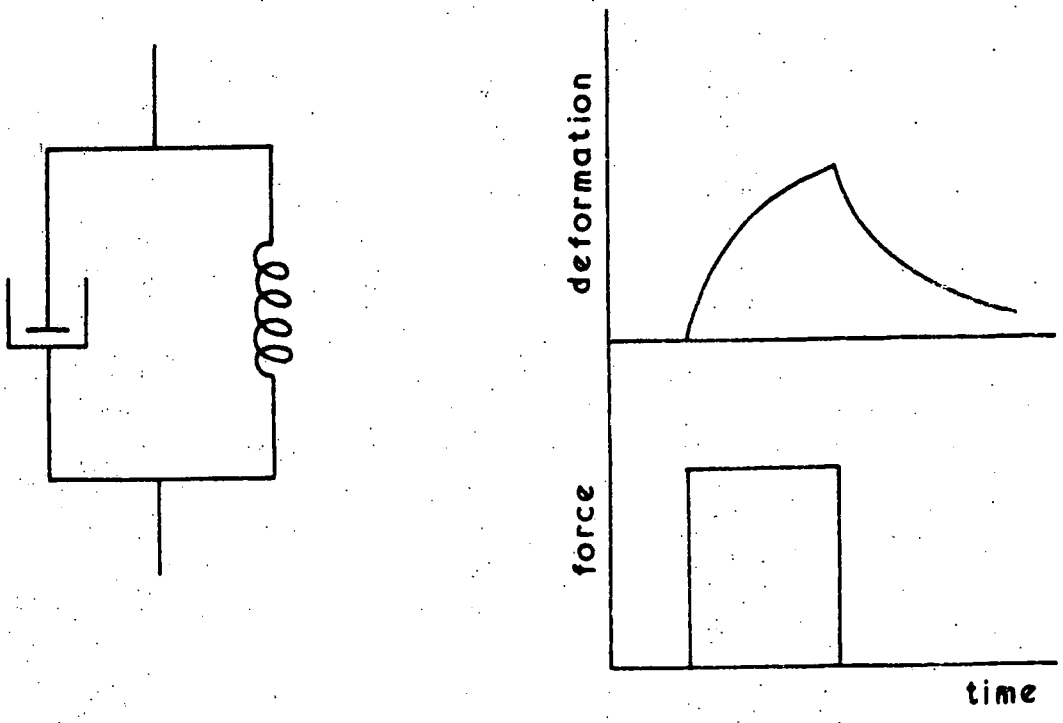

standard linear solid

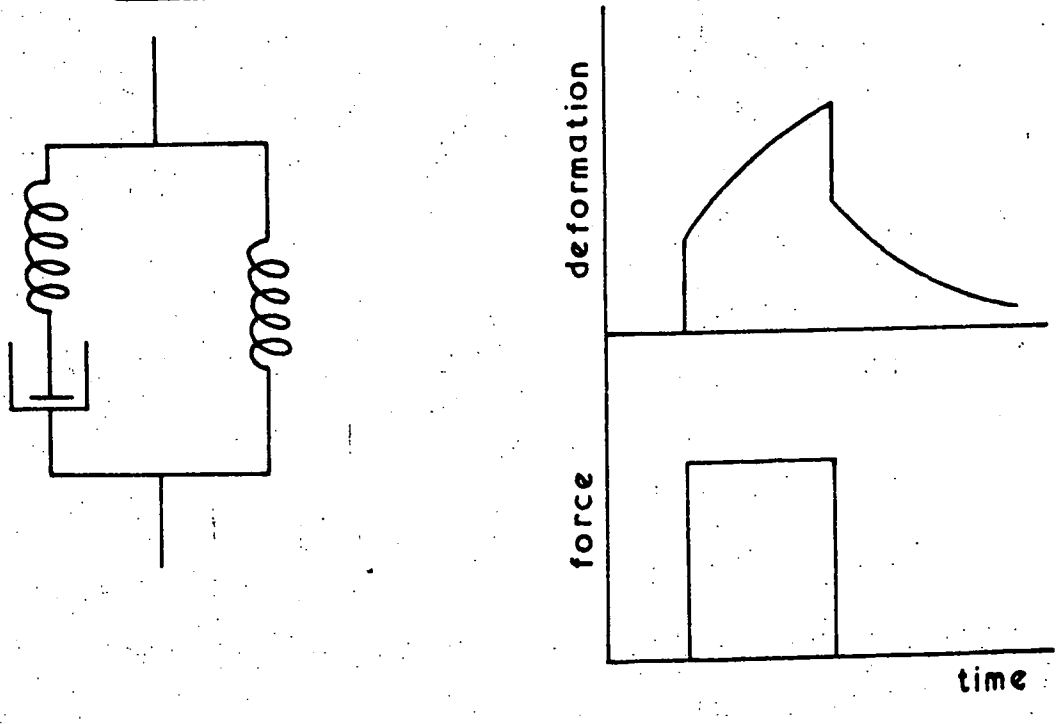

A comparison of the Voigt and Standard Linear solid models and their mechanical behaviour.

FIGURE 4.1

The units of α derived above are neper cm^{-1}. Conversion to the more usual decibel cm^{-1} units is by

$$\text{neper} = 8.686 \text{ dB}$$

Measurement of the attenuation coefficient is in units of dB sec^{-1}, so measured values must be divided by the ultrasonic velocity to obtain the results in dB cm^{-1}. The most useful expression for attenuation as a function of frequency F is in terms of the logarithmic decrement Δ, which is

$$\Delta = \frac{\alpha \text{ (dB sec}^{-1})}{8.686 \text{ F(Hz)}} \qquad (4.25)$$

The frequency dependence of Δ for the standard linear model of a solid is illustrated in Figure 4.2.

4.3 CONSEQUENCES OF THE LACK OF A CENTRE OF SYMMETRY

The propagation of ultrasonic waves can be markedly affected by piezoelectric effects in materials which lack a centre of symmetry. In ordinary solids a stress σ merely causes a proportional strain ε related by an elastic modulus, $\sigma = C\varepsilon$, whereas in a piezoelectric material there is also creation of electric charge by applied stress due to the direct piezoelectric effect. The dielectric displacement D is

$$D = \frac{Q}{A} = d.\sigma \qquad (4.26)$$

where (Q/A) is the charge per unit area and d a constant. The converse piezoelectric effect of strain produced by an applied electric field E is also possible:

$$\varepsilon = d.E \qquad (4.27)$$

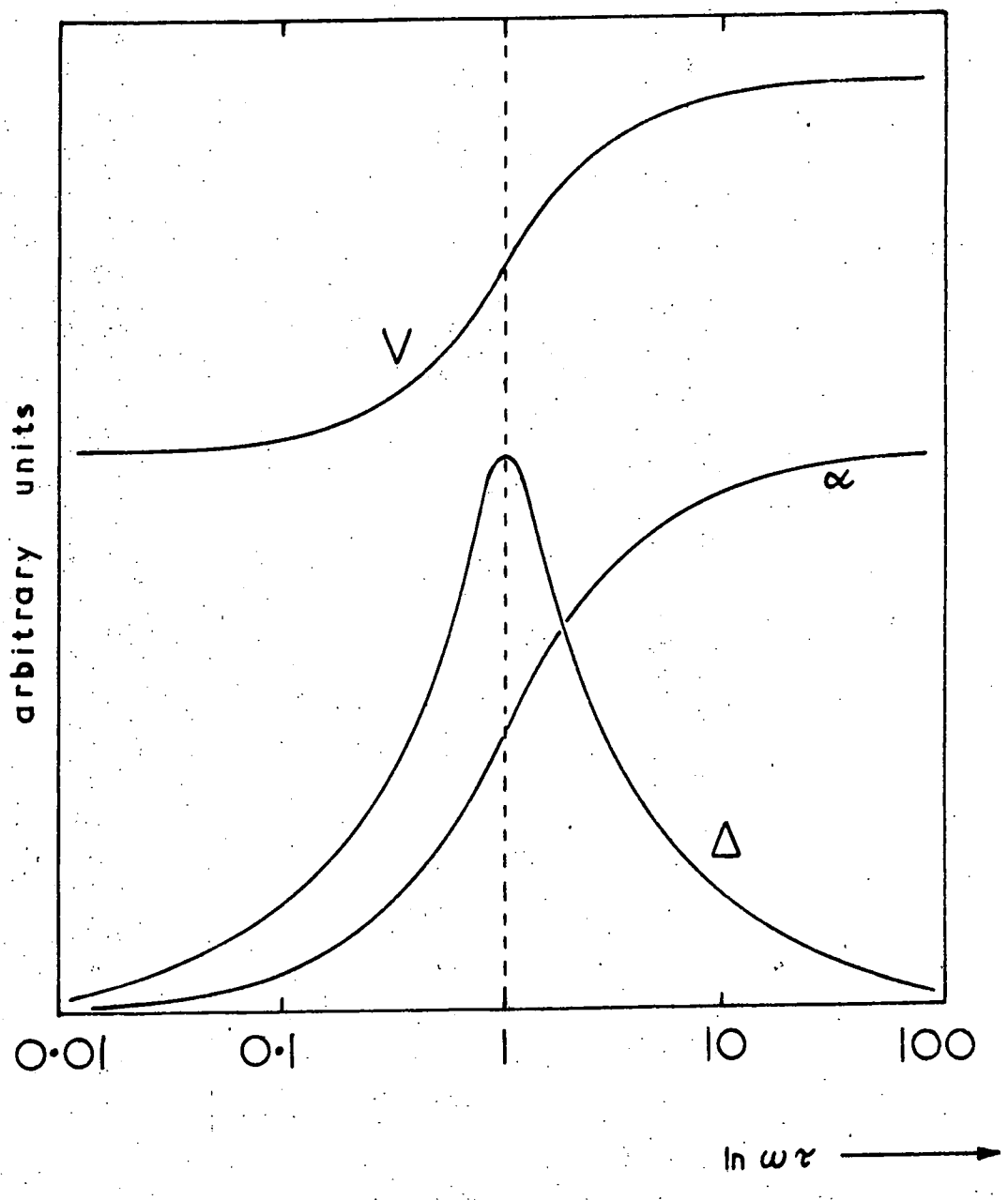

The frequency dependence of the elastic wave velocity (V), attenuation (α) and logarithmic decrement (Δ) in the Standard Linear solid model.

FIGURE 4.2

In both cases the constant of proportionality is the piezoelectric constant d. A total of four related piezoelectric constants may be defined as partial derivatives evaluated at constant stress (subscript σ), constant field (subscript E), constant displacement (subscript D) or constant strain (subscript ε): these are

$$\begin{aligned} d &= \left(\frac{\partial \varepsilon}{\partial E}\right)_\sigma = \left(\frac{\partial D}{\partial \sigma}\right)_E \\ g &= \left(-\frac{\partial E}{\partial \sigma}\right)_D = \left(\frac{\partial \varepsilon}{\partial D}\right)_\sigma \\ e &= \left(-\frac{\partial \sigma}{\partial E}\right)_\varepsilon = \left(\frac{\partial D}{\partial \varepsilon}\right)_E \\ h &= \left(-\frac{\partial \sigma}{\partial D}\right)_\varepsilon = \left(-\frac{\partial E}{\partial \varepsilon}\right)_D \end{aligned} \tag{4.28}$$

For strain ε and electric field E as variables, the equation of state for a piezoelectric crystal is a set of 9 relations (six elastic, three electrical) represented by the tensor equations

$$\sigma = C_E \varepsilon - e_t E \tag{4.29}$$

$$D = e \varepsilon + \zeta_\varepsilon E \tag{4.30}$$

where C_E represents the "constant field" elastic constants, ζ_ε the "constant strain" dielectric permittivity and subscript t a transposition. The tensor multiplication of the two equations may be represented in terms of the elasto-piezo-dielectric (EPD) matrix, which is simply an extension of the condensed elastic constant matrix discussed in Section 4.1(a). (I.R.E. standards, 1958):

c_{11}	c_{12}	c_{13}	c_{14}	c_{15}	c_{16}	e_{11}	e_{21}	e_{31}
c_{21}	c_{22}	c_{23}	c_{24}	c_{25}	c_{26}	e_{12}	e_{22}	e_{32}
c_{31}	c_{32}	c_{33}	c_{34}	c_{35}	c_{36}	e_{13}	e_{23}	e_{33}
c_{41}	c_{42}	c_{43}	c_{44}	c_{45}	c_{46}	e_{14}	e_{24}	e_{34}
c_{51}	c_{52}	c_{53}	c_{54}	c_{55}	c_{56}	e_{15}	e_{25}	e_{35}
c_{61}	c_{62}	c_{63}	c_{64}	c_{65}	c_{66}	e_{16}	e_{26}	e_{36}
e_{11}	e_{12}	e_{13}	e_{14}	e_{15}	e_{16}	ζ_{11}	ζ_{12}	ζ_{13}
e_{21}	e_{22}	e_{23}	e_{24}	e_{25}	e_{26}	ζ_{21}	ζ_{22}	ζ_{23}
e_{31}	e_{32}	e_{33}	e_{34}	e_{35}	e_{36}	ζ_{31}	ζ_{32}	ζ_{33}

Crystal symmetry not only reduces the number of independent non-zero elastic constants (Section 4.1(b)) but also the number of non-zero piezoelectric and dielectric constants in the EPD matrix above. For crystals with a centre of symmetry all the piezoelectric constants e_{ij} disappear: piezoelectric effects are absent. 20 of the 21 crystal classes lacking a centre of symmetry can show piezoelectricity (the exception being the cubic class 432). For the $\bar{4}3m$ class (i.e. for GaAs, HgTe) the EPD matrix becomes

c_{11}	c_{12}	c_{12}	0	0	0	0	0	0
c_{12}	c_{11}	c_{12}	0	0	0	0	0	0
c_{12}	c_{12}	c_{11}	0	0	0	0	0	0
0	0	0	c_{44}	0	0	e_{14}	0	0
0	0	0	0	c_{44}	0	0	e_{14}	0
0	0	0	0	0	c_{44}	0	0	e_{14}
0	0	0	e_{14}	0	0	ζ_{11}	0	0
0	0	0	0	e_{14}	0	0	ζ_{11}	0
0	0	0	0		e_{14}	0	0	ζ_{11}

with 3 independent elastic constants c_{11}, c_{12} and c_{44}, one dielectric constant ζ_{11} and one piezoelectric constant e_{14}.

For a material exhibiting piezoelectricity the wave velocity - elastic constant relations derived from the elastic constant tensor alone do not necessarily hold for all crystallographic directions. If the conductivity is too low to enable rapid complete local cancellation of the induced piezoelectric fields accompanying an elastic wave by carrier "bunching," then there is an apparent "stiffening" of the material caused by the elastic wave/carrier interaction. The wave attenuation will also be affected, being related to the elasticity through the propagation constant (see equation 4.22).

(a) PIEZOELECTRIC STIFFENING

Hutson and White (1962) have anlysed the effect of piezoelectricity on elastic wave propagation in solids. Differentiation of the piezoelectric equation of state (4.29) results in a wave equation of

$$\rho \frac{\partial^2 u}{\partial t^2} = C\left(1 + \frac{e^2}{C\zeta}\right) \frac{\partial^2 u}{\partial x^2} \qquad (4.31)$$

for D constant a condition equivalent to that of zero electrical conductivity; for high conductivity the condition of E constant holds. Intermediate values require that the electric field be eliminated from the wave equation by using an expression for the current density in terms of carrier drift and diffusion. To obtain the propagation properties of acoustic waves, the electric field is expressed in terms of the strain, then substituted into equation (4.29) to give an effective elastic constant. Neglecting carrier diffusion, the resulting expression for the wave velocity V is

$$V = V_o \left[1 + \frac{e^2}{2C\zeta} \left(\frac{1}{1+(\omega_c/\omega)^2}\right)\right] \qquad (4.32)$$

where ω_c is the "conductivity frequency" $\omega_c = S/\zeta$, S is the conductivity, V_o is the unstiffened velocity and ω the angular frequency of the wave. At very low frequencies V approaches the limit of V_o, while at very high frequencies

$$V = V_\infty = V_o \left[1 + \frac{e^2}{2C\zeta}\right] \qquad (4.33)$$

as shown in Figure 4.3(a).

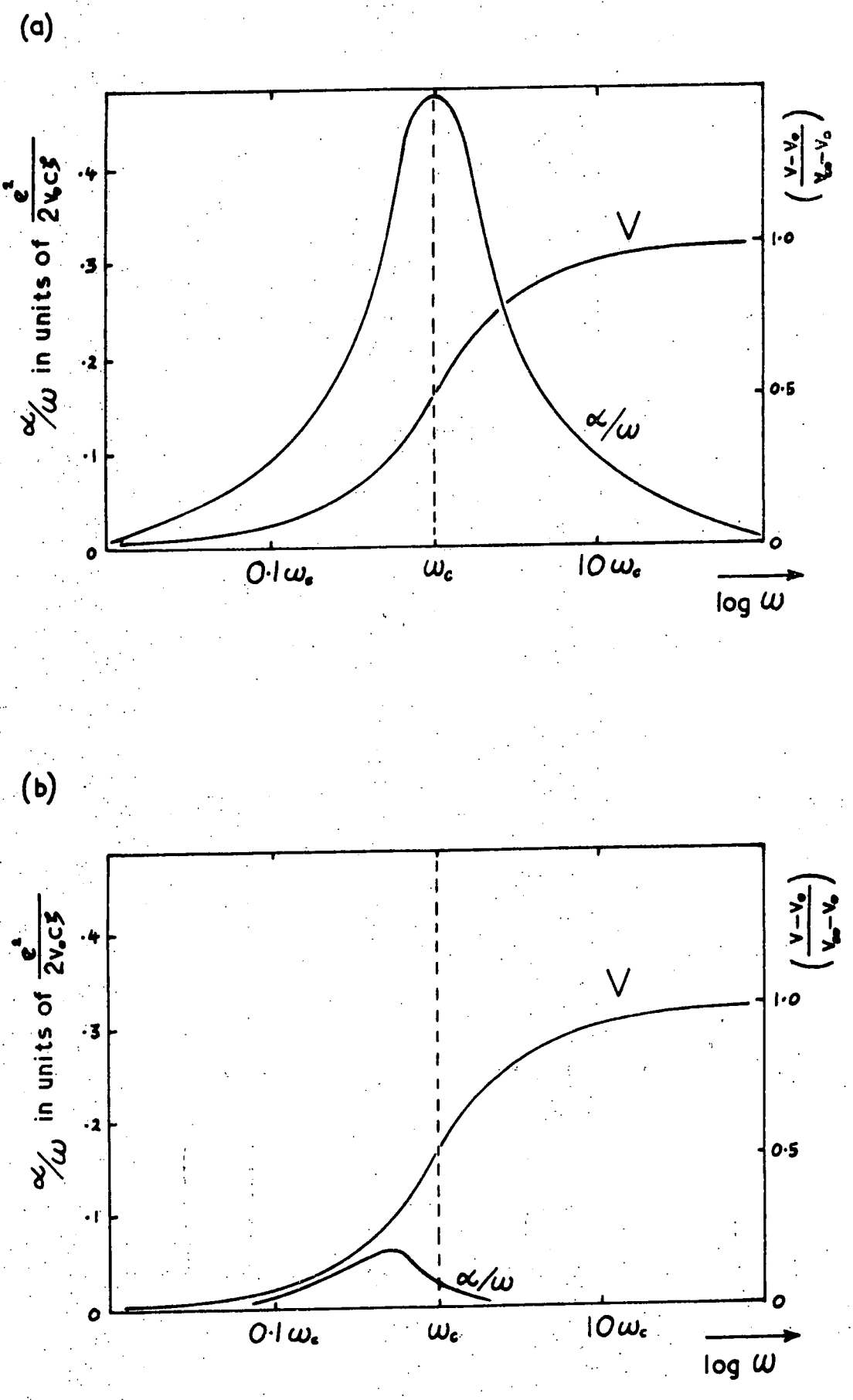

The effects of acoustoelectric interaction on the acoustic velocity and loss

(a) neglecting carrier diffusion

(b) for $\omega_C = 100\ \omega_D$ (after Hutson and White, 1962)

FIGURE 4.3

Taking account of carrier diffusion effects the expression for the wave velocity is

$$V = V_o \left[1 + \left(\frac{e^2}{2C\zeta} \right) \frac{1 + (\omega_C/\omega_D) + (\omega/\omega_D)^2}{1+2(\omega_C/\omega_D) + (\omega/\omega_D)^2 + (\omega_C/\omega)^2} \right] \quad (4.34)$$

where the "diffusion frequency" ω_D is that frequency above which the wavelength is sufficiently short for diffusion to smooth out carrier density fluctuations having the periodicity of the acoustic wave:

$$\omega_D \simeq \left(\frac{qV^2}{f\mu kT} \right) \quad (4.35)$$

where q is the electronic charge, μ the carrier mobility, k Boltzmann's constant, T the temperature and f the fraction of the space charge which is in the conduction band. For $\omega_D >> \omega_C$ equation (4.32) accurately describes the velocity behaviour; for $\omega_D << \omega_C$ the velocity goes from V_o to V_∞ as before, but the halfway point is now at $\omega = (\omega_D \omega_C)^{\frac{1}{2}}$, not at ω_C as in Figure 4.3.(a).

Hutson and White (1962) have shown that the propagation of plane waves in the 1 direction of an orthogonal coordinate system 1,2,3 is described by the solution of the determinant

$$\begin{vmatrix} \frac{C_{1111}}{\rho} - \frac{\omega^2}{k^2} & \frac{C_{1112}'}{\rho} & \frac{C_{1113}'}{\rho} \\ \frac{C_{1211}'}{\rho} & \frac{C_{1212}'}{\rho} - \frac{\omega^2}{k^2} & \frac{C_{1213}'}{\rho} \\ \frac{C_{1311}'}{\rho} & \frac{C_{1312}'}{\rho} & \frac{C_{1313}'}{\rho} - \frac{\omega^2}{k^2} \end{vmatrix} = 0 \quad (4.36)$$

where

$$C_{1i1k}' = C_{1i1k} + \frac{e_{11i}\, e_{11k}}{(\zeta_{11} + iS_{11}/\omega)} \quad (4.37)$$

These elastic and piezoelectric constants are obtained by a coordinate rotation such that the 1 coordinate direction lies along the required crystallographic wave propagation direction. If such a rotation is performed for all the wave modes listed in Table 4.A, it turns out that the only modes for which piezoelectric stiffening occurs are the

[110] propagation [001] polarisation shear and the [111] propagation longitudinal modes.

Away from these exact mode orientations the stiffening rapidly falls away: for evaluation of the "constant field" (or "zero field") elastic constants, any combination of the modes listed in Table 4.A not including the [110]S [001] or the [111]L may be used, and piezoelectric stiffening may then be ignored.

(b) ACOUSTOELECTRIC ATTENUATION

Hutson and Whites' (1962) analysis of the effects of piezoelectricity on elastic wave propagation includes a consideration of the consequential wave attenuation. In the absence of carrier diffusion the attenuation α is given by

$$\alpha = \frac{\omega e^2}{2V_o C\zeta} \left[\frac{(\omega_c/\omega)}{1+(\omega_c/\omega)^2}\right] \qquad (4.38)$$

At very low frequencies α tends to zero, while at high frequencies

$$\alpha = \alpha_\infty = \frac{\omega_c e^2}{2V_o C\zeta} \qquad (4.39)$$

Inclusion of diffusion effects gives

$$\alpha = \frac{\omega e^2}{2V_o C\zeta} \left[\frac{(\omega_C/\omega)}{1 + 2(\omega_C/\omega_D) + (\omega/\omega_D)^2 + (\omega_C/\omega)^2} \right] \qquad (4.40)$$

For $\omega_D >> \omega_C$ the behaviour is well described by Figure 4.3(a), but for ω_D becoming much smaller than ω_C the peak in attenuation moves to lower frequencies as $(\frac{1}{3}\ \omega_D\ \omega_C)^{\frac{1}{2}}$ and falls markedly (see Figure 4.3(b)). Here again the parameters C and e in equations (4.38-40) must be correctly chosen by coordinate rotation, as for the stiffened velocity.

CHAPTER 5

"EXPERIMENTAL TECHNIQUES"

5.1 SOLID STATE ULTRASONICS

(a) INTRODUCTION

To investigate the propagation of ultrasonic stress waves in a solid through electronic instrumentation, we require firstly a system for transduction of electrical to mechanical energy and vice versa, and secondly a driving source for the transduction. In this work the transducers used were of the piezoelectric kind, both resonant and non-resonant. One of the prime variables in an investigation of this type is the stress wave frequency: some degree of monochromacity in the source energy output is desirable.

Piezoelectric transducers may be excited by a variety of techniques, including the application of continuous sinusoidal electrical waves, step-voltages and pulses of sine waves. The most monochromatic source is that of a continuous sinusoidal wave (see Figure 5.1), but continuous-wave systems are notoriously difficult to handle, particularly in the aspect of signal leakage. Of the two other common techniques listed, that using a pulsed-sine wave has the

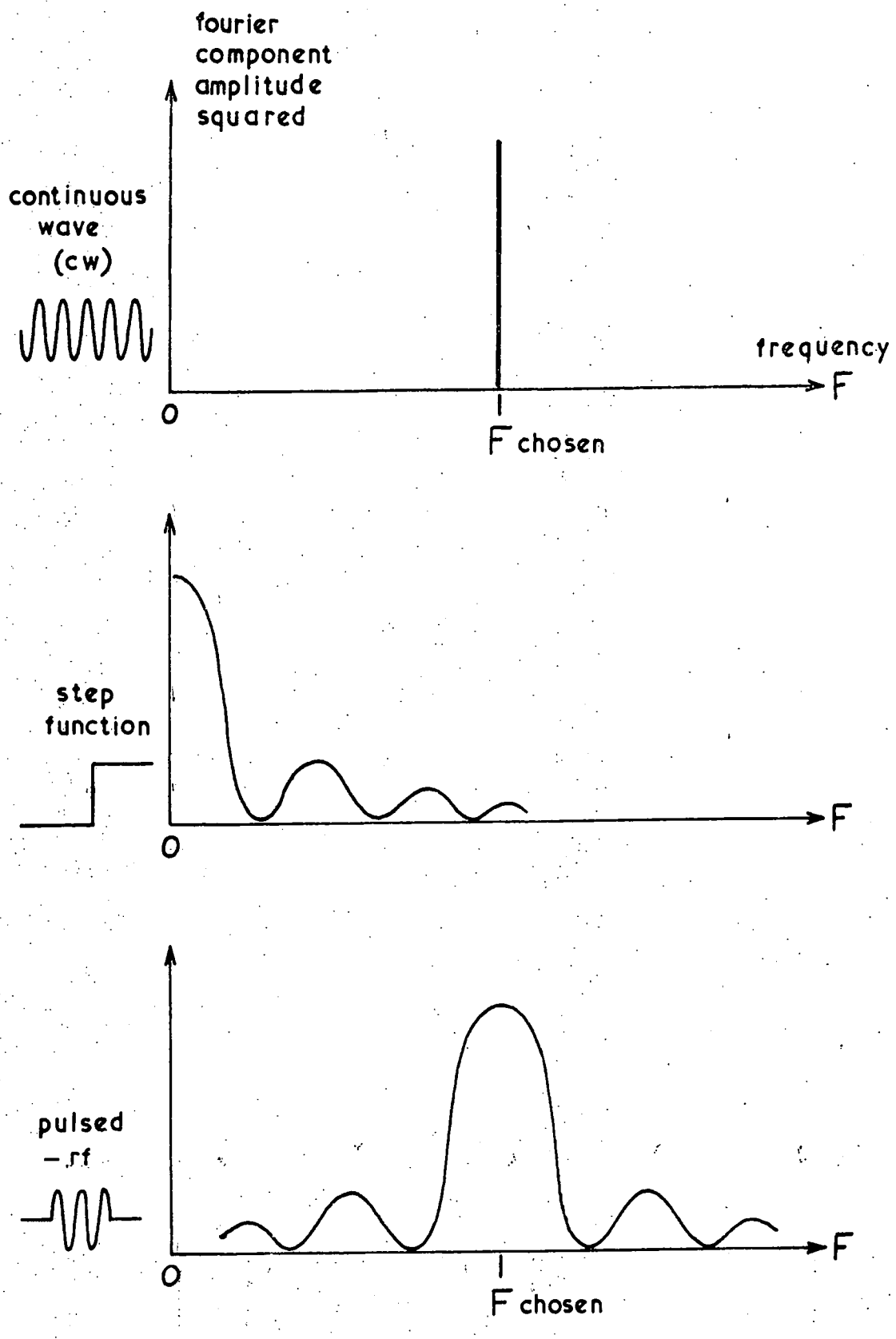

The frequency spectra of the continuous-wave, step-function and pulsed-RF ultrasonic techniques.

FIGURE 5.1

advantage of high concentration of wave energy in the region of a chosen operating frequency, and the average power input can be made low enough to avoid any possible sample heating. Increase in pulse length gives greater monochromacity; this is applied in this work in a sampled-continuous wave (-CW) investigation of the validity of measurements made using the pulsed-sine wave technique.

(b) QUARTZ ULTRASONIC TRANSDUCERS

Transduction between electrical and mechanical energy at ultrasonic frequencies is most conveniently effected by use of the piezoelectric properties of quartz. The choice of quartz is governed not only by electromechanical coupling considerations, but also by availability of accurately cut crystals and their mechanical handling characteristics. Ultrasonic waves propagating in the X-direction may be generated in quartz by the application of an alternating electric field parallel to this direction; polarised transverse waves propagating in the Y-direction by the application of a parallel alternating field. Plates are cut to have their thickness, parallel to these directions, equal to a half-wavelength ($\lambda/2$) of these modes of the lowest ultrasonic frequency required. A gold film on both sides makes electrical contact, and the plates then act as resonant mechanical filters to alternating electrical voltages applied across them: resonance occurs at the frequency defined by the $\lambda/2$ condition given above and at its odd harmonics. Intimate coupling to a flat sample face results in loss of mechanical energy from the resonator,

that is, injection of a wave of equivalent mode into the sample.

X-cut and Y-cut transducers of 10 MHz and 50 MHz fundamental frequency were used in this work. The low acoustic losses and exact cutting and finishing of the quartz transducers available commercially cause them to have a very high Q-factor: they are only usable very close to their fundamental and odd-harmonic frequencies and not in between, where conversion efficiency is negligible. The power insertion loss is usually of the order of 30 dB at the fundamental, and increases rapidly with harmonic number.

(c) TRANSDUCER TO SAMPLE BONDING

Coupling between the transducer and sample is normally effected by bonding the two together with a thin film of glue, oil or a glassy material.

Over the complete temperature range of 1.5 K to 320 K covered in this work, Nonaq stopcock grease (manufactured by the Fisher Scientific Co.) was found to be an excellent bonding material for mercury telluride. Bonds were made by applying a small drop of Nonaq to the flat sample face, placing the transducer on top and moving it with a circular motion until it appeared to "stick," evidencing a thin bond between the sample and transducer.

Nonaq was found to give excellent bonding to gallium arsenide crystals at room temperature, but exhaustive attempts failed to maintain bonding below about 100 K. Similar results followed the testing of a wide range of bonding materials (silicone oils, 4-methyl 1-pentene, Dow-Corning resins, etc.). Eventually the use of bonded

transducers on gallium arsenide below 200 K was abandoned, and thin-film cadmium sulphide transducers were used instead.

(d) ULTRASONIC REFLECTIONS AT A BONDED TRANSDUCER

In making measurements of ultrasonic velocity by pulse techniques reliance is placed on the absence of, or a knowledge of, phase changes on reflection at the two ends of the sample. At the free end of the sample the reflection phase shift is zero, as the acoustic impedance mismatch from sample to air is effectively infinite. However, the transducer end of the sample presents a real problem. McSkimin and Andreatch (1962) have presented an analysis of the phase shift on reflection at a bonded transducer (see Figure 5.2) in terms of acoustic impedances, which results in an expression for the impedance Z_d looking from the sample into the bond of

$$Z_d = i\, Z_1 \left[\frac{(Z_1/Z_2)\tan\beta_1\ell_1 + \tan\beta_2\ell_2}{(Z_1/Z_2) - \tan\beta_1\ell_1 . \tan\beta_2\ell_2} \right] \qquad (5.1)$$

where Z_j is the acoustic impedance, β_j is the propagation phase constant, ℓ_j is the length and $j = 1,2$ refers to the bond and transducer, respectively. In the case of a transducer at resonance, its impedance looking in from the bond is infinite (for Q large), and the impedance Z_d may be written simply as a mass loading on the end of the sample,

$$Z_d = i\, \omega\, M_1 \qquad (5.2)$$

writing $M_j = \rho_j\, \ell_j$ and $\tan \beta_j\, \ell_j = \omega\, \ell_j / V_j$, where ρ_j is the density and V_j the sound velocity. The phase shift on reflection (γ) is found by insertion of the calculated value for Z_d into

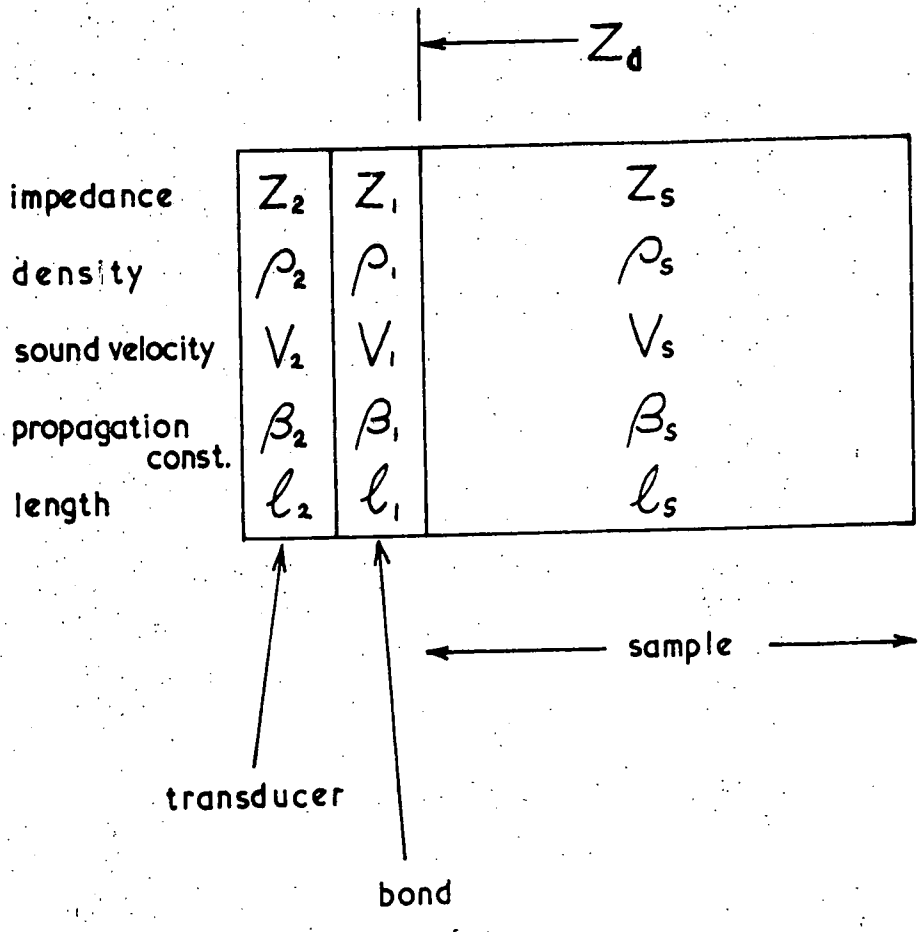

A schematic diagram of an ultrasonic sample with bonded transducer : Zd is the impedance looking into the bond.

FIGURE 5.2

$$\gamma = -2 \tan^{-1}\left(\frac{Z_d}{iZ_s}\right) \qquad (5.3)$$

where Z_s is the acoustic impedance of the sample. The phase shift due to the bond alone (for transducer impedance infinite, as at resonance) is a slowly decreasing function of frequency, but comparatively large phase shifts are imposed by slight off-tuning of the transducer from resonance. In practice it is very difficult to calculate a phase-shift correction from measurements of the shift as a function of frequency, as exact harmonic tuning is not easy to achieve, and the situation is further complicated by external electrical loadings on the transducer.

(e) THIN-FILM ULTRASONIC TRANSDUCERS

In this work the use of thin-film cadmium sulphide transducers was primarily made necessary by the failure of transducer bonding to gallium arsenide at low temperatures; however, there are several consequent advantages. The most usual cause of transducer bond failure is the dissimilar thermal contraction between the sample, transducer and bonding material on cooling. Thin-film transducers are more resilient to temperature changes than bonded transducers as they consist of many small crystallites, each firmly attached to the sample face, and the transducer can more easily follow microscopic shape changes of the sample.

The electromechanical coupling factor k (0.154) of cadmium sulphide is much greater than that (0.071) of quartz, and transduction is more efficient. Consequently the use of non-resonant transducers is more practicable. For a thin-film transducer in operation far below its

resonant frequency (that is, with a thickness much less than $\lambda/2$), the change in reflection phase shift for a change in operating frequency is correspondingly smaller than in the resonant condition. An analysis of the phase shift has been carried out along the same lines as those of McSkimin and Andreatch's (1962) work on bonded transducers (see Section 5.1(d)), but here the bond and transducer were replaced by the cadmium sulphide film and an evaporated silver backing film, respectively. Writing

$$\tan \beta_j \ell_j = \frac{\omega \ell_j}{V_j}$$

and

$$M_j = \rho_j \ell_j$$

again, we find a similar mass-loading relation for the impedance Z_d of

$$Z_d = i\omega \left[\frac{M_1 V_1^2 (M_1 + M_2)}{M_1 V_1^2 - \omega^2 \ell_1^2 M_2} \right] \qquad (5.4)$$

where $j = 1, 2$ refers to the transducer and backing film, respectively. The variation in reflection phase angle γ is is now dominated by a shift which changes slowly with frequency, as the resonance condition is relaxed. In the simplest case, with no silver backing layer, the situation is equivalent to that of a bonded exactly-resonant transducer, but now operation is possible over a wide frequency range and not just at spot frequencies as with quartz transducers: the phase shift correction may be easily evaluated experimentally.

(f) THE FABRICATION OF THIN-FILM CdS TRANSDUCERS ON GaAs

Cadmium sulphide thin-film transducers have been fabricated on gallium arsenide single crystal substrates by vapour deposition. Figure 5.3(a) shows the general scheme of the apparatus. Cadmium sulphide is evaporated from a heated boat in an evacuated enclosure and deposited on to the flat surface of a crystal via a mask which limits the area of deposition. The substrate is heated to prevent a too-rapid condensation of the vapour. The resulting film consists of an array of small crystallites of cadmium sulphide of varying orientations, plus "impurities." The crystallites exhibit a strong tendency to align themselves with their hexagonal c-axis parallel to the substrate normal, and in this orientation they will act as longitudinal-wave transducers for the substrate on application of an electrical wave across the film thickness. The film is characterised by the angle of spread of the crystallite c-axes relative to the substrate normal. "Impurities" in the film are most commonly in the form of free cadmium, which results from dissociation of cadmium sulphide during evaporation and the rapid boil-off of excess sulphur from the heated substrate (King, 1969).

There is disagreement between many workers on the optimum conditions for production of the well-aligned, high-resistivity, cadmium-free films required for efficient transduction. A detailed study (Wilson, 1971) of the deposition of CdS films carried out using the same evaporation equipment showed the following trends:

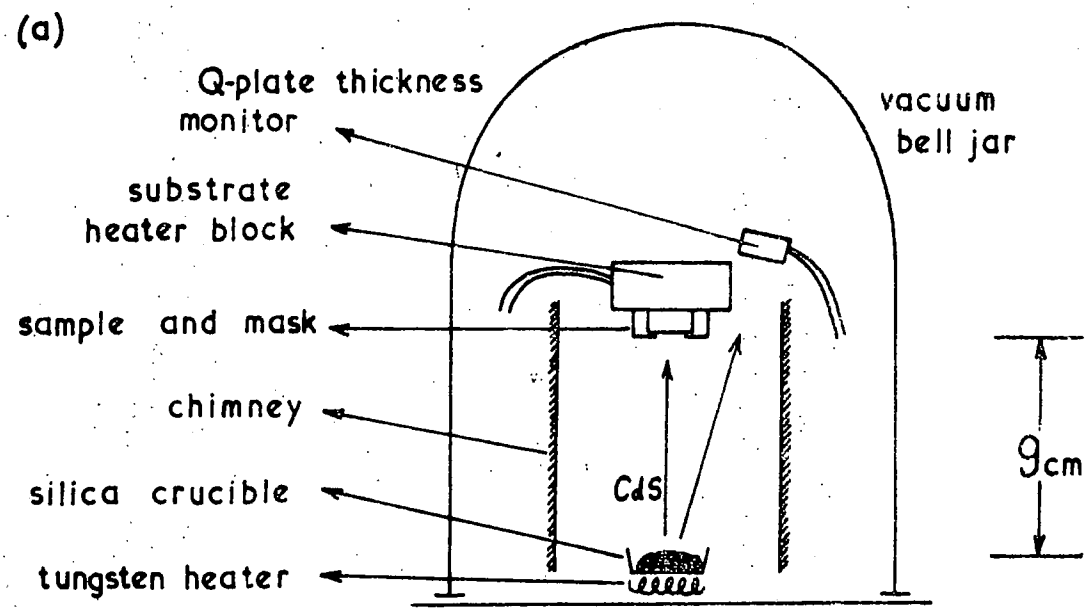

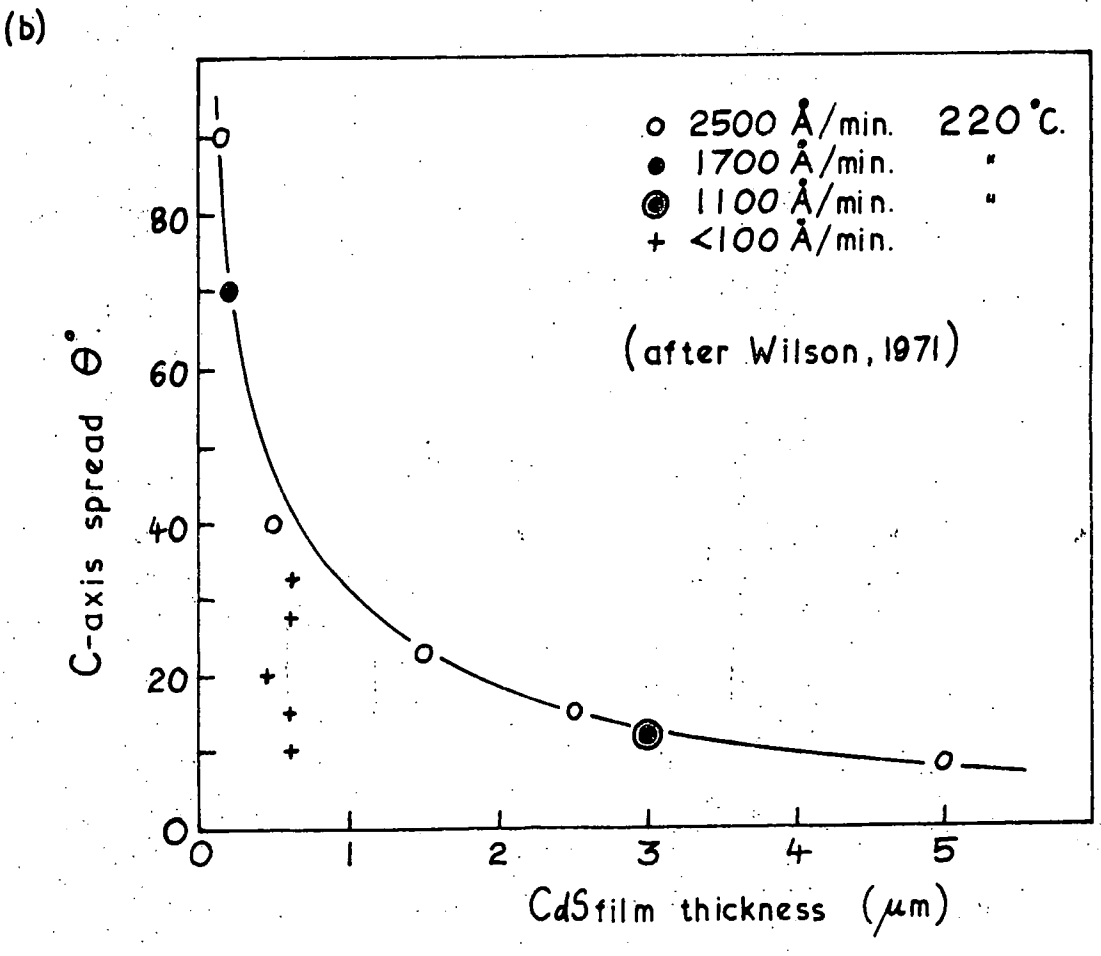

The evaporation of cadmium sulphide thin-film transducers:

(a) the evaporation equipment

(b) C-axis spread as a function of film thickness for CdS deposited on glass.

FIGURE 5.3

(i) Increase in film thickness decreased the c-axis spread (see Figure 5.3(b)).

(ii) Increase in substrate temperature increased the c-axis spread, but this influence was not so great as that of film thickness.

(iii) Lower deposition rates decreased the c-axis spread. The most satisfactory deposition rate was found to be about 1000Å/min.

(iv) In the substrate temperature range of 200°C to 300°C the film resistivity increased with temperature: a somewhat higher temperature than that commonly used (about 200°C) seems to give a more useful film for transduction. This finding is at variance with that of King (1969), but his experimental conditions were quite different.

Deposition was carried out on (111), (100) and (110) faces of the gallium arsenide single crystals by evaporation of B.D.H. optran 12a grade polycrystalline cadmium sulphide from a distance of 9 cm along the normal to the crystal faces. The substrate temperature was 300°C, the deposition rate averaged about 1000Å/min (see Figure 5.4(a)), the pressure remained below 10^{-5} torr throughout the evaporation and the final film thickness was 4 μm. Glancing angle X-ray photographs showed a fair degree of crystallite ordering (see Figure 5.4(b)). A 2 μm layer of silver was evaporated on to the film, as shown in Figure 5.5(a), to give the required electrical contact. The resulting transducers gave, at this stage, poor signal-to-noise ratios and substantial shear as well as longitudinal mode generation, owing to the spread in c-axis

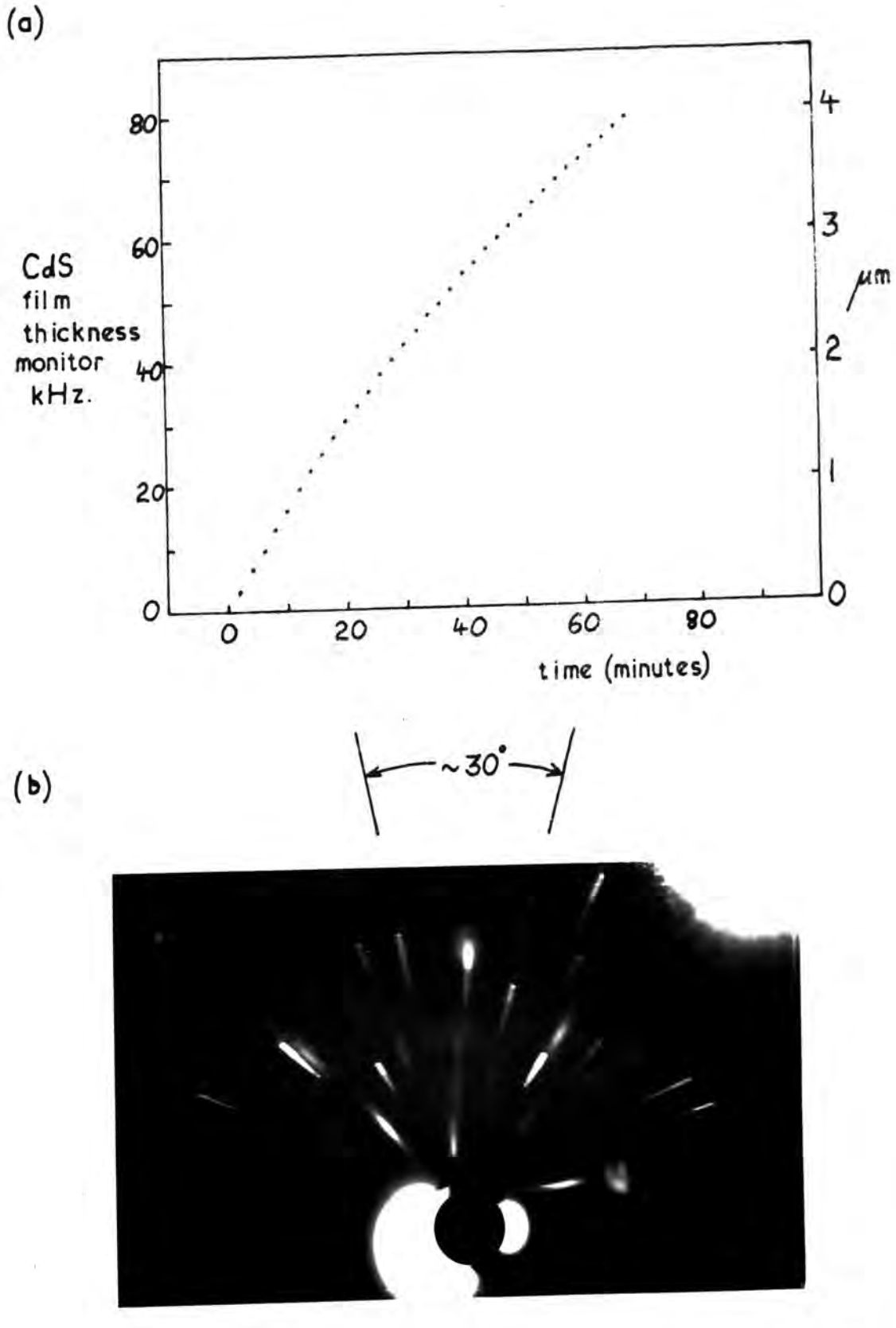

The evaporation of cadmium sulphide thin-film transducers on GaAs:

(a) a typical deposition rate

(b) glancing-angle X-ray photograph of a 4 μm film on a (111) substrate.

FIGURE 5.4

(a)

(b)

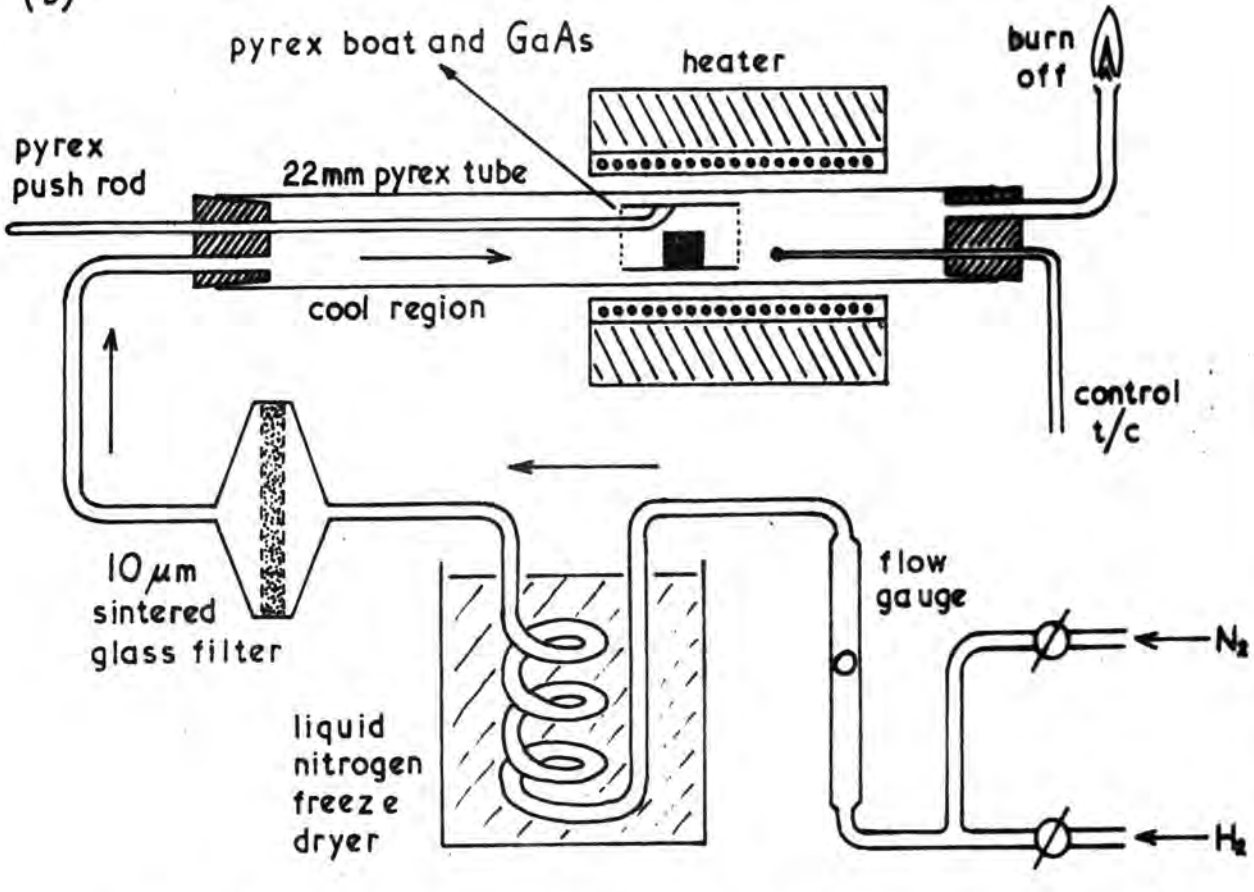

The fabrication of cadmium sulphide thin-film transducers on GaAs:

(a) a crystal with a deposited CdS film, and with the evaporated silver contact layer.

(b) the recrystallisation furnace.

FIGURE 5.5

orientations. A recrystallisation technique was used to increase the cadmium sulphide grain size and resistivity and to improve the overall crystallite orientation; the substrate and film were heated to 500°C for 5 minutes under dry hydrogen in the furnace shown in Figure 5.5(b). The presence of silver has been found to accelerate the recrystallisation process (Vecht, 1966). After heat treatment the silver layer was more resistant to scratching. The signal-to-noise ratio - the best measure of performance in this context - was much improved after recrystallisation (Figure 5.6), as was the crystallite orientation, as evidenced by the lack of shear-wave generation. A shear-wave transducer was fabricated on a (100) GaAs face by the scheme of Foster et al (1968) of evaporating from a source at an angle of 50° to the substrate normal.

The resonant frequencies of these films were about 500 MHz: for operation in the region of 50 MHz, the phase-shift condition is that described in Section 5.1(e).

5.2 ULTRASONIC SYSTEMS

(a) THE SIMPLE PULSE-ECHO TECHNIQUE

The simple pulse-echo system shown in Figure 5.7 is that used in this work for the measurement of ultrasonic attenuation. It is also the basis of the more complicated pulse-superposition system used here for ultrasonic velocity measurements. R.F. pulses with a chosen carrier frequency between 10 and 750 MHz, of 0.5 to 5 μ sec. length and 1 kV amplitude, are available at repetition rates of up to 1000 sec^{-1}, in this case from a Matec 9000 ultrasonic

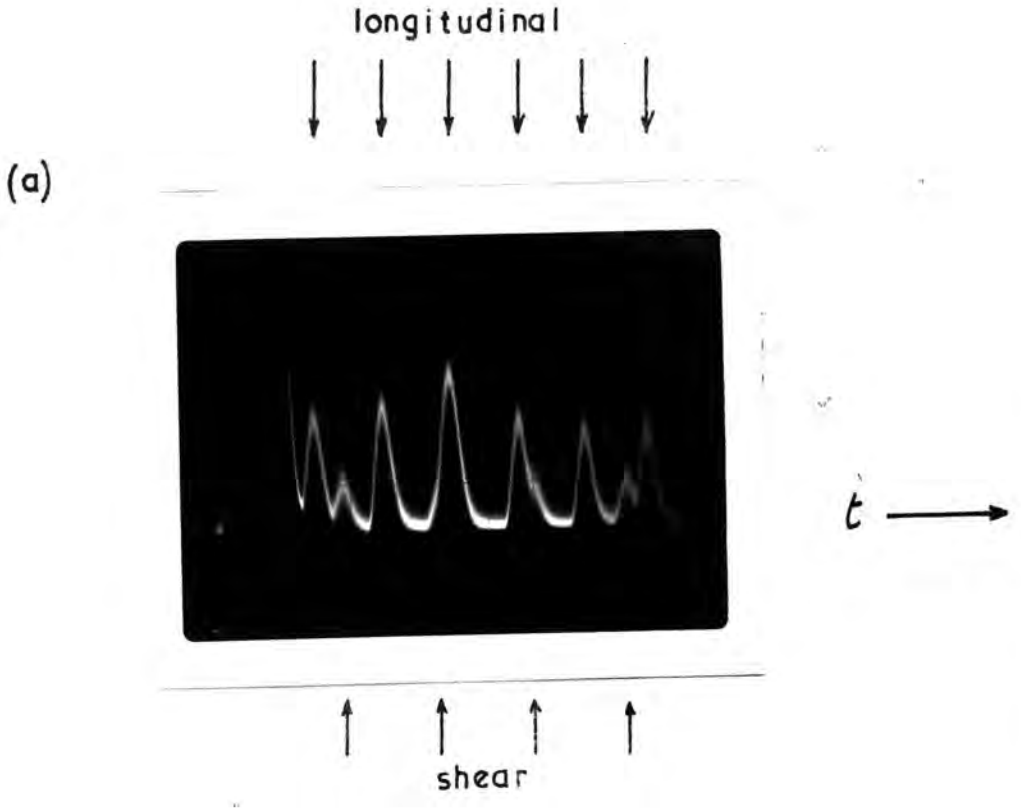

Ultrasonic echo trains in GaAs using a CdS transducer

(a) before recrystallisation

(b) after recrystallisation of the CdS film.

FIGURE 5.6

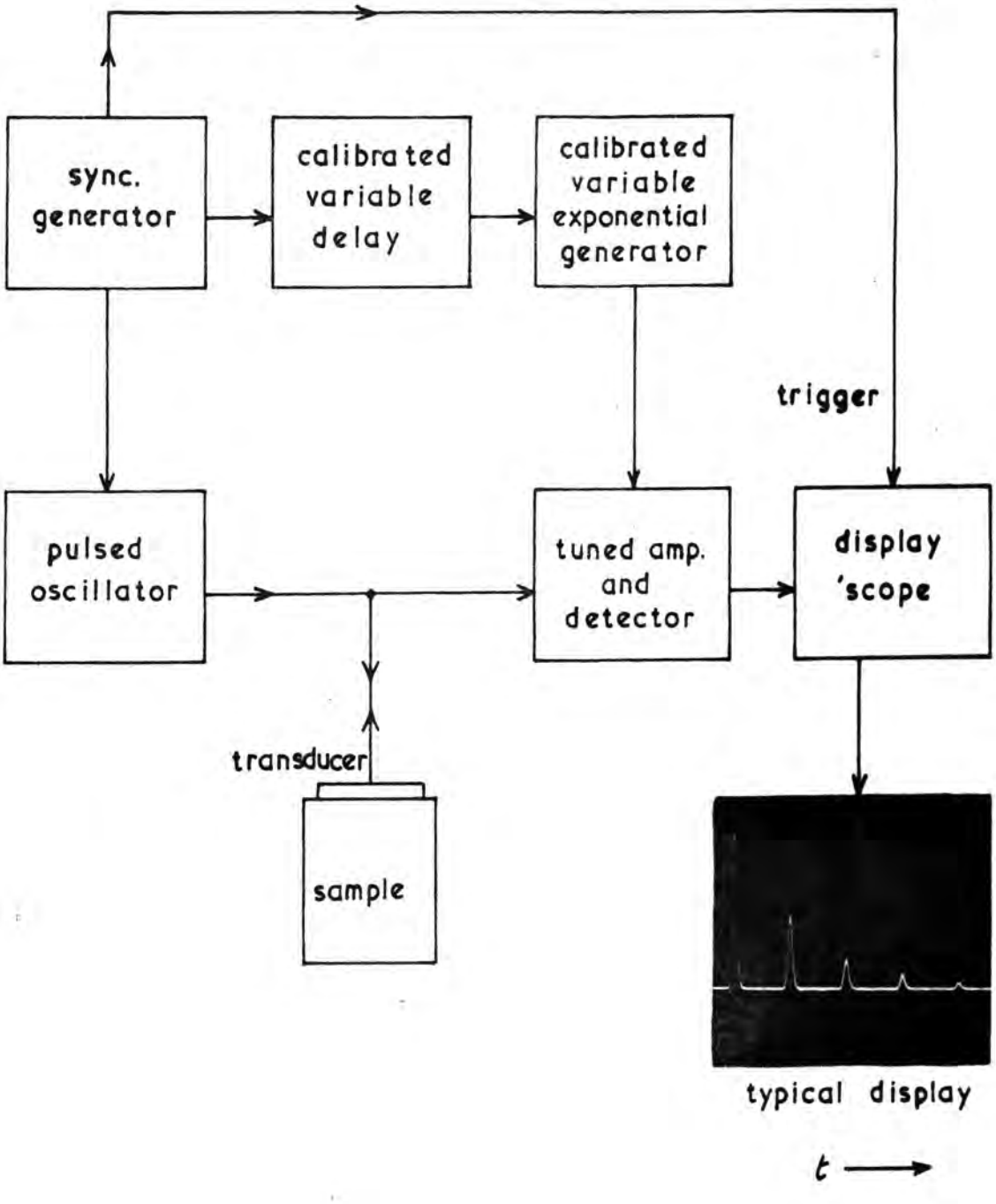

A block diagram of equipment used in the simple pulse-echo technique.

FIGURE 5.7

comparator. The bandwidth of the tuned amplifier is 4 MHz and the gain is high (maximum 80 dB) to compensate for the high insertion loss associated with the use of quartz transducers (typically 30 to 60 dB). The oscilloscope displays alternately the ultrasonic echo train (Figure 3.3) and a calibrated exponential curve. Round trip echo times are measured by matching the leading edge of the exponential to successive echoes with the variable delay, and attenuation by fitting the exponential curve to the echo train decay.

In the single-ended technique shown in Figure 5.7 the initial R.F. pulse saturates the tuned amplifier, which must then recover before the ultrasonic echoes return. In principle all the echoes may be used in making measurements, but by comparing echo shapes it can be shown that the first few are substantially affected, particularly in loss of amplitude, by lingering effects of the receiving recovery (see Figure 5.8). Also, internal delays in the equipment cause the time interval between the initial pulse and the first echo of the display to be different from the succeeding inter-echo times (Figure 5.9). Echo shapes are not exactly equivalent to the shape of the initial R.F. pulse; this is due to the restricted bandwidth (4 MHz) of the tuned amplifier.

(b) THE PULSE SUPERPOSITION TECHNIQUE

The pulse superposition technique of velocity measurements devised by McSkimin (1961) is fundamentally the same as the simple pulse-echo technique, in that a succession of pulses of ultrasound is injected into the crystal and observation made of echoes returning to the transducer. In the simple case the pulse repetition rate

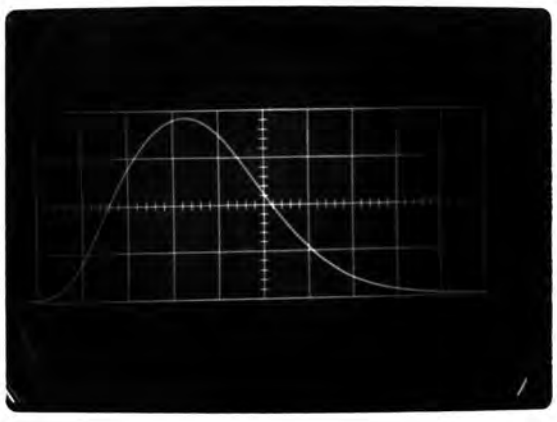

1st echo

t →

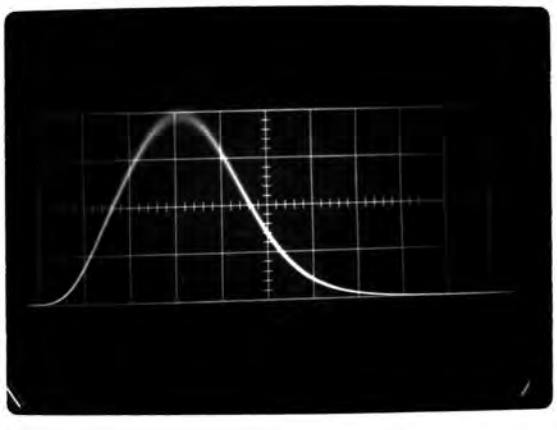

8th echo

t →

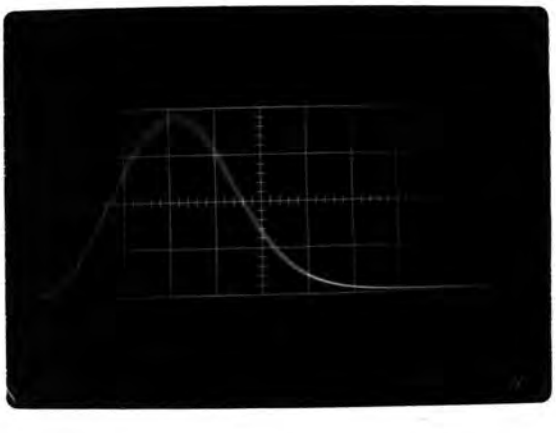

28th echo

t →

The effect of receiver-recovery on echo shapes in the simple pulse-echo technique.

FIGURE 5.8

(a)

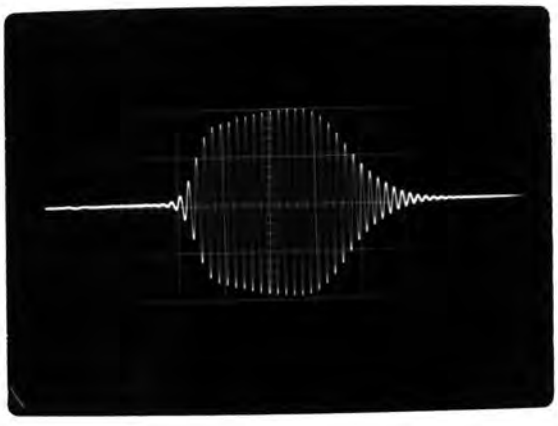

t →

(b)

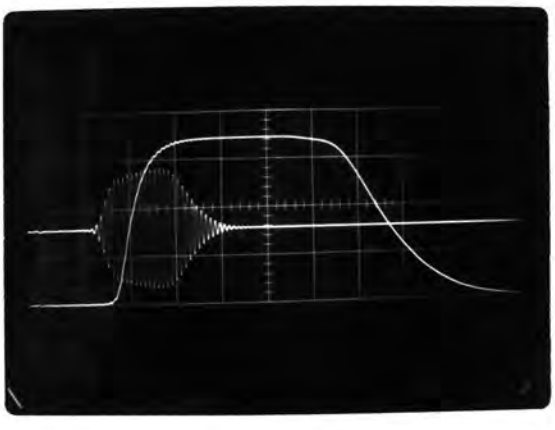

t →

(c)

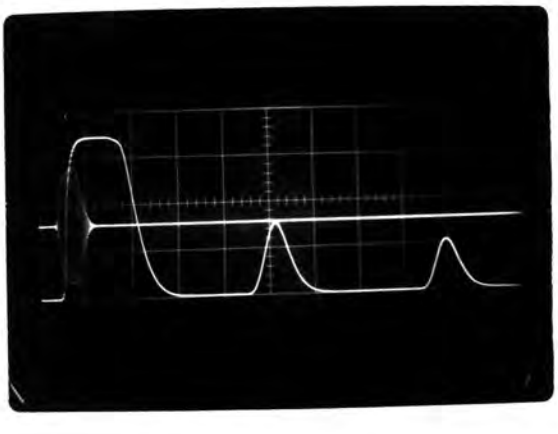

t →

The simple pulse-echo technique:

(a) the R.F. pulse shape

(b) receiver delay and saturation caused by the R.F. pulse.

(c) increased apparent transit time in the first round trip

FIGURE 5.9

is set low enough to avoid interference between successive echo trains, but for pulse-superposition it is raised so that the time between R.F. pulses is a small integral multiple (p) of the pulse round-trip time in the crystal. If this time interval is set at twice (p=2) the round-trip time T the situation is as shown in Figure 5.10: the oscilloscope displays a summation of all the pulses and echoes, thus all the even-numbered echoes are obscured by following R.F. pulses but the odd numbered echoes appear superimposed in the gaps between the pulses. Fine adjustment of the pulse repetition rate gives maximum amplitude of the echo sum for exact superposition. The transit time can now be derived from the repetition rate.

The closer together that the superimposed echoes are in amplitude, the higher is the sensitivity of the amplitude summation to slight changes in pulse repetition rate: the method is most sensitive in the condition p=1. However, for p=1, all the echoes will be obscured, so to observe the superposition of the echoes a gap must be left after the injection of a number of pulses. Figure 5.11 shows the equipment used to perform this function. The display oscilloscope is a Tektronix 585A, which provides a second timebase (A) to intensify parts of the display: the gate signal from this timebase is used to blank off some of the pulses from a continuously-running General Radio 1217c pulse generator. Figure 5.12 is a schematic of waveforms in the system. A Codasyn CS201S frequency sythesiser, adjustable to 0.1 Hz, is used to drive the pulse generator, which modulates an Arenberg PG650C pulsed oscillator. A

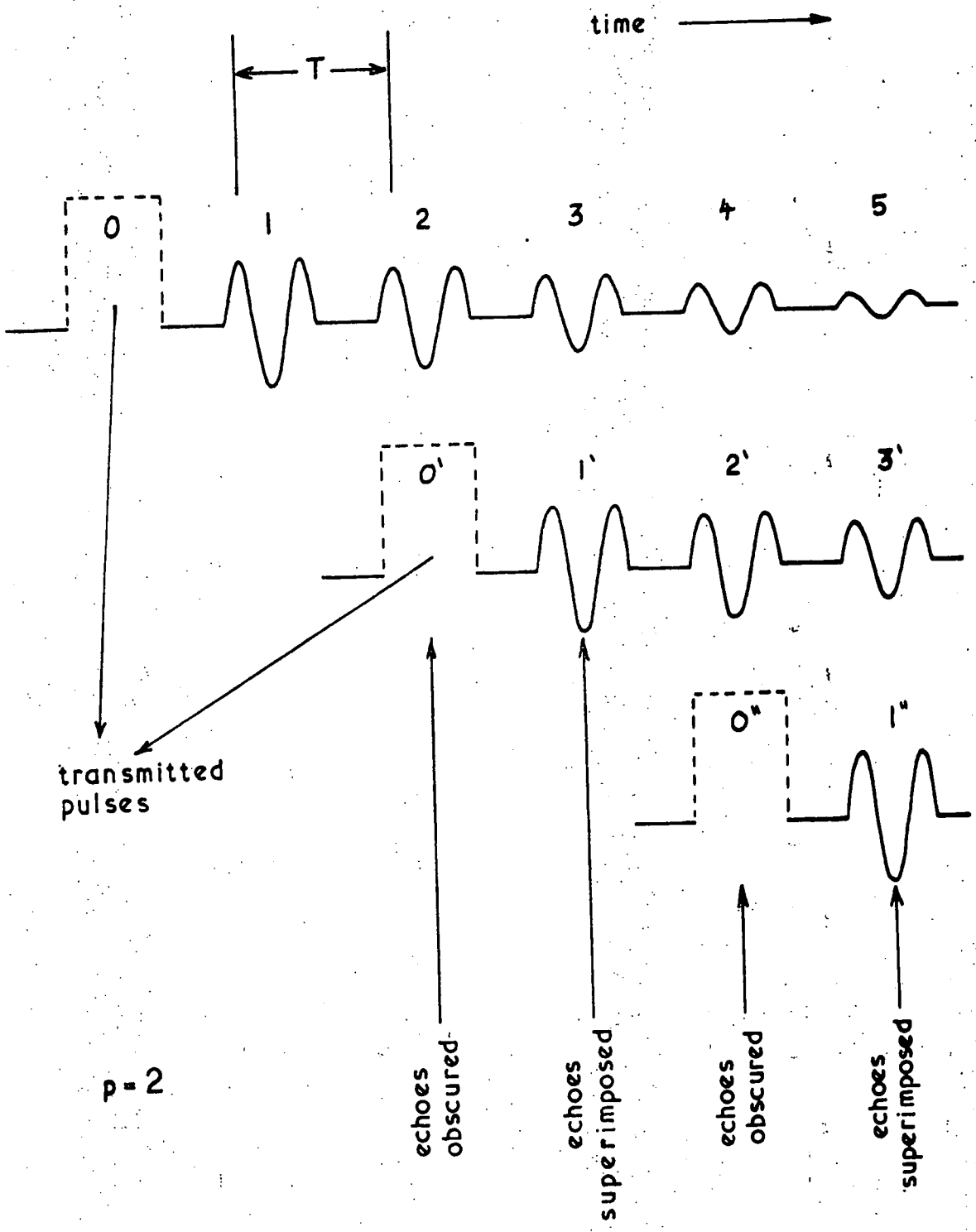

A schematic diagram of pulse-superposition in the p = 2 condition : alternate echo-summations are obscured.

FIGURE 5.10

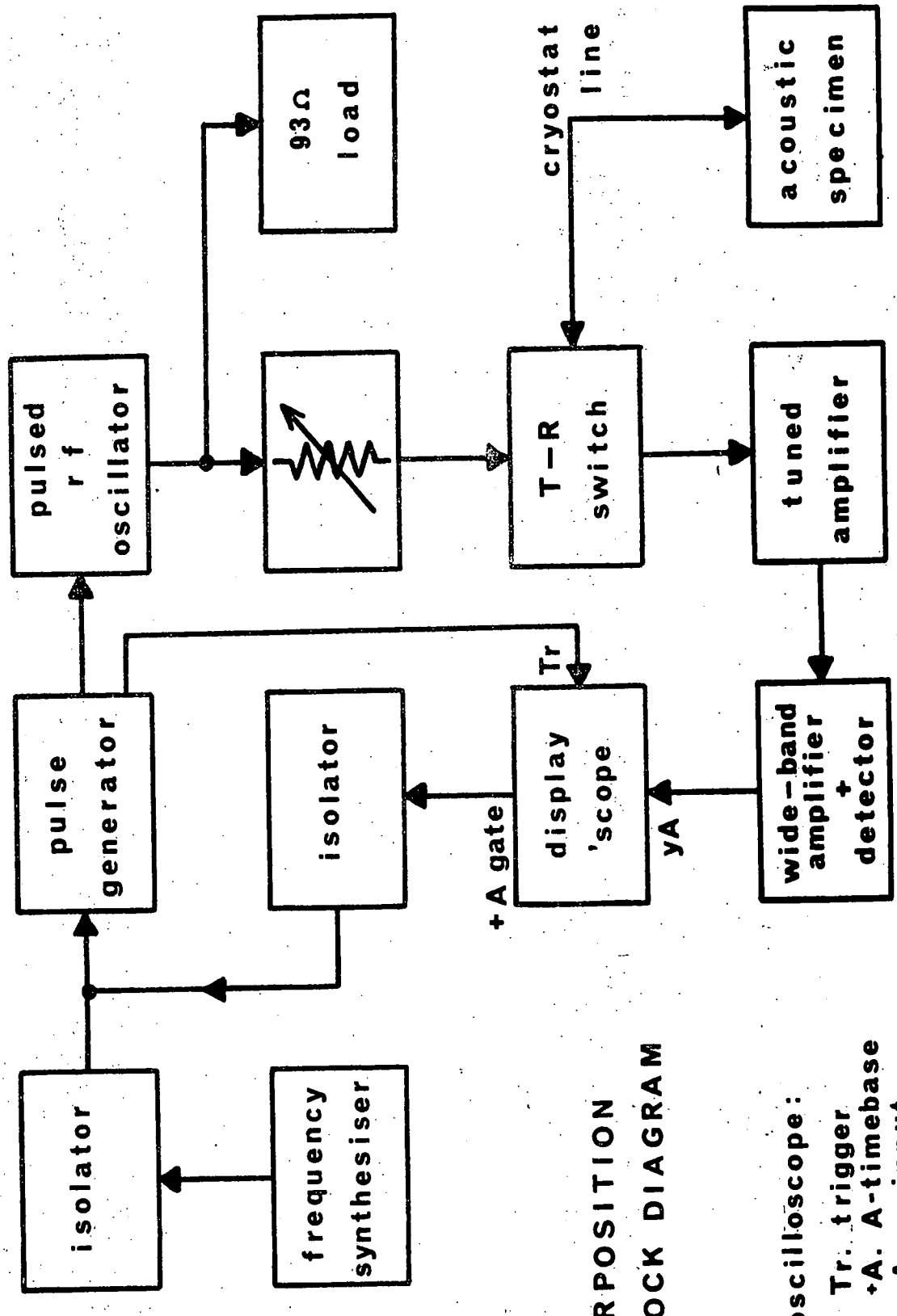
93Ω load
cryostat line
acoustic specimen
pulsed r f oscillator
T—R switch
tuned amplifier
pulse generator
isolator
Tr
+A gate
display 'scope
yA
wide—band amplifier + detector
isolator
frequency synthesiser
PULSE SUPERPOSITION
SYSTEM BLOCK DIAGRAM
oscilloscope:
Tr. trigger
+A. A-timebase
yA. y-input

FIGURE 5.11

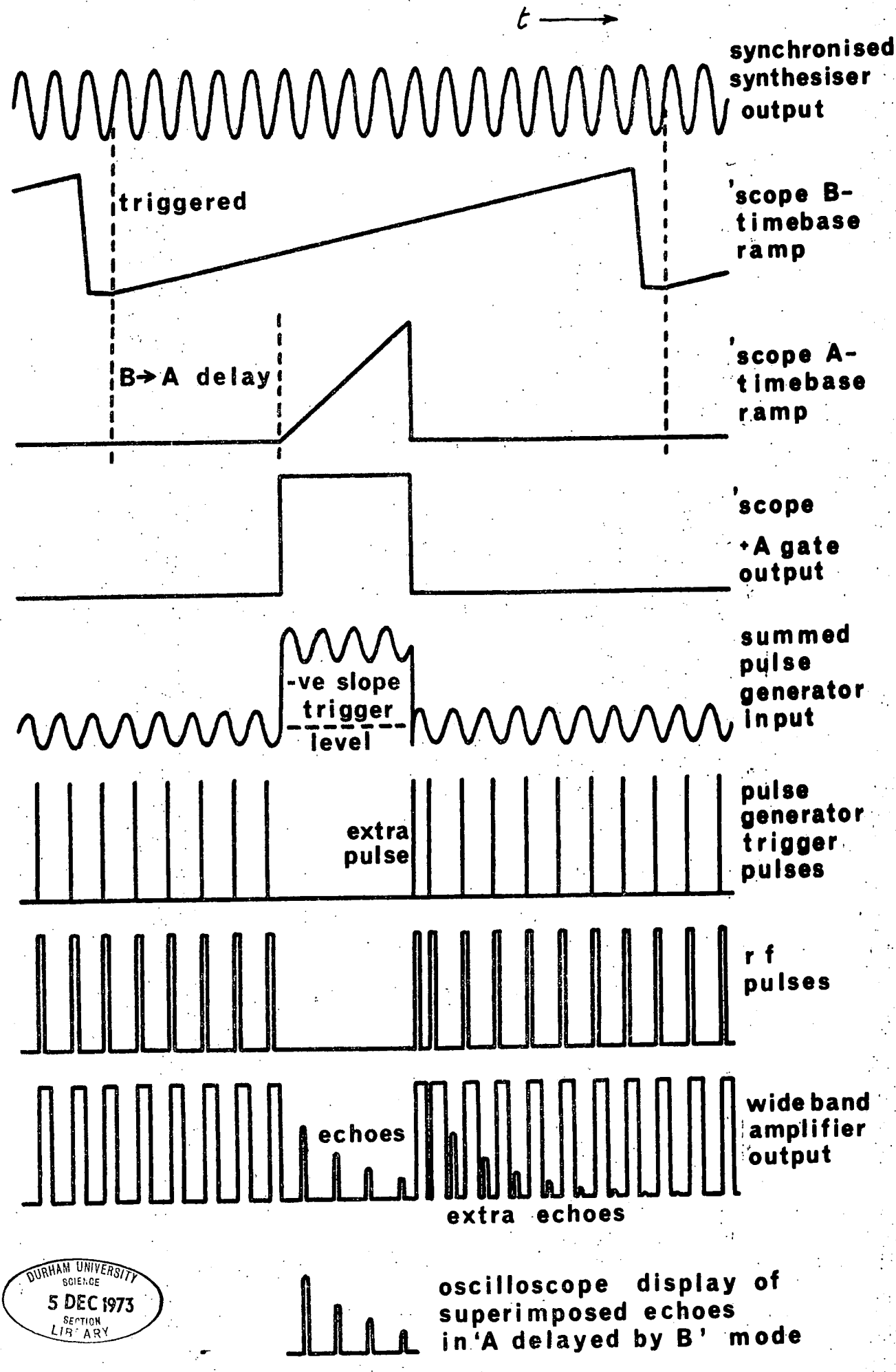

oscilloscope display of superimposed echoes in 'A delayed by B' mode

PULSE SUPERPOSITION SYSTEM;
TIMING SEQUENCE AND WAVEFORMS

FIGURE 5.12

diode T-R switch is used to protect the Arenberg PA620 tuned amplifier from the high-voltage initial R.F. pulses. Echoes pass from the tuned amplifier to the Arenberg WA600E wide-band amplifier and detector, and thence to the display oscilloscope. The pulse generator is triggered at zero voltage by a negative going waveform; addition of the oscilloscope A gate to the input causes one extra pulse to be generated at a somewhat random time (see Figure 5.12); the time period between regions gapped out for observation of the correctly superimposed echoes must be great enough to avoid interference by echoes resulting from this extra pulse. Maximisation of the superimposed echo amplitudes is performed by adjustment of the frequency synthesiser output, using the 'A-delayed-by-B' oscilloscope mode to expand the relevant display section.

(c) AN ANALYSIS OF PULSE-SUPERPOSITION

In the pulse-superposition technique selection of the correct value for p may be made by examination of the summed echo trains around exact superposition. Figure 5.13 shows recordings of displayed echo trains in the simple pulse echo mode and in the pulse superposition mode for pulse repetition rate f_c equal to 0.82 f_{co}, 0.88 f_{co}, 0.94 f_{co}, f_{co}, 1.06 f_{co}, 1.12 f_{co} and 1.18 f_{co}, where f_{co} is the repetition rate giving exact superposition for p=1. However, summation (or superposition) of the echoes takes place before rectification and smoothing of the echo envelopes, so it is a function of phase as well as amplitude; a number of maxima may be observed in measurements of the summed amplitude over a range of repetition rates (see

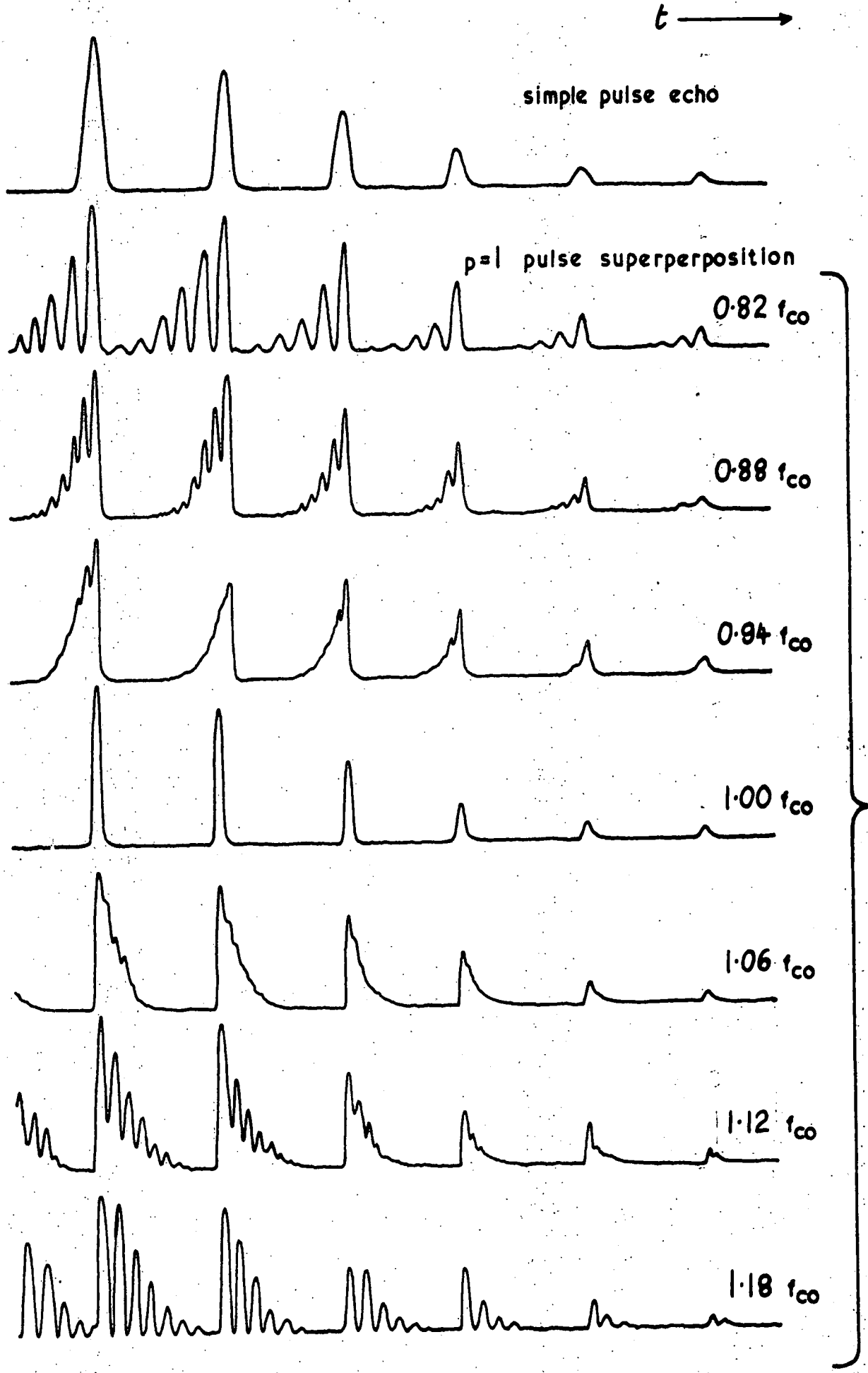

The echo trains observed in the p = 1 pulse superposition technique for repetition rates slightly displaced from fco.

FIGURE 5.13

Figure 5.14(a)), p remaining the same. The modes of superposition causing these maxima are those giving phase coincidence between consecutive echoes, as shown in Figure 5.14(b). Measurements of the positions of these maxima result in a set of repetition rates f_{Cn} corresponding to a set of apparently different round-trip times;

$$f_{Cn} = \frac{V}{2\ell \pm n\lambda} \tag{5.5}$$

where V is the sound velocity, ℓ the crystal length, λ the ultrasonic wavelength and n a small integer. The correct rate f_{CO} may be chosen by careful direct transit-time measurements using a calibrated-delay oscilloscope at low ultrasonic frequencies. As the ultrasonic frequency F is increased, the separation between adjacent superposition repetition rates f_{Cn} falls, making correct selection of f_{CO} by means of the simple pulse-echo technique very difficult; as F tends to infinity the separation vanishes, as $n\lambda \rightarrow 0$ in equation 5.5. Figure 5.15(a) shows the general form of this phenomenon for V independent of F; f_{CO} is the "n=0" repetition rate and f_{Cn} are related to it by

$$f_{Cn} = f_{CO} \frac{2\ell}{2\ell \pm n\lambda} \tag{5.6}$$

Consequently, as $2\ell/(2\ell \pm n\lambda)$ is simply an arithmetic factor, all of the set f_{Cn} show the dispersive properties, if any, of f_{CO}, including the transducer reflection phase-shift dependence described in sections 5.1(d) and 5.1(e). Figure 5.15(b) shows measurements of part of the set f_{Cn} as a function of frequency for a gallium arsenide crystal, using a cadmium sulphide thin-film transducer. The frequency

(a)

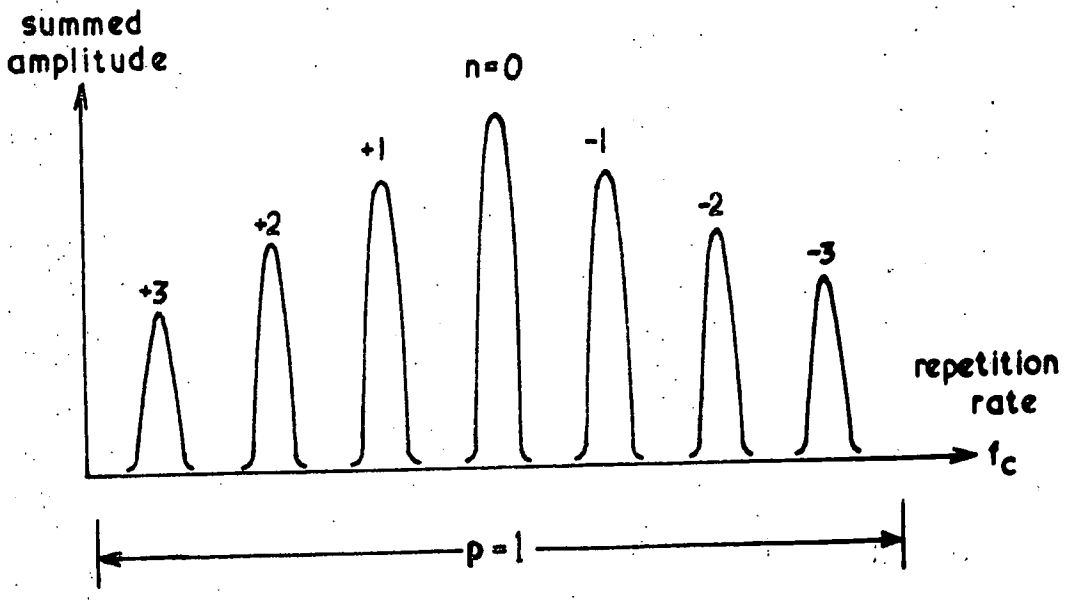

(b)

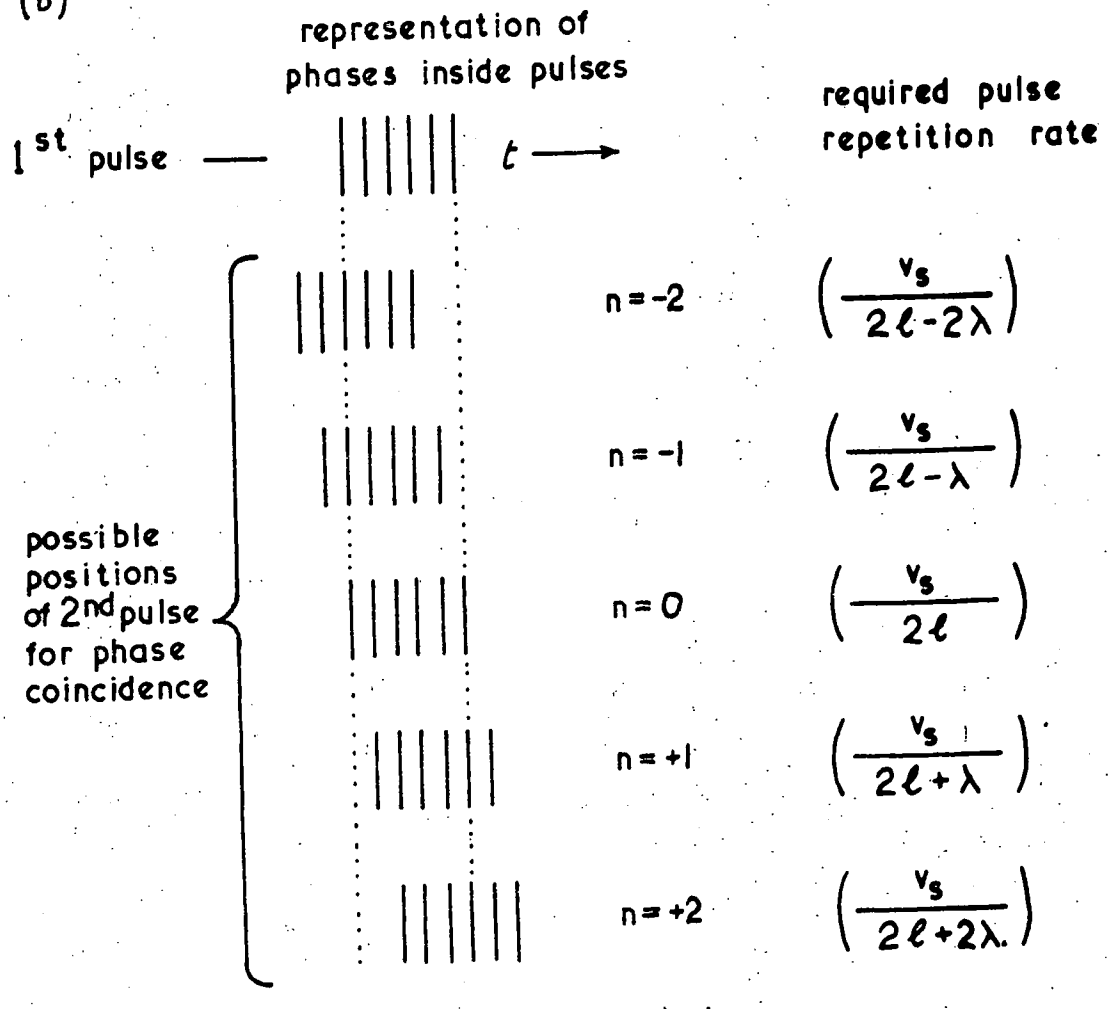

The p = 1 pulse superposition technique:

(a) the pulse summation amplitude as a function of repetition rate.

(b) the possible phase coincidence conditions.

FIGURE 5.14

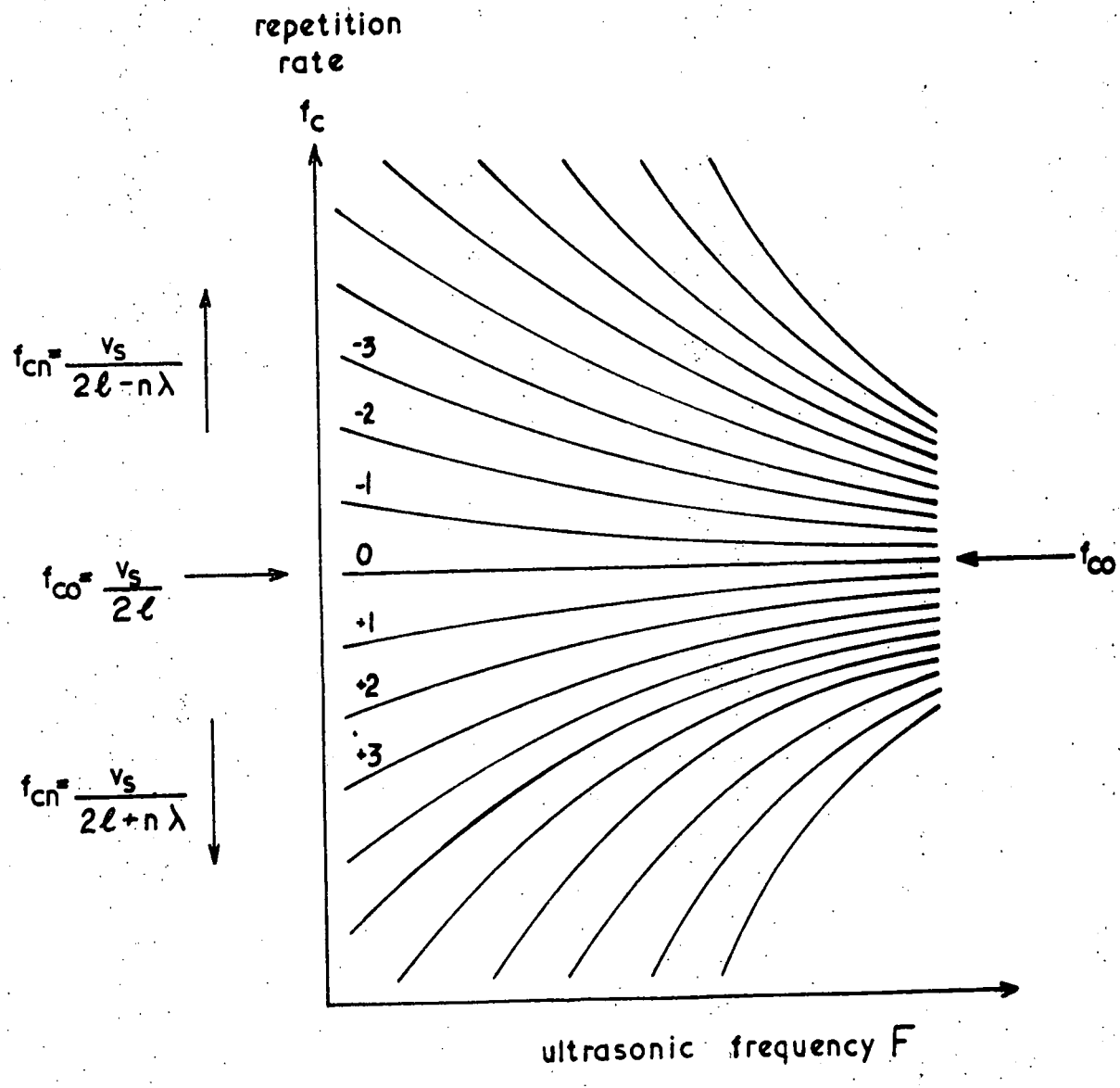

The pulse superposition technique : the expected curves of repetition rate against ultrasonic frequency for n constant : all converge to the value of f_{CO} at infinite frequency.

FIGURE 5.15.a

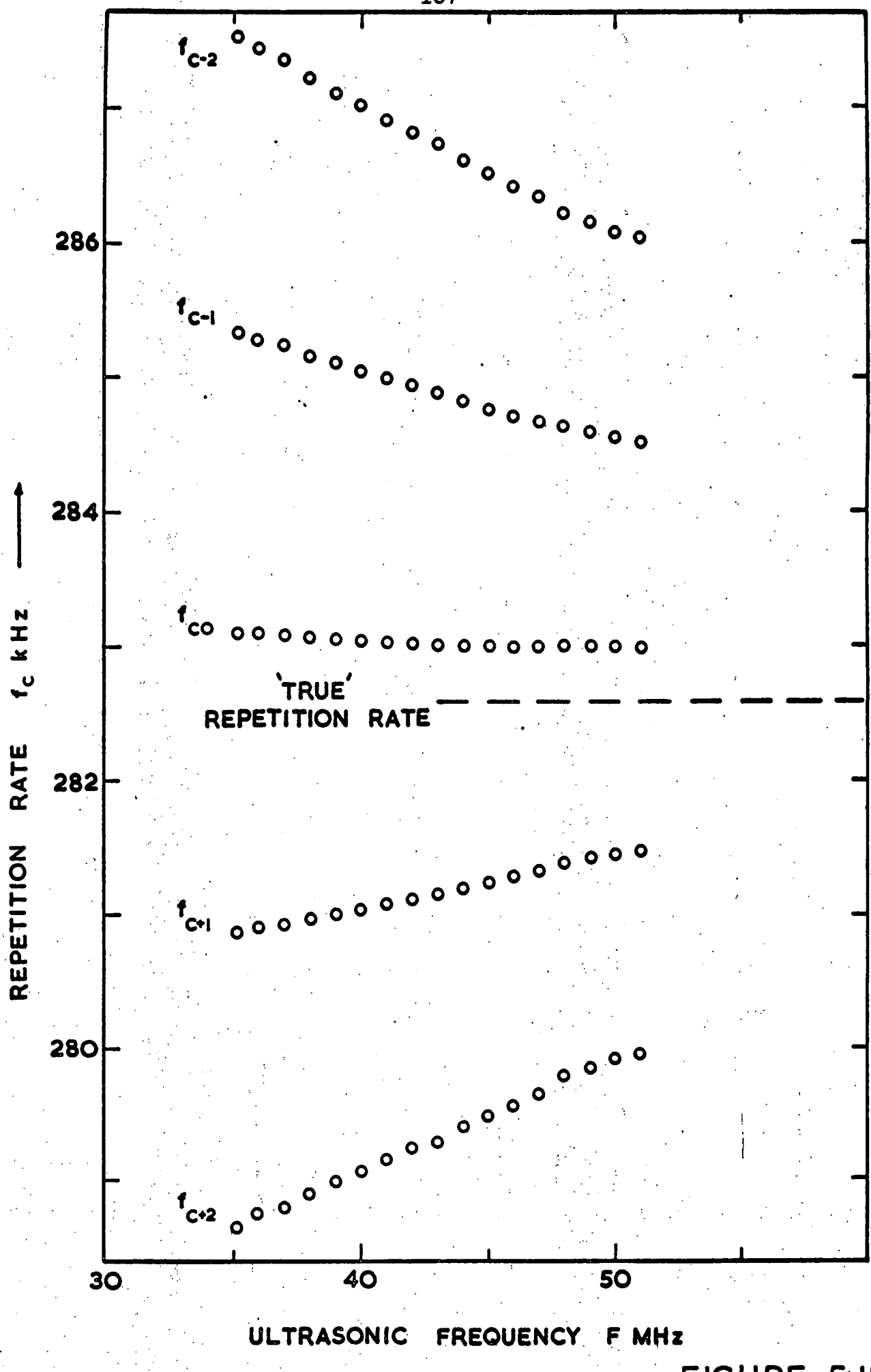

FIGURE 5.15.b

The pulse superposition technique : measurements of repetition rate as a function of ultrasonic frequency in a [111] GaAs sample for n = -2, -1, P, +1, +2.

dependence of the p=1, n=0 repetition rate (f_{CO}) due to the transducer-reflection phase shift is shown expanded in Figure 5.16. The anomaly around 48 MHz is due to an equipment electrical resonance; the sampled-CW plots (see Section 5.2(d)) of the frequency response of the sample show a broad maximum centred on 48.5MHz which partially obscures the sample resonances in this region but which disappears below 46 MHz; the resonances over the rest of the range are clear from any external interference. The complete equation for the repetition rate in the pulse superposition case derived by McSkimin (1961) includes the transducer reflection phase-shift in terms of a phase angle γ;

$$\frac{1}{f_C} = pT - \frac{p\gamma}{360F} + \frac{n}{F} \qquad (5.7)$$

The frequency dependence of the repetition rate f_{CO} has been fitted by equation 5.7 in the range 35 to 45 MHz (Figure 5.16), giving a "free-space" repetition rate of 282,581 Hz. A consequence of equation 5.6 is that equation 5.7 applies equally well to all of the set f_{Cn}. Fitting of equation 5.7 to the dependences of the f_{C+2}, f_{C+1}, f_{C-1}, f_{C-2} in Figure 5.15(b) gives values for the "free-space" repetition rate of 282,720 Hz, 282,649 Hz, 282,538 Hz and 282,475 Hz respectively, a spread of only 0.1% of f_{CO}: to a high degree of accuracy it is irrelevant whether correct selection of the n=0 condition is made if measurements are possible as a function of frequency. With quartz transducers this is difficult to achieve, as measurements must be made exactly at the transducer harmonic frequencies and a wide

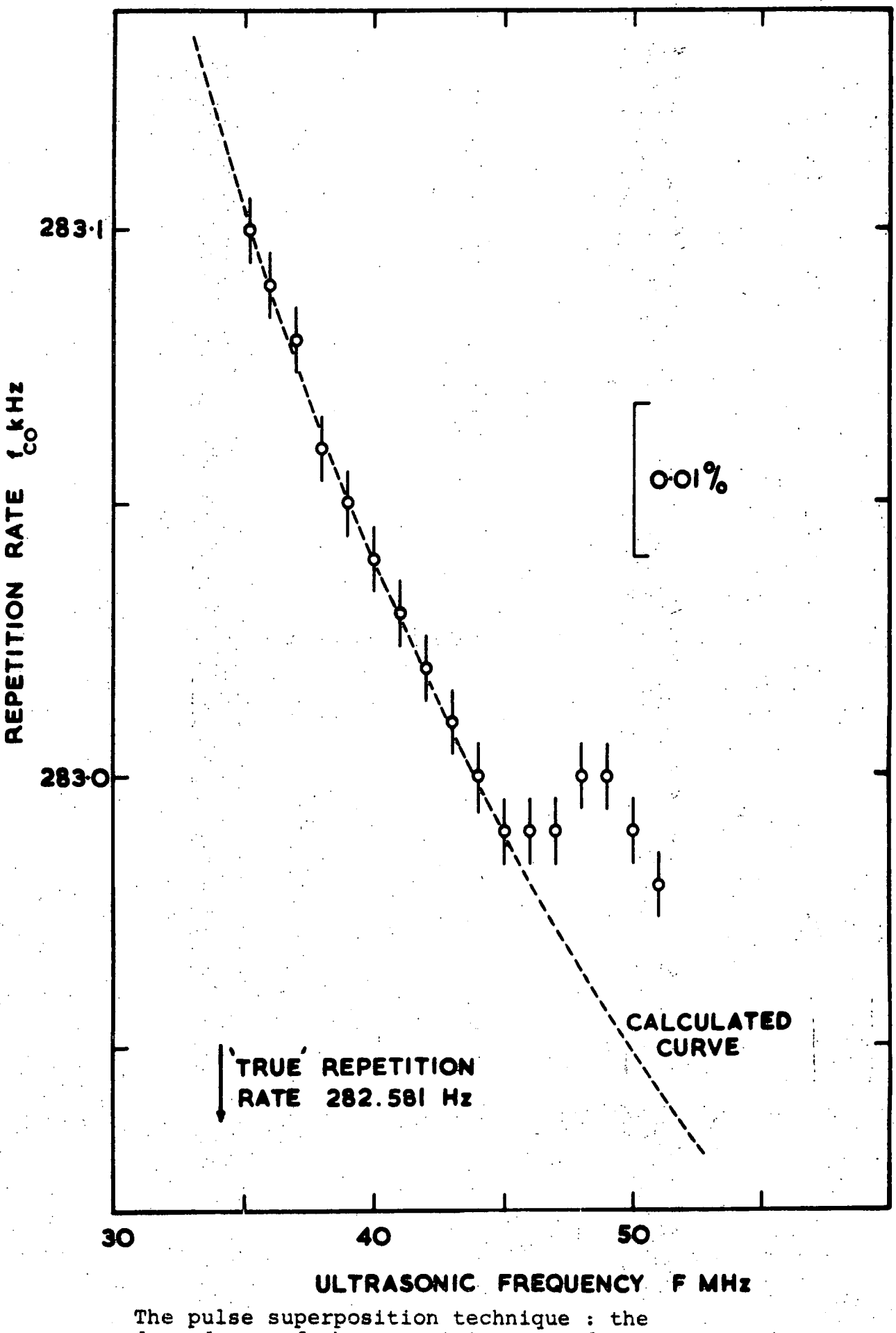

The pulse superposition technique : the dependence of the repetition rate f_{CO} on ultrasonic frequency.

FIGURE 5.16

frequency range must be covered. The results quoted above are derived from measurements over a frequency range of only about 25% at 40 MHz.

Figure 5.14(a) is a diagram of a vertical section of Figure 5.15(b): the measured points in the latter are repetition-rate values at the peaks of the "pseudo-resonance" curves drawn in the former. Figure 5.17 shows measurements of the shape of one of these pseudo-resonance curves. The slower fall on the low repetition-rate side of the curve is consistent with calculations for a slightly non-parallel sample made by Miller and Bolef (1970). The width of the curve at half height is about 0.1% of f_c. The dashed curve is calculated from a summation of sine waves

$$A = \sum_{i=0}^{\infty} a_i \sin (wt + i\phi) \qquad (5.8)$$

for a_i decreasing exponentially with i.

(d) THE SAMPLED - CONTINUOUS WAVE TECHNIQUE

If the length of the R.F.-pulse used in the simple pulse-echo case is made greater than twice the length of the sample (see Figure 3.3), interference results between the beginning and end of the pulse. If the condition $2\ell = n\lambda$ is met, where n is an integer and λ the ultrasonic wavelength, then the interference is constructive and the amplitudes add. Monochromacity of the response increases with increase in pulse-length, to the limit of perfect monochromacity at infinite length. However, such continuous-wave ultrasonic investigations require the use of two transducers for input and output, and at MHz frequencies the signal leakage between the two transducers is a serious

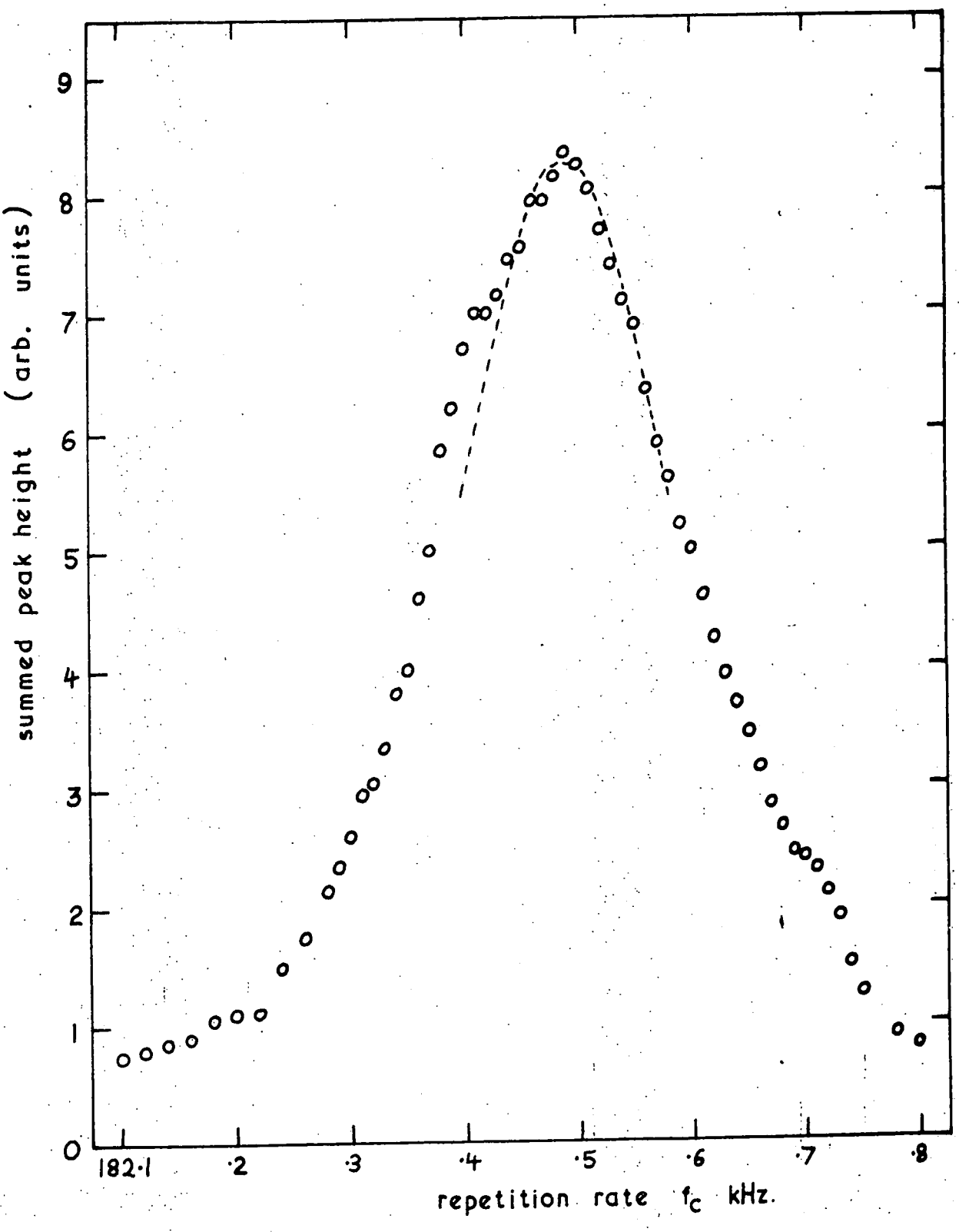

The pulse superposition technique : measurements of the shape of one of the pseudo-resonance curves shown in Figure 5.14(a).

FIGURE 5.17

problem. The advantages of both pulsed and continuous-wave (CW) operation are combined in the sampled-CW technique devised by Miller and Bolef (1969). The RF-pulse is made long enough to remove the influence of the leading edge on observations of the response decay made after the pulse has ended (see Figure 5.18).

A block diagram of the equipment used is shown in Figure 5.19. The frequency synthesiser (operating at 150 Hz) controls the generation of long (150 μS) RF pulses which are applied to the thin-film transducer on the sample. The resulting time response of the sample is amplified and displayed on an oscilloscope. Figure 5.20 is a schematic of waveforms in the system. Using the scan-delay generator the time response (see Figure 5.18) or the frequency response may be recorded at a chosen delay after the end of the RF pulse. The same equipment may be operated in the simple pulse-echo configuration, by reducing the pulse length to about 1 μS. With the equipment used in this work, the RF frequency could not be measured simply by switching the oscillator to a true CW mode as this changed the oscillator loading and frequency; therefore a gated frequency counter was constructed to measure frequencies inside the long RF pulses. An attenuator was inserted in the RF line to allow measurements as a function of RF amplitude without changes in the transducer or pulsed oscillator loading. The frequency range available was restricted to between 35 MHz and 51 MHz for pulse-superposition by pulsed oscillator/transducer matching limitations.

The time response in the sampled - CW mode is a stepwise decay (Miller and Bolef 1970) of time period equal

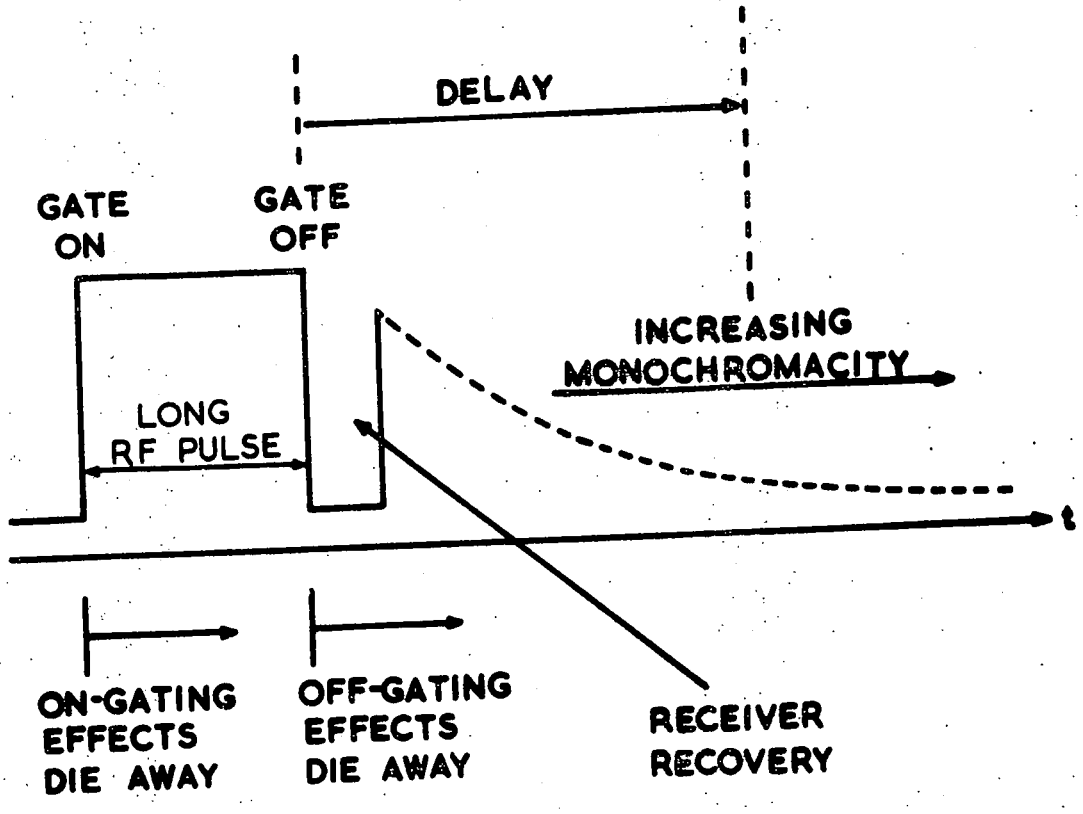

General form of the display of a sample-CW time response, showing the gating decay.

FIGURE 5.18

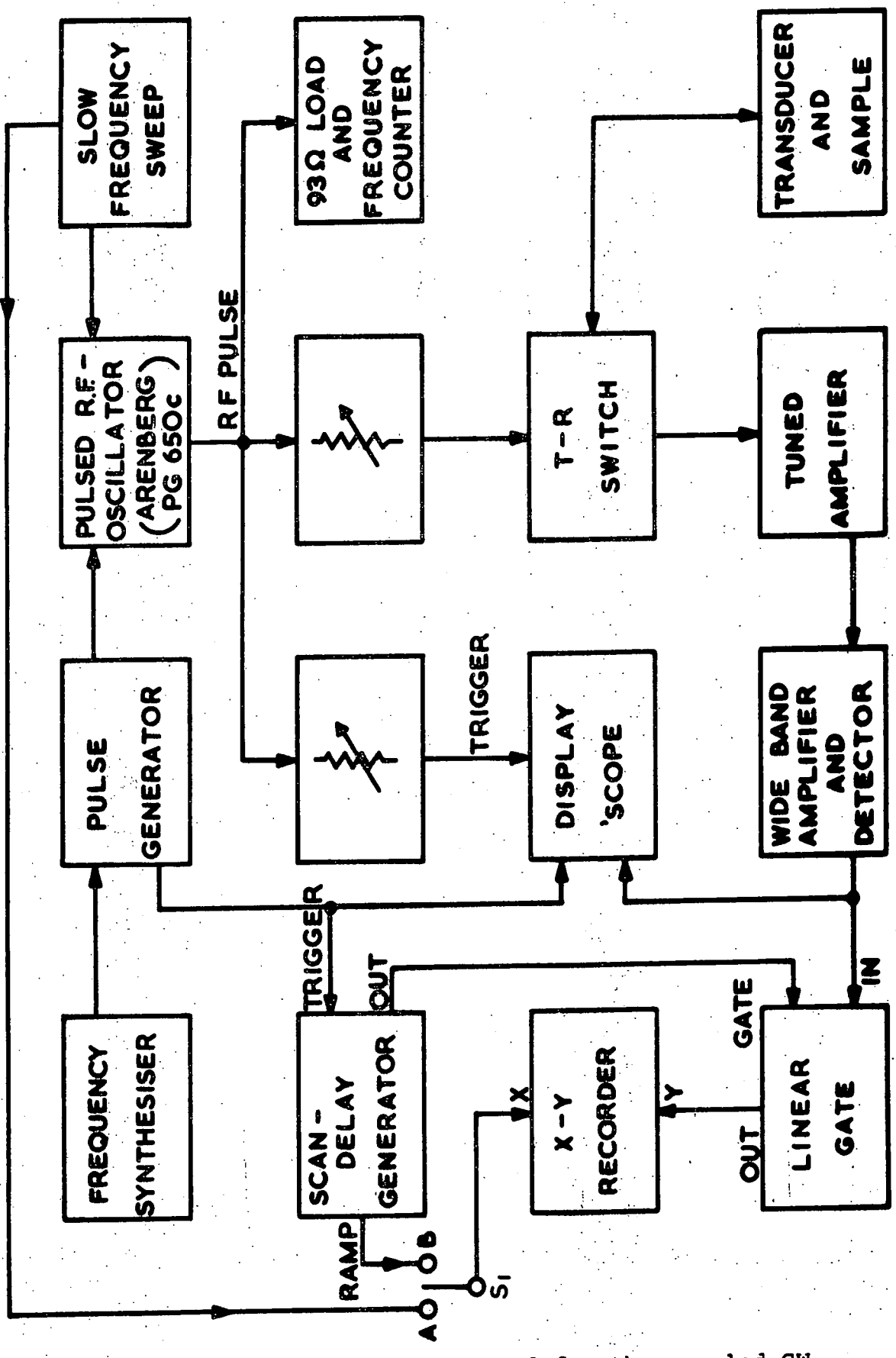

Block diagram of the equipment used for the sampled-CW technique. Switch S_1 : position A for frequency response, position B for time response.

FIGURE 5.19

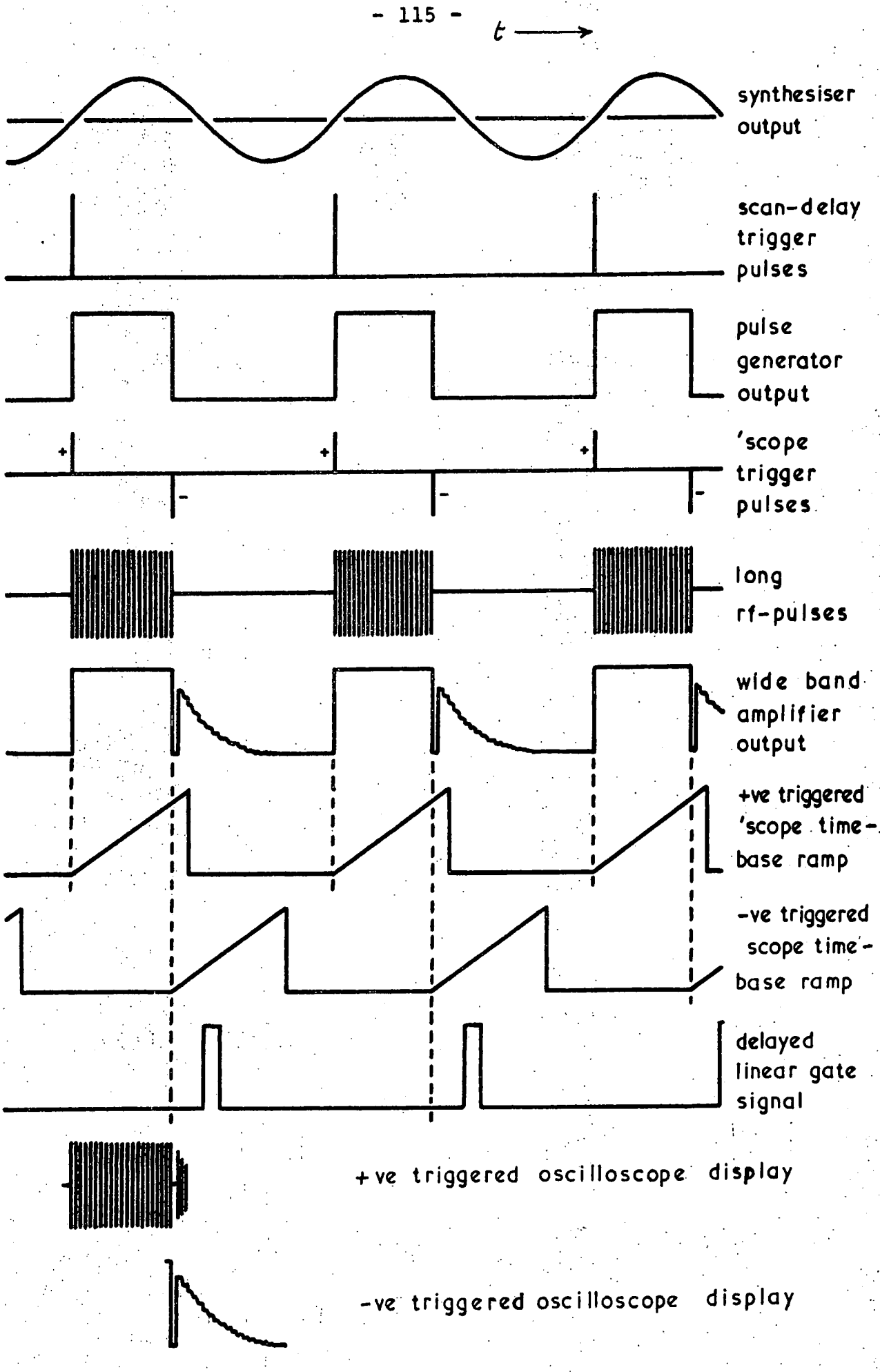

FIGURE 5.20

SAMPLED - C.W. SYSTEM
TIMING SEQUENCE AND WAVEFORMS

to the round-trip ultrasonic transit time (Figure 5.21(a)). By adjusting the pulse-engtth it is possible to compare the decays in the sampled - CW and simple pulse-echo cases. The pulse-echo train (Figure 5.21(c)) shows a slightly faster decay than the sampled - CW response (Figure 5.21(b)), but this difference is due to the longer receiver recovery time after saturation in the sampled - CW mode. The sampled - CW frequency response around 40 MHz of a [111] GaAs sample ground to a non-parallelicity of 10^{-3} rad is illustrated in Figure 5.22. The non-parallelicity and sidewall effects detailed by Miller and Bolef (1970) are present as subsidiary "inhomogeneous" resonances around the true resonance which fulfils the condition $2\ell = n\lambda$. Successive resonances (for n increasing) show similar main features; the small differences in shape are due to n being finite.

(e) COMPARISON BETWEEN THE SAMPLED - CW AND PULSE-SUPERPOSITION TECHNIQUES

In view of the disturbingly large influences on ultrasonic velocity measurements of "inhomogeneous" effects, investigated by Miller and Bolef (1970), using their sample - CW technique, the question arises of the validity of pulse-superposition measurements.

The continuous-wave resonance of the sampled - CW technique and the pseudo-resonance of pulse-superposition may be compared as in Figure 5.23. In both cases the "round-trip" phase difference is zero. For the sampled - CW reasonance this condition is met by $2\ell = n\lambda$ at the sample harmonic frequencies, whereas for pulse-superposition it

(a)

sampled
-cw
unrectified

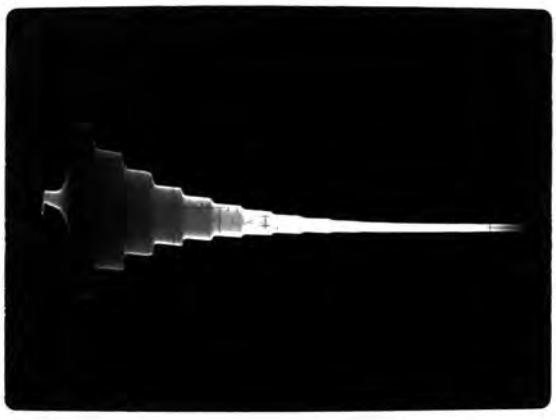

t →

1 2 3 4 5 transit time steps ------- 16

(b)

sampled
-cw
rectified

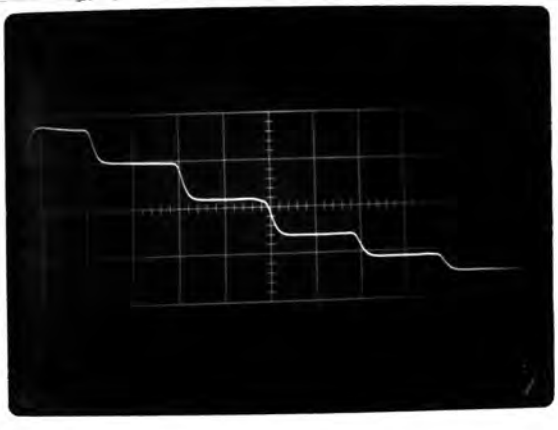

t →

(c)

pulse
echo
rectified

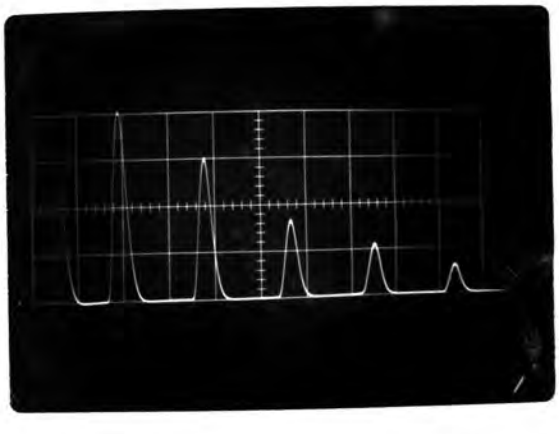

t →

The time responses of a [111] GaAs sample in the sampled-CW and simple pulse-echo modes.

FIGURE 5.21

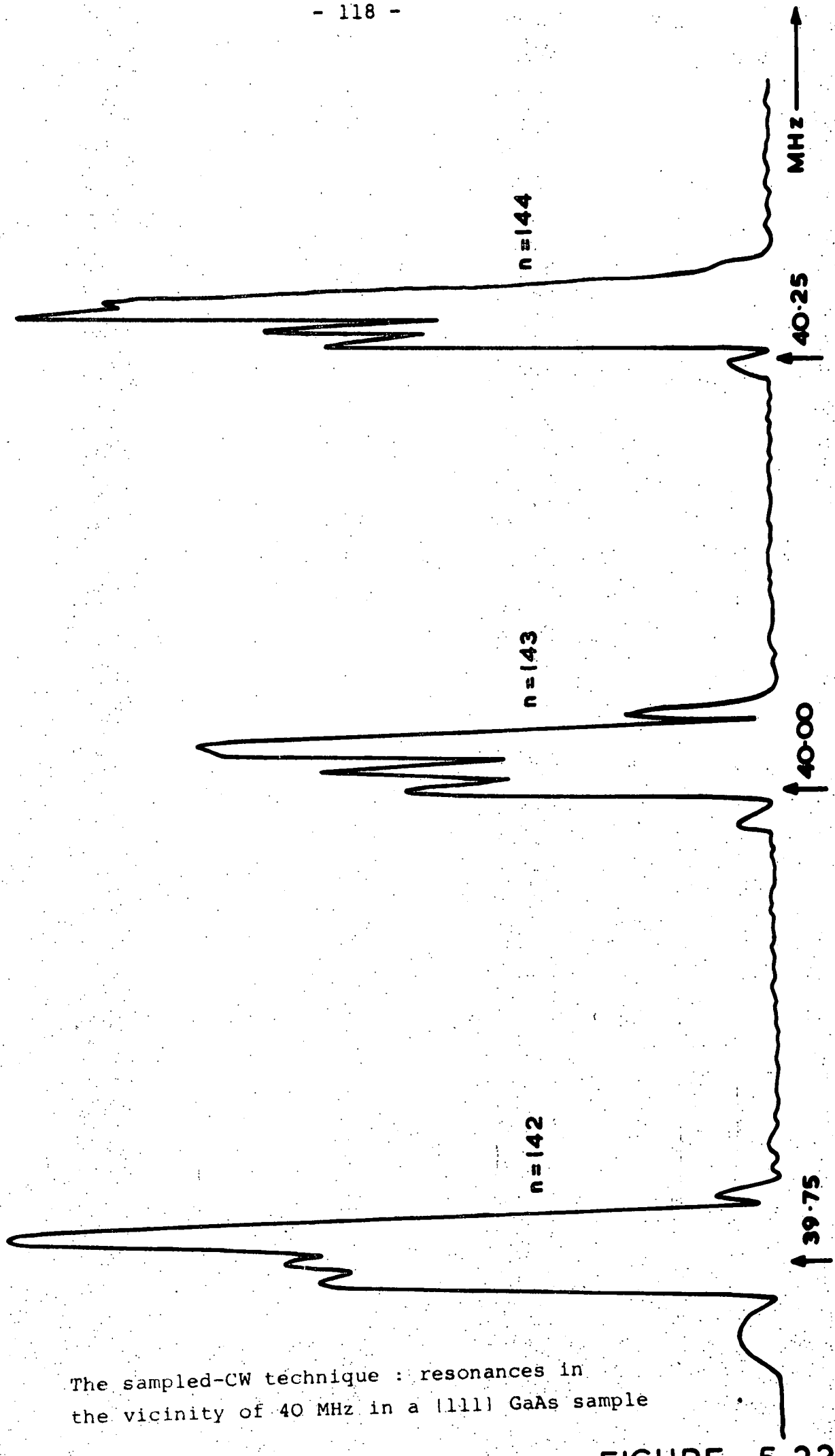

The sampled-CW technique : resonances in the vicinity of 40 MHz in a [111] GaAs sample

FIGURE 5.22

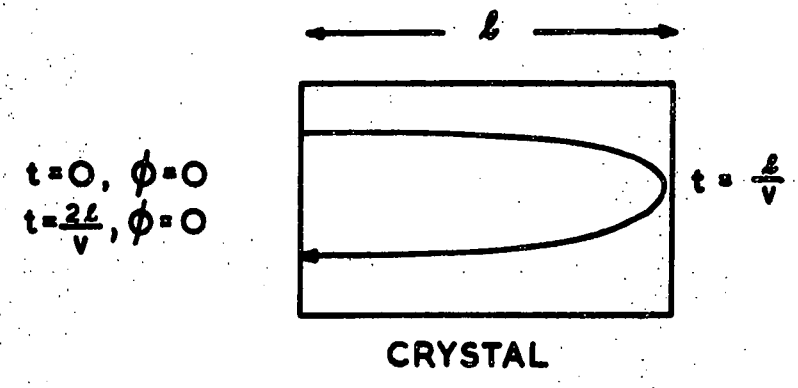

THE RESONANCE CONDITION

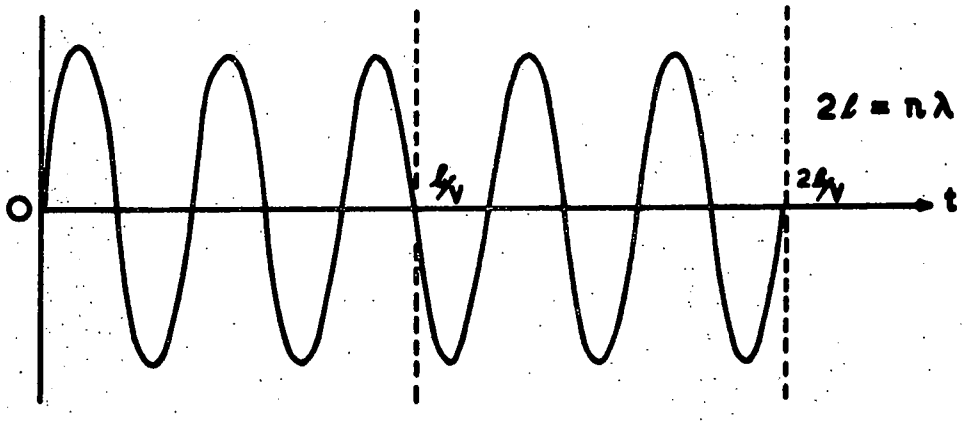

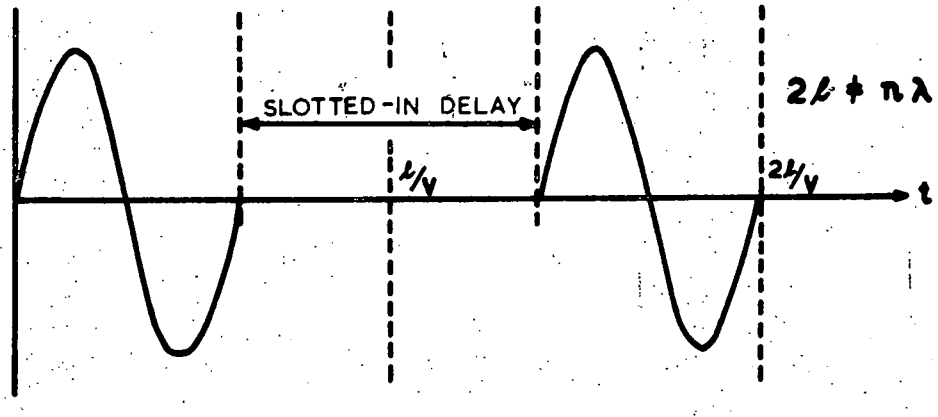

PULSE - SUPERPOSITION

A schematic comparison of the CW resonant and pulse-superposition pseudo-resonant conditions. ϕ and t are phase and time respectively

FIGURE 5.23

is synthesised by slotting in an adjustable delay: the pulse-superposition pseudo-resonant condition can be achieved at any ultrasonic frequency. If F_o is the resonant frequency giving $2\ell = n\lambda$ (n large), then the round trip phase shift in the sampled - CW case caused by a change from F_o to $(F_o + \Delta F)$ is

$$\phi_{RT} = \frac{2\pi\, n\Delta F}{F_o} \qquad (5.9)$$

If the pulse-superposition "resonance" condition is satisfied at F_o by a pulse repetition rate f_{CO}, where $f_{CO} = V/2\ell$ (V being the ultrasonic velocity), then changing from f_{CO} to $(f_{CO} + \Delta f_C)$ gives a "round trip" phase shift of

$$\phi_{RT} = \frac{2\pi\, F_o\, \Delta f_C}{f_{CO}(f_{CO} + \Delta f_C)} \qquad (5.10)$$

Equating ϕ_{RT} to find the relation between Δf_C and ΔF for similar round-trip phase shifts, and writing $(f_{CO} + \Delta f_C)$ as f_{CO} (for $\frac{\Delta F}{F_o}$, $\frac{\Delta f_C}{f_{CO}} \ll 1$) we find

$$\Delta f_C = \left[\frac{n\, f_{CO}^{\,2}}{F_o^{\,2}}\right] \Delta F \qquad (5.11)$$

Consequently, to a first approximation, plots of response amplitude as a function of ultrasonic frequency (F) for the sampled - CW case and repetition-rate (f_C) for the pulse-superposition case should be equivalent at about the same ultrasonic frequency (when n is large). Differences in the shapes of the two curves will be linked with the resolution along the frequency axis in each case. Measurement of a true CW response would involve perfect resolution, but if there are any frequency-gating components present these will affect the response, and true monochromacity will

not result. Most of the gating components will decay with time (by scattering and interference) much faster than the sample resonances, and the longer after any frequency-gating operation that an observation of response is made, the lower will be the gating components and the higher the frequency resolution (see Figure 5.18). In the pulse-superposition case the pulse is very short, and low resolution cannot be avoided.

To compare the sample - CW and pulse-superposition responses, we first need to know the position and shape of a nearly "true" CW resonance without interference. The technique of Miller and Bolef (1970) has been adopted: the sample faces have been progressively damped (in this case using Apiezon Q-compound) to cut out unwanted reflections (Figure 5.24). The receiver amplification in Figure 5.24(d) is much higher than that in 5.24(a,b,c); the damping not only reduces the amplitude of the unwanted reflections, but also to some extent that of the required ones, particularly for end-damping (see Figure 5.25). The pseudo-resonant and resonant frequencies have been shown experimentally to be independent of ultrasonic amplitude in the range available. As found by Miller and Bolef (1970), the highest response in the undamped condition is not necessarily at the position of the true resonance. Some slight trace of the subsidiary "inhomogeneous" resonances can still be seen in the most heavily damped case (Figure 5.24(d)).

The influence of gating effects on the monochromacity of responses can be reduced by using increased delays between the final gating ("gate-off" in Figure 5.18)

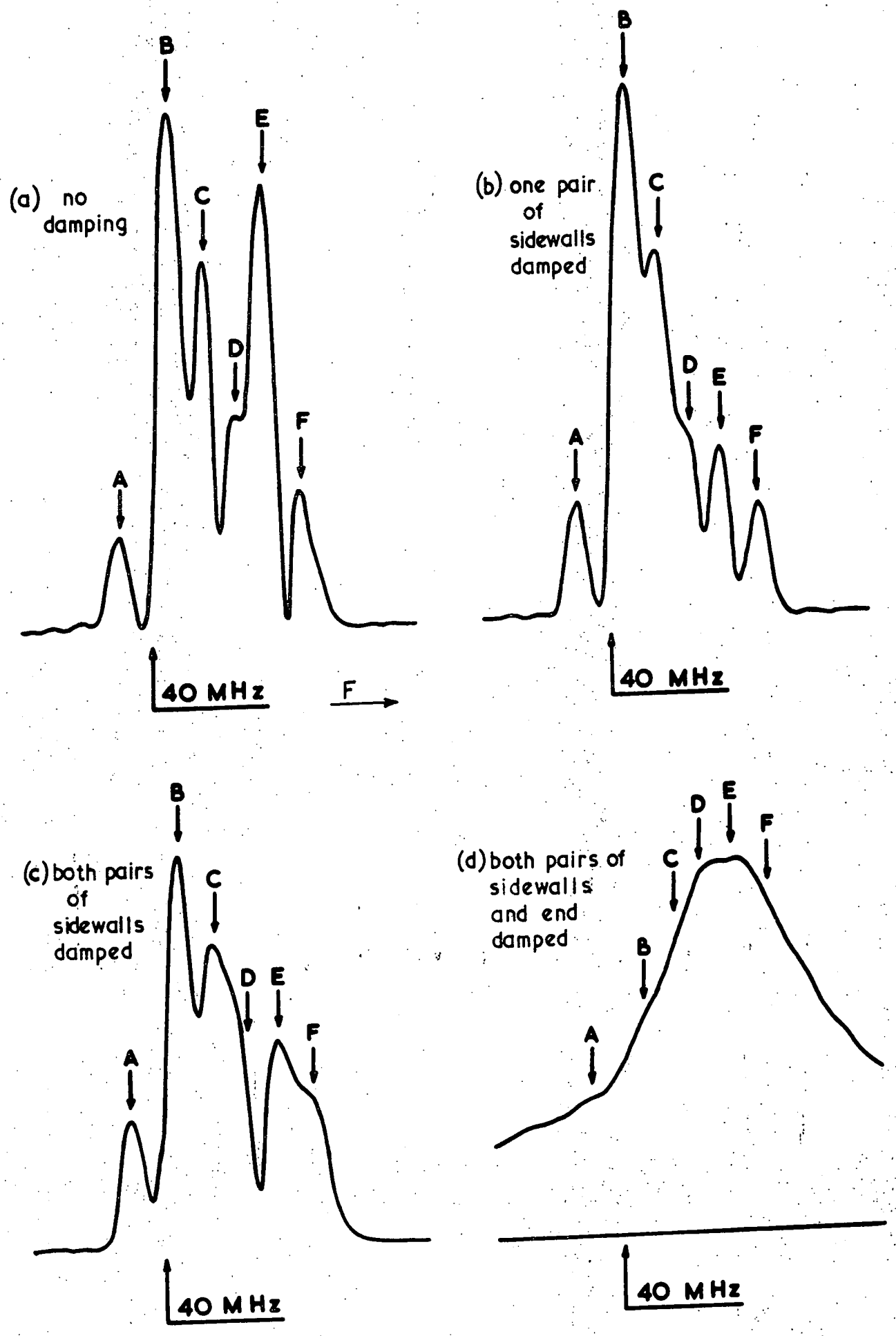

The progressive damping of a sampled-CW resonance in a [100] GaAs sample.

FIGURE 5.24

(a) undamped

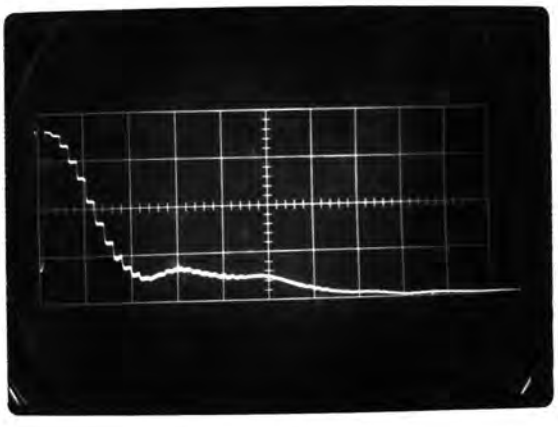

t →

(b) damped

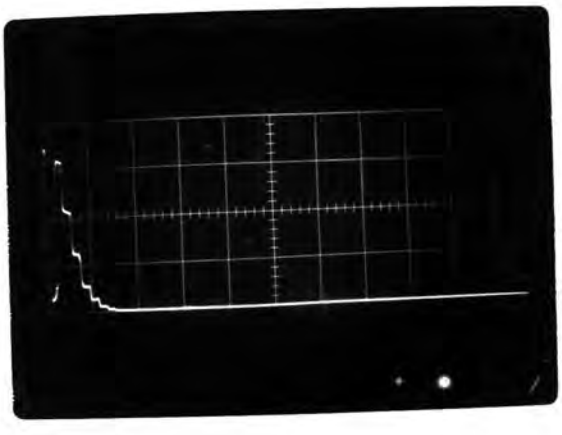

t →

The time responses of the undamped and damped resonances shown in Figures 5.24(a) and 5.24(d) respectively. The ultrasonic frequency is that indicated by the letter E in Figure 5.24.

FIGURE 5.25

and the sampling point. Conversely, the high-interference pulse-superposition case can be simulated by progressively reducing the delay. Figure 5.26(a-e) shows the frequency response plots for the same resonance as shown in Figure 5.24(a) for delays corresponding to transit-time steps 1, 2, 3, 4 and 16 in Figure 5.21(b). The monochromacity decreases with the step number. Figure 5.26(f) is a plot of the frequency response of the f_{CO} pulse-superposition pseudo-resonance of the sample at 40 MHz. A scaling factor of $(n\ f_{CO}^2/F_o^2)$ has been applied to the repetition rate (f_c) values (see equation 5.11). It is evident from Figure 5.26 that the pulse-superposition pseudo-resonance curve is equivalent to the short-delay limit of the sequence of sampled - CW resonance curves. Traces of all the sampled CW partial resonances A to F labelled in Figure 5.26(a) can be seen in the pseudo-resonance curve. The pulse-superposition plot is also similar in shape to that of the high resolution (67 μS delay) sampled - CW resonance from which the "inhomogeneous" partial resonances have been removed by damping (Figure 5.24(d)). The implication is that decrease of the frequency resolution (the limit being the pulse-superposition case) gives better cancelling of the "inhomogeneous" partial resonances and results in a resonance curve much closer to the "true" one than would be observed in a high resolution case. The large gating effects present in the pulse-superposition mode make the "inhomogeneous" effects almost negligible in comparison with the more obvious velocity-measurement uncertainties, such as transducer phase shift effects.

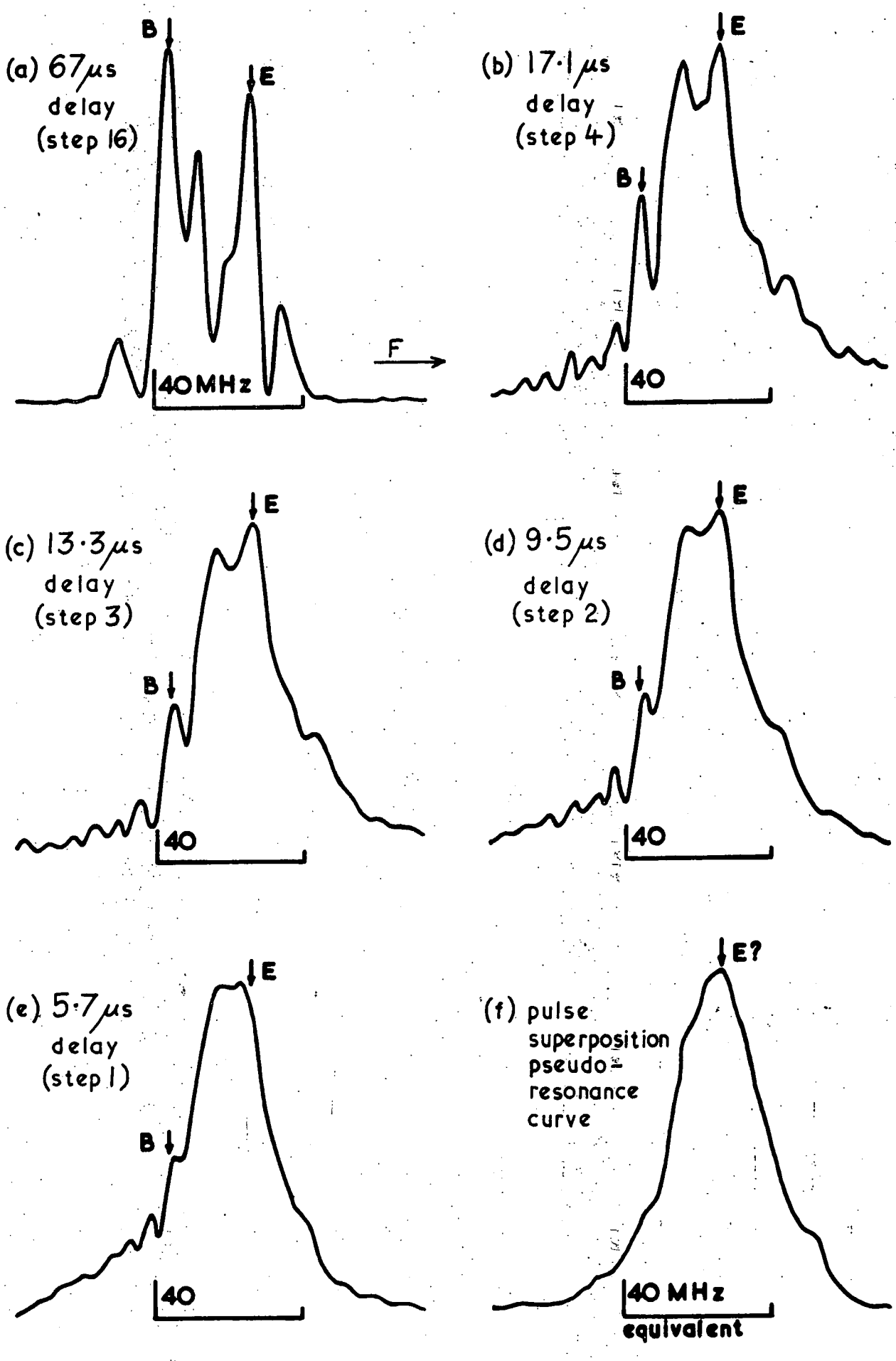

Comparison of the sampled-CW responses at varying delays (a-e) with the pulse-superposition pseudo-resonance (f). The step numbers referred to are those indicated in Figure 5.21.

FIGURE 5.26

5.3 ANCILLARY EQUIPMENT

(a) THE SAMPLE HOLDER

A photograph of the ultrasonic sample-holder appears in Figure 5.27. The cubic sample of GaAs is supported on a spring-loaded insulated platform. Contacts to the transducer are made by the brass collar above the sample (via two small aluminium spacers) and by a spring-loaded centre contact. To ensure total insulation of the sample apart from the transducer connections, the brass sample-holder frame is covered with polythene tubing, and the assembly is held together with nylon line. Electrical contacts are available via the circuit board visible at the top of Figure 5.27, and there is a screw fitting to allow the sample holder to be held in place in the cryostat. The design provides for simplicity of insertion of samples using either bonded or thin-film transducers and proved mechanically stable down to helium temperatures.

(b) THE CRYOSTAT AND VACUUM SYSTEM

Measurements down to helium temperatures were made in a standard cryostat (Figure 5.28(a)) surrounded by a nitrogen jacket. A dual vacuum system (Figure 5.29) enabled both evacuation of the inner dewar and measurement of the pressures in the system; the ultimate pumped pressure was 0.05 torr; down to 40 torr a mercury manometer was used in measuring, and below 40 torr a manometer containing silicone fluid of density 1/14 that of mercury. The sample holder frame was constructed of thin-wall stainless steel tubing to reduce heat leaks. Electrical leads into the system were passed through neoprene compression vacuum

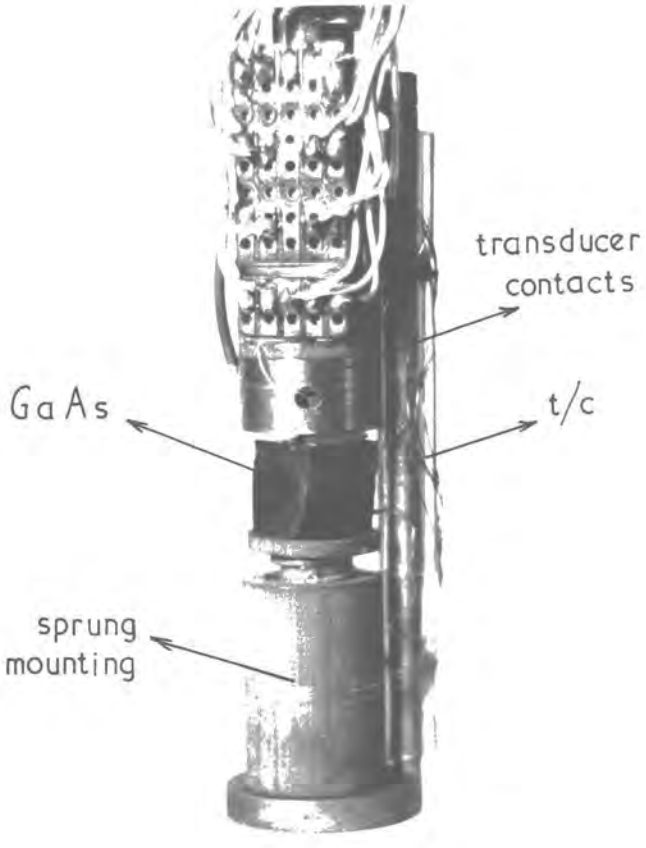

The ultrasonic sample holder.

FIGURE 5.27

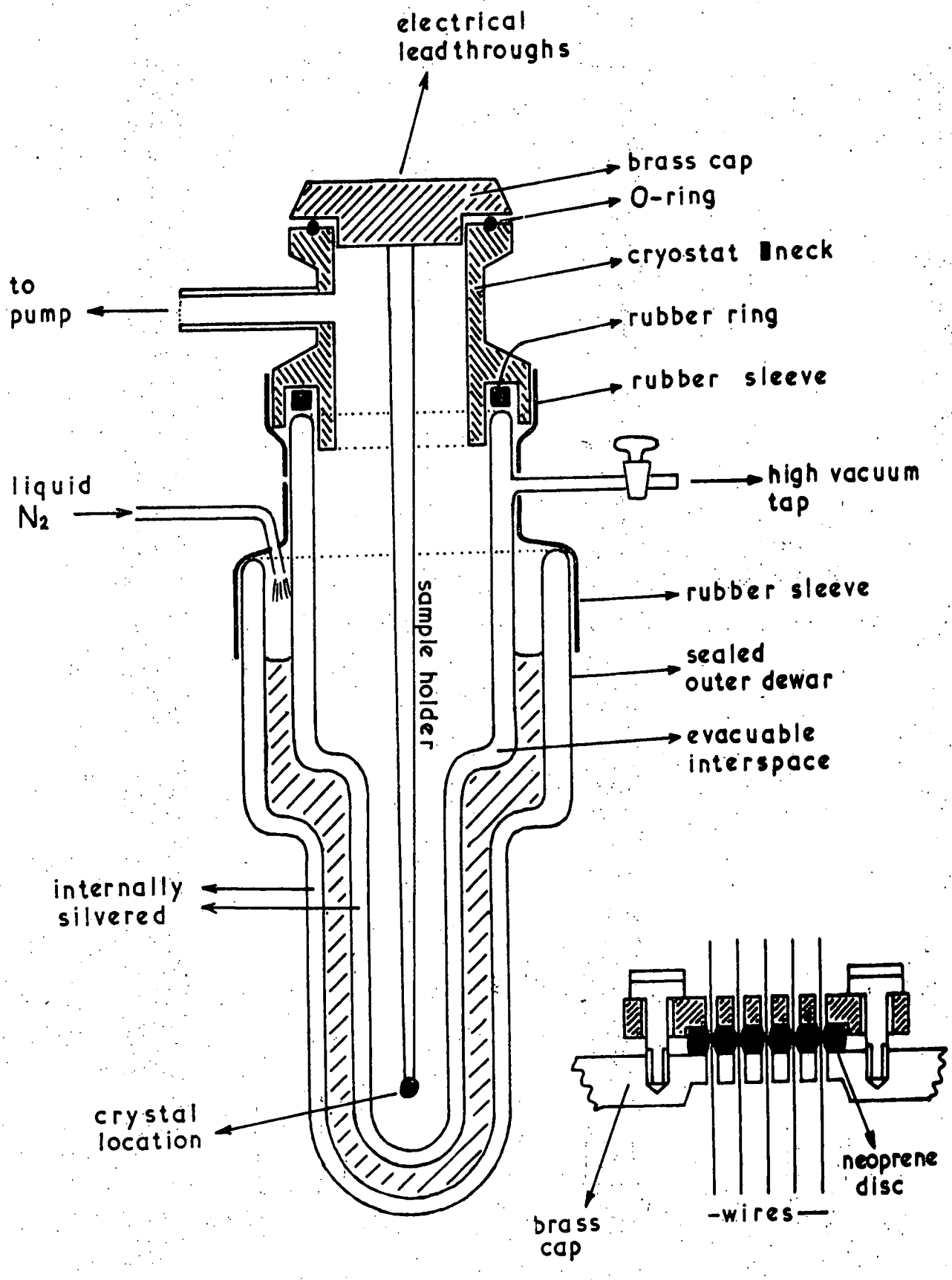

The cryostat.

FIGURE 5.28

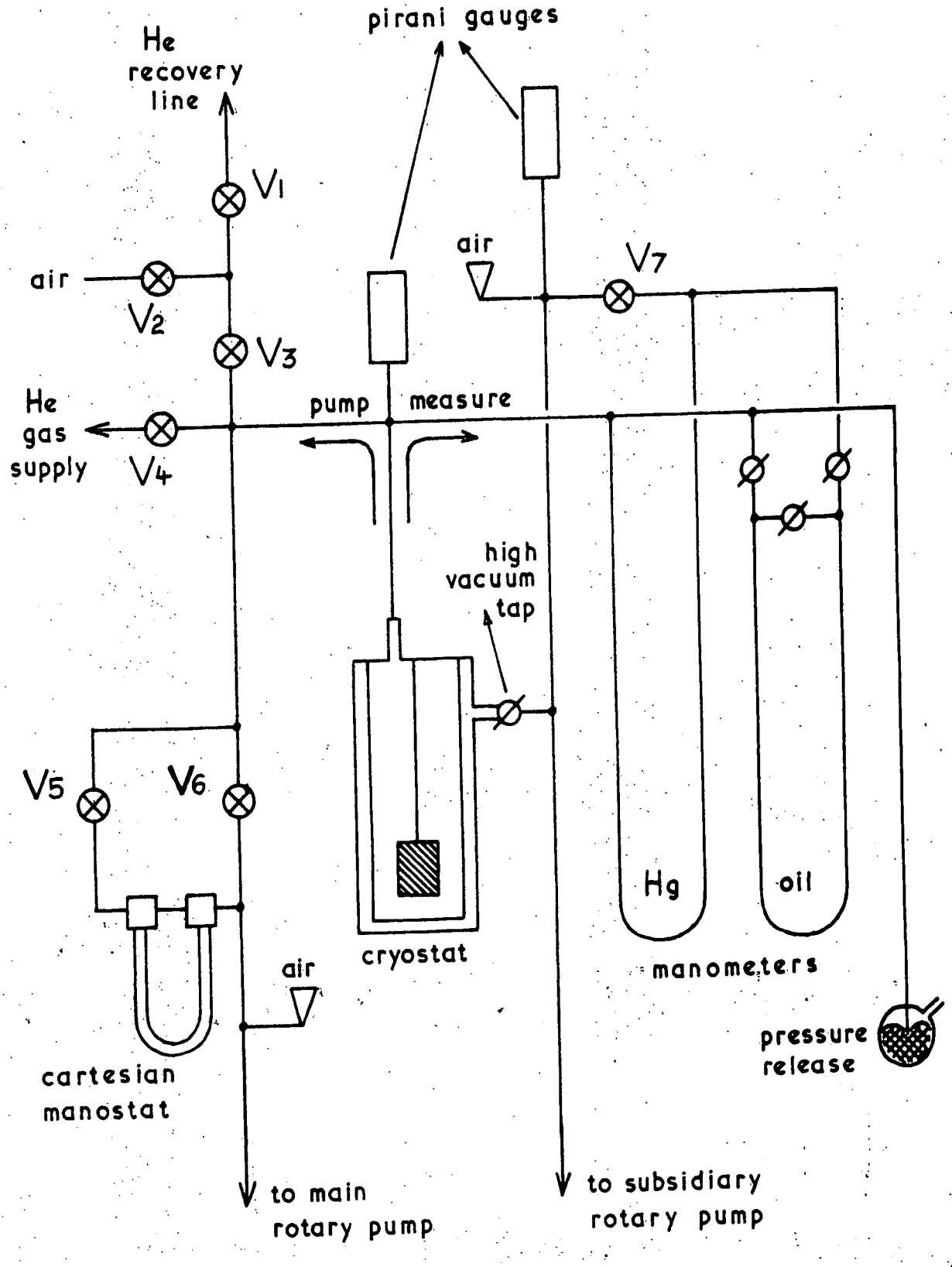

A schematic of the cryostat vacuum system

FIGURE 5.29

seals of the type described by Batchelder and Sidey (1969) (see Figure 5.28(b)).

(c) TEMPERATURE CONTROL

A technique of controlled temperature drift was used in making measurements over the temperature range of 4.2 K to 320 K. The feasibility of this method depends on a balance between the time needed to perform a single measurement and the required accuracy of temperature definition. The drift rate was controlled by regulation of the heat leak through the space surrounding the sample holder; Figure 5.30 shows examples of the temperature drift profiles obtained using helium gas as the heat-transfer medium. The transfer of small volumes of liquid nitrogen to maintain a slow drift rate and control the nitrogen level in the cryostat jacket was made by an automatic pumping system using carbon liquid-level sensors (see Figure 5.31). Temperatures down to 1.5 K were achieved by pumping on the liquid helium surface; the liquid level was monitored by the circuit shown in Figure 5.32. The most critical region proved to be at around 40 K (see Figure 5.30). The drift rate in this region can be reduced using charcoal desorption techniques, but in this work speed of operation was found to be a suitable substitute!

(d) TEMPERATURE MEASUREMENT

Copper/constantan thermocouples were used to measure temperatures down to liquid nitrogen, gold-iron/chromel thermocouples for temperatures between liquid

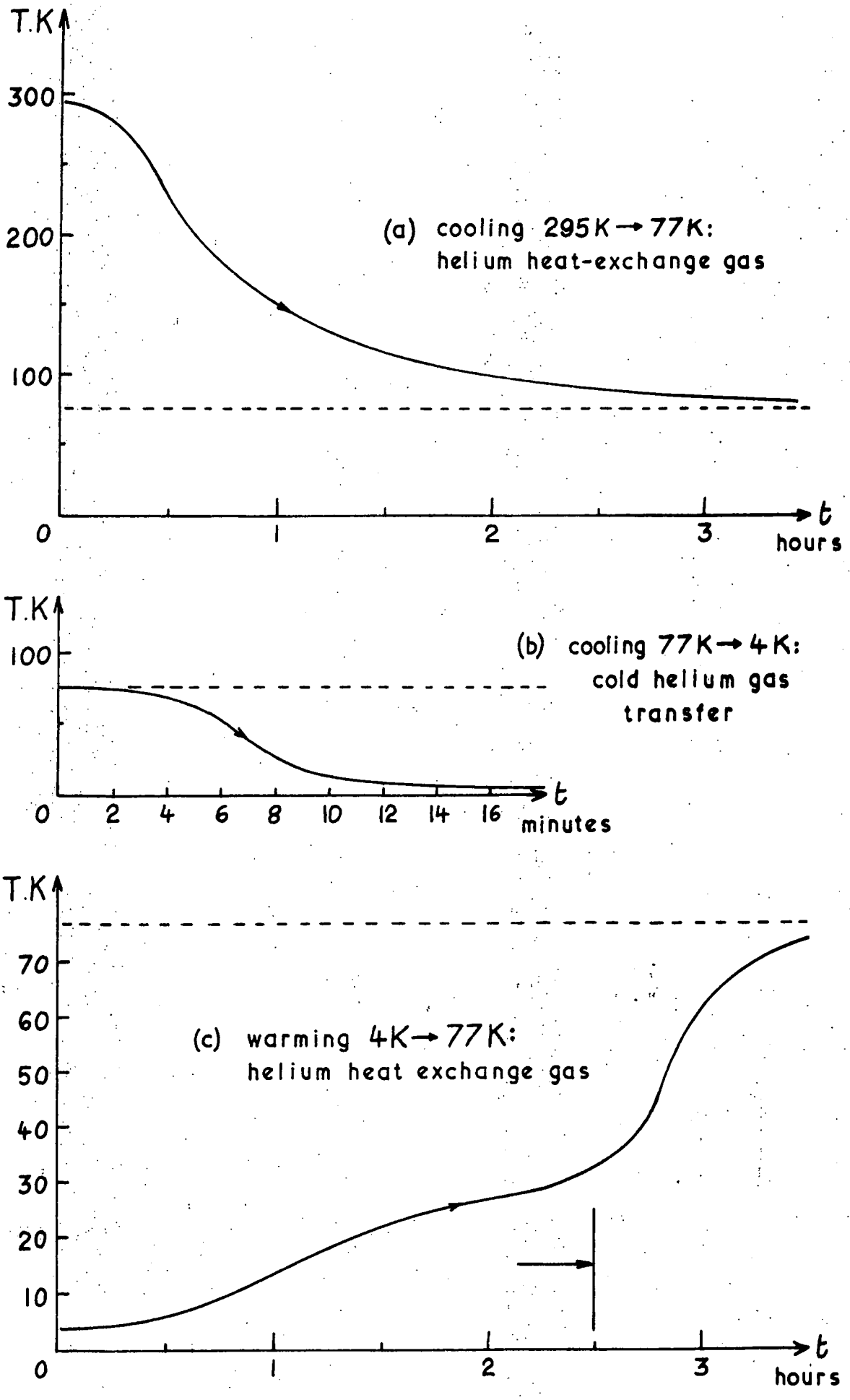

Temperature drift profiles obtained during the experimental work.

FIGURE 5.30

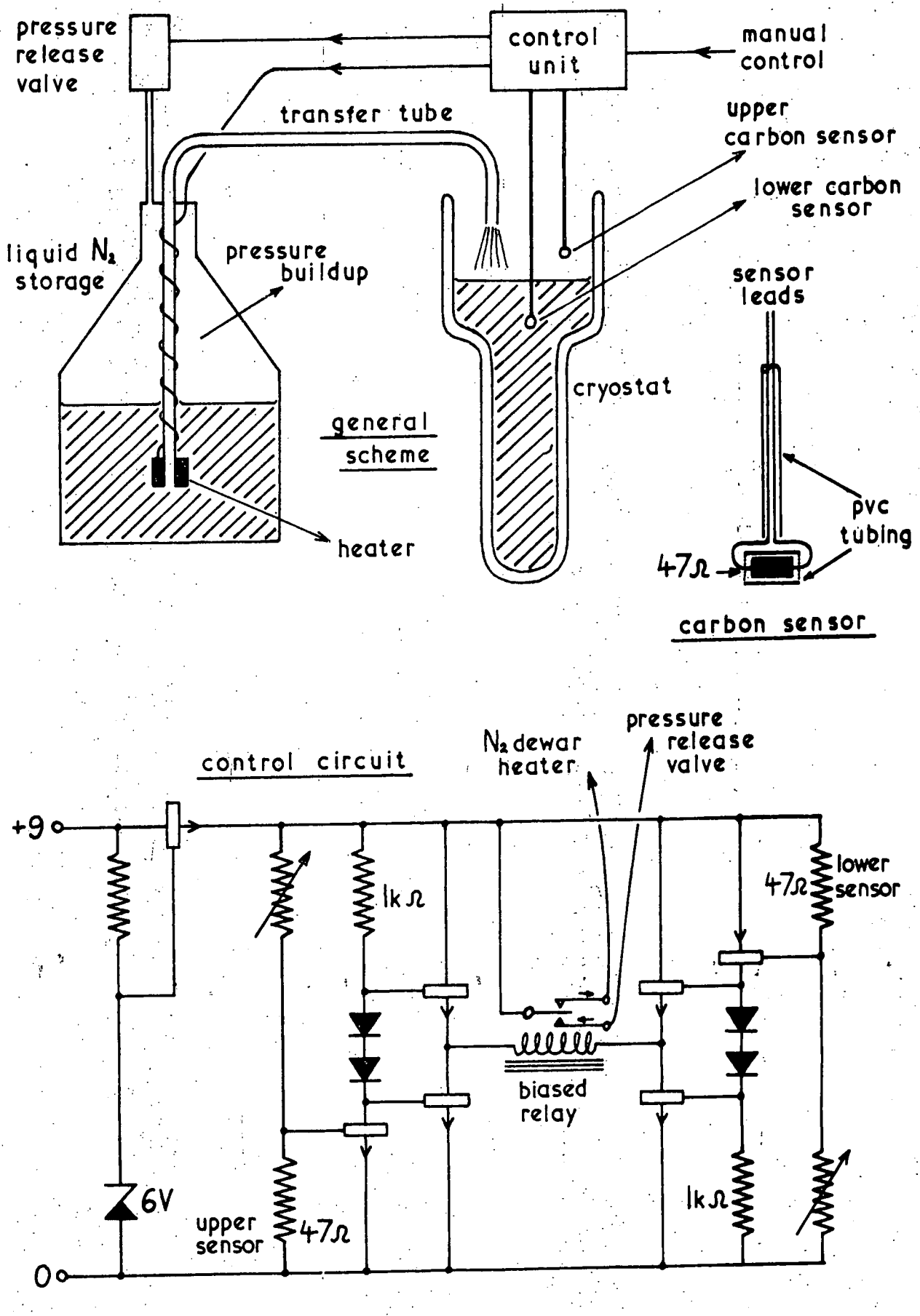

The automatic liquid-nitrogen filler.

FIGURE 5.31

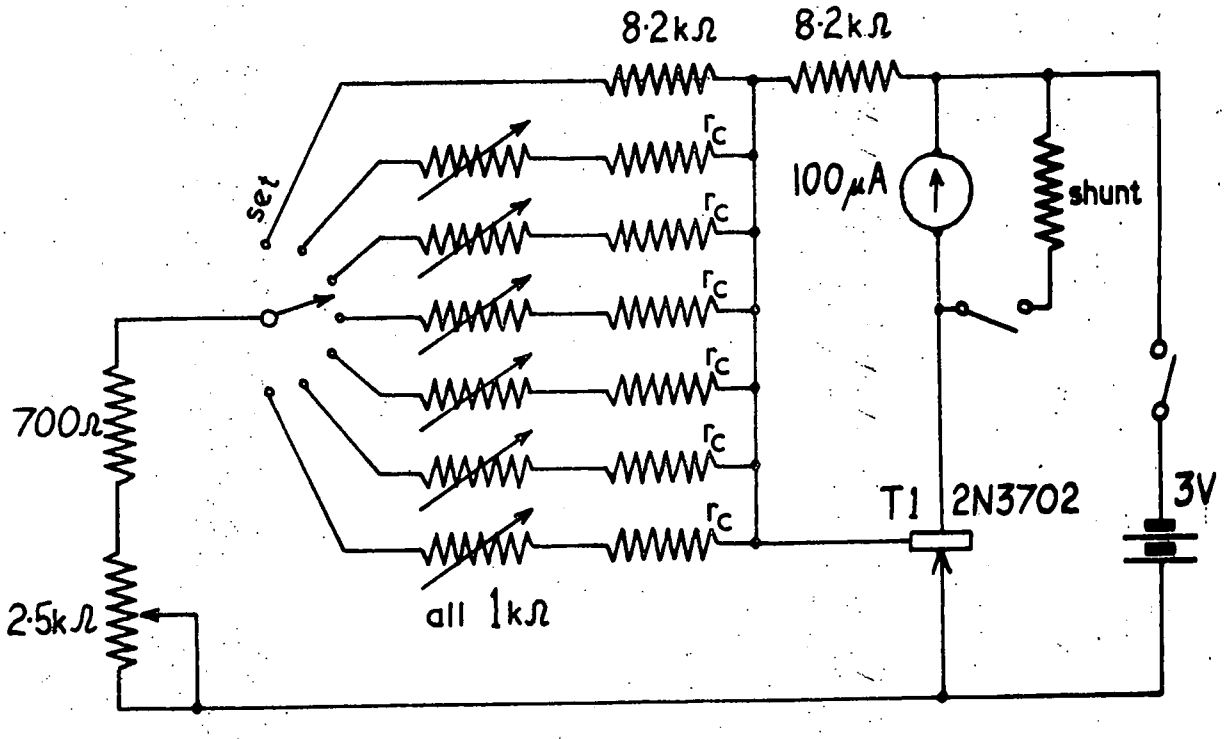

r_c all 56Ω Allen-Bradley carbon resistors at 10cm intervals down cryostat: at 4·2K a change of 0·001K ≡ 0·3μA at meter

Circuit diagram for the liquid helium depth gauge.

FIGURE 5.32

nitrogen and liquid helium, and mercury and oil manometers for those below 4.2 K.

The copper, constantan and chromel thermocouple wires used were of 0.12 mm diameter and the gold 0.03% iron of 0.08 mm diameter. All junctions were made by spark-welding under nitrogen gas and insulated by a very thin layer of GE 7031 low-temperature varnish. The reference junctions were situated at the ends of 1.5 mm diameter stainless steel tubes and thermally grounded to copper end caps with cigarette paper soaked in GE 7031 varnish and toluene (Anderson, 1969). Measurement junctions were similarly attached to the crystal faces and covered with a layer of Apiezon Q-compound to ensure a more intimate contact with the crystal than with the surroundings. Connections were made via a low-thermal switch box to a Pye 7600 potentiometer, with a Pye 11330 galvanometer preamplifier and a 7903/S galvanometer as the null detector; the system was operated with a galvanometer sensitivity of 3 cm per μV.

The most satisfactory reference for the copper/constanton thermocouples was found to be a large dewar of liquid nitrogen. The nitrogen suppliers confirmed that oxygen content was not sufficient to change the boiling point from 77.36 K at atmospheric pressure. Each thermocouple was calibrated against substandards of boiling liquid helium (4.2 K), boiling liquid nitrogen (77.4 K), stirred dry CO_2 and acetone (194.7 K) and an NPL thermometer at room temperature. Charts of temperature versus voltage were computed from the cubic expression (White, 1959)

$$v = AT^3 + BT^2 + CT + D \qquad (5.12)$$

where v is the thermocouple voltage at a temperature T. Reproducibility on cycling between room temperature and helium temperature was better than 1 μV.

Temperatures below 4.2 K were measured with oil and mercury manometers, using the gold-iron/chromel thermocouple for interpolation between pressure measurements: between 1.5 K and 4.2 K the thermocouple voltage was found to be linear to within 0.1 K. A dewar of liquid helium was used as the gold-iron/chromel reference.

5.4 COMPUTATION AND CORRECTIONS

(a) ULTRASONIC VELOCITIES AND ELASTIC CONSTANTS

For measurements made of the pulse-superposition repetition rate f_{CO} Hz in the condition p=1, n=0 (see Section 5.2(c)), the apparent ultrasonic transit time is equal to $1/f_{CO}$ seconds. A correction to f_{CO} of f_x Hz is required to allow for the phase shift on reflection at the transducer (see Section 5.1(e)), and for the phase shift due to integration of the waves arriving at a point on the transducer from a range of angles. The first of these has been calculated from measurements made of f_{CO} as a function of frequency (see Figure 5.15(b)), and the second from tables of phase shift due to integration presented by Bradfield and Goodwin (1961). In the case of a thin-film transducer operated far away from resonance this correction will be independent of temperature and the corrected repetition rate can be written as $[(f_{CO})_T + f_x]$, where $(f_{CO})_T$ is the measured repetition rate at the temperature T. The expressions for the corrected velocity V_T at this temperature and the

relevant elastic constant combination C_T are

$$V_T = 2L_R \, m \left[(f_{CO})_T + f_x \right] \tag{5.13}$$

$$C_T = \frac{4\rho_R L_R^2}{m} \left[(f_{CO})_T + f_x \right]^2 \tag{5.14}$$

where m is $\prod_{293K}^{T} (1+\alpha_j')$, α' is the thermal expansion coefficient and L_R and ρ_R are the sample length and density at room temperature (298 K).

Computation of the uncertainties in parameters has been approached from two viewpoints, both in accord with the recommendations of Ku (1966) on the propagation of errors. Firstly the extreme limits of uncertainty (that is the estimated 100% certainty limits, assuming accurate quotation of uncertainties in data taken from other workers) have been determined. Secondly, to allow assessment of the elastic constant change with temperature, the relative uncertainty limits have been calculated assuming absolute accuracy in the data at 298 K; systematic errors appearing in the temperature variation are small in comparison with the relative uncertainties and will be referred to later. The uncertainty due to misorientation ($\pm\frac{1}{2}^{o}$) of the specimens with respect to the crystal axes has been calculated by the technique described by Truell, Elbaum and Chick (1969).

(b) ULTRASONIC ATTENUATION

Values of the attenuation coefficient measured as described in Section 5.2(a) are subject to various "apparent-loss" contributions resulting from diffraction losses, "nonparallelism" losses, transducer coupling losses

and phase effects in the transducer. A discussion of all these effects has been presented by Truell et al (1969); only the main results will be reproduced here.

Since the transducer-source of ultrasonic energy in a sample is finite in size, the beam produced diverges, and the wave front is neither planar nor spherical. Phase interference occurs on the return of the wave to the transducer, and the observed decay of the echo-train will not be exponential, but will exhibit a maximum at a distance from the source of a^2/λ (see Figure 5.33(a)). The apparent loss in echo-height due to the diffraction loss alone is approximately 1dB times the distance from the source in units of (a^2/λ). The measured attenuation can be corrected more exactly using the curve of loss against distance shown in Figure 5.33(b).

In the case of a non-parallel sample, the observed echo-decay is not an exponential but a Bessel function, as pictured in Figure 5.34(a). From the positions and amplitudes of the maxima in the echo train envelope the intrinsic attenuation may be calculated. When non-parallel effects are small, as with the sample parallelisms achieved in this work, the apparent attenuation caused by the effect is given by

$$\beta = \frac{8.686\ \pi^2\ F^2\ a^2\ \theta^2\ \bar{n}}{V\ell} \quad \text{dB/S} \qquad (5.15)$$

at the $\bar{n}^{th}$ echo, where θ is the non-parallel angle (see Figure 3.2(a)). If the sample cross-section is not appreciably greater than the transducer, and the ultrasonic frequency is low, then diffraction and sidewall reflections

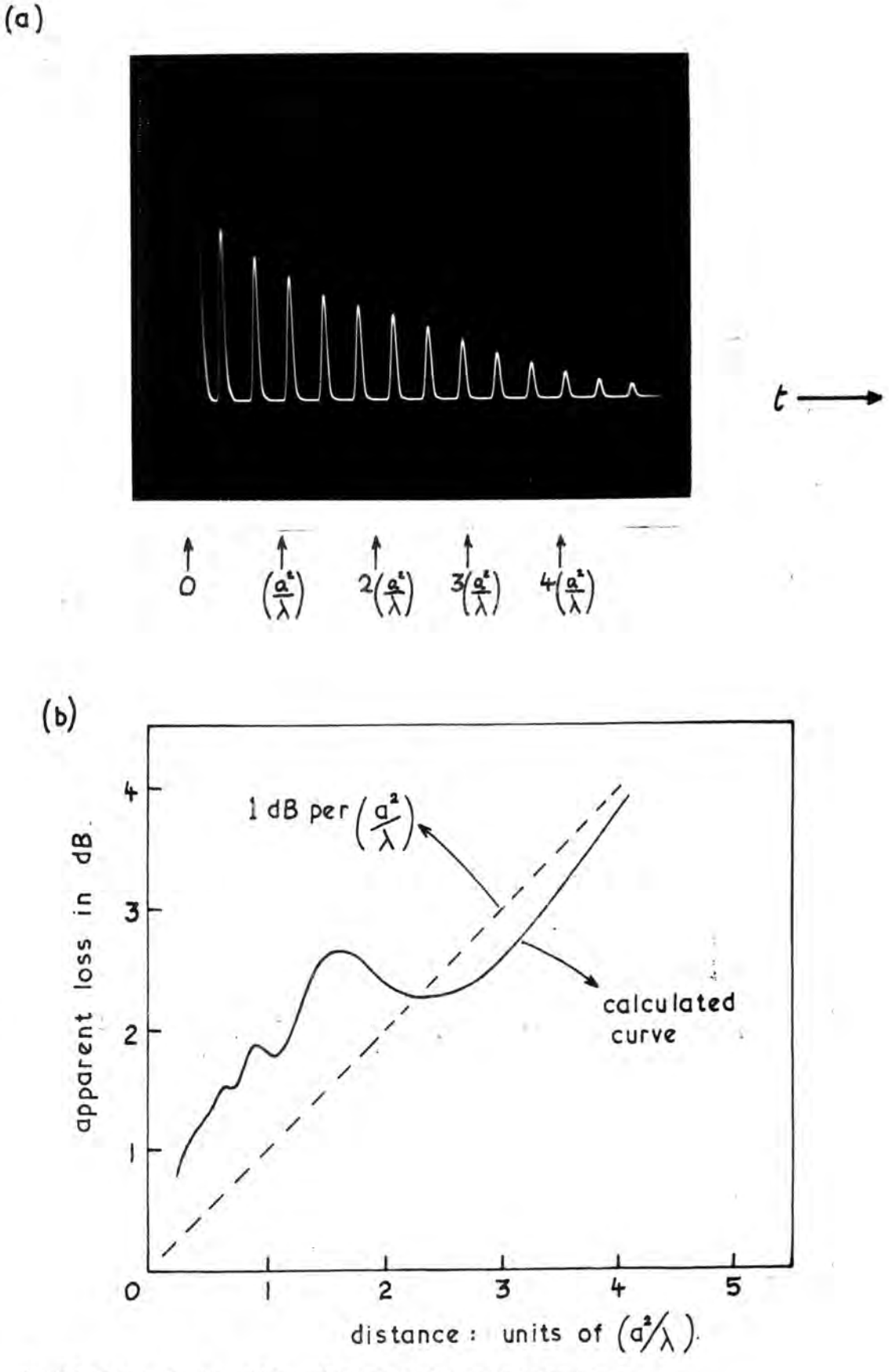

Diffraction in the ultrasonic echo train:

(a) non-exponential display

(b) theoretical curve of apparent loss versus distance from the transducer (after Truell et al, 1969).

FIGURE 5.33

(a)

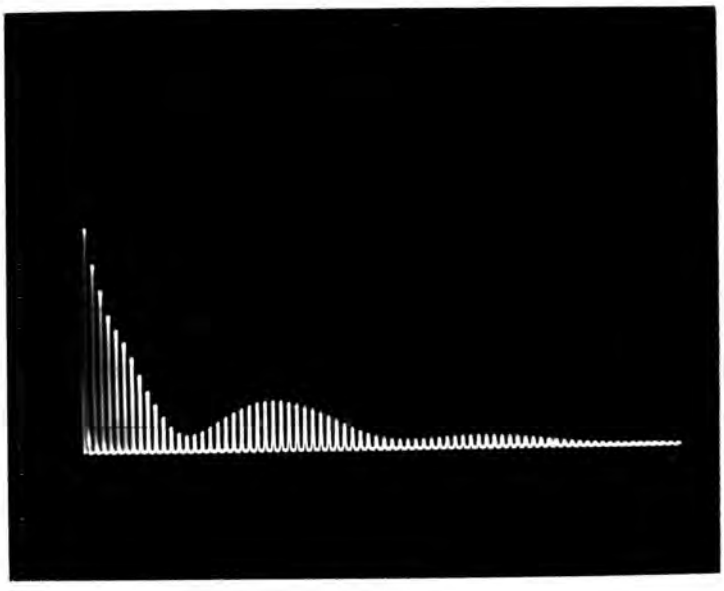

(b)

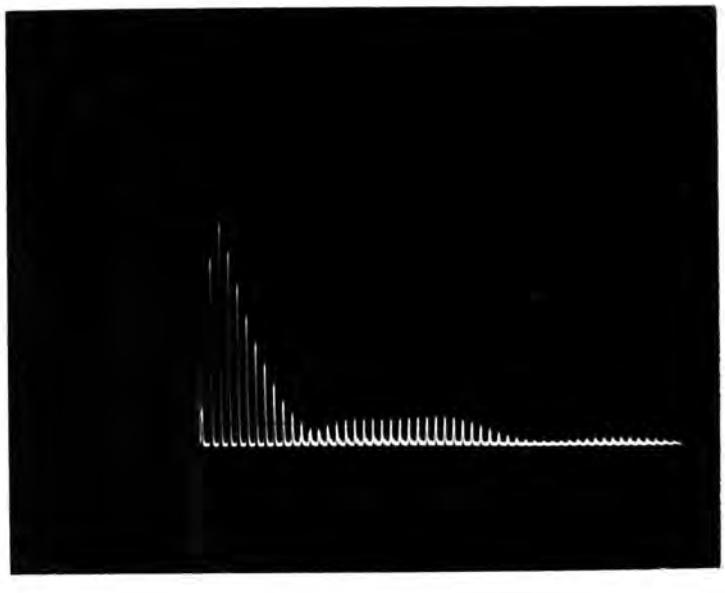

Non-exponential echo-trains caused by
(a) non-parallelicity
(b) side-wall reflections.

FIGURE 5.34

together can cause an echo-train modulation similar to that of a non-parallel sample, as shown in Figure 5.34(b). However, the two effects may be distinguished by their frequency dependences: with increase in frequency the bumps due to non-parallelicity move towards the source, while the sidewall-reflection bumps move away.

The "apparent" losses described above are to a first approximation independent of temperature: they affect the absolute values of attenuation measured but not the calculated relative uncertainties in the temperature dependence.

All the corrections listed above have been made to the measurements of ultrasonic velocity and attenuation wherever applicable.

CHAPTER 6

THE ELASTIC CONSTANTS OF GALLIUM ARSENIDE

Velocities of ultrasonic waves propagated in single crystals of GaAs have been measured by the pulse superposition technique. Results obtained extend the elastic constant data for this material down to liquid helium temperatures. Previously, the room temperature elastic constants have been measured by techniques of varying degrees of accuracy by Bateman, McSkimin and Whelan (1959), Garland and Park (1962), Charlson and Mott (1963), Drabble and Brammer (1966), Bobylev and Kravchenko (1967), McSkimin, Jayaraman and Andreatch (1967) and Beilin, Vekilov and Krasil'nikov (1969). Measurements at 77 K have been reported by Garland and Park (1962) and at a number of temperatures between 78 K and 520 K by Beilin, Vekilov and Krasil'nikov (1969). The published data for the elastic stiffness constants C_{11}, C_{12} and C_{44} exhibit a somewhat random variation covering a much wider range than the quoted experimental errors, which in some cases seem to have been underestimated. Nor are the magnitudes of the temperature dependences given by Garland and Park (1962) and by Beilin, Vekilov and Krasil'nikov (1969) in

agreement - there is a factor of three difference for that of C_{12}. To resolve these disagreements, particular attention has been paid to assessment of the total uncertainties involved in the present experiments.

With its zinc blende cubic structure GaAs is a peizoelectric material and stiffening of some modes of ultrasonic wave propagation is expected. To obtain the elastic constant set in the absence of piezoelectric contributions, appropriate modes were chosen: longitudinal and shear waves propagated along the [100] direction, the longitudinal wave along the [110]. To evaluate the piezoelectric stiffening, measurements of velocity have also been made along the [111] direction; these are discussed in Section 6.8, but first the piezoelectric-free, or "zero-field" elastic constants will be considered.

6.1 RESULTS AND UNCERTAINTIES

The elastic stiffness constants C_{11}, C_{12} and C_{44} calculated as a function of temperature from the measured repetition rates f_{CO} and equation 5.14 are shown in Figures 6.1, 6.2 and 6.3. Each set of measurements corresponding to a given temperature has been treated independently throughout with no recourse to data smoothing techniques. The data for C_{12} possess the combined scatter from three velocity measurements. Numerical values at 0 K, found by extrapolation, 78 K and 298 K, together with derived elastic parameters, are collected in Table 6.A. Wave velocities quoted, other than measured ones, have been calculated assuming the absence of non-centrosymmetric effects such as piezoelectric contributions.

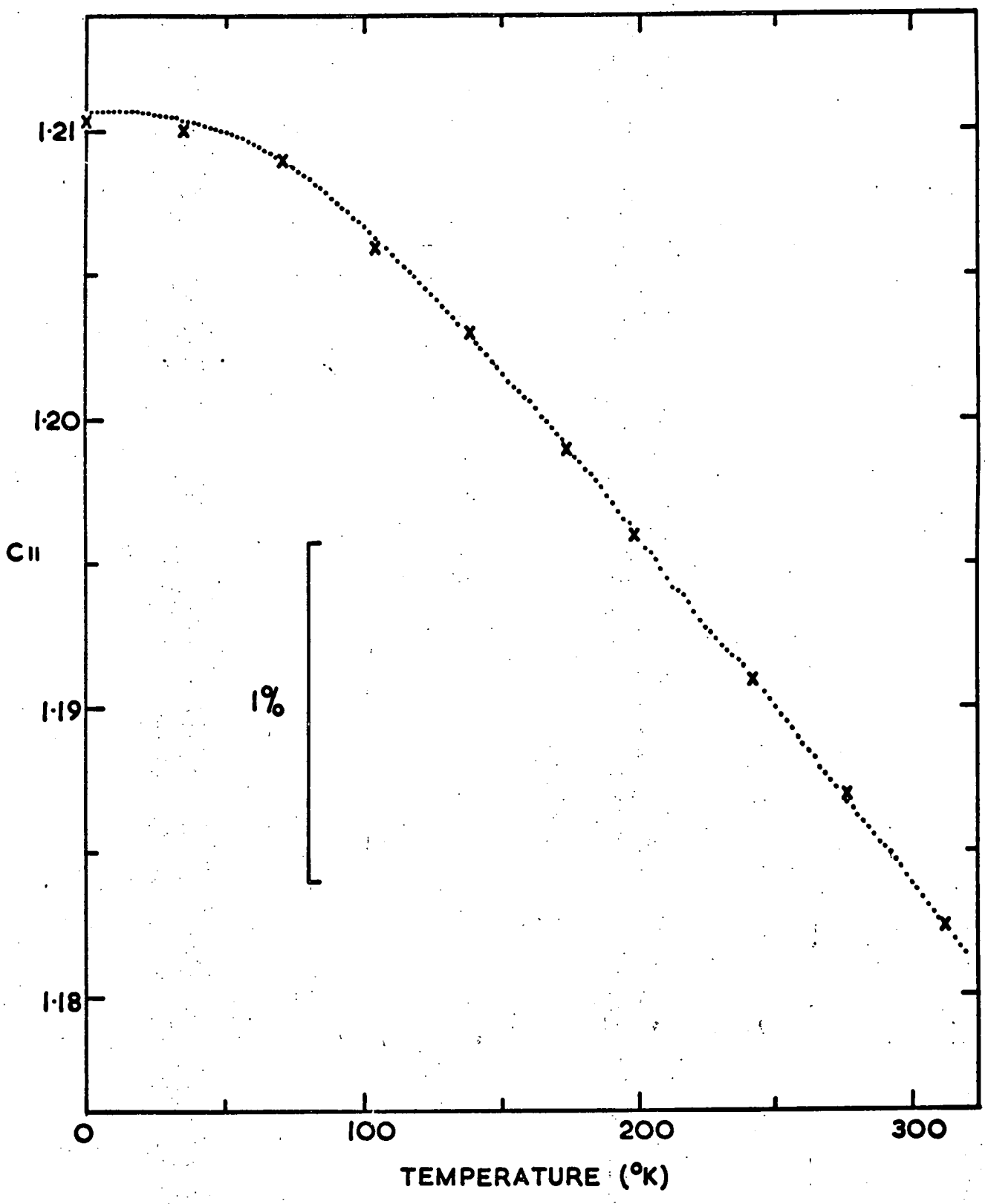

The temperature dependence of the elastic stiffness constants of GaAs: C_{11}. The points are the experimental data and the crosses (x) the fit computed from Lakkad's (1971) model.
Units: 10^{12} dyne cm^{-2}.

FIGURE 6.1

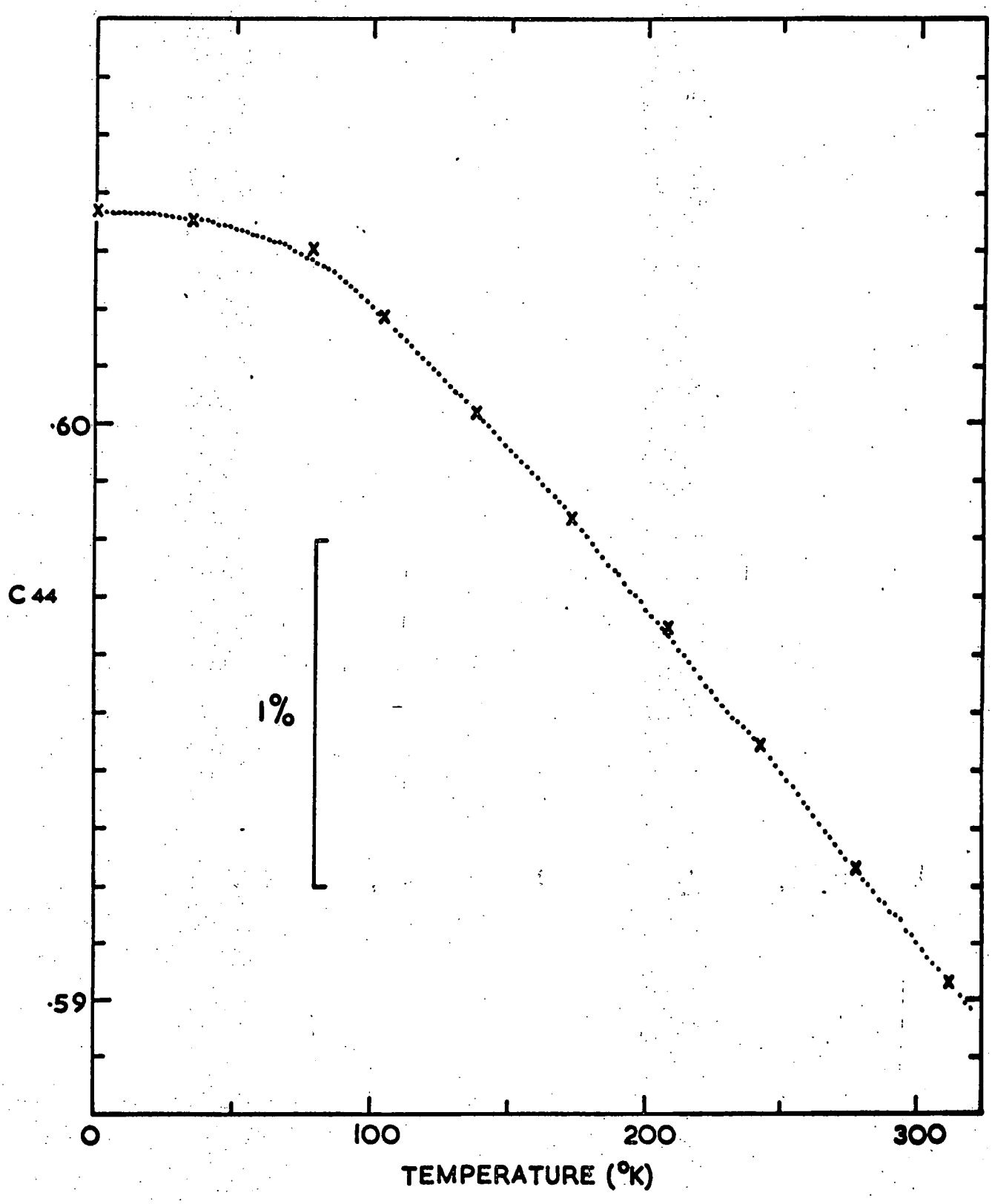

The temperature dependence of the elastic stiffness constants of GaAs: C_{44}. The points are the experimental data and the crosses (x) the fit computed from Lakkad's (1971) model. Units: 10^{12} dyne cm^{-2}.

FIGURE 6.2

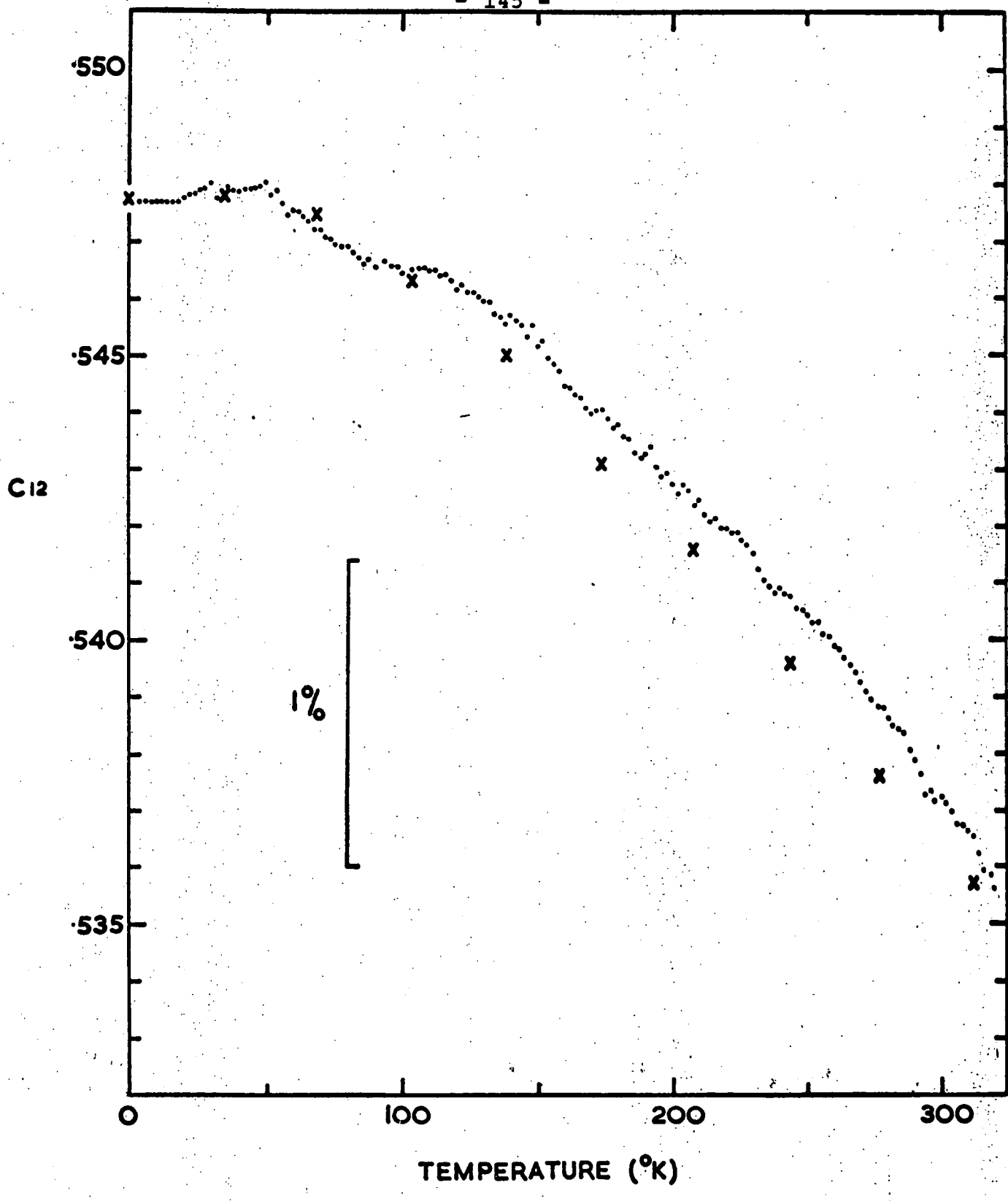

The temperature dependence of the elastic stiffness constants of GaAs: C_{12}. The points are the experimental data and the crosses (x) the fit computed from Lakkad's (1971) model. Units: 10^{12} dyne cm^{-2}.

FIGURE 6.3

TABLE 6.A

The elastic properties of GaAs at 0 K, 78 K and 298 K

Units : Elastic moduli 10^{12} dynes cm^{-2}, ultrasound wave velocities 10^{5} cm sec^{-1}.

	0 K.	78 K.	298 K.
C_{11}	$1.2107^{+.0039}_{-.0034}$	$1.2085^{+.0039}_{-.0034}$	$1.1841^{+.0037}_{-.0032}$
C_{12}	$0.5477^{+.0165}_{-.0143}$	$0.5469^{+.0165}_{-.0143}$	$0.5372^{+.0157}_{-.0136}$
C_{44}	$0.6036^{+.0019}_{-.0017}$	$0.6029^{+.0019}_{-.0017}$	$0.5912^{+.0018}_{-.0016}$
$v[100]L$ *	$4.7700^{+.0068}_{-.0058}$	$4.7657^{+.0068}_{-.0058}$	$4.7193^{+.0063}_{-.0053}$
$v[100]S$ *	$3.3682^{+.0049}_{-.0042}$	$3.3660^{+.0049}_{-.0042}$	$3.3345^{+.0043}_{-.0038}$
$v[110]L$ *	$5.2790^{+.0070}_{-.0060}$	$5.2749^{+.0070}_{-.0060}$	$5.2256^{+.0064}_{-.0054}$
$v[110]S[001]$ †	3.368 ±.005	3.366 ±.005	3.334 ±.005
$v[110]S[1\bar{1}0]$ †	2.500 ±.034	2.497 ±.034	2.467 ±.032
$v[111]L$ †	5.446 ±.026	5.442 ±.026	5.384 ±.025
$v[111]S$ †	2.821 ±.024	2.819 ±.024	2.786 ±.023
C_{11}/C_{12}	2.210 ±.064	2.210 ±.064	2.204 ±.062
C_{11}/C_{44}	2.006 ±.012	2.005 ±.012	2.003 ±.012
C_{12}/C_{44}	0.907 ±.033	0.907 ±.033	0.909 ±.032
$B=\frac{1}{3}(C_{11}+2C_{12})$	0.769 ±.012	0.767 ±.012	0.753 ±.012
$G_V=\frac{1}{5}(C_{11}+2C_{12}+3C_{44})$	0.495 ±.005	0.494 ±.005	0.484 ±.005
$G_R=\frac{(3C_{11}-3C_{12}+3C_{44})}{[5C_{44}(C_{11}-C_{12})]}$	0.454 ±.018	0.454 ±.018	0.444 ±.018
Born Stability Criterion $\frac{4C_{11}(C_{11}-C_{44})}{(C_{11}+C_{12})^2}$	0.951 ±.034	0.950 ±.034	0.948 ±.032
Anisotropy Factor $2C_{44}/(C_{11}-C_{12})$	1.821 ±.062	1.823 ±.062	1.828 ±.061

* Measured velocity

† Calculated velocity

TABLE 6.A

TABLE 6.B

Uncertainty limits required in the determination of those for C_{11}, C_{12}, C_{44} : in percentages.

	0 K, 78 K	298 K
ρ	-	±0.05
m	±0.01	±0.00
L_R [100] L, S	-	±0.04
L_R [110] L	-	±0.03
f_{CO} [100] L	±0.003	±0.003
f_{CO} [100] S	±0.004	±0.004
f_{CO} [110] L	±0.003	±0.003
f_x*	+0.07 -0.05	+0.07 -0.05
V_{ORIENT}	±0.02	±0.02

* Uncertainty in f_x is quoted as a percentage of f_{CO}.

The sources of uncertainty and their magnitudes are collected in Table 6.B. The X-ray density (5.3169 gcm^{-3}) found by Straumanis and Kim (1965) for stoichiometric GaAs has been used. These workers observed a change in lattice parameter, and therefore in X-ray density, across the narrow homogeneous phase extent of this compound; however, the appropriate limits fall inside those (± 0.0026 gcm^{-3}) of the displacement measured density, which have been taken here. Available information on the thermal expansion of GaAs is sparse and to some extent contradictory. Here an estimate has been made (Figure 6.4) of the temperature dependence of the thermal expansion coefficient based on the work of Novikova (1961), Pierron, Parker and McNeely (1967), Sparks and Swenson (1967) and Feder and Light (1968). However, an arbitrary adoption of a 10% error leads to an almost negligible uncertainty in the parameter m (see Table 6.B) and thus in the elastic constants; even though the coefficient α becomes negative below 50 K, its effect is so small as to be completely insignificant at low temperatures. The correction factor f_x for the transducer reflection phase shift was evaluated from measurements of repetition rate as a function of frequency between 35 and 45 MHz for each of five different n-values. Finally, an error (V_{orient}) occurs in the measured velocity due to misorientation ($\pm\frac{1}{2}^{o}$) of the specimen with respect to the crystal axes, and the uncertainty arising has been calculated by the technique described by Truell, Elbaum and Chick (1969).

The total uncertainties in the measured velocities and subsequently in the elastic stiffness constants C_{11}, C_{12}

The thermal expansion coefficient (α) of GaAs estimated from the data of Novikova (1961), Pierron, Parker and McNeely (1967), Sparks and Swenson (1967) and Feder and Light (1968). Bars represent an error of ±10%.

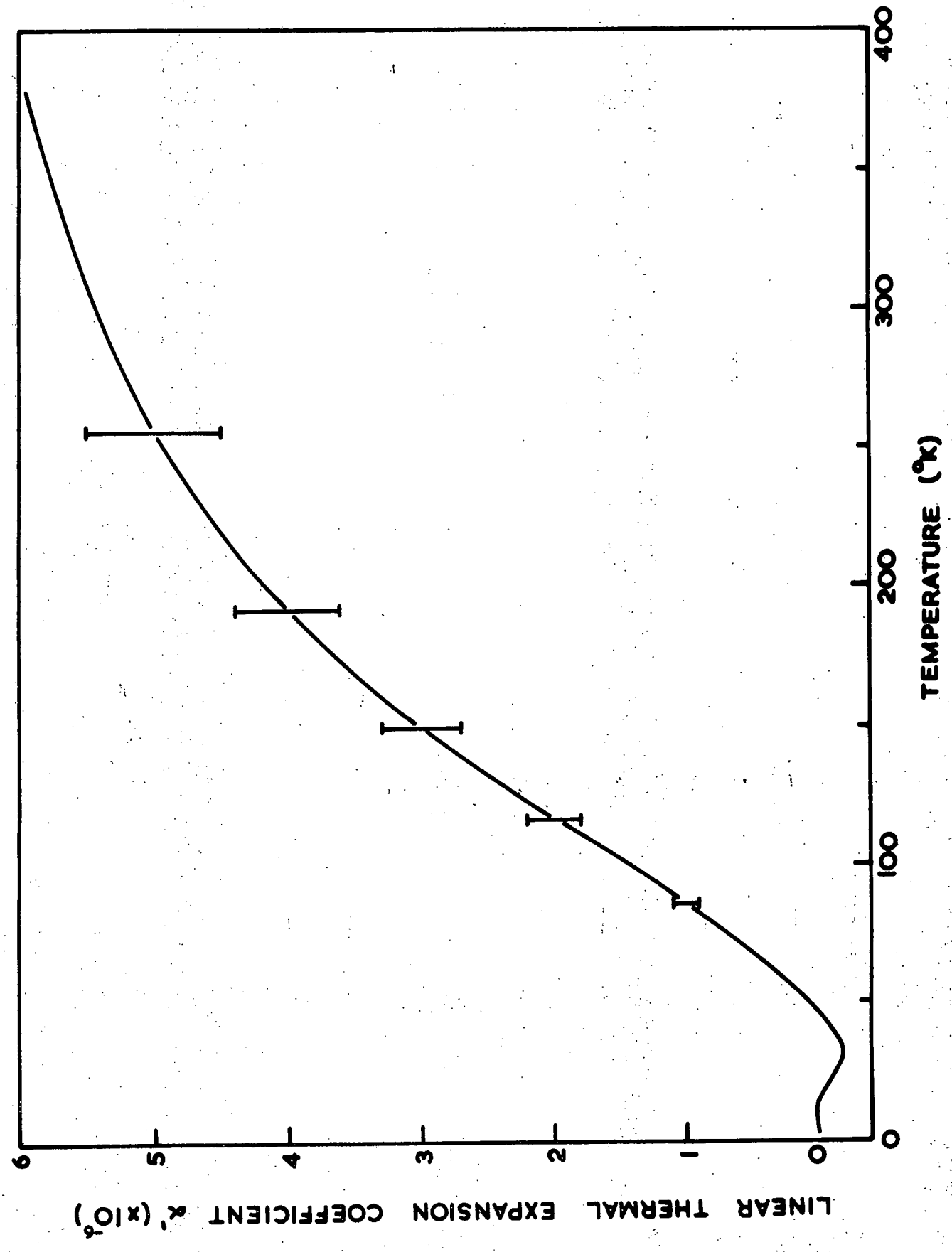

FIGURE 6.4

C_{44} presented in Table 6.A have been calculated using the data in Table 6.B in conjunction with equations 5.13 and 5.14. Comparisons made in the following sections of this work suggest an error much smaller than the extreme limits of uncertainty, but the quoted limits cannot be reduced on that basis. The relative uncertainties calculated for the temperature dependences of C_{11}, C_{12} and C_{44} are 0.02%, 0.1% and 0.02% respectively.

6.2 COMPARISON WITH PREVIOUS WORK

A comparison between the room temperature elastic constants measured here and those of other workers is given in Figure 6.5. For the purpose of this pictorial representation, and on the basis of information gleaned from the respective papers, a carrier density of about 10^{17} cm^{-3} has been assigned to the crystals used by Bateman, McSkimin and Whelan (1959), Garland and Park (1962), Drabble and Brammer (1966) and McSkimin and Andreatch (1967); the present results are in excellent agreement with those of these particular workers. However, even assuming extreme uncertainties in all the previous measurements as large as those quoted in the present work, there are discrepancies between the elastic stiffness constants found for samples of different or even the same carrier density - the important finding of Bobylev and Kravchenko (1967) that the elastic constants of GaAs show little dependence on carrier density between 7.7×10^{15} cm^{-3} and 2.5×10^{18} cm^{-3}, taken to evidence parabolicity of the conduction band edge, cannot be considered quite proven: their values of C_{11} and C_{44}

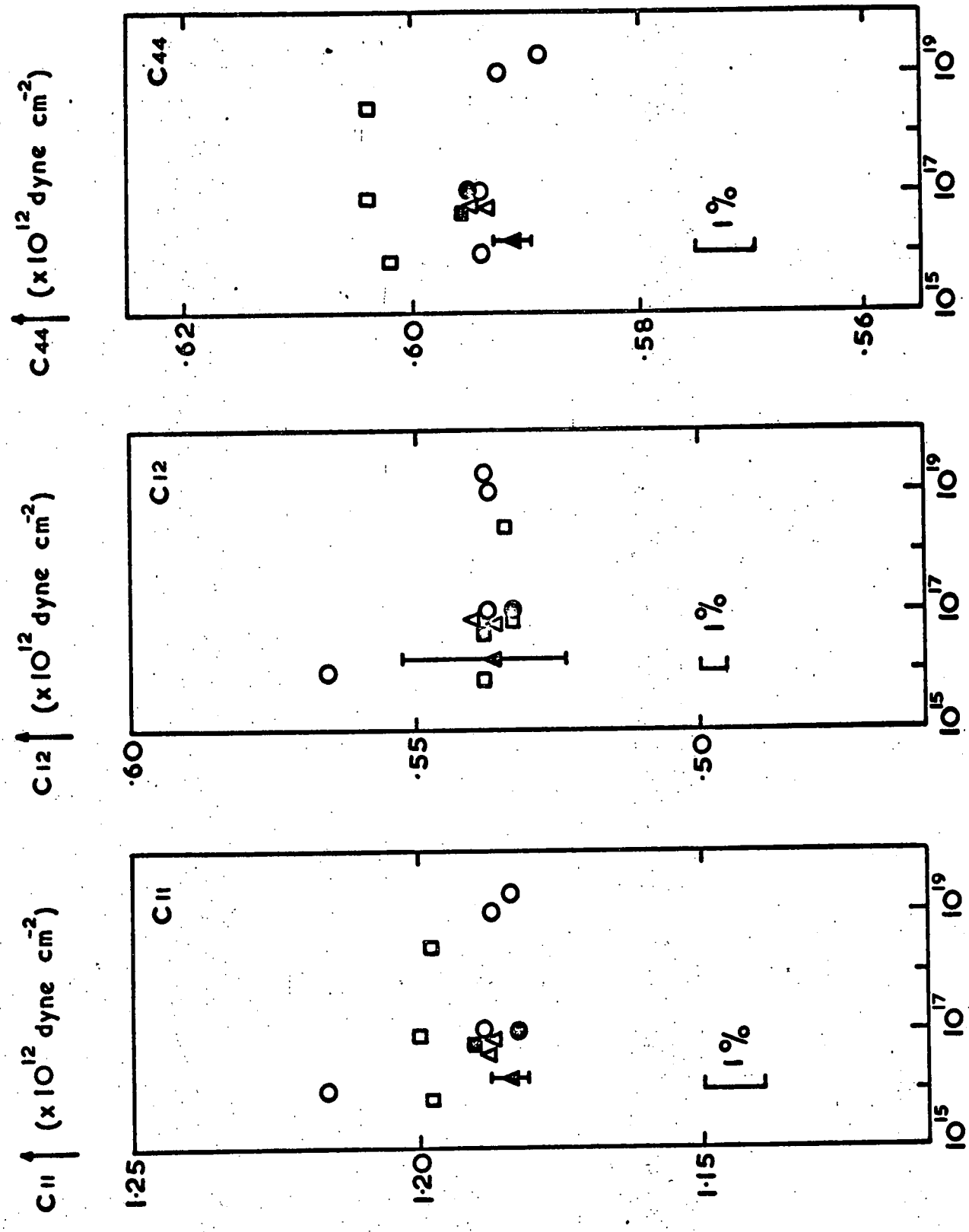

Comparison between the available data for the elastic stiffness constants of GaAs at 298 K .

▲This work (with extreme error limits),

● Garland and Park (1962)

△Bateman, McSkimin and Whelan (1959)
McSkimin, Jayaraman and Andreatch (1967)

■Drabble and Brammer (1966),

□Bobylev and Kravchenko (1967) and

OBeilin, Vekilov and Krasil'nikov (1969).

FIGURE.6 5

lie well away from those of other workers (as do the C_{11} and C_{12} quoted by Beilin, Vekilov and Krasil'nikov, 1969). One possible source of this spread in the measured values of the elastic stiffness constants is the defect nature of the crystals studied. In the II-VI, zinc-blende structured compound HgTe the dominant ultrasound dissipation mechanism is forced dislocation motion which leads to an associated modulus change (Alper and Saunders, 1969); annealing removes some dislocation pinning points and has pronounced effects on the elastic behaviour (Alper and Saunders, 1967, 1969). As a result of the phase extent of gallium arsenide (Straumanis and Kim, 1965), crystals can grow with high dislocation or point defect concentrations and these would exhibit elastic constants different from those of more perfect crystals.

One of the two previous measurements of C_{11}, C_{12} and C_{44} at other than room temperature is restricted to 77.3 K; therefore, the temperature dependencies can be compared best by using the parameter $(C_{77.3\ K} - C_{298\ K})/C_{298\ K}$ (Figure 6.6). The values quoted from Garland and Park (1962) contain a minor correction from 300 K to 298 K; if other ultrasound velocities reported by these workers are used to estimate $(C_{77.3\ K} - C_{298\ K})/C_{298\ K}$, quite different values result: as Garland and Park (1962) pointed out themselves, there are internal inconsistencies in their measured temperature dependencies. The present results for $(C_{77.3\ K} - C_{298\ K})/C_{298\ K}$ agree with those of Beilin, Vekilov and Krasil'nikov (1969) to within the quoted relative uncertainties. In accord with the suggestion of Bobylev and Kravchenko (1967) of a parabolic conduction

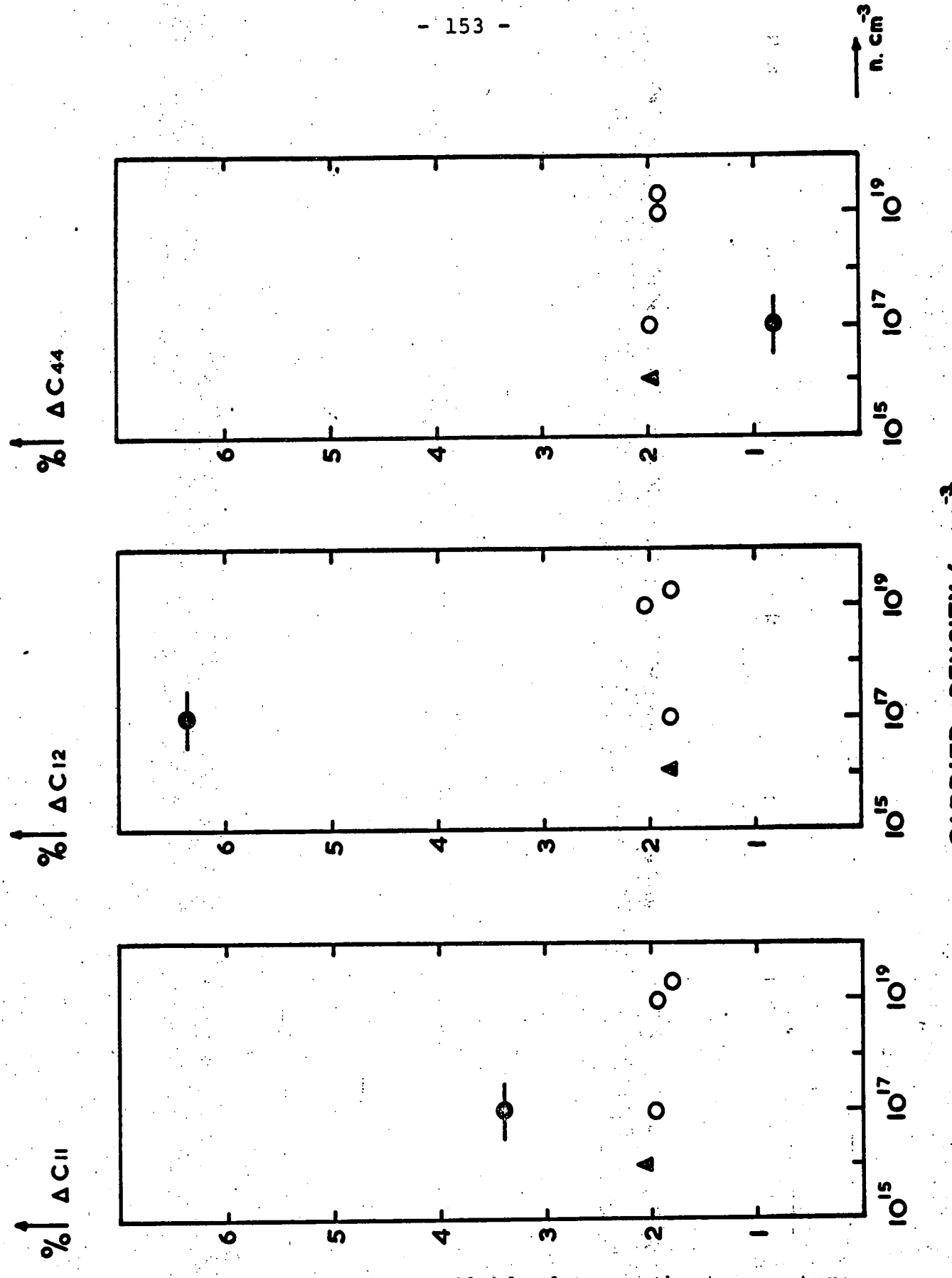

Comparison between the available data on the temperature dependence

$$\Delta C = \frac{C_{77.3K} - C_{298K}}{C_{298K}}$$

of the elastic stiffness constants of GaAs.

▲This work, ●Garland and Park (1962) and ○Beilin, Vekilov and Krasil'nikov (1969).

FIGURE 6.6

band, $(C_{77.3\ K} - C_{298\ K})/C_{298\ K}$ is independent of carrier concentration.

6.3 THE DEBYE TEMPERATURE

The most successful single-parameter model of the lattice properties of solids is that formulated by Debye in terms of a characteristic temperature θ_D. The comparison of values of θ_D derived from different physical observations may be used to evaluate the model validity.

The Debye temperature ($\theta_o^{elastic}$) has been calculated from the elastic constant data extrapolated to 0 K by the relation

$$\theta_o^{elastic} = \frac{h}{k}\left(\frac{9N}{4\pi}\right)^{\frac{1}{3}} f^{\frac{1}{3}}, \qquad (6.1)$$

$$f = \int_o^{4\pi} \sum_i \frac{1}{V_i^3} \frac{d\Omega}{4\pi} \qquad (6.2)$$

where N is the number of atoms per unit volume, V_i the velocity of propagation of a low frequency vibration as a function of direction and Ω is a solid angle. To evaluate the integral f the graphical procedure of de Launay (1956, 1959) has been applied. The value of 346.8 K obtained for $\theta_o^{elastic}$ is in excellent agreement with that (346.7 K) calculated from the low temperature (1 K to 30 K) specific heat data of Cetas, Telford and Swenson (1968). In the long wavelength limit achieved at low temperatures ($<\theta_D/50$) such agreement is expected (Alers, 1965). The small difference of 0.03% between these two values is more consistent with those quoted by Alers (1965) for a wide range of cubic materials than are those found for other III-V

compounds (see Truell et al, 1969).

There is a difference between the polycrystalline shear moduli G_V derived for uniform local strain (Voigt 1928) and G_R derived for uniform local stress (Reuss, 1929) (see Table 6.A). Hill (1952) suggested two empirical formulae for the true polycrystalline shear modulus G, namely

$$G = \tfrac{1}{2}(G_R + G_V) \tag{6.3}$$

and

$$G = \sqrt{G_R . G_V} \tag{6.4}$$

Zucker (1969) has compared Debye temperature calculations based on these two formulae and suggested that $\sqrt{G_R . G_V}$ is a better approximation to the polycrystalline rigidity modulus than $\frac{1}{2}(G_R + G_V)$. The Debye temperature (349.2 K) calculated in this work using equation (6.4) is closer to that (346.8 K) derived from the de Launay approximation than is that (349.4 K) calculated using equation (6.3), but only by a small margin.

6.4 TEMPERATURE DEPENDENCE OF THE ELASTIC CONSTANTS

The elastic constant temperature dependences shown in Figures 6.1, 6.2 and 6.3 are of the form expected for a crystal exhibiting no phase changes or instabilities in this temperature range; each dependence approaches OK with zero slope and is almost linear at high temperatures. Recently Lakkad (1971) has provided a simple description of the temperature dependence on the basis of a phenomenological model of an anharmonic oscillator together with the Debye lattice vibration spectrum. To a first approximation

the elastic constant (C) is given by

$$C = C_o \left[1 - KF(T/\theta_D)\right] \tag{6.5}$$

where C_o is the elastic constant at O K and K is a constant, and

$$F(T/\theta_D) = 3(T/\theta_D)^4 \int_o^{\theta_D/T} \left\{x^3 [\exp(x) - 1]^{-1}\right\} dx \tag{6.6}$$

where x equal $h\nu/kT$. To test this expression for GaAs, the elastic constant data at $0.9\theta_D$ and $0.25\theta_D$ have first been used to estimate the constant K ($= 9\beta_\infty \theta_D^L (c_1/c)$ in Lakkad's notation) and then the elastic constant computed as a function of temperature (see Figures 6.1,6.2,6.3). Each measured elastic constant curve can be fitted well using the same value (0.039) for K. This, in Lakkad's expression for K, implies that the ratio of the anharmanic to harmonic components of the atomic restoring force, (C_1/C), is independent of direction. For consistency, the ratio of the second order to higher order elastic constants should show the same independence. For the [100], [110] and [111] longitudinal modes the ratio R of 3rd to 2nd order constants has been calculated using the relevant elastic constant combinations:

$$R_{[100]L} = \frac{C_{111}}{C_{11}} \tag{6.7}$$

$$R_{[110]L} = \frac{C_{111}+3C_{112}+12C_{166}}{2(C_{11}+C_{12}+2C_{44})} \tag{6.8}$$

$$R_{[111]L} = \frac{C_{111}+6C_{112}+12C_{144}+24C_{166}+2C_{123}+16C_{456}}{3(C_{11}+2C_{12}+4C_{44})} \tag{6.9}$$

The ratios $R_{[100]L}$, $R_{[110]L}$ and $R_{[111]L}$ calculated from the third order constant measurements of Drabble and Brammer (1966) turn out to be 5.72, 9.86 and 9.18 respectively, and

those calculated from the measurements of McSkimin and Andreatch (1967) are 5.11, 9.44 and 7.14: complete consistency with the independence of K in C_{11}, C_{12} and C_{44} is not evident up to third order.

6.5 ANHARMONICITY AND THE GRÜNEISEN PARAMETER

Lakkad's model predicts that the ratio of the specific heat to the thermal expansion is constant, that is that the Grüneisen law is obeyed. This is certainly not the case for GaAs; the temperature dependence of the Gruneisen parameter γ' (= $V\beta K_{Th}/C_v$) - calculated using the thermal expansion estimate in Figure 6.4 and the specific heat data of Piesbergen (1963) down to 40 K together with that of Cetas et al (1968) below 40 K - is illustrated in Figure 6.7. Bobylev and Kravchenko (1970) calculated $\gamma'/\gamma'_{300\ K}$ using the thermal expansion data of Novikova (1961) and elastic constant data; they also estimated $\gamma'/\gamma'_{300\ K}$ from measurements of ultrasonic attenuation between 20 K and 300 K; both results - normalised to γ'_{300} of this work - are also given for comparison in Figure 6.7. The Grüneisen parameter obtained from the attenuation does not exhibit the negative excursion. Room temperature Grüneisen parameter values obtained previously from third order elastic constants are 0.455 (Krasil'nikov et al 1969) and 0.97 (Lewis 1968); Ivanov et al (1971) fitted results of [111] longitudinal attenuation with a value of 0.9; Lewis (1968) also calculated γ' from $V\beta T_{Th}/C_v$, finding a value at 300 K of 0.84, which is larger than the $\gamma_{300\ K}$ (= 0.71) of this work by simply the difference in the thermal expansion data used. The sharp rise in γ' at low temperatures is consistent with

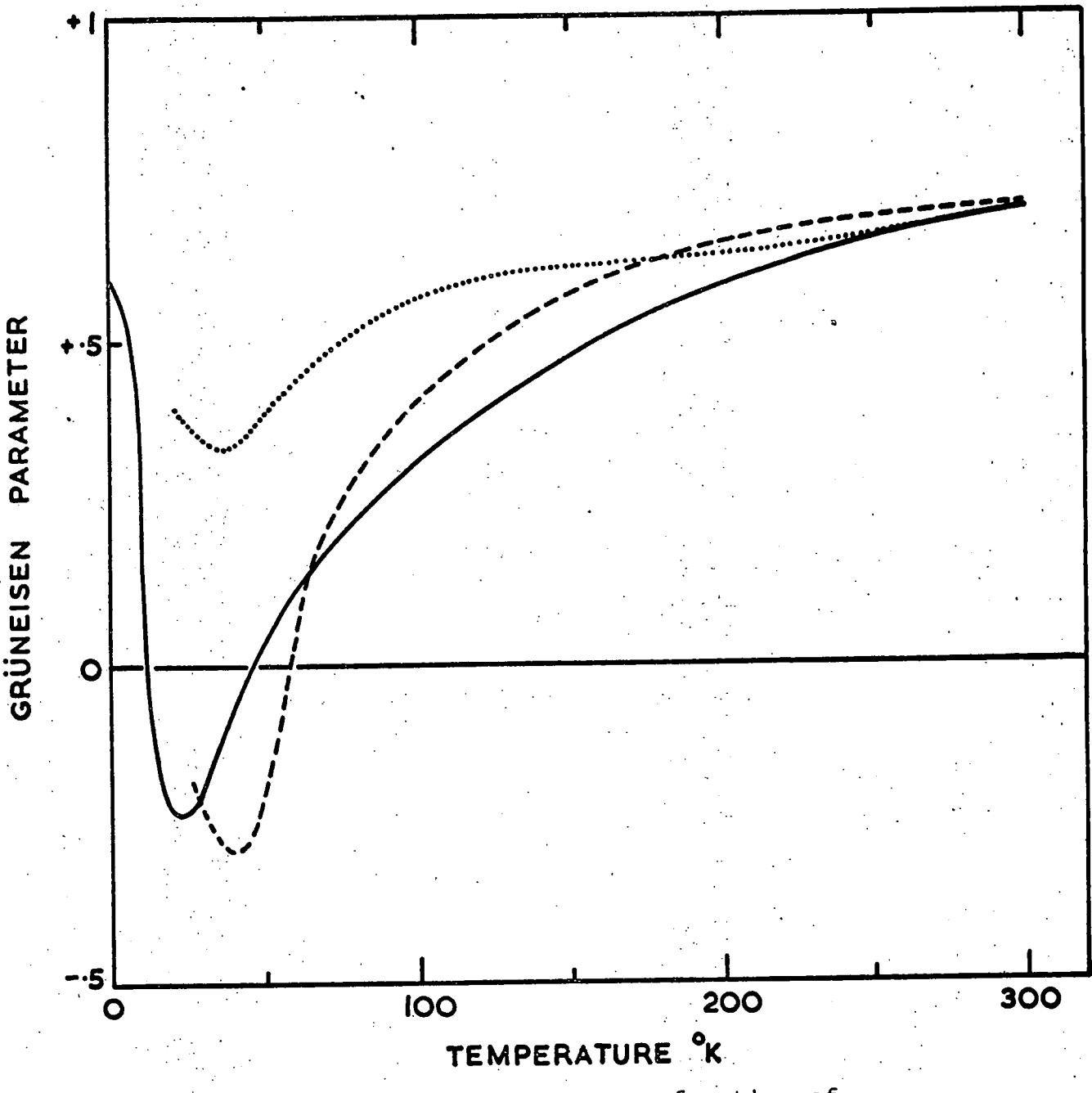

The Grüneisen parameter of GaAs as a function of temperature. Full line, this work; dashed line, Bobylev and Kravchenko (1967); dotted line, Bobylev and Kravchenko (1970) - estimated from the attenuation of longitudinal waves.

FIGURE 6.7

Ruppin's (1972) discussion of the lithium halides in terms of their anisotropy (∿1.9).

Lakkad's model suffers from exactly the same limitations as the Debye model for specific heat: its basis is similar and variation in the anharmonic component of the atomic restoring force with temperature is not considered: we can approach the model discrepancies in a similar way. As presented in Figures 6.1 and 6.3 the temperature dependences of C_{11} and C_{44} appear to be fitted extremely well (that for C_{12} in Figure 6.2 being limited by the scatter); in fact there is a deviation on approaching lower temperatures. If, instead of calculating the elastic constants from θ_D, we calculate first K, then the Debye temperature as a function of temperature from the elastic constants, we find a curve similar to that of the Debye temperature derived from an exact fit of the Debye model to the specific heat data of Piesbergen (1963) and Cetas et al (1968) (see Figure 6.8). This would be expected in view of the similarity of the models.

6.6 CRYSTAL BINDING AND IONICITY

Banerjee and Varshni (1969) have calculated excellent fits to the phonon dispersion curves (see Figure 2.12) and specific heat Debye temperature variation (see Figure 6.8) using a second neighbour ionic model. Vetelino and Mitra (1969) have extended the calculations, giving an invariance relation for zinc-blende crystals in terms of the elastic constants and zone-centre frequencies which gallium arsenide obeys well. We have calculated the force constants for gallium arsenide on

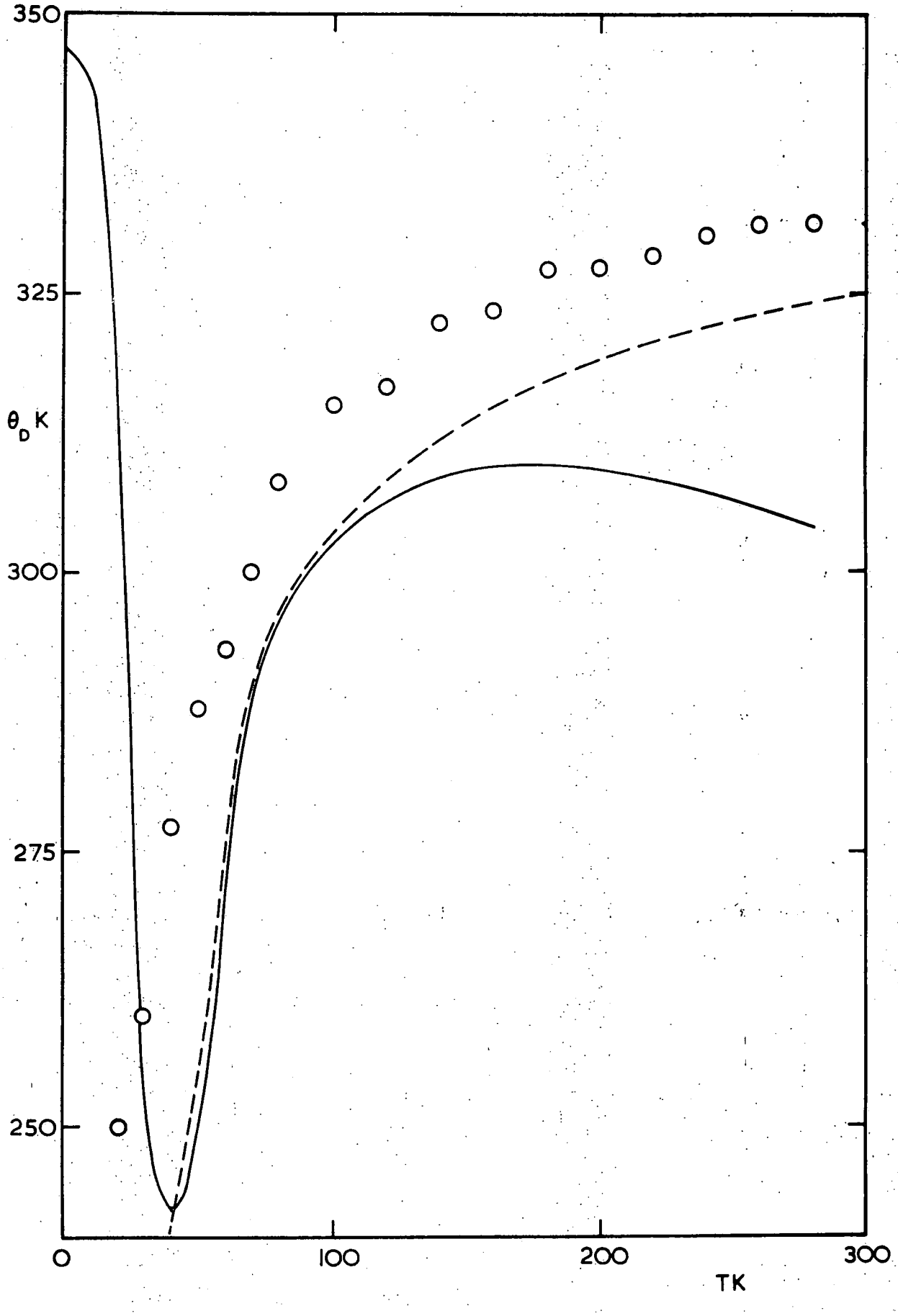

The Debye temperature θ_D of gallium arsenide calculated from Lakkad's fit to the elastic constant data (O,C_{11} this work), the specific heat (——, Piesbergen, 1963; Cetas et al, 1968) and a Rigid ion model (----. Baneriee and Varshni, 1969).

FIGURE 6.8

the basis of Vetelino and Mitra's (1969) model: the first neighbour radial (α) and non-central (β) force constants and the second neighbour radial constant (μ) are 3.926×10^4, 3.074×10^4 and 0.340×10^4 dyne cm^{-1} respectively. Banerjee and Varshni (1969) obtained $\alpha = 3.95 \times 10^4$, $\beta = 3.40 \times 10^4$, $\mu_1 = 0.45 \times 10^4$ and $\mu_2 = 0.37 \times 10^4$ dyne cm^{-1}. The force constants found using the Born (1914) model are $\alpha = 6.1 \times 10^4$ and $\beta = 4.4 \times 10^4$ dyne cm^{-1}; the Born stability criteria (Table 6A) show no significant changes with temperature.

Polar character is associated with the bonding in III-V compounds. The "Szigeti" effective charge e_s^* is related to the restrahlen frequency ω_R by (Szigeti 1950)

$$se_s^* = \frac{3(\zeta_o - \zeta_\infty)\, m_i\, \omega_R^2\, V_a}{4\pi\, (\zeta_\infty + 2)^2} \qquad (6.10)$$

and ω_R to the bulk modulus B by

$$\omega_R^2 = \frac{3V_a}{4m_i\, P_o^2} \left(\frac{\zeta_\infty + 2}{\zeta_o + 2} \right) B \qquad (6.11)$$

Here V_a is the unit cell volume, P_o the nearest neighbour distance and s a distortion parameter. Published data for the static (ζ_o) and infinite frequency (ζ_∞) dielectric constants are conflicting; the recent careful work of Johnson, Sherman and Weil (1969) gives ζ_o as 12.8 ± 0.5 and ζ_∞ as 10.9 ± 0.4 at 300 K. Using these values and the bulk modulus at 298 K, and assuming the Lyddane-Sachs-Teller rule $\omega_R^2 = \omega_{LO}^2 (\zeta_\infty / \zeta_o)$, we find ν_R $(= \omega_R / 2\pi) = 7.9 \times 10^{12}$ Hz, ν_{LO} $(= \omega_{LO}/2\pi) = 8.6 \times 10^{12}$ Hz, $\lambda_{LO} = 34.9\mu$ and $e_s^* = \pm 0.56e$ when s is unity. λ_{LO} compares well with the measured

transverse optical mode wavelength of 37.2 μ (Johnson, Sherman and Weil 1969) and ν_{LO} with that of 8.55 x 10^{12} Hz at [0, 0, 0] by neutron spectroscopy (Waugh and Dolling 1963) (see Figure 2.12). The ω_{LO} and ω_R values above have been used to find the effective charge from Vetelino and Mitra's (1969) model. The calculated value of ±0.63 e is in reasonable agreement with the Szigeti effective charge.

The ionicity of GaAs has been calculated by a variety of methods (see Table 2.B). In view of the approximations inherent in each approach, particularly with regard to electronic polarizability effects, these results are in excellent agreement. The negative sign of e*/e indicates charge transfer from the group III (Ga) atom to the group V (As) atom, equivalent to a more convalent than neutral bond character (Suchet 1965); no sign (+ or -) is available from either ultrasonic or optical measurements.

6.7 YOUNG'S MODULUS AND VELOCITY SURFACES

Knowledge of the complete set of elastic constant tensor coefficients allows determination of the material response to any applied stress system. An important case is the response to a simple tension which provides the technical constant Young's modulus Y. The surface showing the variation of this modulus with orientation is a useful aid in visualizing the crystal's elastic anisotropy. For a cubic material Y in terms of the elastic compliances S_{ij} is

$$Y = S_{11} - 2(S_{11} - S_{12} - \tfrac{1}{2}S_{44})(\ell_1^2\ell_2^2 + \ell_2^2\ell_3^2 + \ell_3^2\ell_1^2) \qquad (6.12)$$

where $\underset{\sim}{\ell}$ is a unit vector in the direction of the applied stress. (001) and (110) plane cross-sections of the Young's

modulus are shown in Figure 6.9. To compile further the elastic behaviour, cross-sections of the phase velocity surfaces have been calculated. For a specified crystallographic direction denoted by direction cosines n_1, n_2, n_3, three orthogonal elastic waves can be propagated with velocities given by the eigenvalues of the Christoffel equations.

$$[L_{ik} - \rho V^2 \delta_{ik}] u_{Ok} = 0 \; ; \; (i,k = 1, 2, 3) \qquad (6.13)$$

Here u_{O1}, u_{O2}, u_{O3} are the direction cosines of the particle displacement vectors and

$$\begin{aligned} L_{11} &= n_1^2 C_{11} + n_2^2 C_{44} + n_3^2 C_{44} \\ L_{22} &= n_1^2 C_{44} + n_2^2 C_{11} + n_3^2 C_{44} \\ L_{33} &= n_1^2 C_{44} + n_2^2 C_{44} + n_3^2 C_{11} \\ L_{23} &= n_2 n_3 (C_{12} + C_{44}) \\ L_{13} &= n_1 n_3 (C_{12} + C_{44}) \\ L_{12} &= n_1 n_2 (C_{12} + C_{44}) \end{aligned} \qquad (6.14)$$

The three wave velocities have been obtained for propagation directions taken at 1° intervals around the (001) and (110) planes (see Figure 6.10). The polarisation vectors of each mode, obtained by substituting the velocity back into equation (6.13) and solving for u_{Ok}, have been calculated for propagation directions in the (001) plane; the result for the quasi-longitudinal mode is shown as an angular deviation from the propagation direction in Figure 6.11; that for the pure shear mode is always

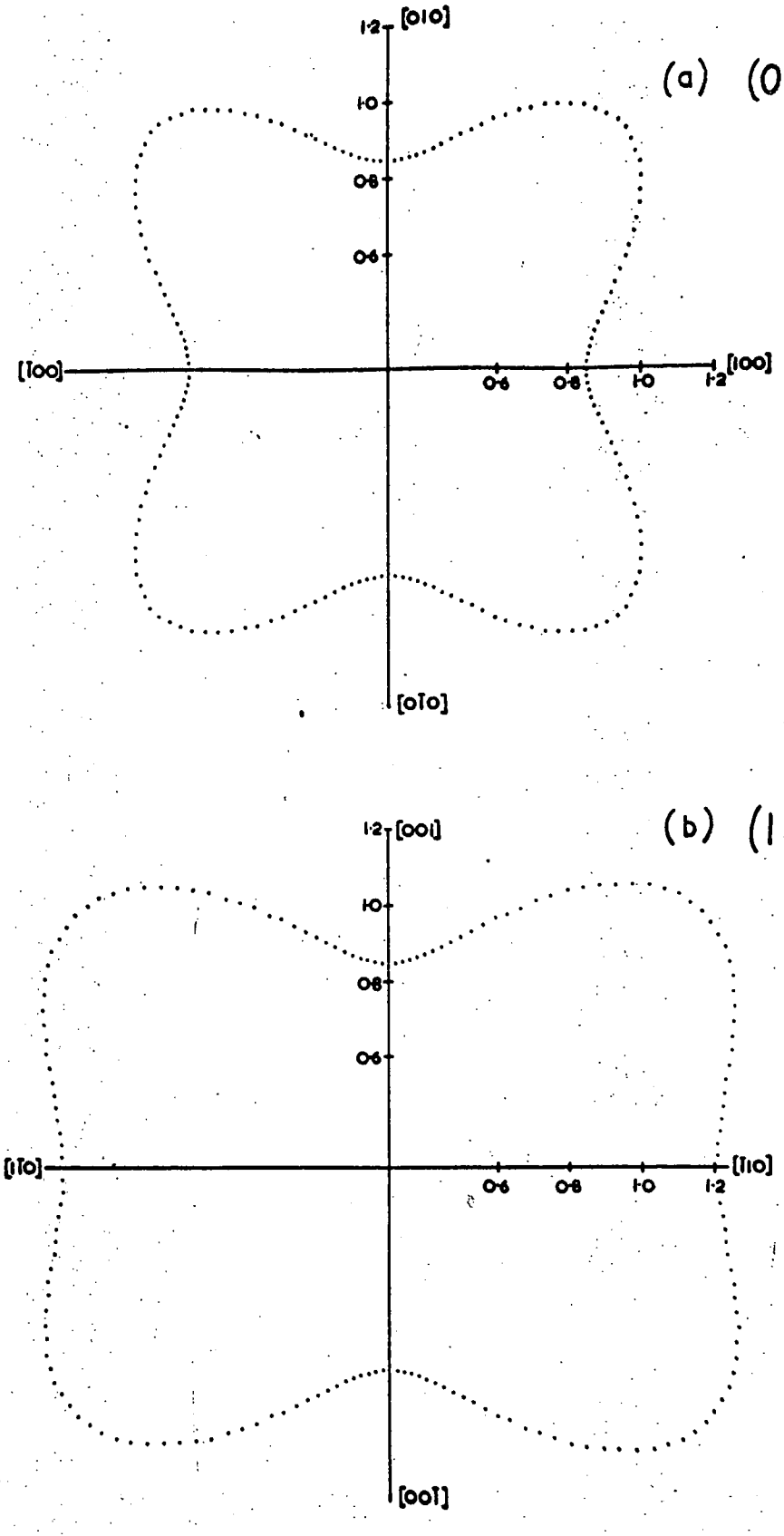

The (001) (a) and (110) (b) cross-sections of the Young's modulus surface of GaAs. Units: 10^{12} dyne cm^{-2}.

FIGURE 6.9

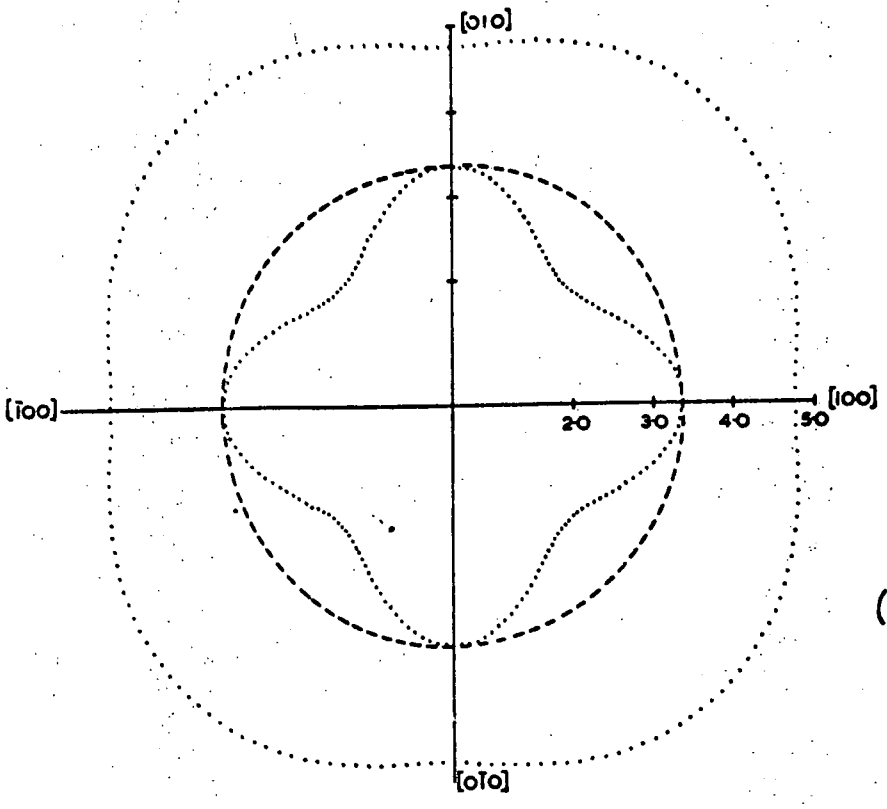

(a) (001) section

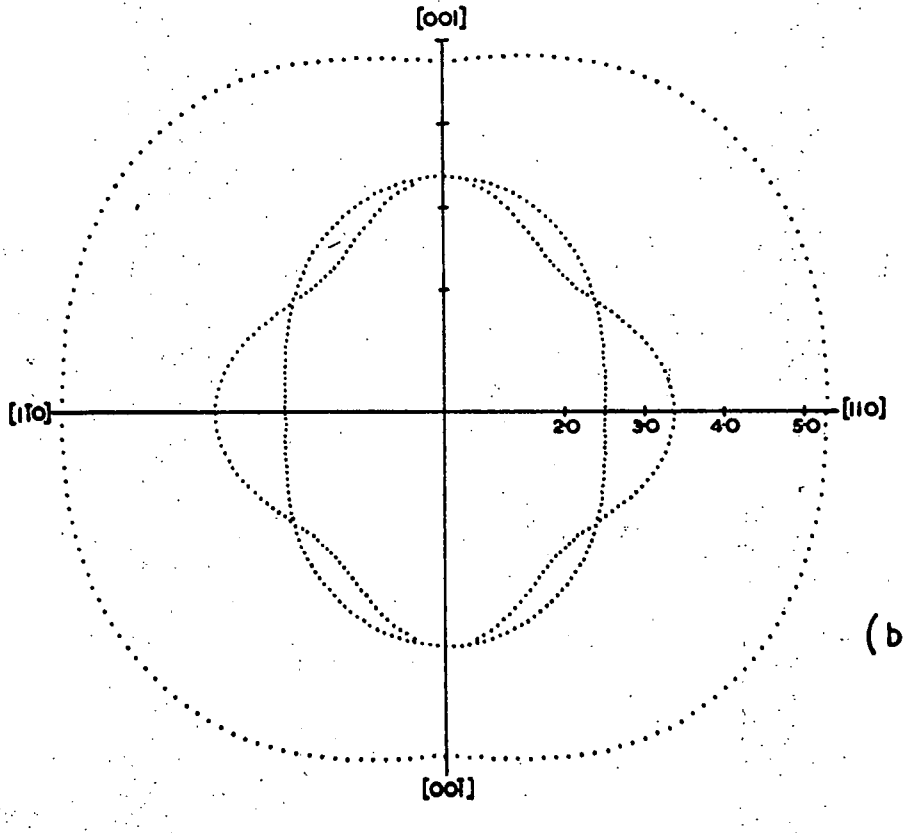

(b) (110) section

The (001) (a) and (110) (b) cross-sections of the velocity surface of GaAs. Units are 10^5 cm sec^{-1}. The dashed line refers to the pure shear which can be propagated at any direction in the (001) plane.

FIGURE 6.10

The deviations from propagation directions in the (001) plane of the particle displacement vector (———) of the quasi-longitudinal wave and the energy flux vectors of the quasi-longitudinal (·····) and the quasi-shear (-·-·-·-·) waves.

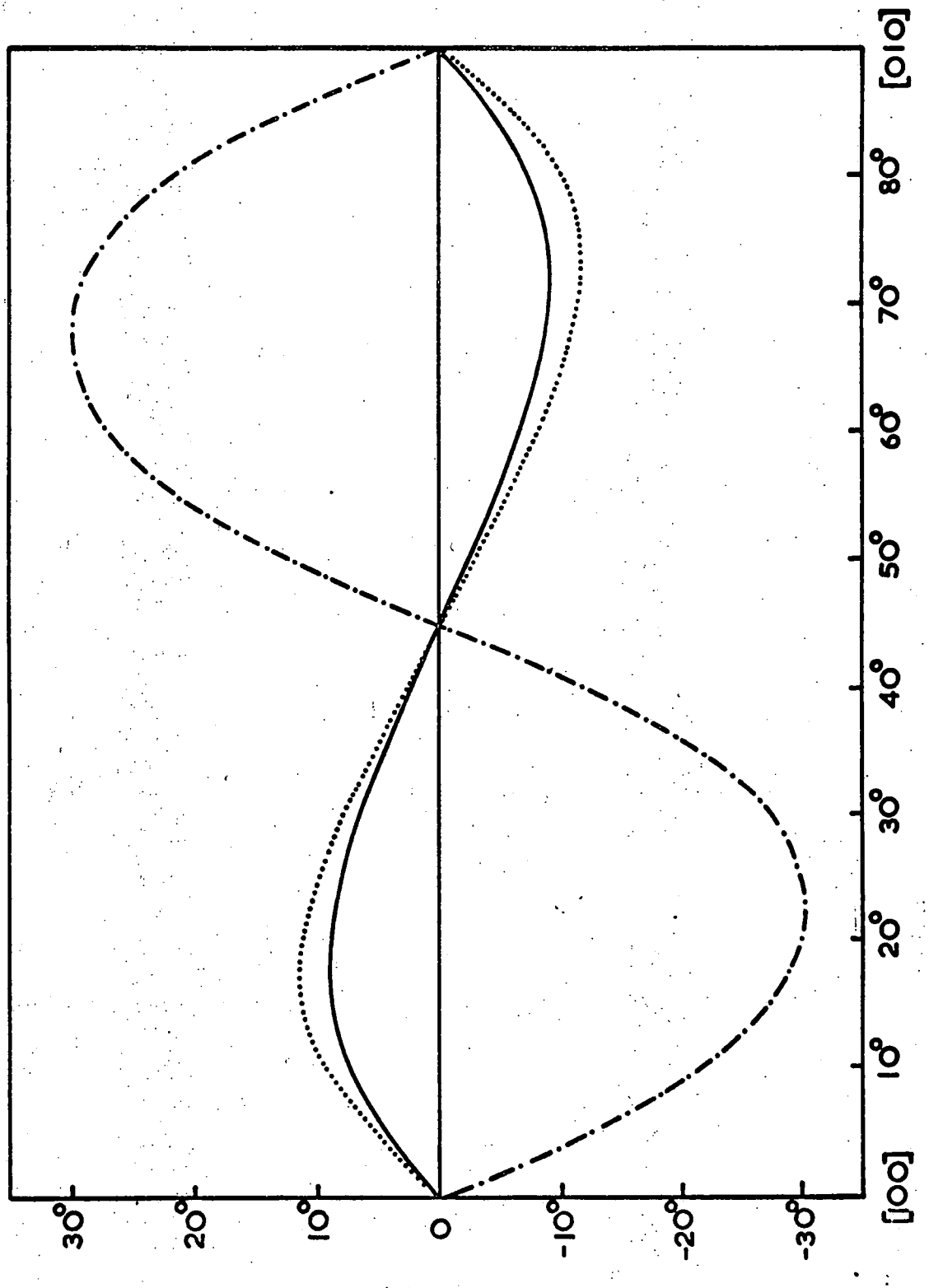

FIGURE 6.11

perpendicular to the (001) plane while that for the quasi-shear mode always differs by $\pi/2$ from that for the quasi-longitudinal mode. Finally, the angular dependence of the energy flux vector of each mode (g) of velocity V_g propagated in the (001) plane has been calculated from the equation for components

$$p_i^g = - \frac{(p^g \omega)^2}{2V_g} C_{ijkl} u_{oj}^g u_{ok}^g n_\ell^g \qquad (6.15)$$

where p^g is the elastic displacement amplitude. Results for the quasi-longitudinal and quasi-shear modes are plotted in Figure 6.11. The deviation of the energy flux vector from the propagation direction for the quasi-longitudinal mode is small but that of the quasi-shear mode is large, especially for a propagation direction midway between the fourfold axis and the twofold axis and attention must be paid in ultrasonic experiments made with the latter mode to prevention of wall reflections.

6.8 PIEZOELECTRIC CONTRIBUTION TO THE STIFFNESS OF GaAs

The velocity of the [111] 40 MHz longitudinal ultrasonic mode in the GaAs used in these measurements is shown as a function of temperature in Figure 6.12. To show up the anomalous temperature dependence the curve has been normalised at 0 K to that calculated from the elastic constants given in Figures 6.1, 6.2 and 6.3. The difference between the two curves at higher temperatures is greater than the calculated relative uncertainty (see Section 6.1) and systematic errors will be of the same magnitude in each case: there is a real discrepancy.

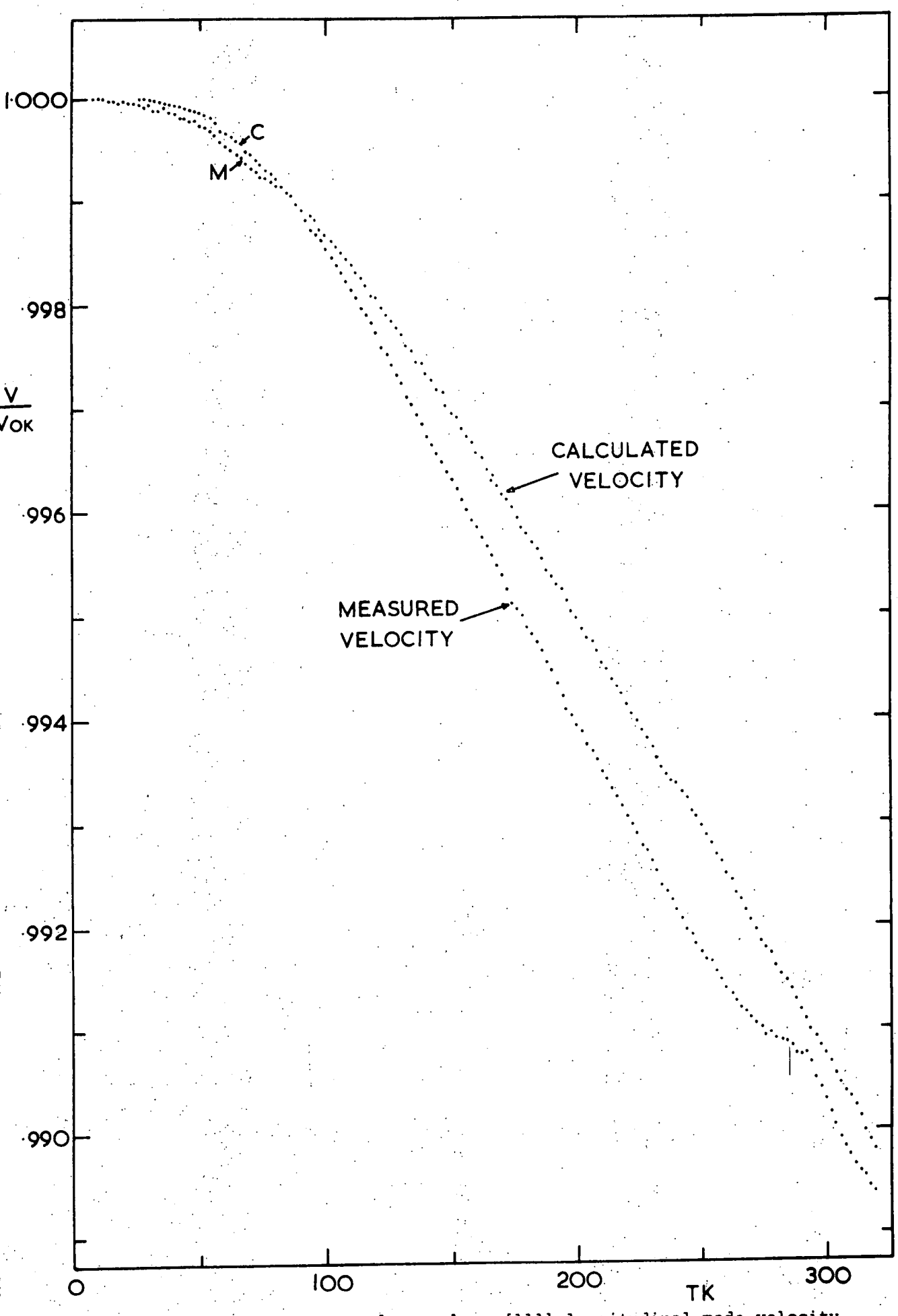

The measured anomalous [111] longitudinal mode velocity in GaAs normalised to the calculated curve at 0 K.

FIGURE 6.12

Boyle and Sladek (1973) have observed a similar effect below 200 K in GaAs for the [110] shear wave polarised along the [001] direction - the only other piezoelectrically coupled pure mode. In this work an extension of the anomaly has been found above 250 K (see Figure 6.12). The comparative rise of the measured velocity at low temperatures and high temperatures implies corresponding regions of low electrical conductivity. This is consistent with the results of Ikoma (1968, 1970) who found a high temperature rise in resistivity for GaAs samples of carrier concentrations between 3.89×10^{14} and 1.06×10^{17} cm^{-3}. The presence of the high temperature anomaly in the [111]L velocity in this material ($n = 1.30 \times 10^{16}$ cm^{-3}) has been confirmed by measurements made using both thin-film and quartz transducers (Figure 6.13).

No large piezoelectric-coupling attenuations were observed in this work (see Figures 8.1 - 8.8).

It is possible that the piezoelectric stiffening of GaAs reported here may be the cause of some of the discrepancies in previous elastic constant determinations (see Section 6.2).

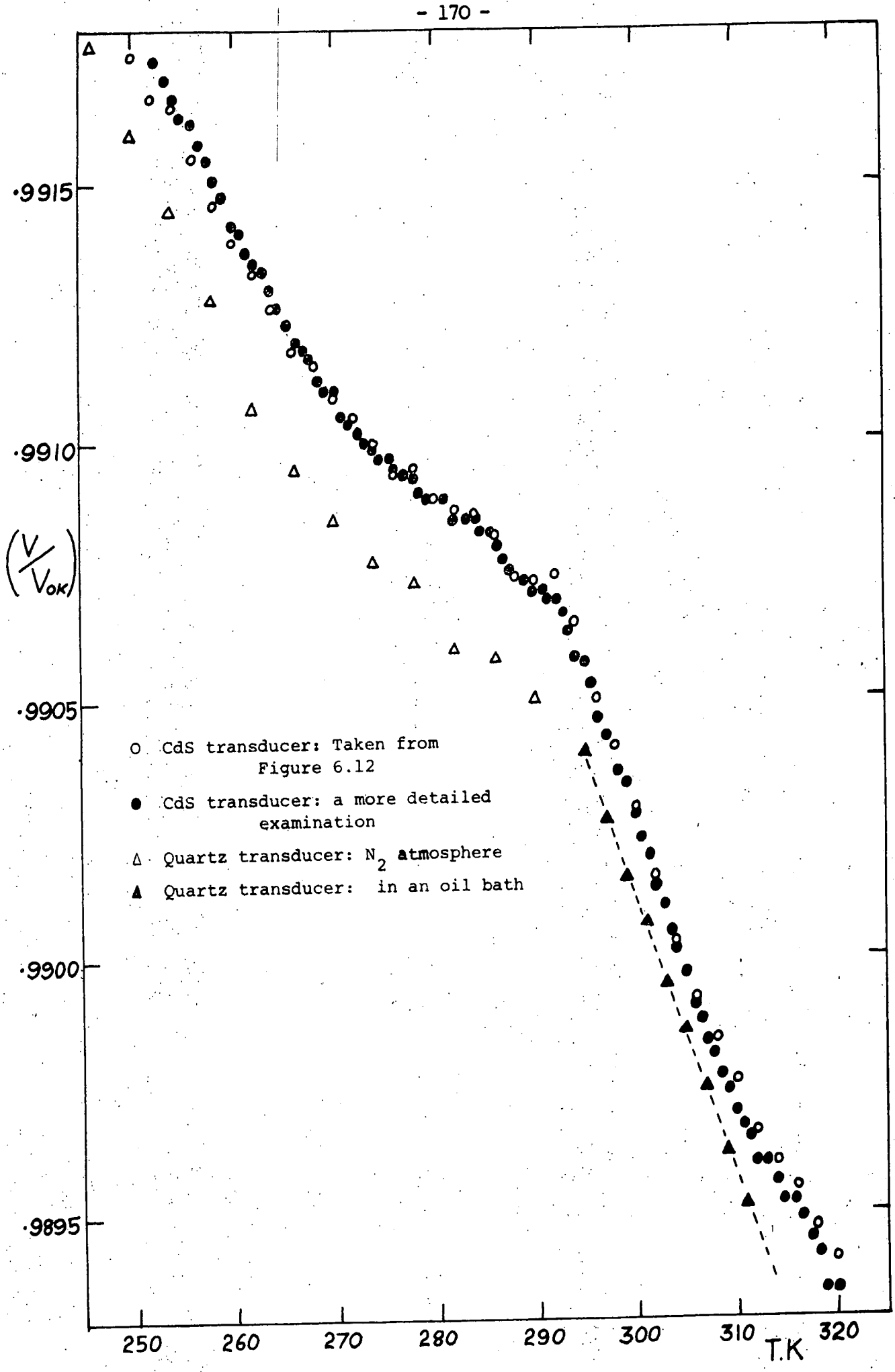

The high temperature anomaly in the [111] longitudinal mode velocity in GaAs

FIGURE 6.13

CHAPTER 7

"THE ELASTIC CONSTANTS OF MERCURY TELLURIDE"

The elastic constants of mercury telluride have previously been calculated at room temperature by Mavroides and Kolesar (1964), at temperatures down to 4.2 K by Alper and Saunders (1967) and at temperatures down to 77 K by Rusakov (1971).

Accurate knowledge of the elastic constant temperature dependence is necessary for the testing of Lakkad's (1971) elastic constant model and for the evaluation of the piezoelectric stiffening of mercury telluride, observed and measured in this work. In view of the diagreement between the data of Alper and Saunders (1967) and Rusakov (1971), and the lack of measurements below 77 K in the case of the latter, remeasurement and comparison has been made in the temperature range 2 K to 320 K. The "zero-field" elastic constants were calculated from pulse-superposition measurements of the velocities of the non-piezoelectric [100] longitudinal and shear, and [110] shear [1$\bar{1}$0] polarisation ultrasonic (50 MHz) wave modes. A piezoelectric

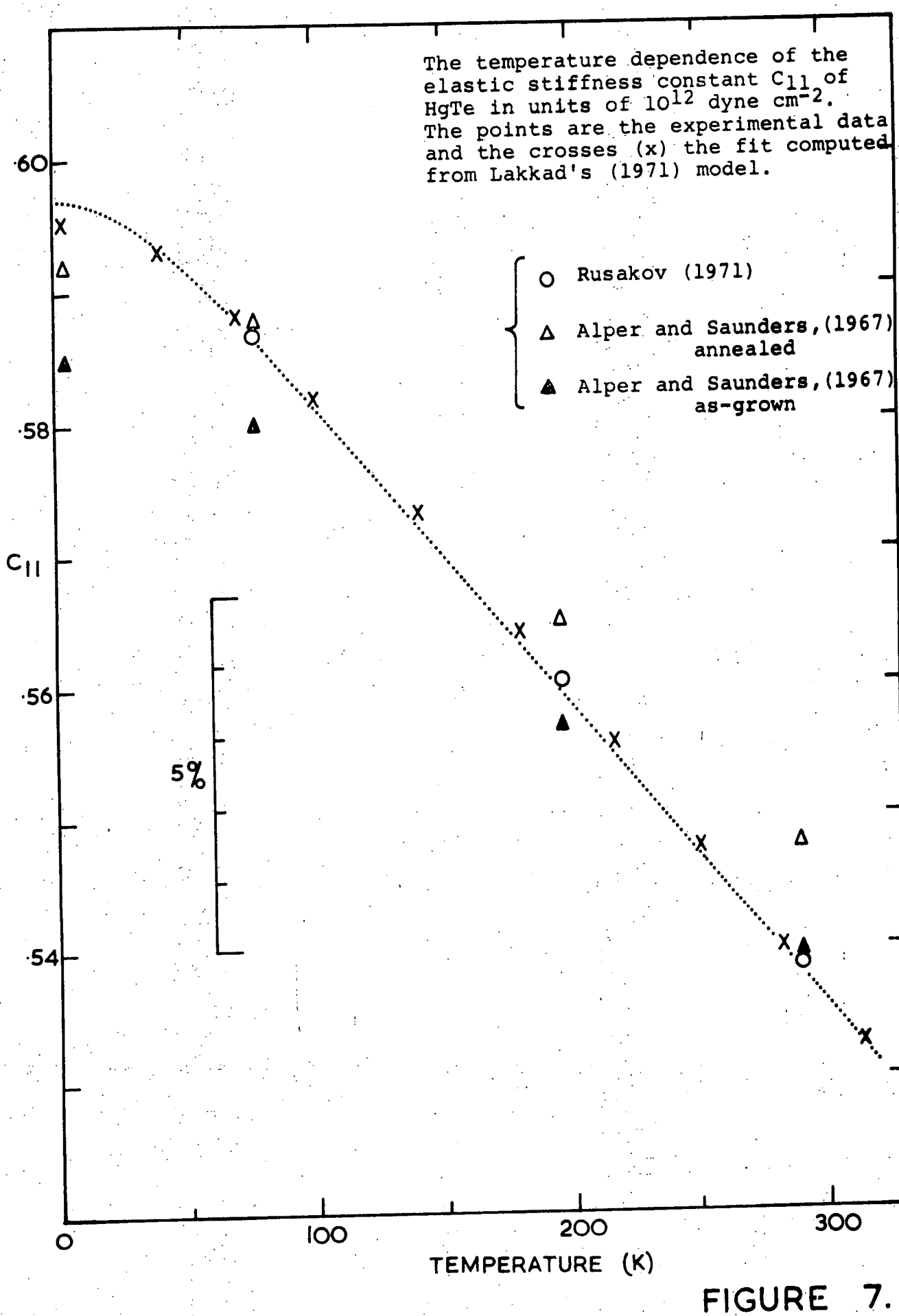
The temperature dependence of the elastic stiffness constant C_{11} of HgTe in units of 10^{12} dyne cm^{-2}. The points are the experimental data and the crosses (x) the fit computed from Lakkad's (1971) model.
Rusakov (1971)
Alper and Saunders, (1967) annealed
Alper and Saunders, (1967) as-grown
.60
.58
.56
.54
C_{11}
5%
0
100
200
300
TEMPERATURE (K)

FIGURE 7.1

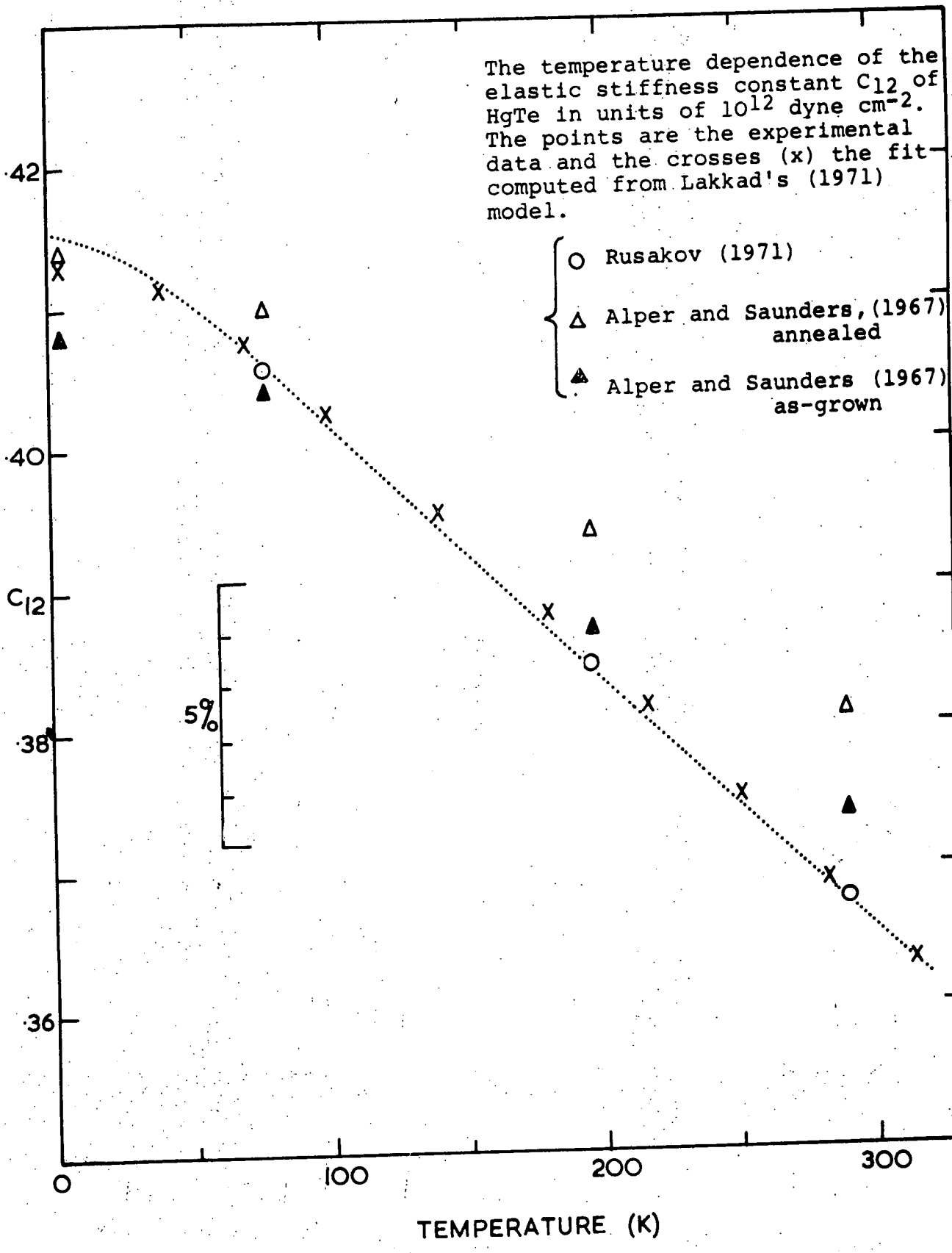
The temperature dependence of the elastic stiffness constant C_{12} of HgTe in units of 10^{12} dyne cm^{-2}. The points are the experimental data and the crosses (x) the fit computed from Lakkad's (1971) model.
Rusakov (1971)
Alper and Saunders, (1967) annealed
Alper and Saunders (1967) as-grown
.42
.40
.38
.36
C_{12}
5%
0
100
200
300
TEMPERATURE (K)

FIGURE 7.2

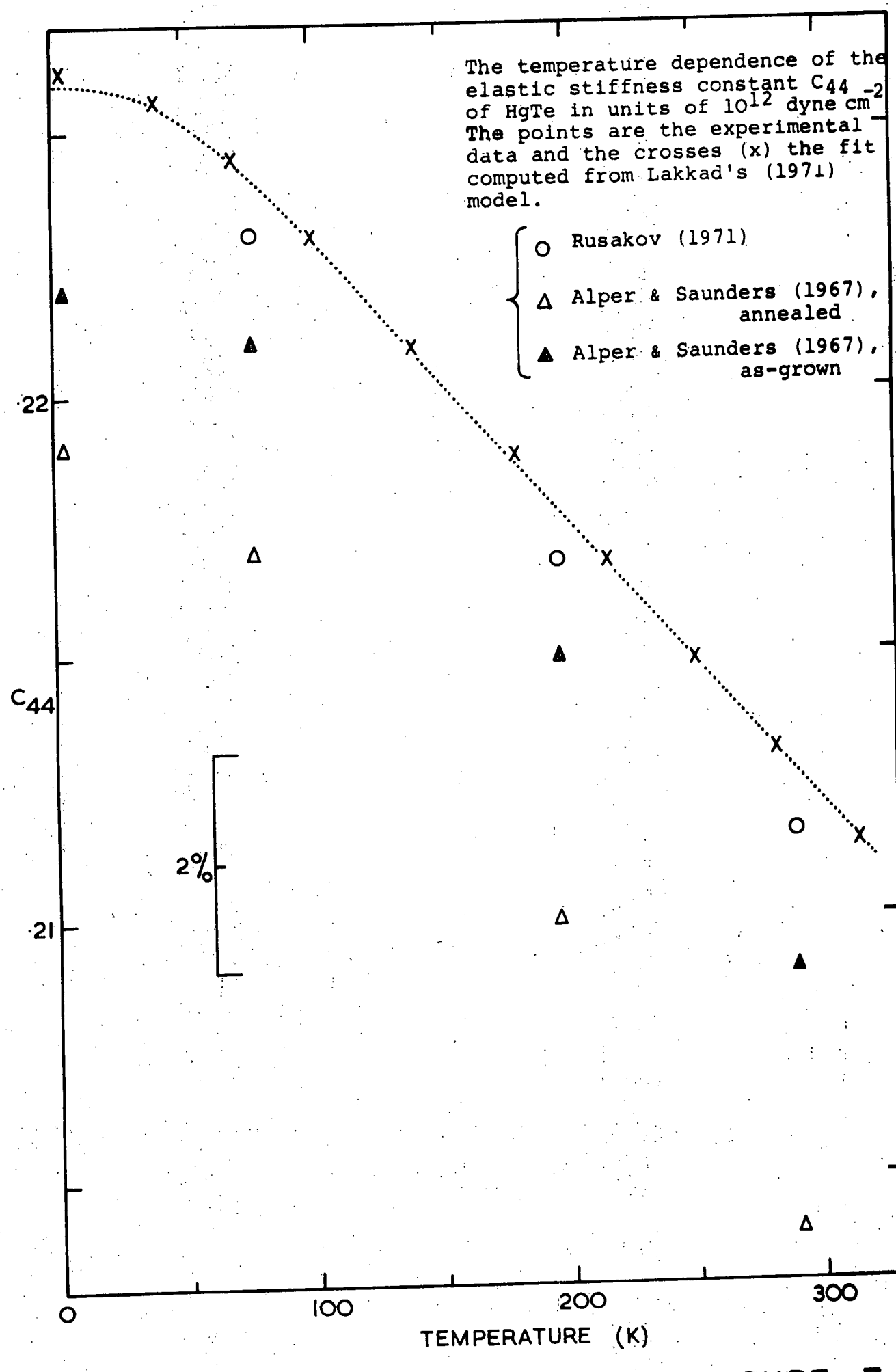
The temperature dependence of the elastic stiffness constant C_{44} in units of 10^{12} dyne cm^{-2}. The points are the experimental data and the crosses (x) the fit computed from Lakkad's (1971) model.
Rusakov (1971)
Alper & Saunders (1967), annealed
Alper & Saunders (1967), as-grown
·22
·21
C_{44}
2%
0
100
200
300
TEMPERATURE (K)

FIGURE 7.3

stiffening has been observed in the propagation of the [111] longitudinal wave mode.

7.1 RESULTS AND UNCERTAINTIES

The elastic stiffness constants C_{11}, C_{12} and C_{44} of annealed mercury telluride, calculated as for gallium arsenide (Section 6.1) are presented as a function of temperature in Figures 7.1, 7.2 and 7.3; data smoothing has been avoided. Numerical values at O K, found by extrapolation from 2K, at 78 K and 298 K are compared in Table 7.A with the values found by Alper and Saunders (1967) and Rusakov (1971). (The latter two sets of values have been corrected slightly from 77 K and 290 K to the temperatures quoted for this work). Rusakov (1971) found differences between the elastic constants of annealed and unannealed HgTe (0.7% for C_{44}), but his quotation of a single set of results does not state whether they are for annealed or unannealed material.

The derived elastic parameters listed in Table 7.B have been calculated assuming the absence of piezoelectric effects. The X-ray density of 8.079 $g.cm^{-3}$ found by Alper (1968) has been employed, together with the quoted uncertainty in displacement-measured density (± 0.01 $g.cm^{-3}$). The thermal expansion data of Novikova and Abrikosov (1963) is more consistent with that of other zinc-blende crystals than are other available data: this has been utilised; below 30 K a linear approximation has been made, the resultant uncertainty being negligible (Figure 7.4). The relative uncertainty in the elastic constant temperature

TABLE 7.A

The elastic constants of HgTe at O K, 78 K and 298 K; comparison with the work of Saunders and Alper (1967), Rusakov (1971) and Mavroides and Kolesar (1964). C_{ij} are in units of ($x10^{12}$ dyn.cm^{-2}).

Parameter	T K	This work C_{ij}	Alper and Saunders (1967) C_{ij}	%age diff. from this work	Rusakov (1971) C_{ij}	%age diff. from this work	Mavroides and Kolesar (1964) C_{ij}	%age diff. from this work
C_{11}	O	0.5971 ±.0026	0.592	0.9	-	-	-	-
	78	0.5863 ±.0025	0.587	0.1	0.5864	0.02	-	-
	298	0.5361 ±.0023	0.563	1.8	0.5366	0.09	0.505	5.8
C_{12}	O	0.4154 ±.0033	0.414	0.3	-	-	-	-
	78	0.4059 ±.0032	0.410	1.0	0.4054	0.12	-	-
	298	0.3660 ±.0030	0.379	3.7	0.3661	0.03	0.358	2.2
C_{44}	O	0.2259 ±.0010	0.219	3.1	-	-	-	-
	78	0.2241 ±.0010	0.217	3.2	0.2230	0.49	-	-
	298	0.2123 ±.0009	0.203	4.1	0.2111	0.56	0.205	3.4

TABLE 7.B

A compilation of the elastic parameters of HgTe at 0 K (extrapolated), 78 K and 298 K:
C_{ij} in units of ($x10^{12}$ dyn.cm^{-2}), V[ijk] in units of ($x10^{5}$ cm.sec^{-1}), $(-\partial C_{ij}/\partial T)(1/C_{ij})$ in units of ($x10^{-4}$ K^{-1}).

Parameter	0 K	78 K	298 K
C_{11}/C_{12}	1.437±.018	1.444±.018	1.465±.018
C_{12}/C_{44}	1.839±.023	1.811±.023	1.724±.022
C_{11}/C_{44} *	2.643±.024	2.616±.023	2.525±.022
V[100]L *	2.716±.004	2.691±.004	2.576±.004
V[100]S *	1.670±.003	1.663±.003	1.621±.003
V[110]L †	3.007±.010	2.982±.010	2.866±.009
V[110]S[001] †	1.670±.005	1.663±.005	1.621±.004
V[110]S[1$\bar{1}$0] *	1.059±.002	1.055±.002	1.026±.002
V[111]L †	3.089±.011	3.073±.011	2.956±.010
V[111]S †	1.295±.012	1.290±.011	1.256±.011
$B=\frac{1}{3}(C_{11}+2C_{12})$	0.476±.003	0.466±.003	0.423±.003
$G_V=\frac{1}{5}(C_{11}-C_{12}+3C_{44})$	0.172±.002	0.171±.002	0.161±.002
$G_R=\frac{5(C_{11}-C_{12})C_{44}}{4C_{44}+3(C_{11}-C_{12})}$	0.142±.007	0.141±.007	0.133±.006
$A=\frac{2C_{44}}{(C_{11}-C_{12})}$	2.487±.094	2.484±.093	2.496±.091
$-\frac{\partial C_{11}}{\partial T}\cdot\frac{1}{C_{11}}$	-	3.52 ±.17	4.66 ±.14
$-\frac{\partial C_{12}}{\partial T}\cdot\frac{1}{C_{12}}$	-	4.28 ±.21	5.19 ±.16
$-\frac{\partial C_{44}}{\partial T}\cdot\frac{1}{C_{44}}$	-	2.26 ±.11	2.41 ±.07
Born criterion $(C_{11}-C_{12})$	0.182 .006	0.180±.006	0.170±.005
Born criterion $\frac{1}{2}(C_{11}+2C_{12})$	0.715 .005	0.700±.004	0.635±.004

* Measured velocity

† Calculated velocity, assuming the absence of piezoelectric effects.

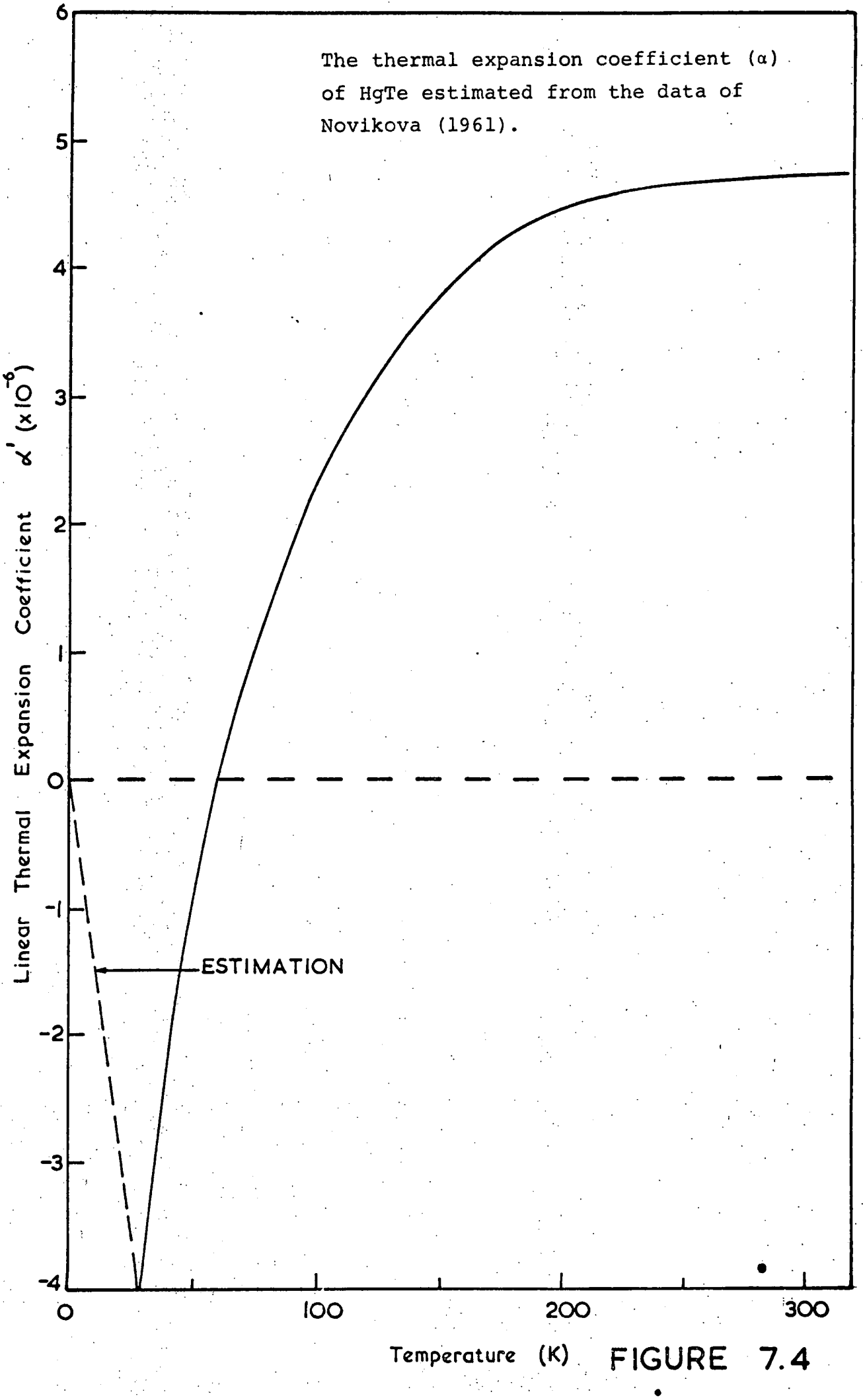
The thermal expansion coefficient (α) of HgTe estimated from the data of Novikova (1961).
Linear Thermal Expansion Coefficient α' (x10⁻⁶)
6
5
4
3
2
1
0
-1
-2
-3
-4
ESTIMATION
0
100
200
300
Temperature (K)

FIGURE 7.4

dependences is 0.02% for C_{11} and C_{44} and 0.04% for C_{12}. Error sources are listed in Table 7.C.

Agreement of the present results with those of Rusakov (1971) above 77 K is excellent. The results of Alper and Saunders (1967) agree to within the experimental uncertainty of the less accurate simple pulse-echo technique. The widest spread in values is for C_{44} (Figure 7.3), where Rusakov (1971) found the greatest change with annealing; it is possible that the annealing technique used by all the workers here quoted does not give such consistent results as previously assumed (Dahake, 1967) (see Section 3.3(b)). The temperature dependences found by Rusakov (1971) and in this work agree to within the relative experimental uncertainties; they may be used with confidence in evaluation of the piezoelectric stiffening of HgTe.

7.2 THE DEBYE TEMPERATURE AND ELASTIC CONSTANT TEMPERATURE DEPENDENCE

The Debye temperature ($\theta_o^{elastic}$) has been calculated from the elastic constant data extrapolated to 0 K (Table 7.A), using de Launay's (1956, 1959) graphical procedure (see Section 6.3). The resultant value of 141.4 K is only slightly different from that (141 K) calculated by Alper and Saunders (1967); at present no low temperature specific heat data are available for comparison.

Lakkad's (1971) model for the elastic constant temperature dependence (see Section 6.4) has been fitted

TABLE 7.C

Uncertainty limits required in the determination of those for C_{11}, C_{12}, C_{44} : in percentages.

	0 K, 78 K	298 K
ρ	-	±0.12
m	± .01	±0.00
L_R[100]L,S	-	±0.03
L_R[110]S	-	±0.03
f_{CO}[100]L	±0.005	±0.005
f_{CO}[100]S	±0.008	±0.008
f_{CO}[110]S	±0.007	±0.007
f_x*	±0.10	±0.10
V_{orient}	± .02	± .02

* Uncertainty in f_x is quoted as a percentage of f_{CO} and includes the uncertainty due to phase integration at the transducer.

to the elastic data shown in Figures 7.1, 7.2, 7.3; the constant K has first been found for each of C_{11}, C_{12}, C_{44} from the elastic constants at 0.5 $\theta_o^{elastic}$ and $2\theta_o^{elastic}$. In contrast to the fit obtained for the similarly zinc-blende gallium arsenide, different values of K are required to match each of the temperature dependences: K is found to be 0.056, 0.064 and 0.035 for C_{11}, C_{12} and C_{44} respectively. Deviation of the model from the experimental data has been calculated in terms of the Debye temperature θ_D (Figure 7.5) in the same way as for gallium arsenide (see Section 6.5). It is not possible to compare the fit directly with that of the Debye model to the specific heat of HgTe owing to the lack of relevant data in the literature.

The values of the elastic constant slopes at room temperature $(\partial C_{ij}/\partial T)x(1/C_{ij})$ (see Table 7.B) are similar to those found for mercury selenide (Lehoczky et al, 1969) of 5.38×10^{-4}, 6.40×10^{-4} and 3.03×10^{-4} K^{-1} for C_{11}, C_{12} and C_{44} respectively. The ratios of the slopes of $C_{11}:C_{12}:C_{44}$ are even more closely related; 1.93:2.15:1 for HgTe and 1.77:2.11:1 for HgSe. The directional dependence of the anharmonic to harmonic force constant ratio (C_1/C in Lakkad's expression for K) should be similar in the two compounds. Figure 7.6 shows the Grüneisen parameter.

7.3 CRYSTAL BINDING AND IONICITY

Vetelino and Mitra (1969) have presented an invariance relation for the application of a rigid ion model to zinc-blende crystals:

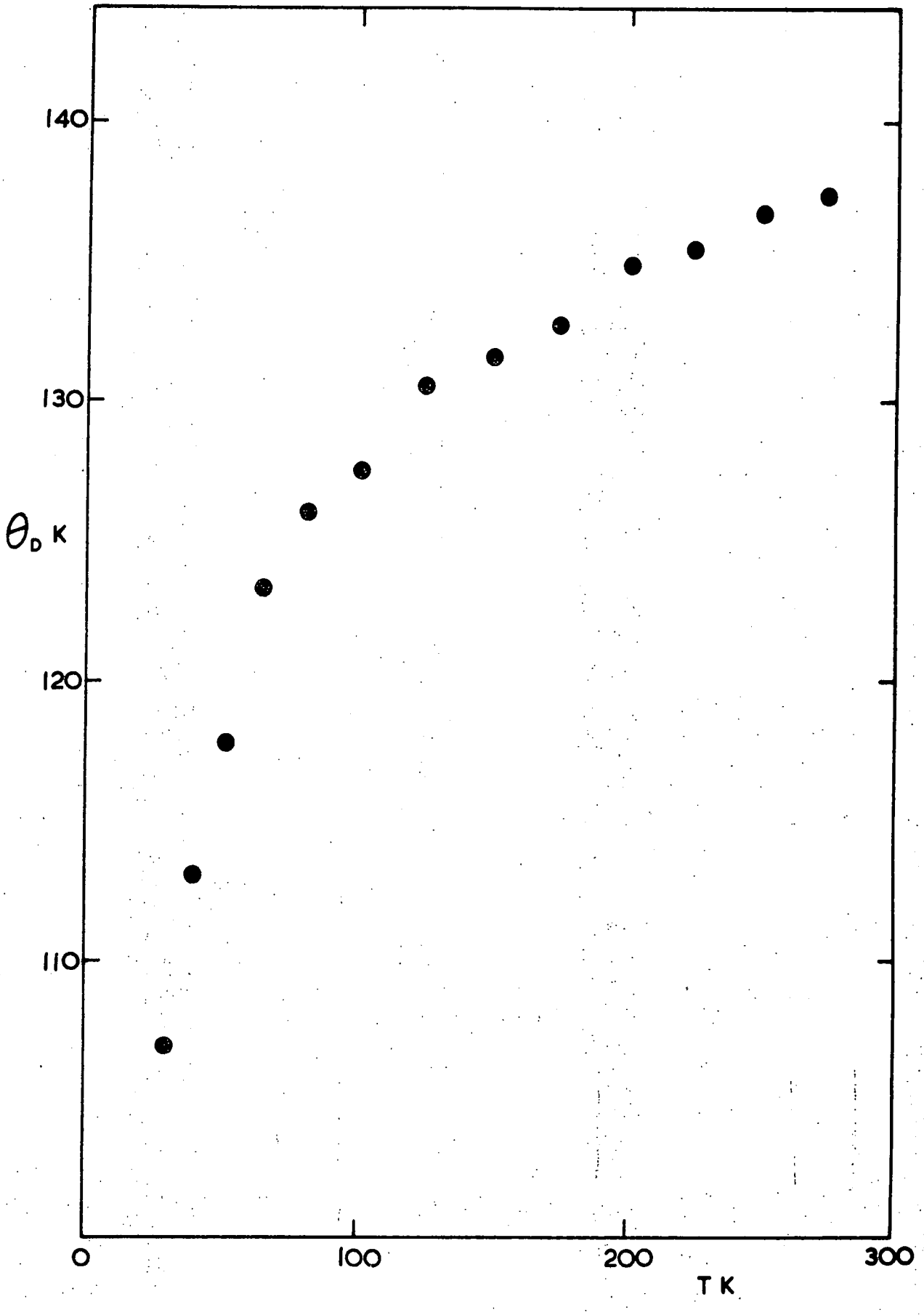

The Debye temperature θ_D of HgTe calculated from Lakkad's fit to the elastic constant data (●, C_{11} this work).

FIGURE 7.5

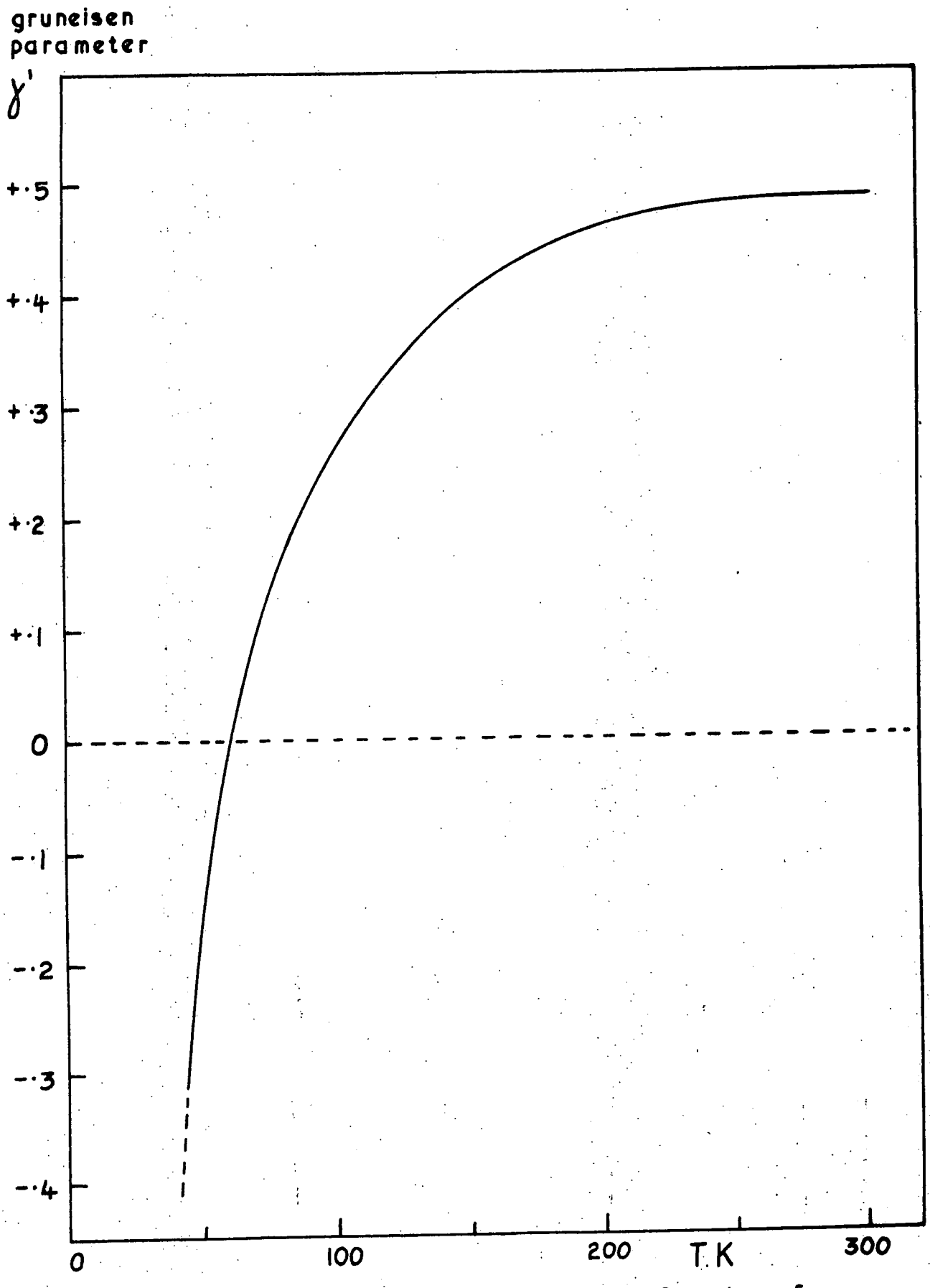

The Grüneisen parameter of GaAs as a function of temperature, calculated from the thermal conductivity data of Whitsett and Nelson (1973).

FIGURE 7.6

$$I_o \equiv \frac{\omega_{TO}^2}{2r_{o\mu}'} \left[\frac{-C_{44}+(C_{11}/2)+(0.01082/\mu' r_o)(\omega_{LO}^2+4.77865\omega_{TO}^2)}{[(C_{11}/2)-C_{12}+(0.02775/\mu' r_o)(\omega_{LO}^2-7.75667\omega_{TO}^2)]^2} \right] = 1 \quad (7.1)$$

where ω_{LO}, ω_{TO} are the zone centre frequencies, r_o is half the zinc-blende lattice constant, and μ' is the reciprocal of the reduced mass

$$\mu' = \frac{1}{m_1} + \frac{1}{m_2} \quad (7.2)$$

where m_1, m_2 are the masses of the two atom types in the crystal. Using the optical data of Dickey and Mavroides (1964) for the zone centre frequencies, and the Lyddane-Sachs-Teller rule $\omega_{TO}^2 = \omega_{LO}^2 (\zeta_\infty/\zeta_o)$, we find that $I_o = 0.934$ for HgTe at 298 K. The Born invariance relation

$$I_B \equiv \frac{4C_{11}(C_{11}-C_{44})}{(C_{11}+C_{12})^2} = 1 \quad (7.2)$$

yields a value of $I_B = 0.85$: the rigid ion model is a substantially better approximation for HgTe.

The effective ionic charge calculated from the equations of Vetelino and Mitra (1969) is ±0.78 e, compared with ±0.63 e derived from the Szigeti relation (Rusakov, 1971). The nearest neighbour radial (α) and non-central (β) force constants and the next-nearest neighbour radial force constant (μ) for the rigid ion model of HgTe are 1.738×10^4, 1.908×10^4 and 0.209×10^4 dyn. cm^{-1} respectively; the corresponding constants for the Born model are $\alpha = 3.44\times10^4$ and $\beta = 2.89\times10^4$ dyn. cm^{-1}.

7.4 YOUNG'S MODULUS AND VELOCITY SURFACES

(001) and (110) cross-sections of the Young's modulus surface of mercury telluride calculated in the same

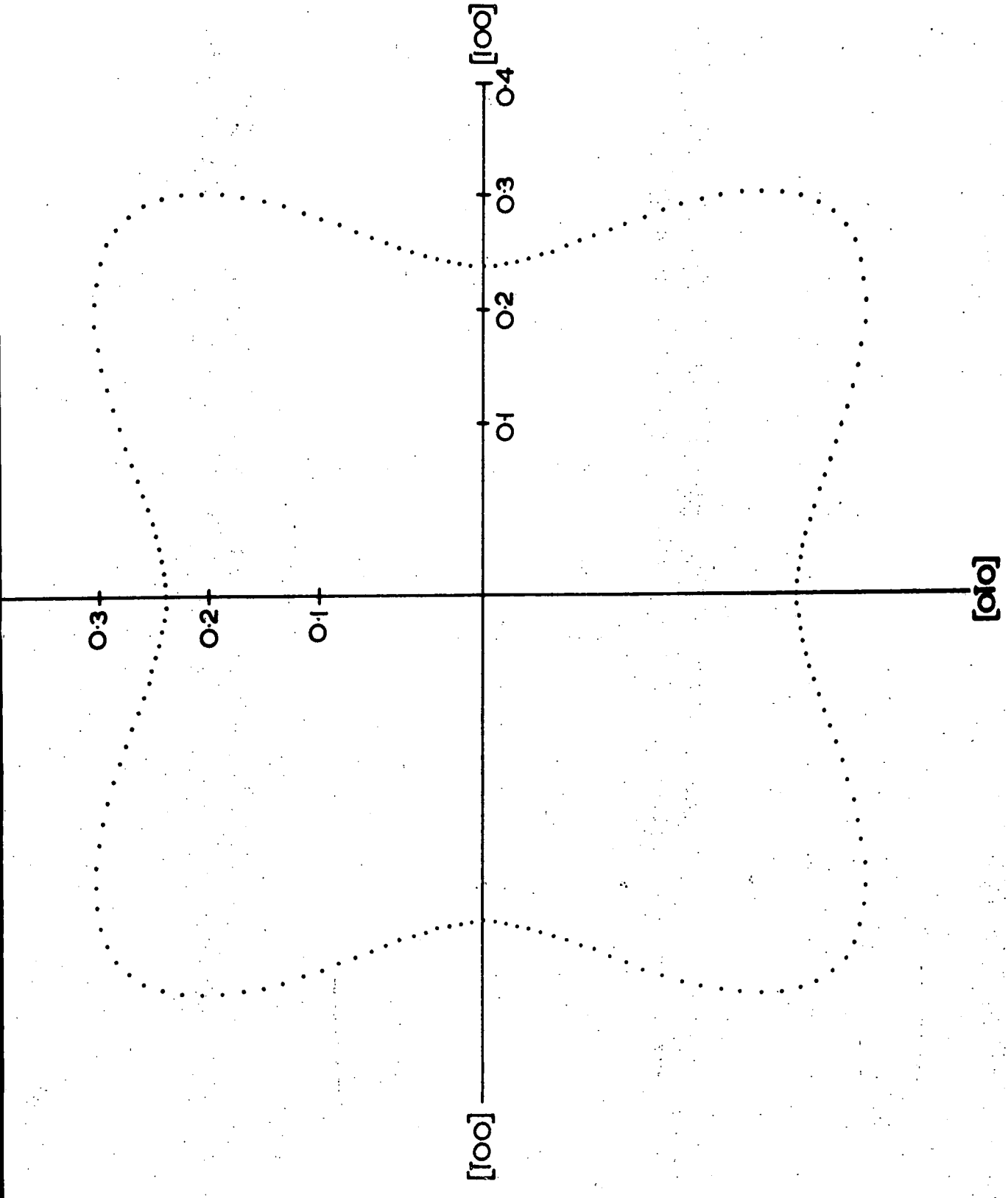

The (001) cross-section of the Young's modulus surface of HgTe. Units : 10^{12} dyne cm^{-2}.

FIGURE 7.7a

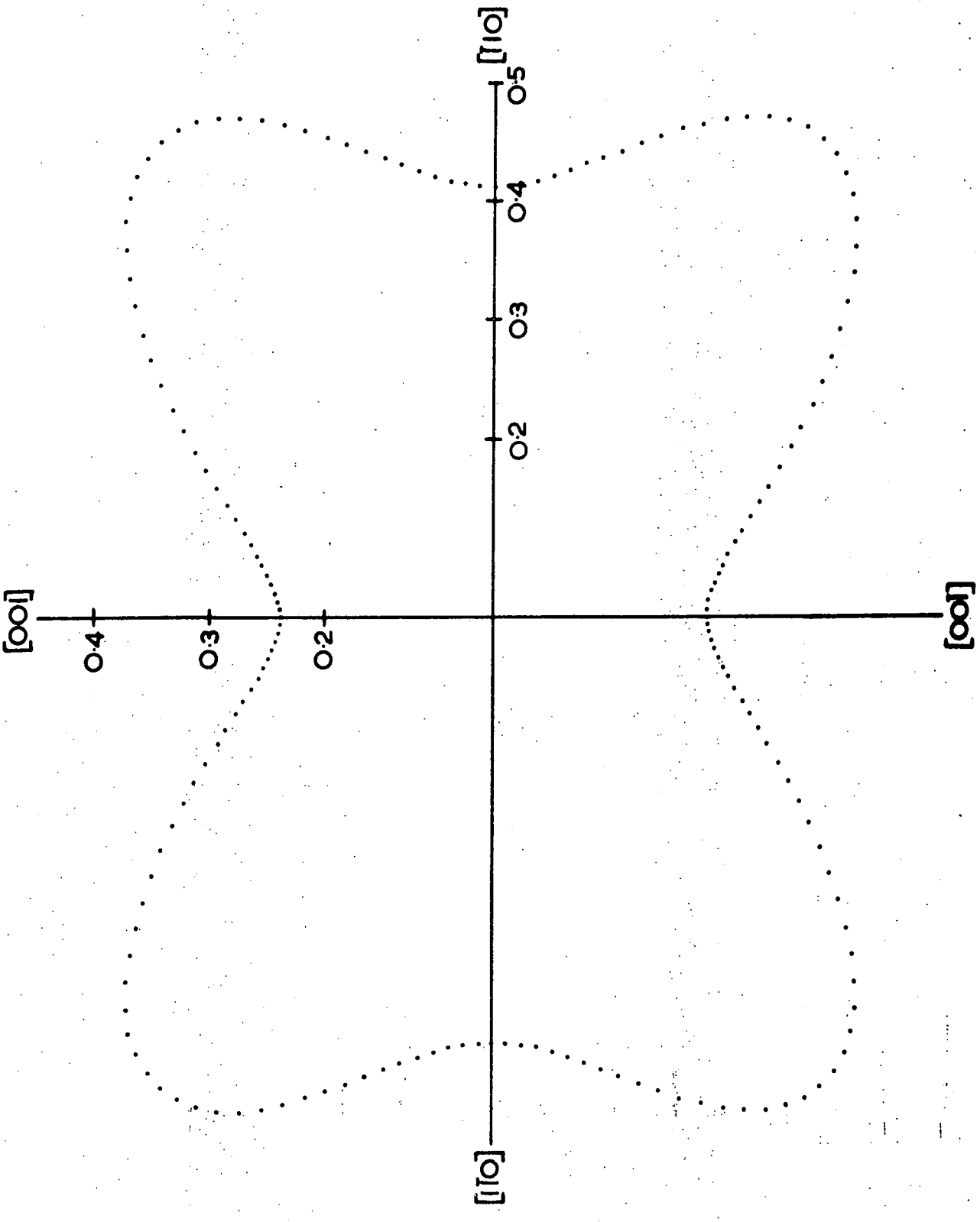

The (110) cross-section of the Young's modulus surface of HgTe.

FIGURE 7.7b

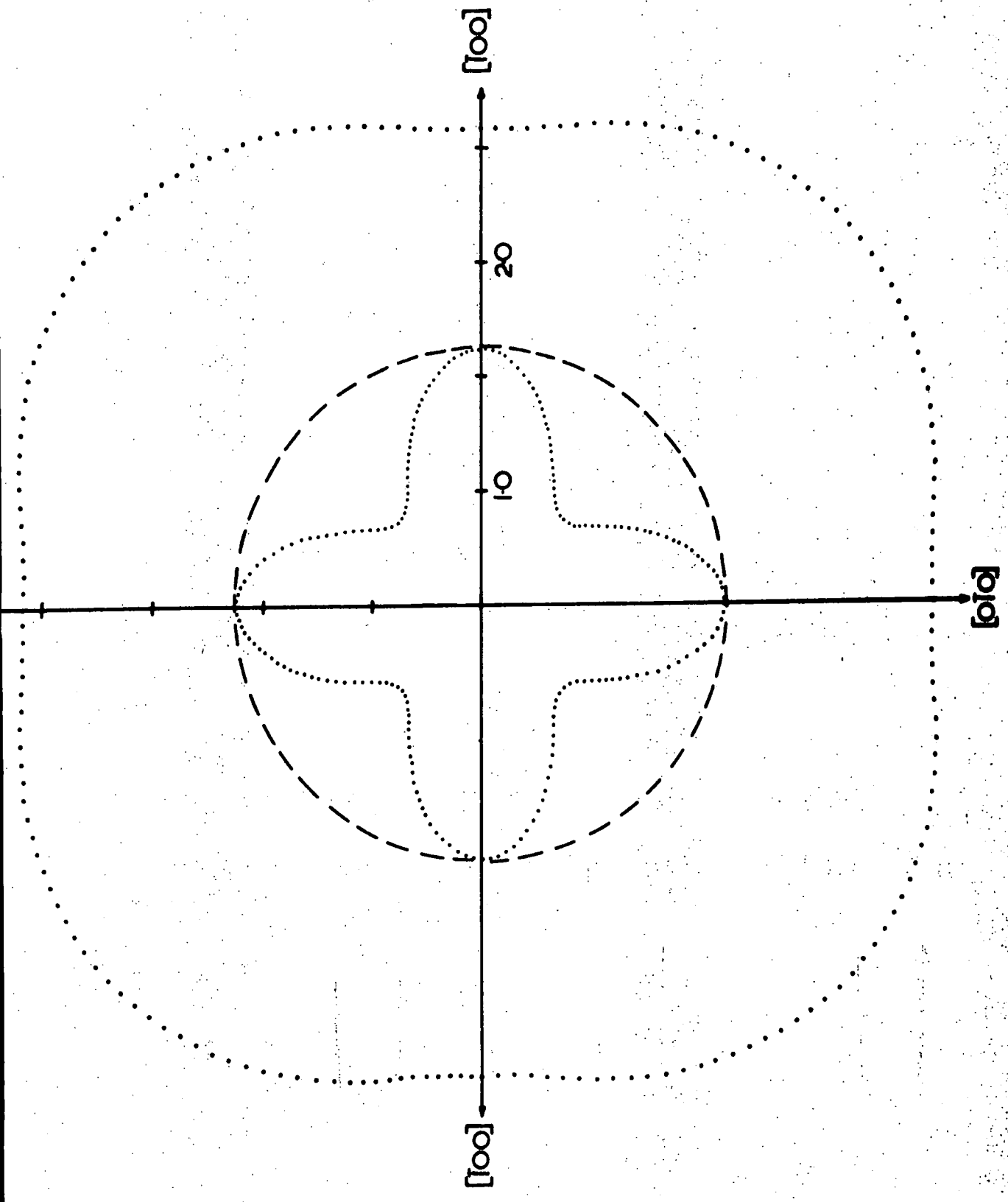

The (001) cross-section of the velocity surface of HgTe. Units: 10^5 cm sec^{-1}. The dashed line refers to the pure shear which can be propagated at any direction in the (001) plane.

FIGURE 7.8a

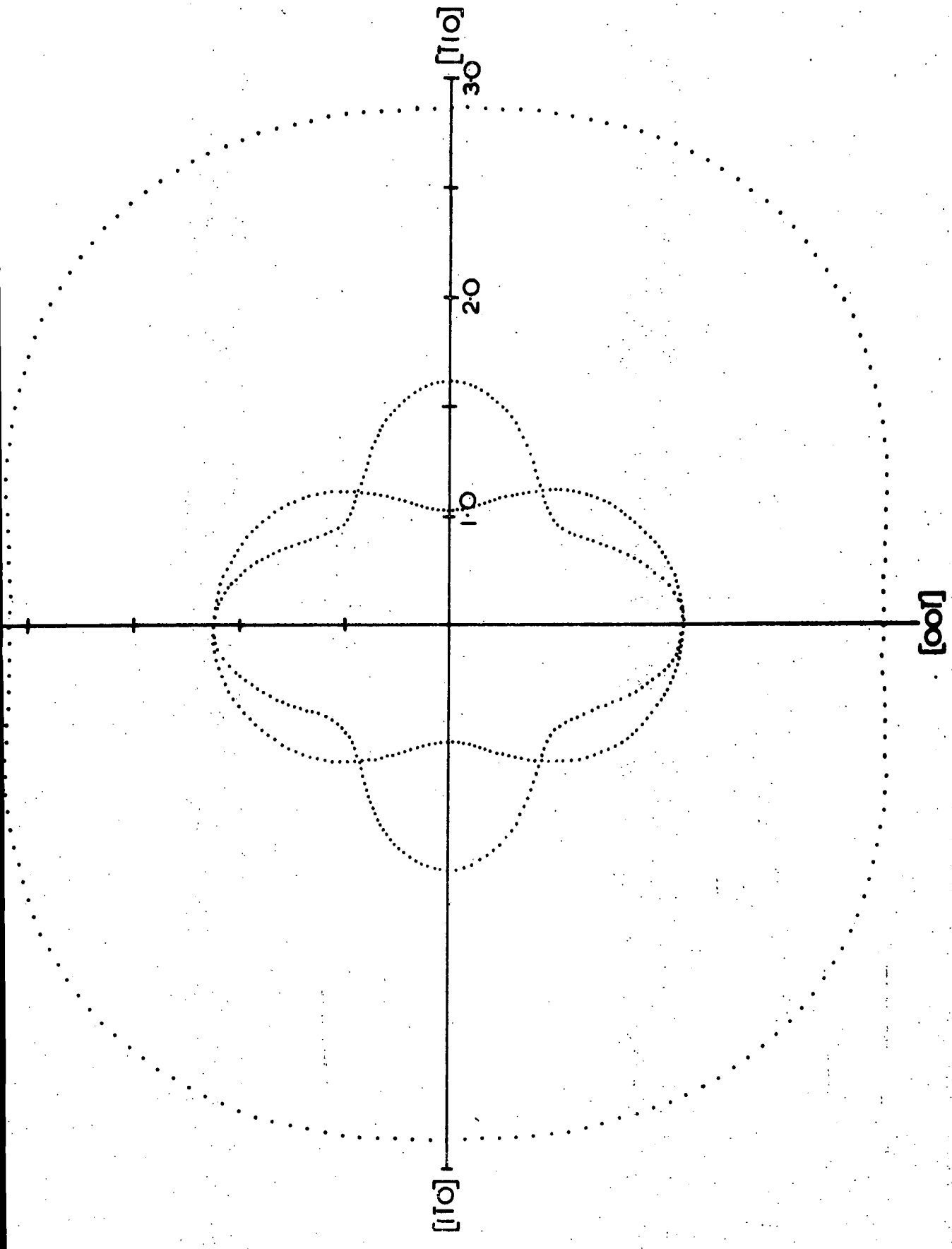

The (110) cross-section of the velocity surface of HgTe. Units: 10^5 cm sec^{-1}.

FIGURE 7.8b

The deviations from propagation directions in the (001) plane of the particle displacement vector (——) of the quasi-longitudinal wave and the energy flux vectors of the quasi-longitudinal (·····) and the quasi-shear (-·-·-·-·) waves.

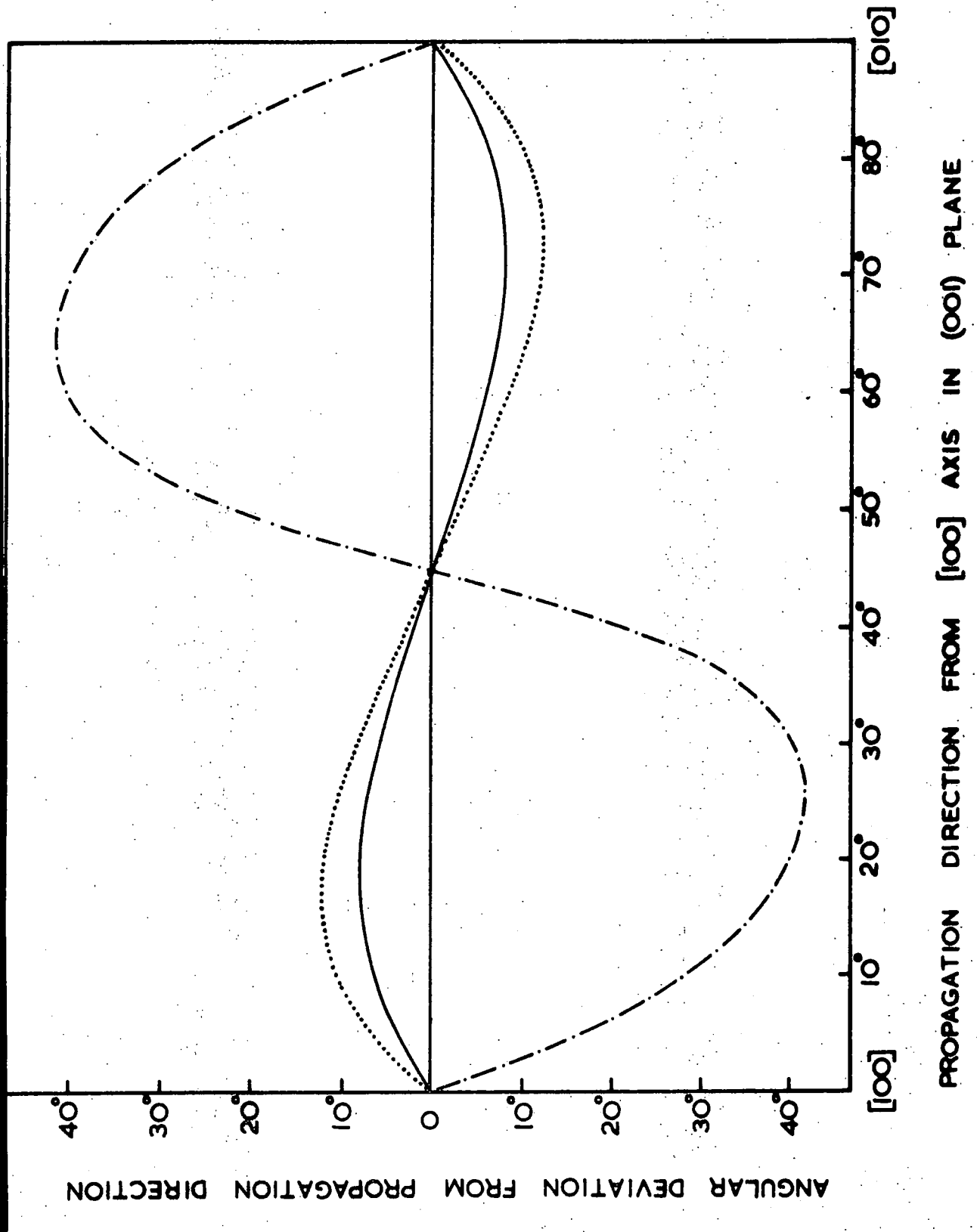

FIGURE 7.9

manner as for gallium arsenide (see Section 6.7) are shown in Figure 7.7. Cross-sections of the velocity surfaces have been calculated (Figure 7.8), and Figure (7.9) shows the polarisation vector for the quasi-longitudinal mode in the (001) plane and the angular dependences of the energy flux vector for the quasi-longitudinal and quasi-shear modes; the energy flux vector of the pure shear mode in the (100) plane is always parallel to the propagation direction. The Young's modulus and velocity surface sections for HgTe (Figures 7.7, 7.8) exhibit a greater anisotropy than do those for GaAs (Figures 6.9, 6.10). This reflects the greater elastic anisotropy of mercury telluride

$$A = \frac{2C_{44}}{(C_{11} - C_{12})} \qquad (7.3)$$

of 2.50 at room temperature, compared with a value for gallium arsenide of 1.83.

7.5 PIEZOELECTRIC CONTRIBUTION TO THE STIFFNESS OF HgTe

Figure 7.10 shows the calculated and measured temperature dependences of the 50 MHz [111] longitudinal mode velocity in HgTe. An anomaly similar to that found for GaAs is apparent (see Section 6.8). The Hutson and White (1962) theory predicts that the stiffening should be inversely proportional to the electrical conductivity. Measurements of the conductivity temperature dependence (Figure 7.11) confirm this dependence: the maximum stiffening occurs where the conductivity is lowest (at about 100 K).

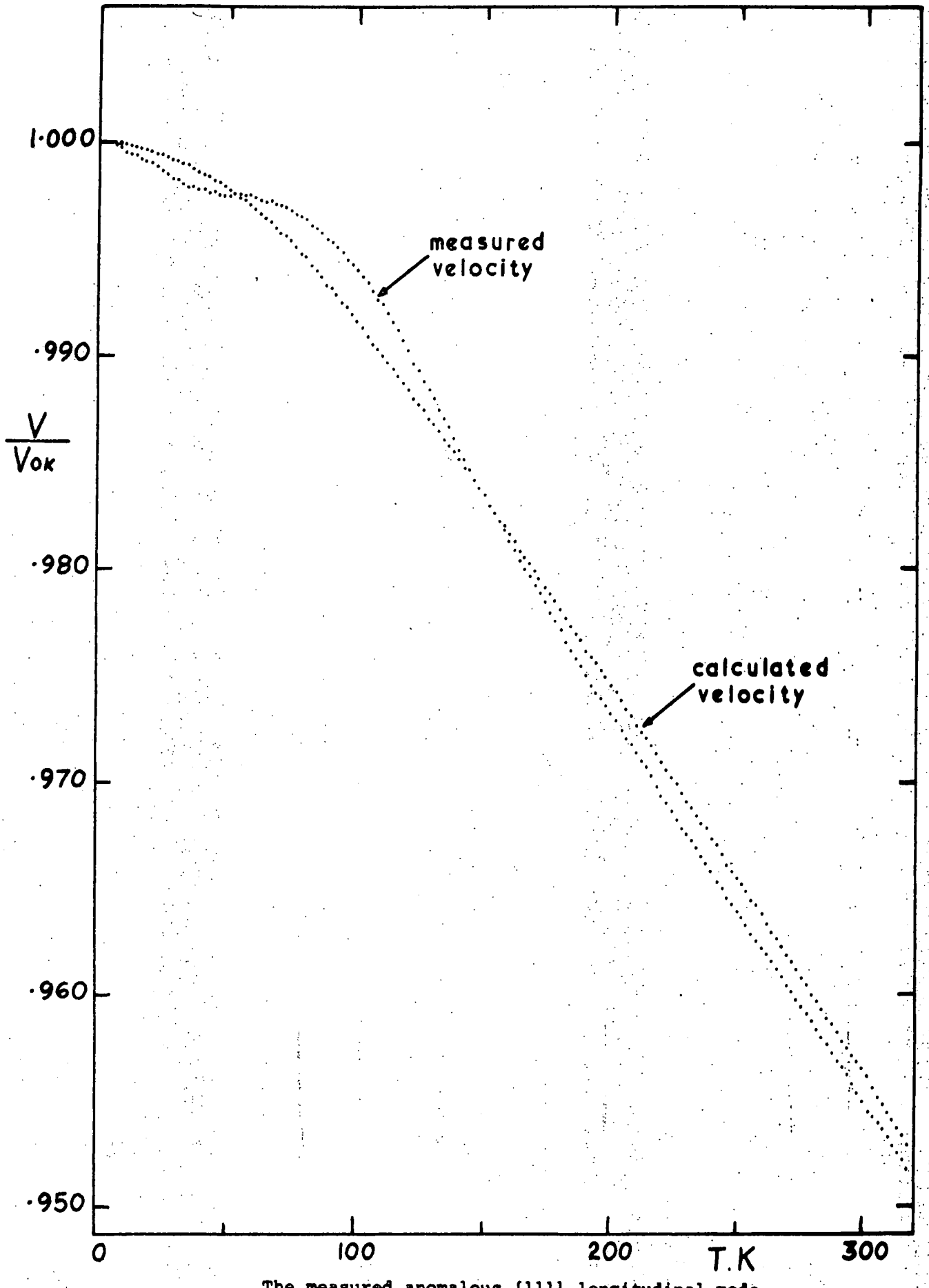

The measured anomalous [111] longitudinal mode velocity in HgTe normalised to the calculated curve at O K.

FIGURE 7.10

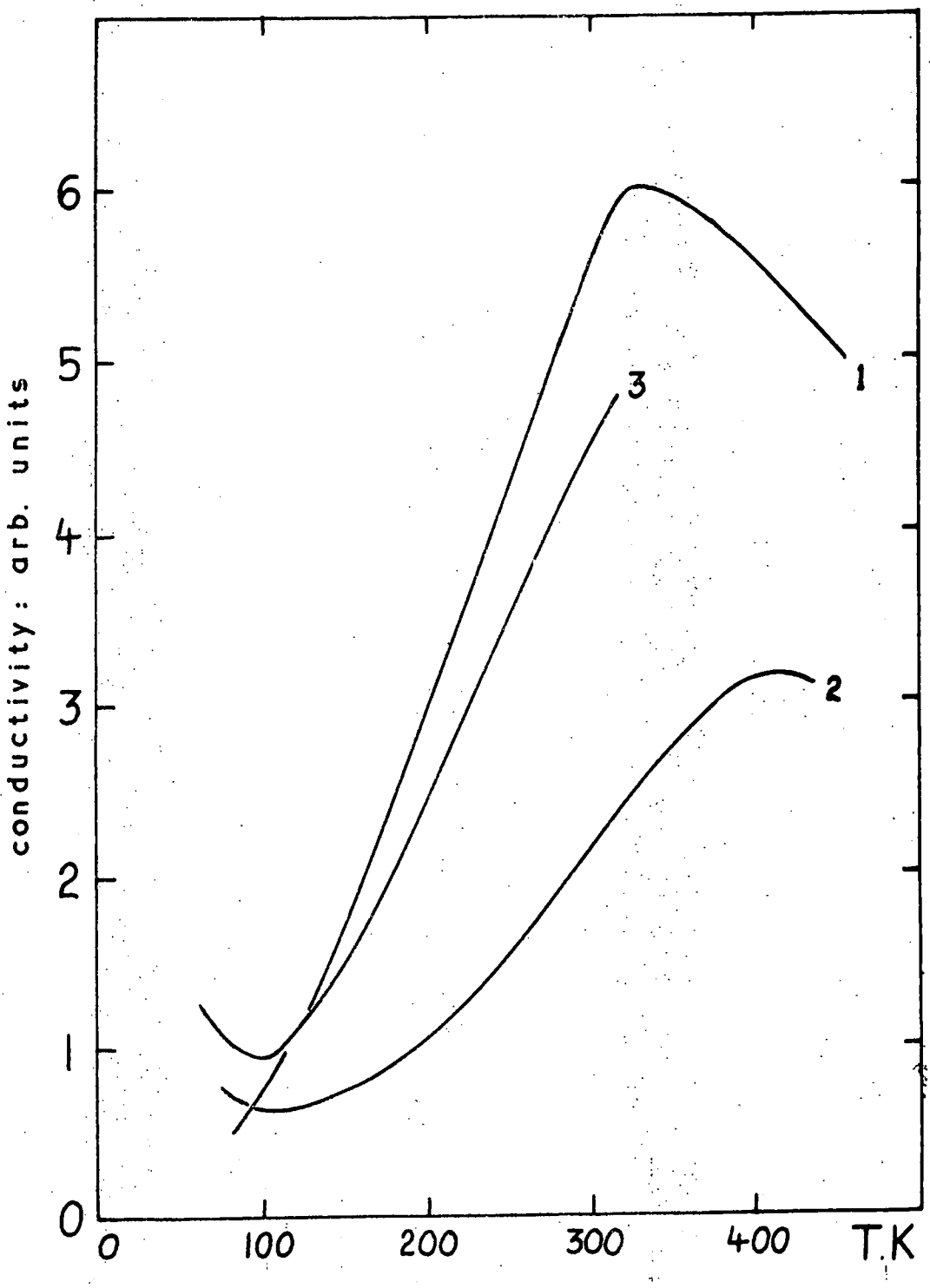

The electrical conductivity of HgTe:

1. Dahake (1967); annealed 100 hours at 300°C
2. Dahake (1967); annealed 250 hours at 300°C
3. This work; annealed 100 hours at 300°C

FIGURE 7.11

CHAPTER 8

ULTRASONIC ATTENUATION IN GALLIUM ARSENIDE

Ultrasonic waves in solids may suffer losses through a variety of mechanisms which can be divided into 'intrinsic' interactions with various excitations (thermal phonons, free electrons, etc.) and 'extrinsic' interactions (with point defects, dislocations, etc.).

The attenuation of ultrasound in GaAs has been studied by a number of workers (Bobylev and Kravchenko, 1967a; Kovar and Hrivnak, 1969; Krasil'nikov et al, 1969; Bobylev and Kravchenko, 1970; King and Rosenberg, 1970; Ivanov et al, 1971) and the major loss mechanism has been found to be thermal phonon - ultrasonic phonon coupling. Qualitative agreement is good, but there is no uniformity in derived values of the parameters which characterise an exact quantitative fit to the experimental data.

At very low temperatures the thermal phonon lifetimes are large, satisfying the condition $\omega\tau >> 1$, where τ is the thermal phonon mean lifetime and ω the ultrasonic

frequency. The attenuation resulting from phonon-phonon coupling falls to negligible values at liquid helium temperatures as the phonon population is frozen out, leaving the residual defect and electronic attenuation. Theoretical evaluation of the phonon-phonon interaction process for $\omega\tau>>1$ was first carried out by Landau and Rumer (1937) for transverse ultrasonic waves, giving good qualitative agreement with experiment but calculated attenuations which are too small by a factor of the order of 20. Akhieser (1939) treated the attenuation for the case $\omega\tau<<1$ as a combination of heat flow losses and viscous damping, but neither this approach nor that of Landau and Rumer (1937) is applicable in the region $\omega\tau\approx1$. The first analysis to cover the complete range $\omega\tau\gtrless1$ with some degree of accuracy was that of Woodruff and Ehrenreich (1961) in terms of local modulation of the thermal phonon frequencies. Since this work numerous refinements of the treatment have been made (see, for example, Mason and Bateman, 1966; Lewis, 1968; Maris, 1969; Ozvold, 1970), but quantitative agreement is less satisfactory. In many cases after approximations necessary in application of the results have been made the expressions for attenuation reduce to those given by Woodruff and Ehrenreich (1961) (see, for example, Ozvold, 1969).

8.1 Woodruff and Ehrenreichs' Phonon-Phonon Attenuation Theory

Akhieser's (1939) calculation of the viscous damping contribution to sound absorption is based on the

modulation of the solid elastic constants by the ultrasonic wave. The consequent local phonon frequency distribution modulation relaxes towards the thermal equilibrium distribution by phonon-phonon interactions made possible by the anharmonic properties of the solid. The relaxation causes an entropy increase, and thus energy is removed from the sound wave. Woodruff and Ehrenreich (1961) extended this approach to include all field and time-dependent terms in the Boltzmann equation and included both normal (N-) and Umklapp (U-) collision processes.

The phonon system is perturbed locally by a small amount, characterised by a Hamiltonian H, and the distribution written simply for first order in sound amplitude. In the steady state two energy transfers must be considered; that from the driving wave to the thermal phonon assembly, and that from the thermal phonons to an external heat sink. The former transfer is covered by the Boltzmann transport equation, which is in this case

$$\left(\frac{\partial N}{\partial t}\right)_{\text{collision}} = \frac{\partial N}{\partial t} + \frac{1}{h}\left(\frac{\partial N}{\partial z}\frac{\partial H}{\partial q_z} - \frac{\partial N}{\partial q_z}\frac{\partial H}{\partial z}\right) \qquad (8.1)$$

where the distribution function N is the number of phonons of mode $\underline{q}$ at position $\underline{z}$ and time t, and h is Planck's constant. For the N-processes there is conservation of $\underline{q}$, but not for the U-processes, and consequently there will be two independent phonon distribution collision-relaxation times τ_N and τ_U. An explicit expression for the collision term $\frac{\partial N}{\partial t}_{\text{collision}}$ is obtained by substitution of the distribution functions (for thermal equilibrium at temperaure T, local perturbation at T, and relaxed thermal equilibrium

at temperature T' locally) and the relaxation times in equation (8.1), using as boundary conditions

(i) conservation of $\underline{q}$ for N-processes,

(ii) conservation of energy for N-processes (to first order). The total Boltzmann equation may now be solved for the perturbed phonon distribution function, which when inserted into the collision term gives two simultaneous equations for ΔT (= T'-T) and the amplitude of the phonon distribution modulation function in terms of a combined relaxation time τ:

$$\frac{1}{\tau} = \frac{1}{\tau_N} + \frac{1}{\tau_U} \tag{8.2}$$

The energy transfer Q from the thermal phonon assembly to an external heat sink may be written as

$$Q = -\sum_{\underline{q}} \left\langle H \left(\frac{\partial N}{\partial t}\right)_{coll} \right\rangle, \tag{8.3}$$

where $\langle\ \rangle$ indicates a time average. Substitution in equation 8.3 of the collision term and H derived from the phonon distribution modulation function gives a general expression for Q, and then the acoustic attenuation α is given by

$$\alpha = \frac{Q}{WV} \tag{8.4}$$

where the sound-wave energy density W is

$$W = \frac{\rho\omega^2 A^2}{2}, \tag{8.5}$$

V is the sound velocity, A the wave amplitude and ρ the density.

In order to apply the results of this evaluation to practical situations, certain approximations must first be made. The angular integrations necessary for the determination of Q may be performed analytically if the phonon equilibrium frequency distribution, the collision time constants τ_N and τ_U, and the Hamiltonian amplitude coefficient a are assumed independent of direction. Two further approximations are required: firstly an analytical expression for the phonon frequency distribution function - for which the Debye model is the most applicable - and secondly the independence of τ_N, τ_U and a of q. This independence is the most significant approximation in the analysis. In most solids there is considerable uncertainty regarding the exact values of τ_N and τ_U, but we may write $(\tau_N/\tau_U) >> 1$ and associate τ_U remaining with the thermal conductivity relaxation time τ. Finally, if the result is particularised to a description of compressional wave attenuation, the Hamiltonian amplitude coefficient may be written in terms of the Gruneisen parameter γ'. The expression for acoustic attenuation now becomes at higher temperatures.

$$\alpha = \frac{C_v T \gamma'^2 \omega^2 \tau}{3 \rho V_{sth}^3}, \quad (\omega\tau << 1), \tag{8.6}$$

which in terms of the thermal conductivity

$$\kappa = \frac{1}{3} C_v V_{sth}^2 \tau \tag{8.7}$$

may be written

$$\alpha = \frac{\gamma'^2 \omega^2 T \kappa}{\rho V_{sth}^5}, \quad (\omega\tau << 1), \tag{8.8}$$

and at low temperatures

$$\alpha = \frac{\pi \gamma'^2 \omega C_v T}{4 \rho V_{sth}^3}, \quad (\omega\tau >> 1), \tag{8.9}$$

where C_v is the specific heat at constant volume and V_{sth} is an average velocity of sound as a function of direction (the Debye velocity). The expression (8.9) has the same dependence on ω and T and independence of τ as that derived quantum - mechanically for $\omega\tau \gg 1$: the temperature shift term arising from ΔT is negligible in this limit.

In view of the approximations adopted in this approach, particularly in letting a single parameter γ' represent the sound wave coupling with the crystal, Woodruff and Ehrenreich (1961) obtained an excellent agreement between their theory and the measured attenuation in Quartz crystals. In particular they calculated the temperature dependence of attenuation using a single value for the Gruneisen parameter, whereas in most solids there is a temperature variation in γ'. Much attention has centred on the correct choice of γ' for use in the Woodruff and Ehrenreich (W-E) theory (see, for example, Lewis, 1968). In many materials the value of γ' required to give quantitative agreement with experimental data is found to be larger by a factor of about 2 than that derived from the Grüneisen relation itself, although there is usually some correlation between the temperature dependences of γ' from the W-E theory (γ'_{WE}) and the Grüneisen relation (γ'_G). In GaAs, for example, Bobylev and Kravchenko (1970) found that γ'_{WE} followed the temperature variation of γ'_G at

higher temperatures, but failed to become negative as does γ'_G below 40 K (see Figure 6.7). It is evident that if the W-E theory is taken to hold true, then the Grüneisen parameter average γ'_{WE} required is not the same average as that appearing in expressions for the thermal conductivity.

8.2 EXPERIMENTAL RESULTS

The ultrasonic attenuation in gallium arsenide has been measured by the pulse echo technique over the temperature range 4 K to 294 K for longitudinal waves propagating in the [111] and [110] directions at frequencies of 40, 80, 160 and 320 MHz: the results are shown in figures 8.1-8.8. Three main features appear in all of the attenuation temperature dependences:

(i) A residual attenuation at temperatures below about 15 K;

(ii) A rapid rise in attenuation above 20 K, of a form characteristic of attenuation due to thermal phonons.

(iii) A strong disturbance in the range 50 K to 80 K in the form of a sharp attenuation peak at 40 MHz and a somewhat arbitrary shape at higher frequencies.

These three features will be considered in order.

8.3 THE RESIDUAL ATTENUATION

Figure 8.9 shows the residual attenuation at 4 K and frequencies of 40, 80, 160 and 320 MHz for both the [111]L and [110]L modes: the frequency dependence approximately follows ω^2 for both modes. Interactions with free carriers and with dislocations are expected to dominate the residual attenuation.

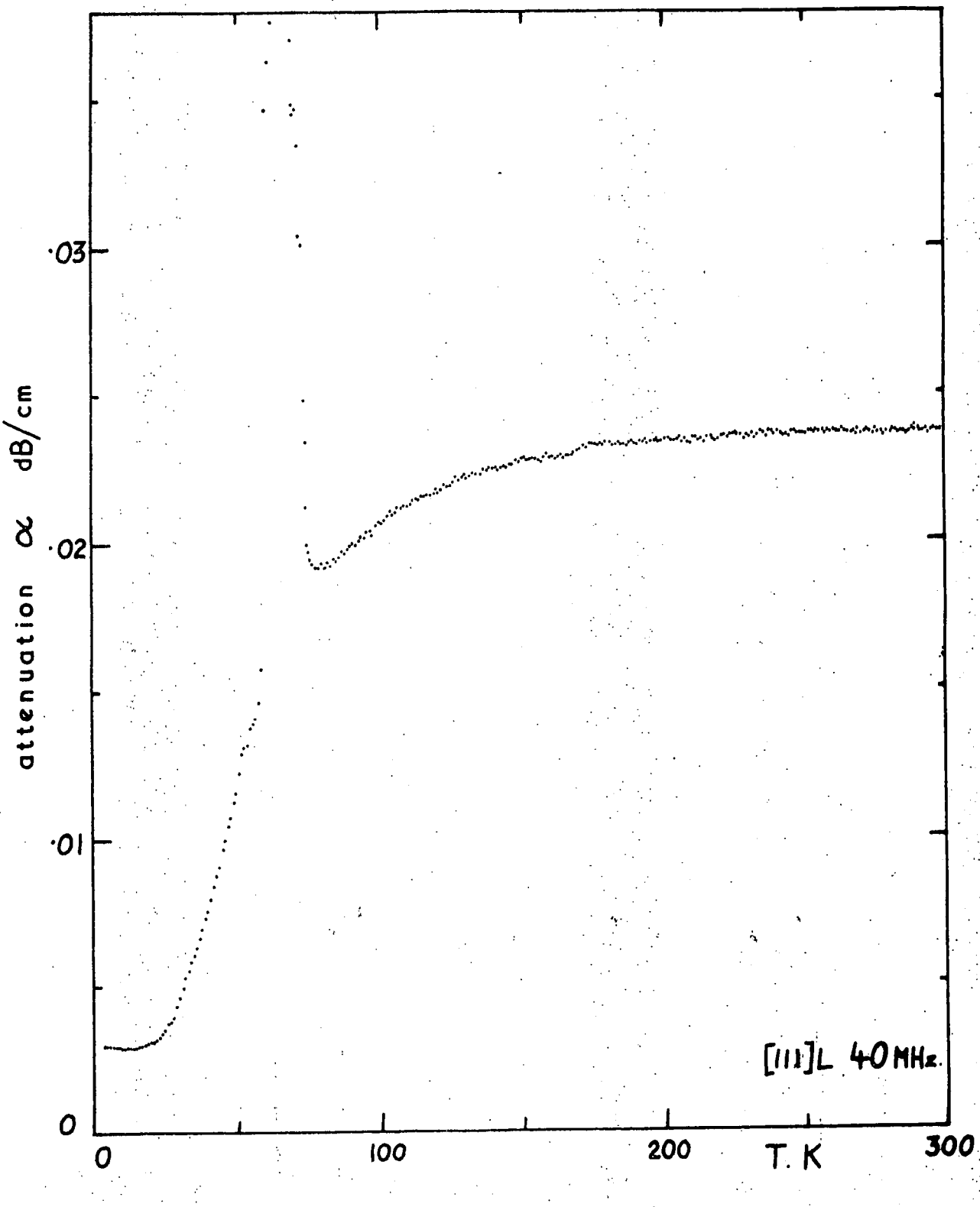

Longitudinal ultrasonic attenuation in the [111] direction of GaAs at 40 MHz.

FIGURE 8.1

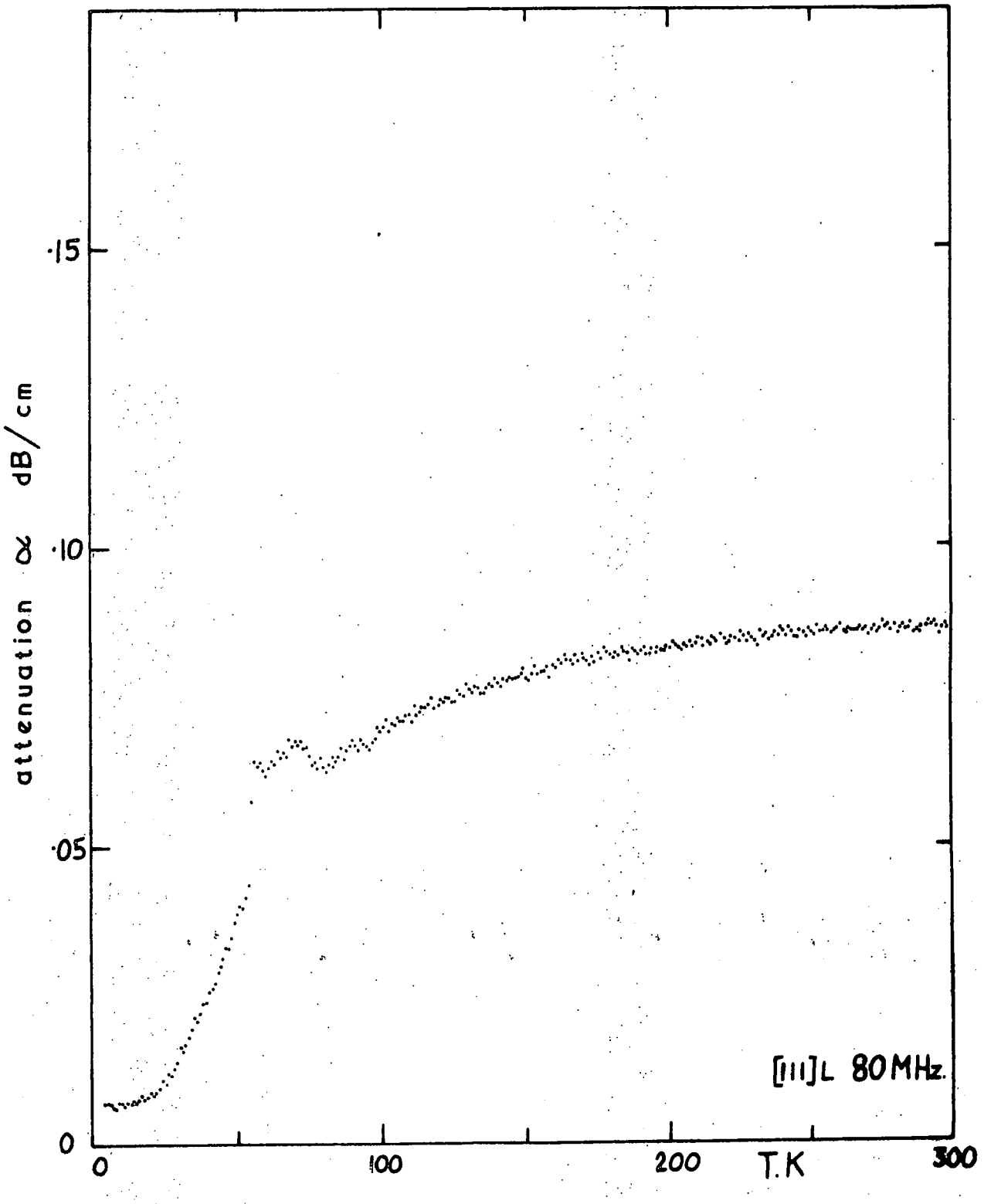

Longitudinal ultrasonic attenuation in the [111] direction of GaAs at 80 MHz.

FIGURE 8.2

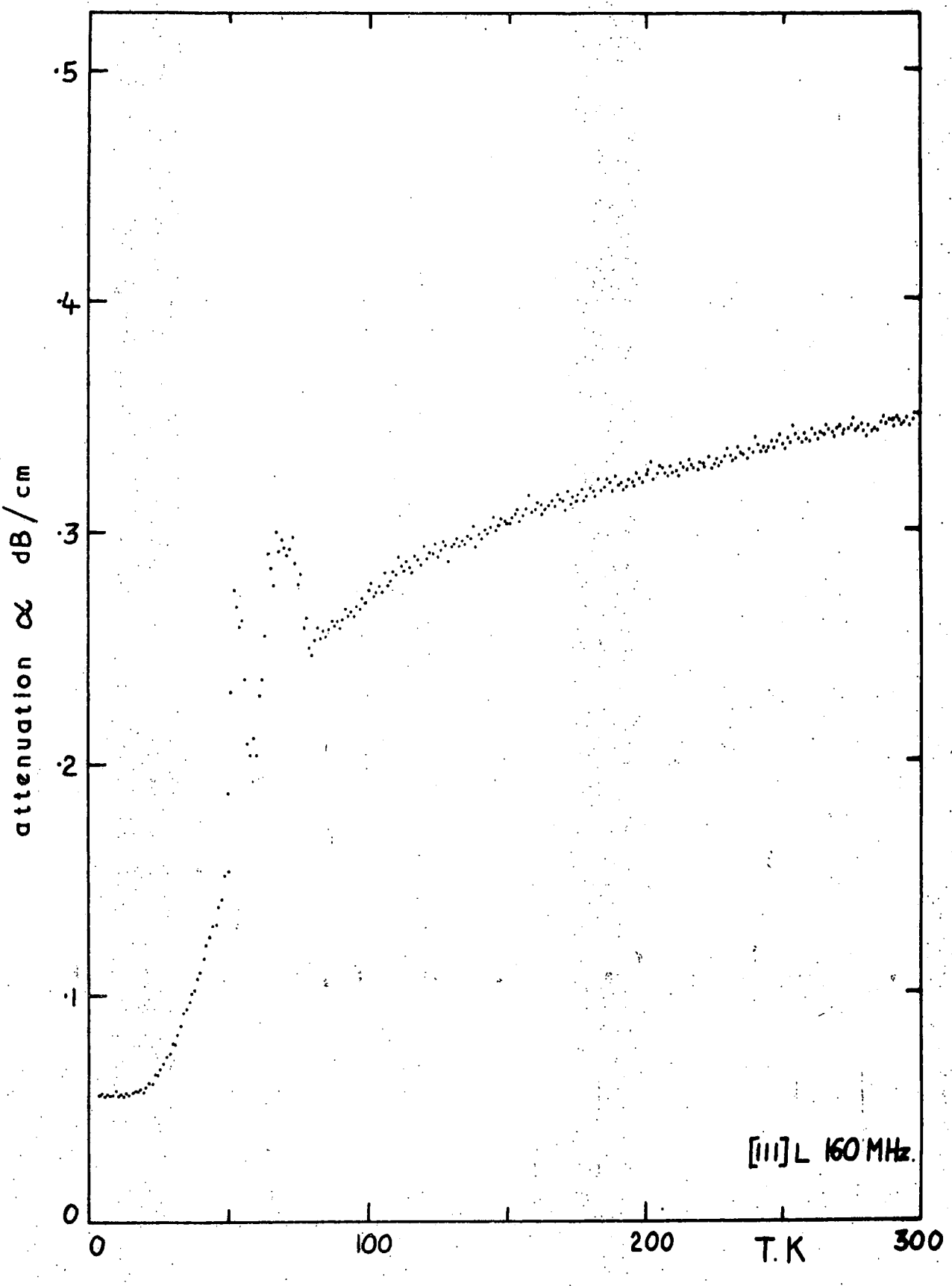

Longitudinal ultrasonic attenuation in the [111] direction of GaAs at 160 MHz.

FIGURE 8.3

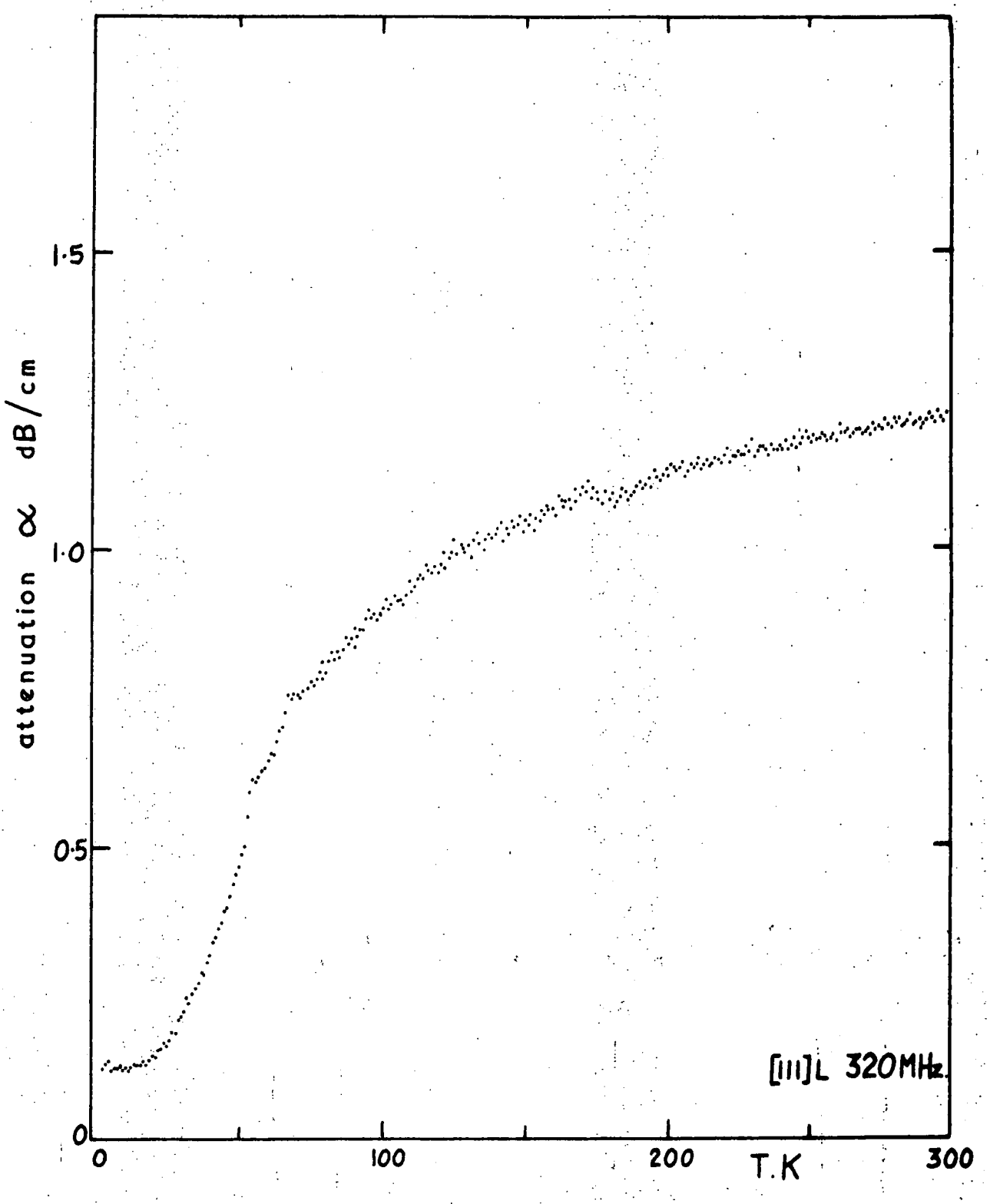

Longitudinal ultrasonic attenuation in the [111] direction of GaAs at 320 MHz.

FIGURE 8.4

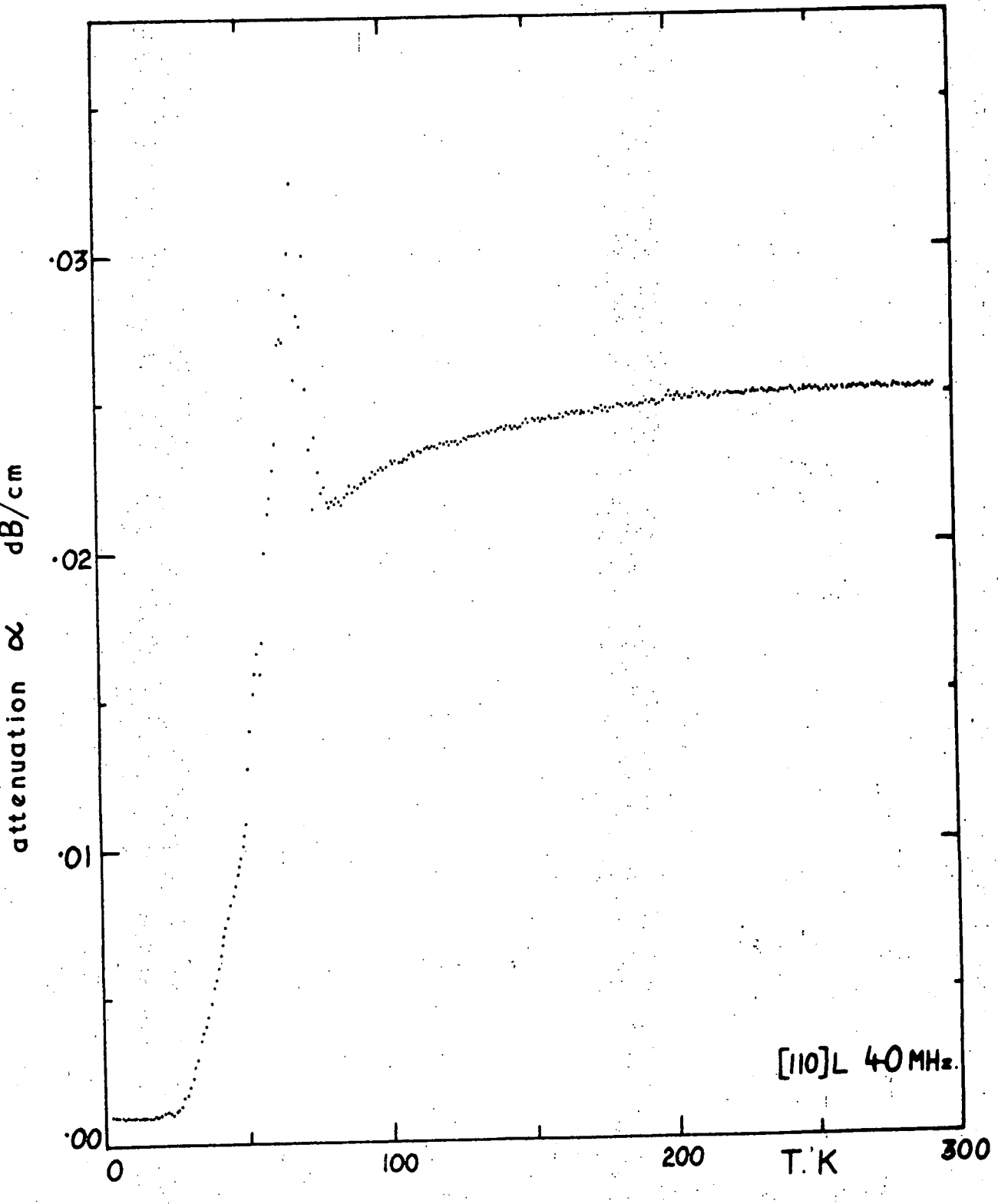

Longitudinal ultrasonic attenuation in the [110] direction of GaAs at 40 MHz.

FIGURE 8.5

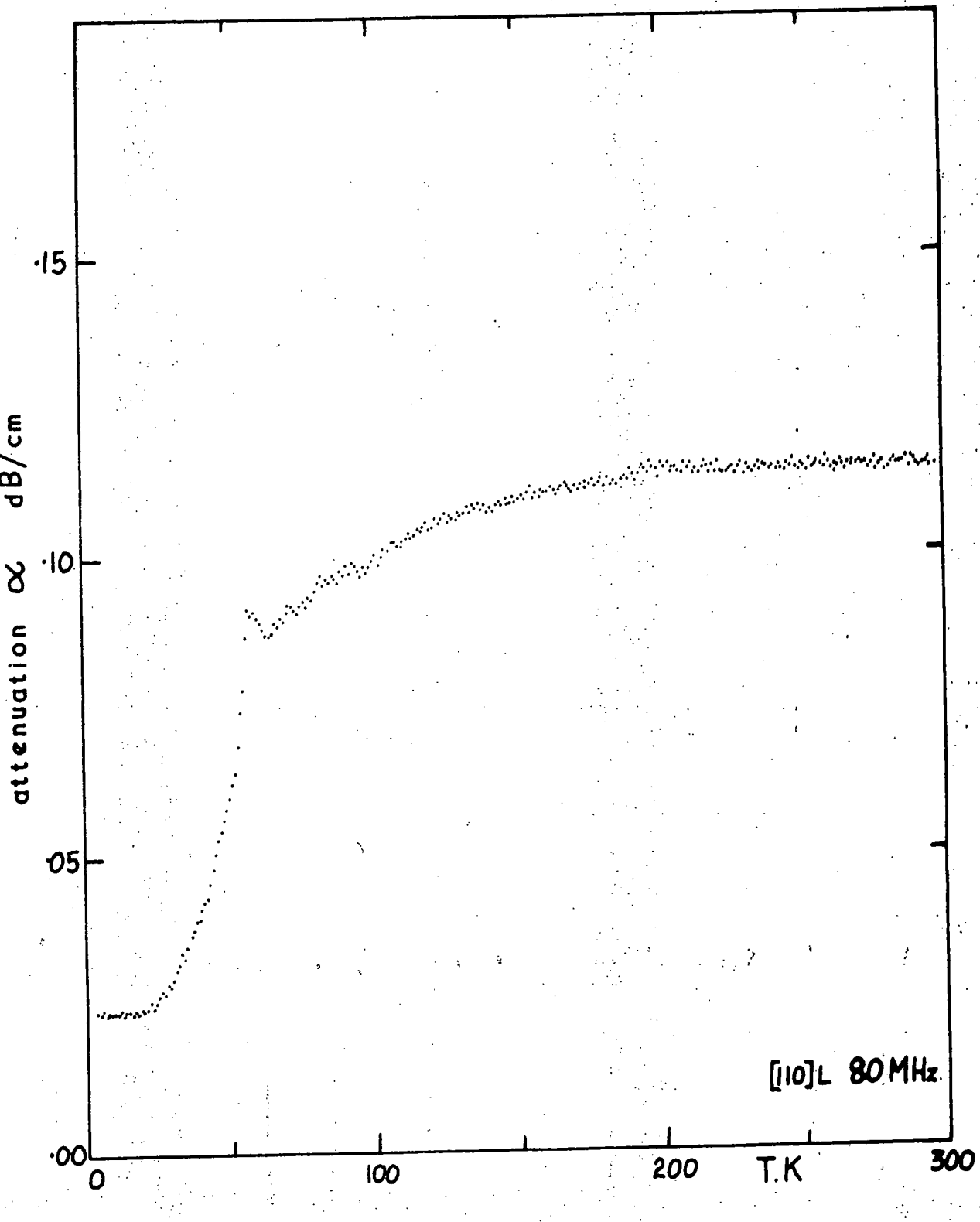

Longitudinal ultrasonic attenuation in the [110] direction of GaAs at 80 MHz.

FIGURE 8.6

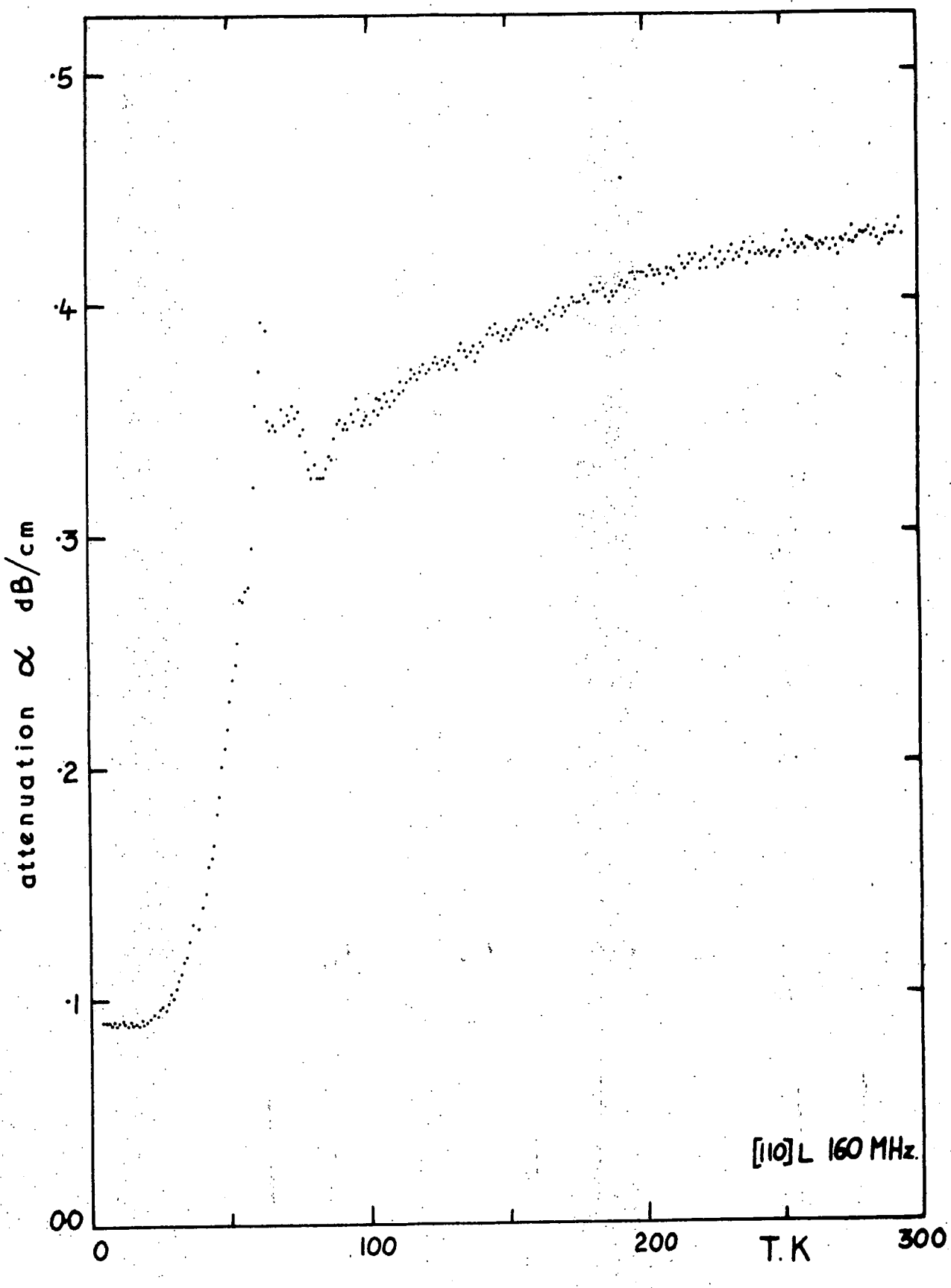

Longitudinal ultrasonic attenuation in the [110] direction of GaAs at 160 MHz.

FIGURE 8.7

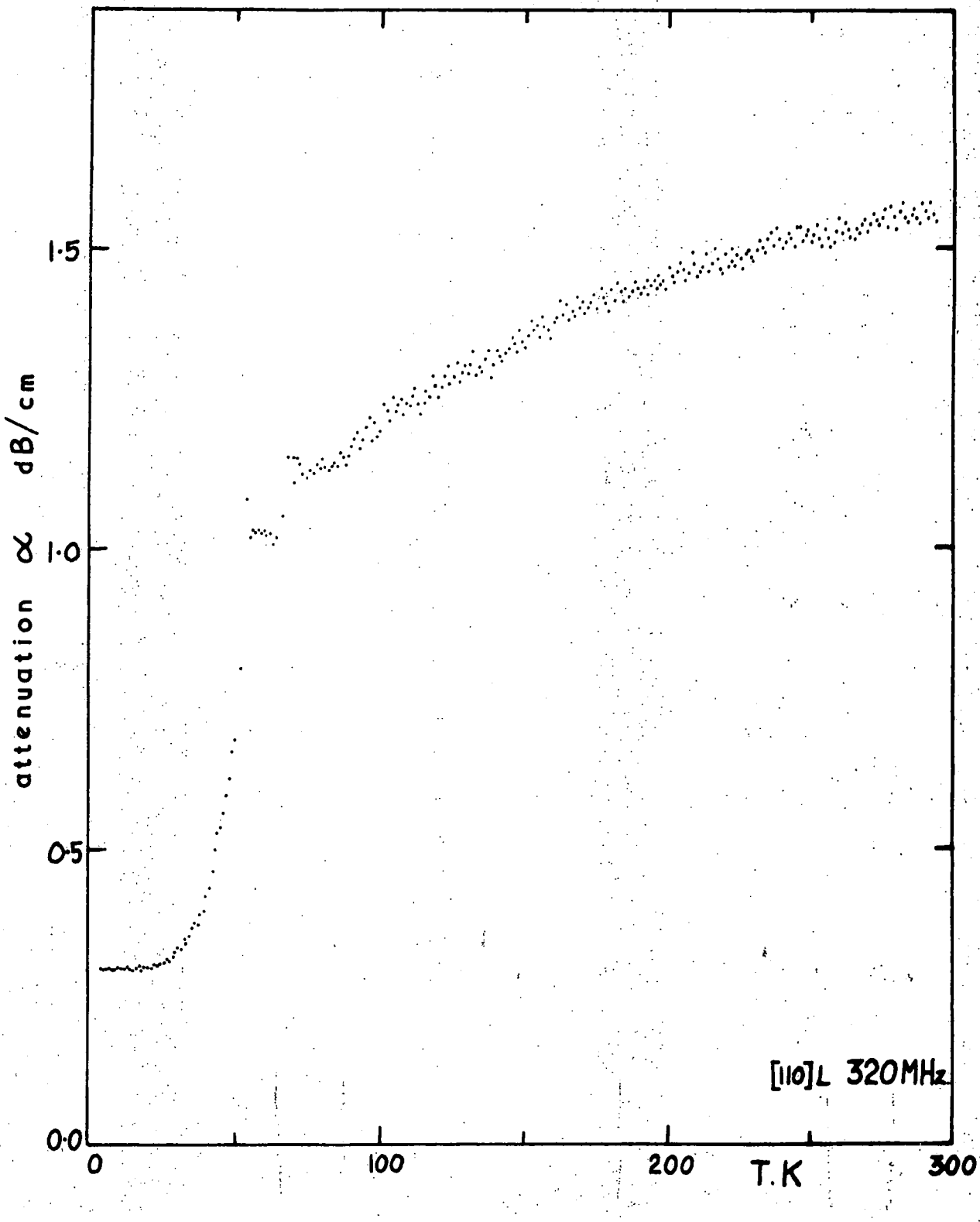

Longitudinal ultrasonic attenuation in the [110] direction of GaAs at 320 MHz.

FIGURE 8.8

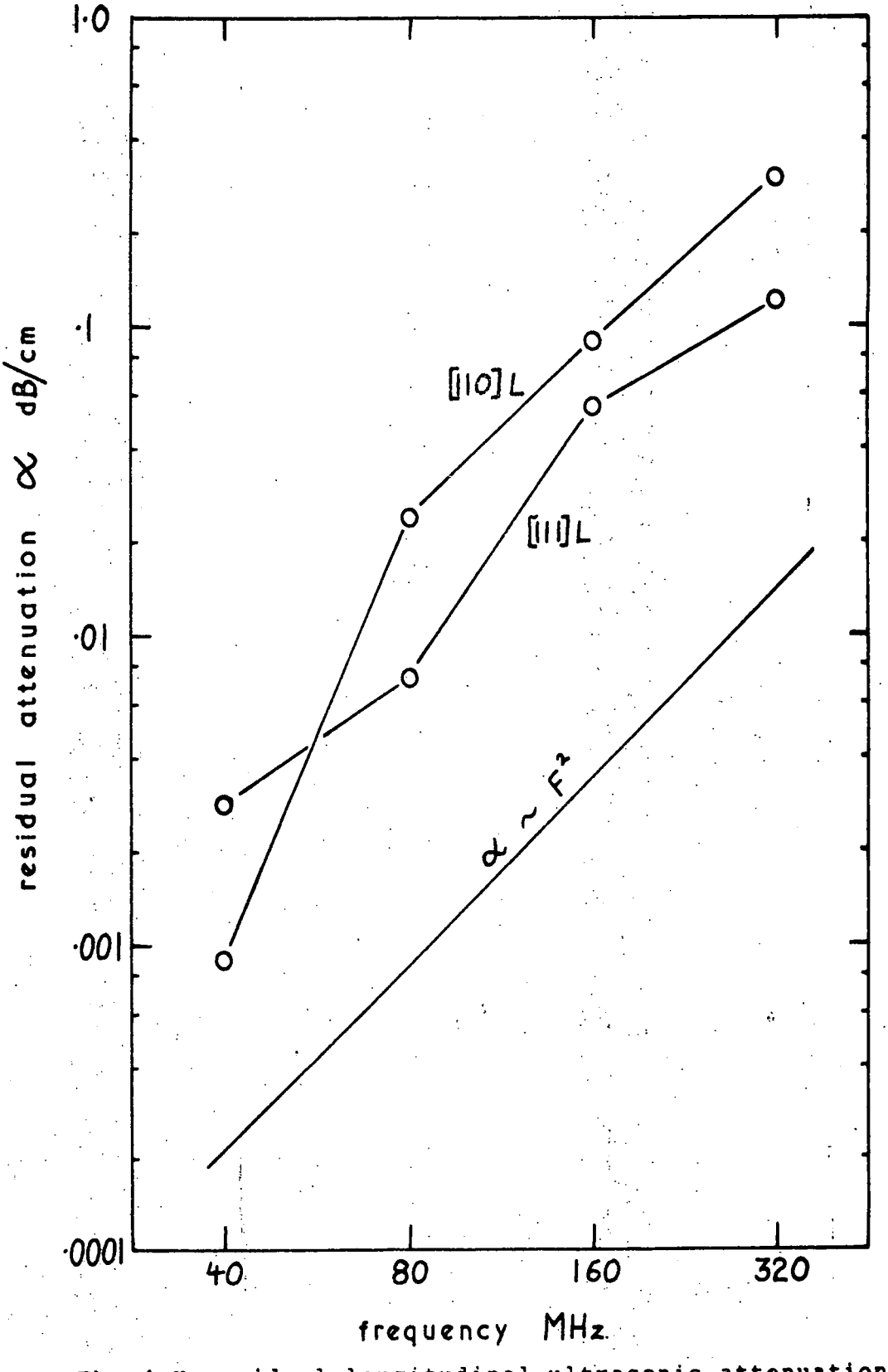

The 4 K residual longitudinal ultrasonic attenuation in the [111] and [110] directions of GaAs as a function of frequency.

FIGURE 8.9

The free carrier attenuation frequency dependence should vary strongly in the temperature range 2 K to 10 K (Elbaum, 1969). Measurements of the attenuation as a function of temperature have been made over this range (Figure 8.10): no great changes are apparent, indicating that the residual attenuation is not dominated by free carrier interactions. Granato and Lücke (1956) have derived expressions for the damping of ultrasonic waves by dislocation loops vibrating under the influence of the high frequency stress. An extensive description of this effect will be given in Chapter 9: the attenuation dependence on intrinsic and extrinsic parameters may be summarised as follows:

α depends on

(i) the square of the loop length L between pinning points;

(ii) the elastic shear modulus;

(iii) the burgers vector squared;

(iv) the total length of dislocation lines in a unit cube which is available for damping;

(v) orientation of the propagation direction with respect to the crystal slip systems;

(vi) the dislocation damping coefficient;

(vii) the dislocation loop resonant frequency.

Alper (1968) found dislocation-damping attenuation at 4K of about 7 dB/cm for [110] longitudinal 300 MHz waves. The dislocation density of the gallium arsenide crystals used here was about 10^4 cm^{-2} (see Section 3.2.(c)) compared with about 10^7 cm^{-2} for mercury telluride (Alper, 1968): on this basis alone the dislocation attenuation for [110]L

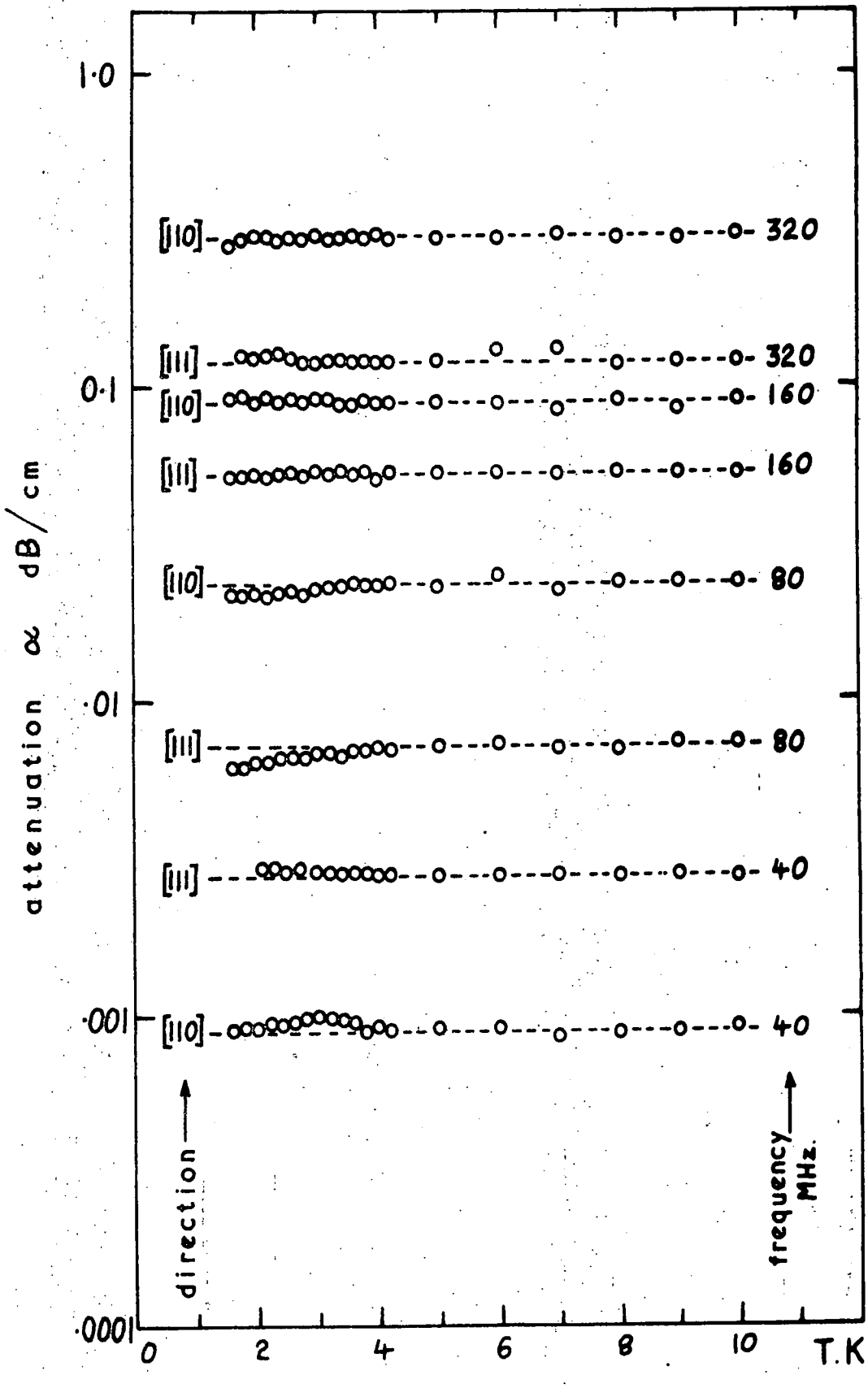

Longitudinal ultrasonic attenuation in the [111] and [110] directions of GaAs as a function of frequency and temperature from 2 K to 10 K.

FIGURE 8.10

320 MHz waves in GaAs should be less than 0.01 dB/cm compared with the residual at 4 K of 0.3 dB/cm. The two other main variables which must be considered are the dislocation loop length (which controls the resonant frequency) and the damping coefficient. Variation in either of these parameters which would raise the level of attenuation would also move the resonant frequency to a value substantially below that of ∿220 MHz found by Alper (1968) for HgTe. No peak is observable in the frequency dependence of the residual attenuation at 4 K: the dislocation attenuation at 320 MHz is unlikely to be more than about 0.01 dB/cm, and correspondingly lower for lower ultrasonic frequencies.

Neither free carrier interaction nor dislocation damping appear to be capable of causing the large frequency dependent residual attenuation at 4 K. It is possible that the effect is due to phase interference at the transducer rather than a true loss phenomenon: in this case the apparent residual attenuation will to first order be independent of temperature (as shown in Figure 8.10) and may be subtracted from the values of attenuation measured over the complete range from 4 K to 300 K. There is no evidence of mechanisms other than phase interference which could cause the observed residual attenuation: it has been treated as being independent of temperature.

8.4 THE PHONON-PHONON ATTENUATION

Transition between the two regimes of phonon-phonon interaction in crystals (Section 8.1) is given by

the condition $\omega\tau = 1$. The temperature and frequency dependence of this equivalence may be calculated from the thermal conductivity and specific heat (equation 8.7): Figure 8.11 shows results calculated from the thermal conductivity data presented by Holland (1966) (Figure 8.12), the specific heat data of Piesbergen (1963) and Cetas et al (1968) and velocity measurements of this work. The Debye velocity V_{STH} (3.293×10^5 at 0 K) has been calculated as in the computation of the Debye temperature (Section 6.3). In the frequency range of 40 to 320 MHz $\omega\tau$ is unity in the region of 30 K: above this temperature we can expect the attenuation to be described by an equation of the form (8.8). At low temperatures $\omega\tau > 1$, and equation (8.9) should apply.

In the W-E theory there is a change in the frequency dependence of attenuation from a square law at high temperatures to a linear law at low temperatures. The frequency dependence of the measured attenuation at 50, 100, 200 and 290 K is shown in Figures 8.13 and 8.14 for the [111]L and [110]L modes, respectively. Both show a dependence of the frequency exponent on temperature. The exponent (n) has been calculated at one degree intervals from 30 K to 294 K (excluding the disturbed region from 50 K to 80 K) assuming the invariance of all other parameters. Figures 8.15 and 8.16 show the temperature dependences of n. Bobylev and Kravchenko (1967a, 1970) have calculated the dependence at 20 K and 300 K (and by implication at 100 K as they show a temperature-independent attenuation between 100 K and 300 K), and Krasilnikov et al (1969) and Ivanov et al (1971) have given values for the 300 K attenuation:

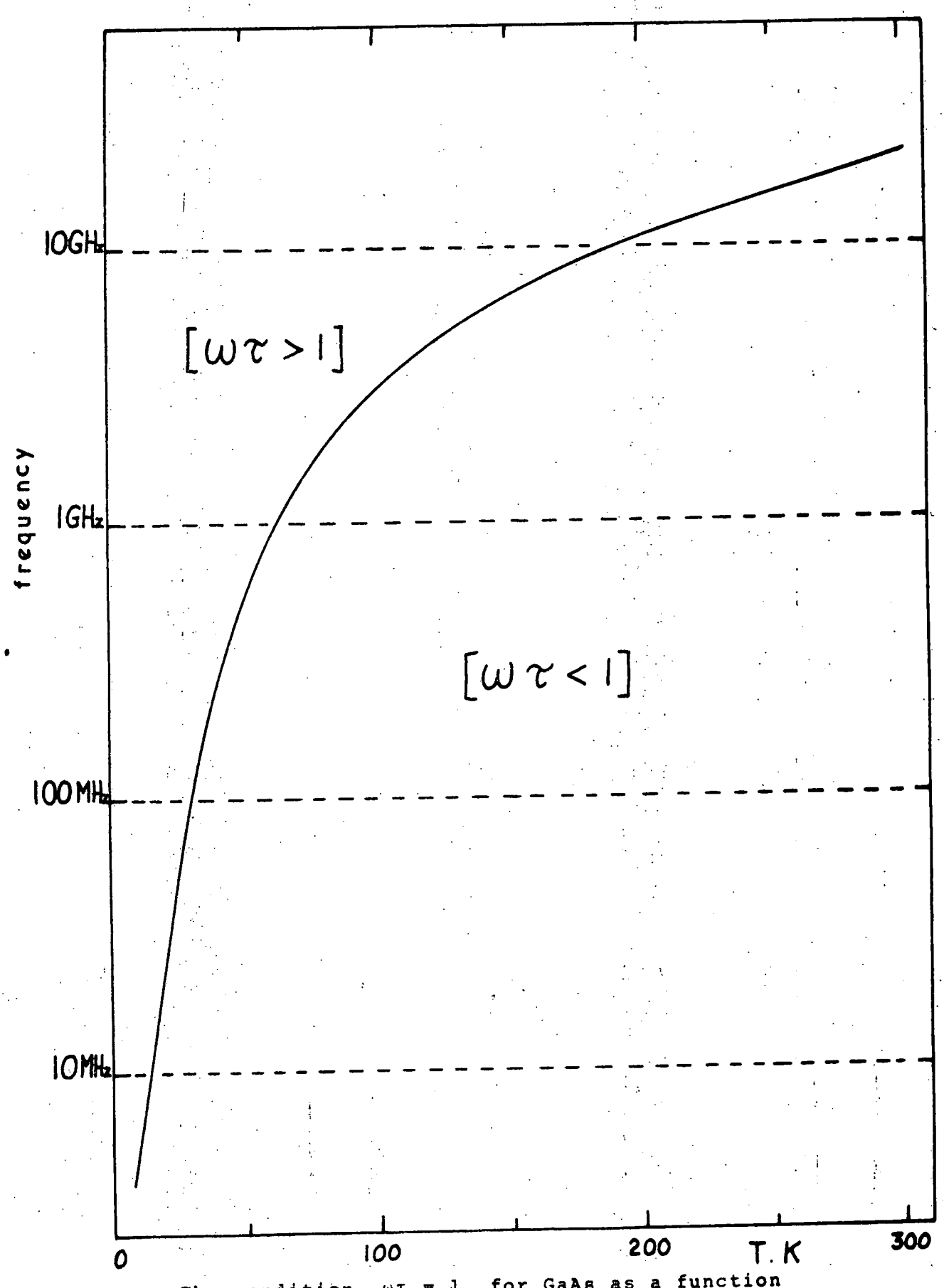

The condition $\omega\tau = 1$ for GaAs as a function of frequency and temperature.

FIGURE 8.11

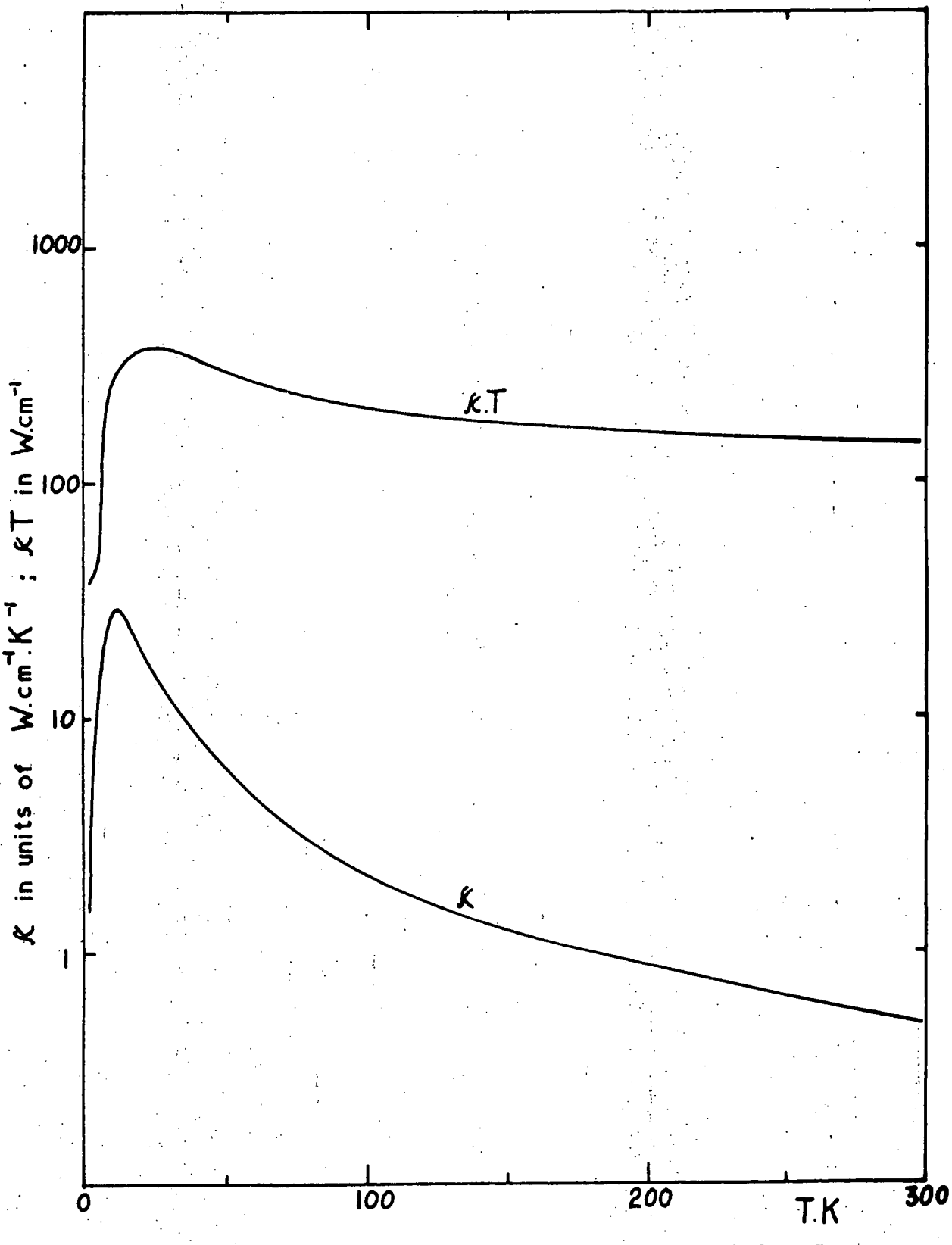

The thermal conductivity κ and the multiple κT as functions of temperature T for GaAs (after Holland, 1966).

FIGURE 8.12

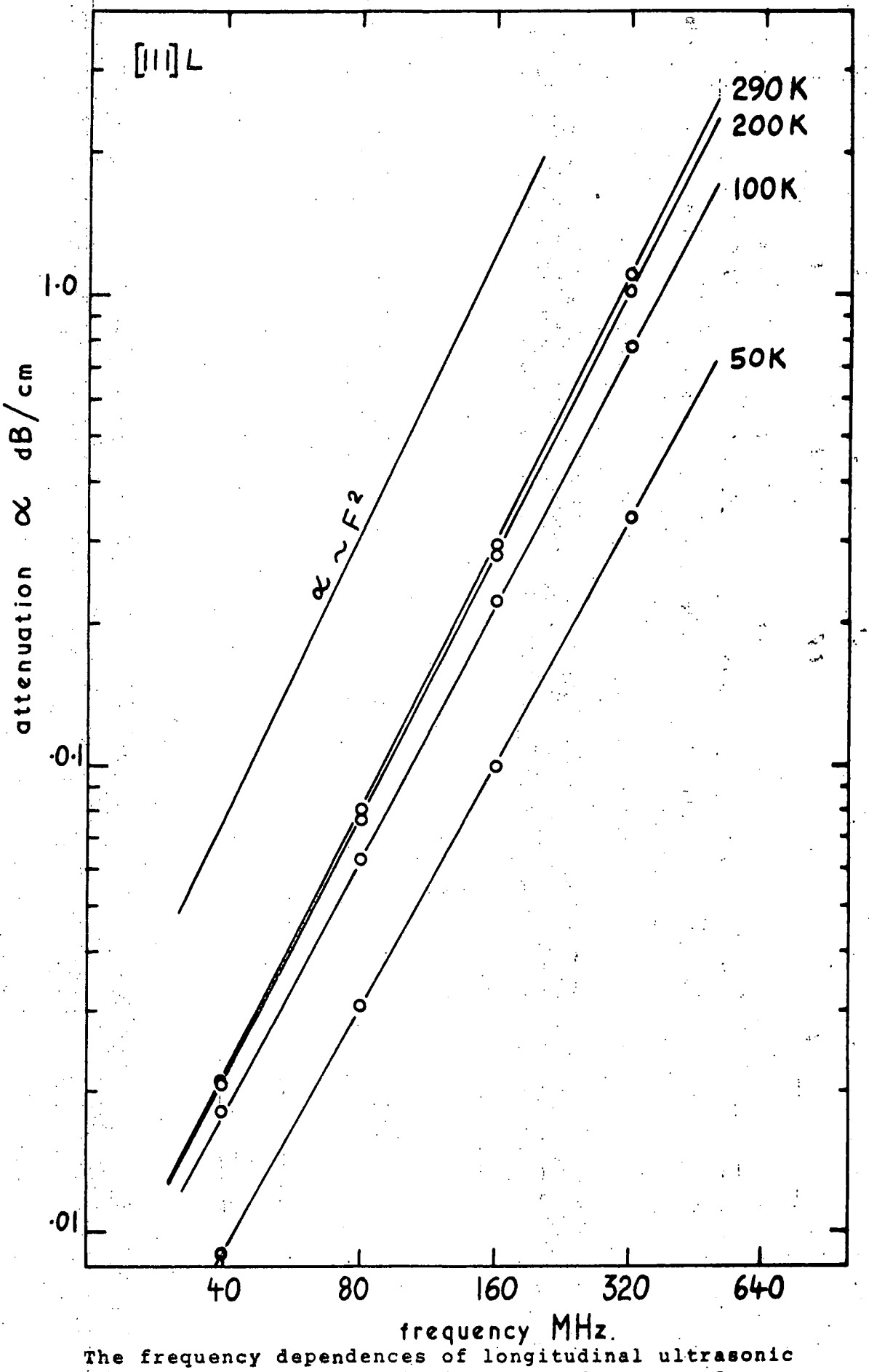

The frequency dependences of longitudinal ultrasonic attenuation in the [111] direction of GaAs at 50 K, 100 K, 200 K and 290 K.

FIGURE 8.13

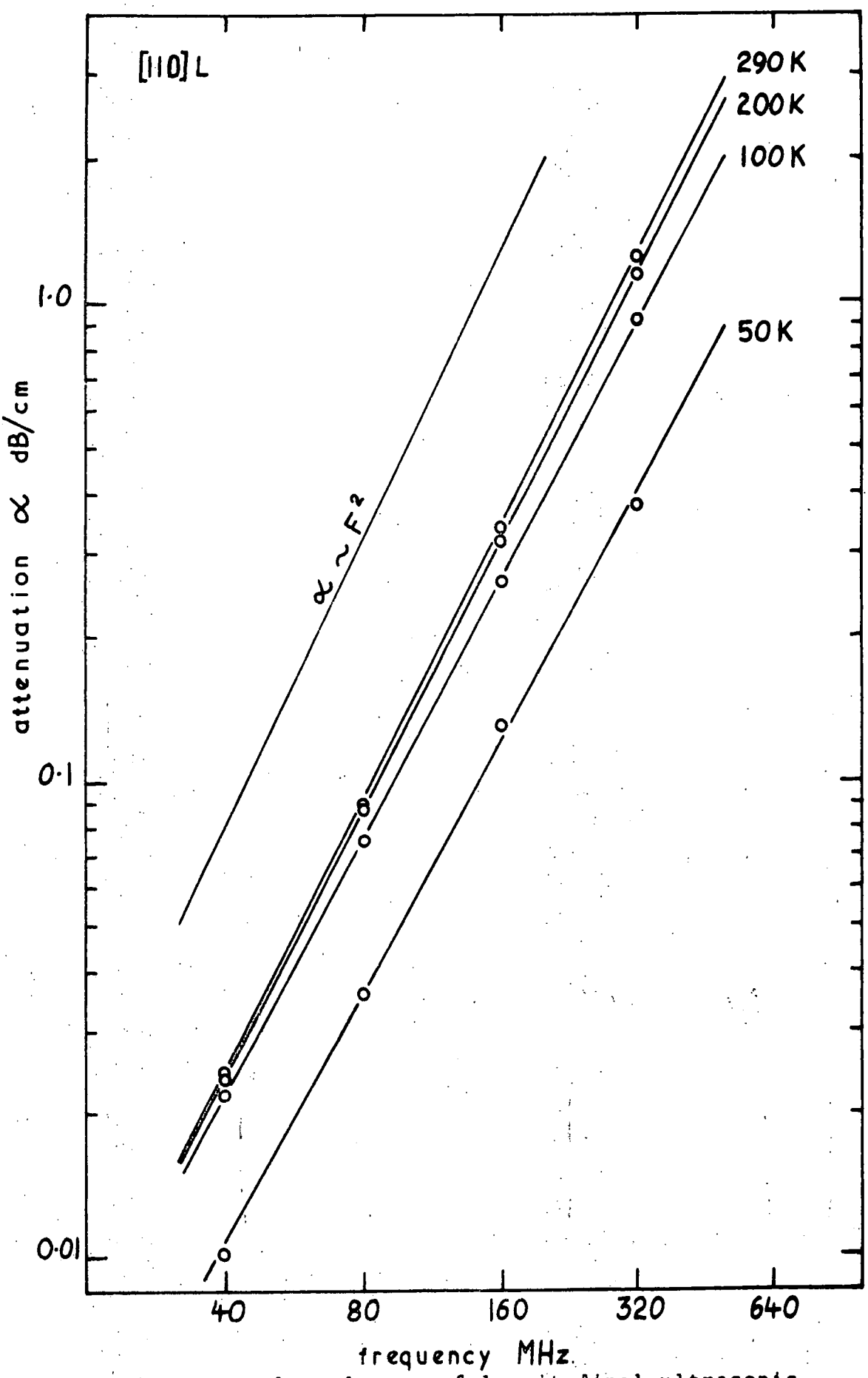

The frequency dependences of longitudinal ultrasonic attenuation in the [110] direction of GaAs at 50 K, 100 K, 200 K and 290 K.

FIGURE 8.14

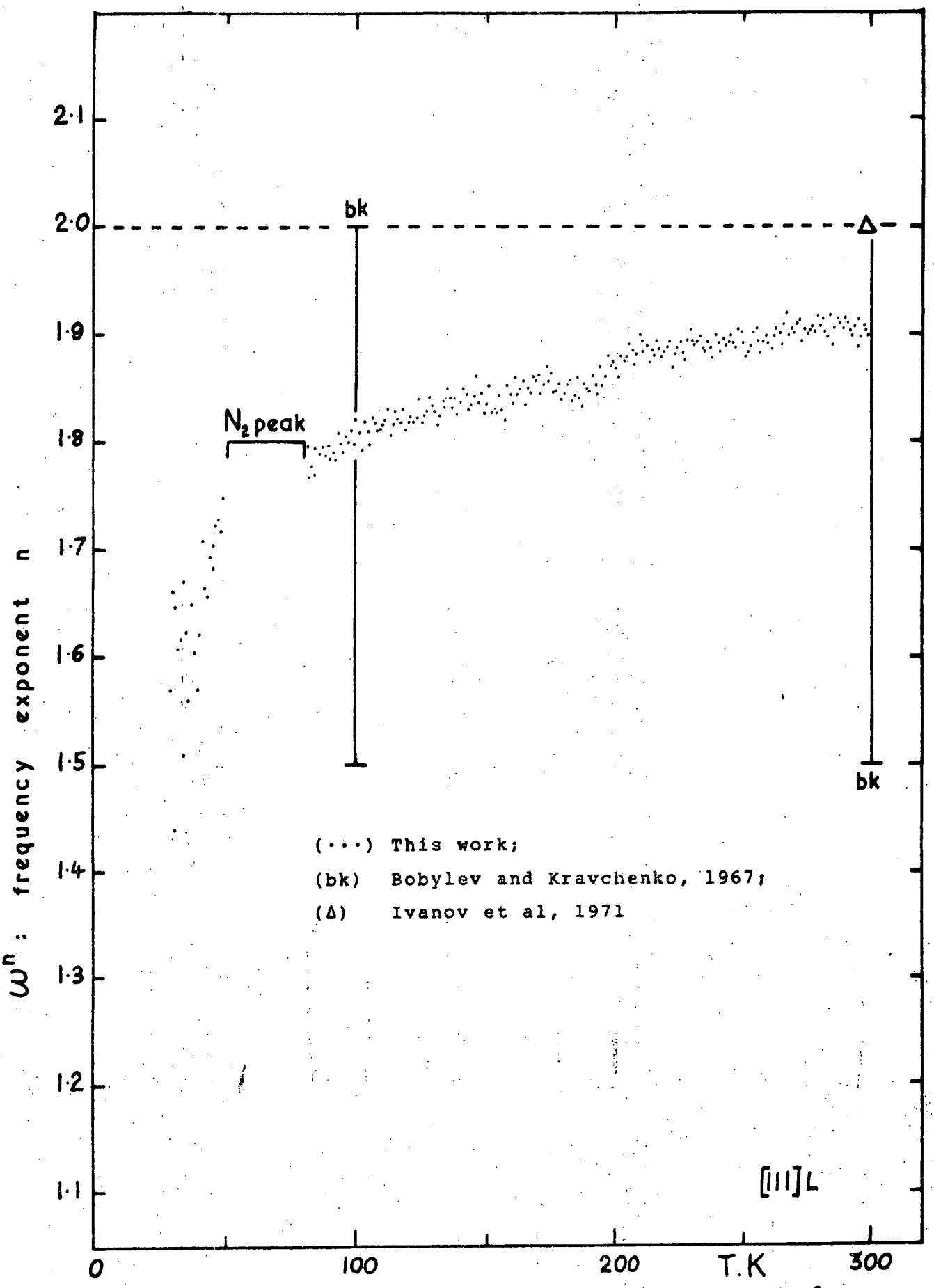

The temperature dependence of the frequency exponent of longitudinal ultrasonic attenuation in the [111] direction of GaAs.

FIGURE 8.15

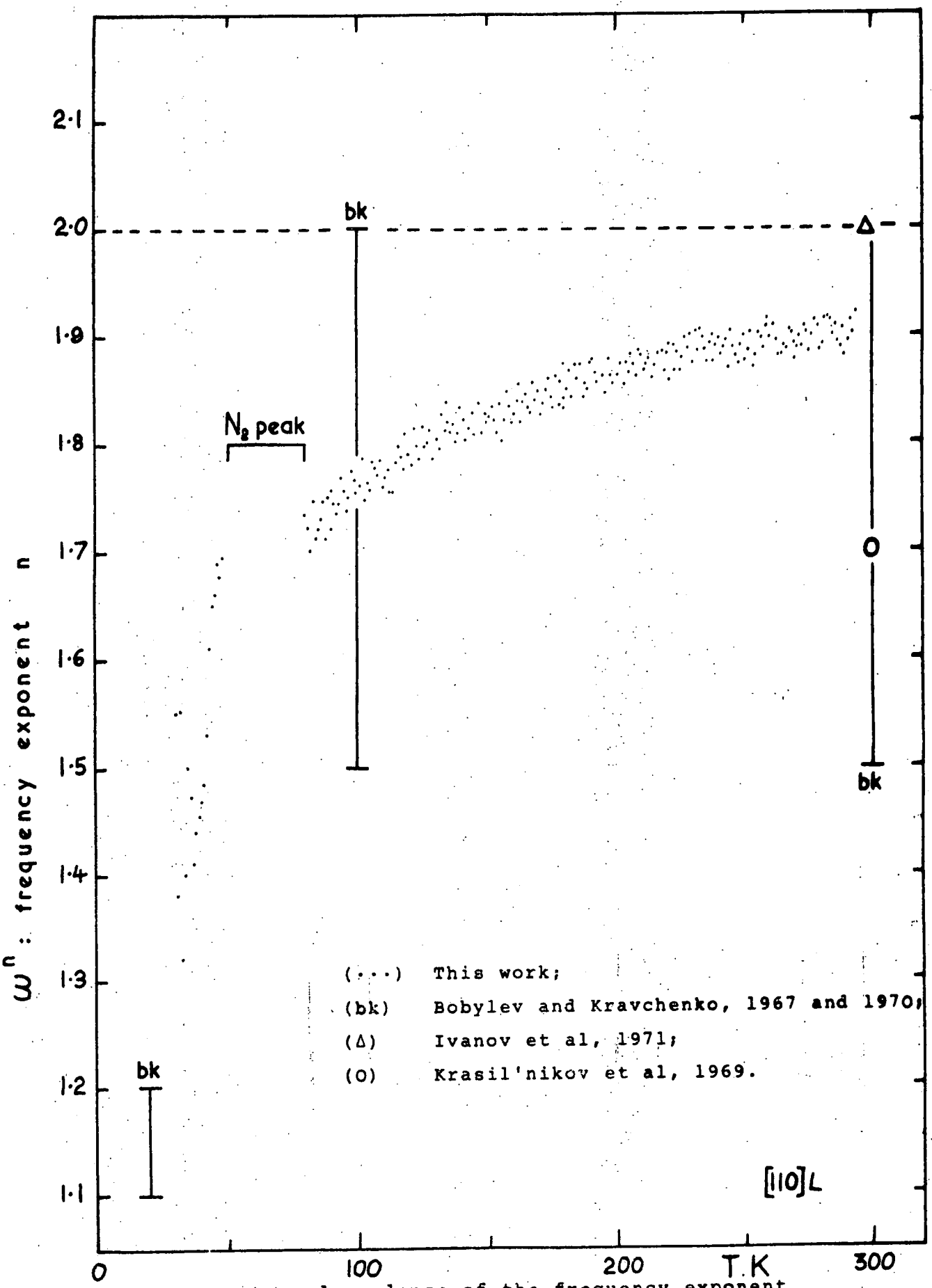

The temperature dependence of the frequency exponent of longitudinal ultrasonic attenuation in the [110] direction of GaAs.

FIGURE 8.16

for comparison these are shown in Figures 8.15 and 8.16. The frequency exponent n approaches 2 at the highest temperatures, and falls towards 1 in the region of $\omega\tau=1$ —— the dependence predicted by Woodruff and Ehrenreich (1961).

It was shown in Chapter 6 that the Grüneisen parameter of GaAs is strongly dependent on temperature. An exact fit of the W-E model to the attenuation temperature dependence has been computed to evaluate the Grüneisen parameter operative in the phonon-phonon interaction. When the frequency exponent obtained above is included, the Gruneisen parameters is found to be insensitive to temperature change above 100 K, but falls off rapidly at low temperatures (see Figure 8.17, curves A). γ'_{WE} has also been calculated as a function of temperature for a temperature-independent frequency exponent of 2 (Figure 8.17, curves B); it is then closer to γ'_G, calculated from the Grüneisen law (Figures 8.17, curve C), and coincides with the temperature variation derived by Bobylev and Kravchenko (1970), where an exponent of 2 was assumed.

It seems likely that some of the temperature dependence ascribed to the frequency exponent is due to variation in the frequency dependence of the Grüneisen parameter: Woodruff and Ehrenreich (1961) did not include this feature in their model. The mode-Grüneisen parameters contributing to γ'_G itself are certainly frequency dependent (Vetelino, Namjoshi and Mitra, 1970) and the average of mode-Grüneisen parameters giving γ'_{WE} will be frequency dependent also. The change in ω^n over the temperature range 100 K to 290 K is large (a factor of

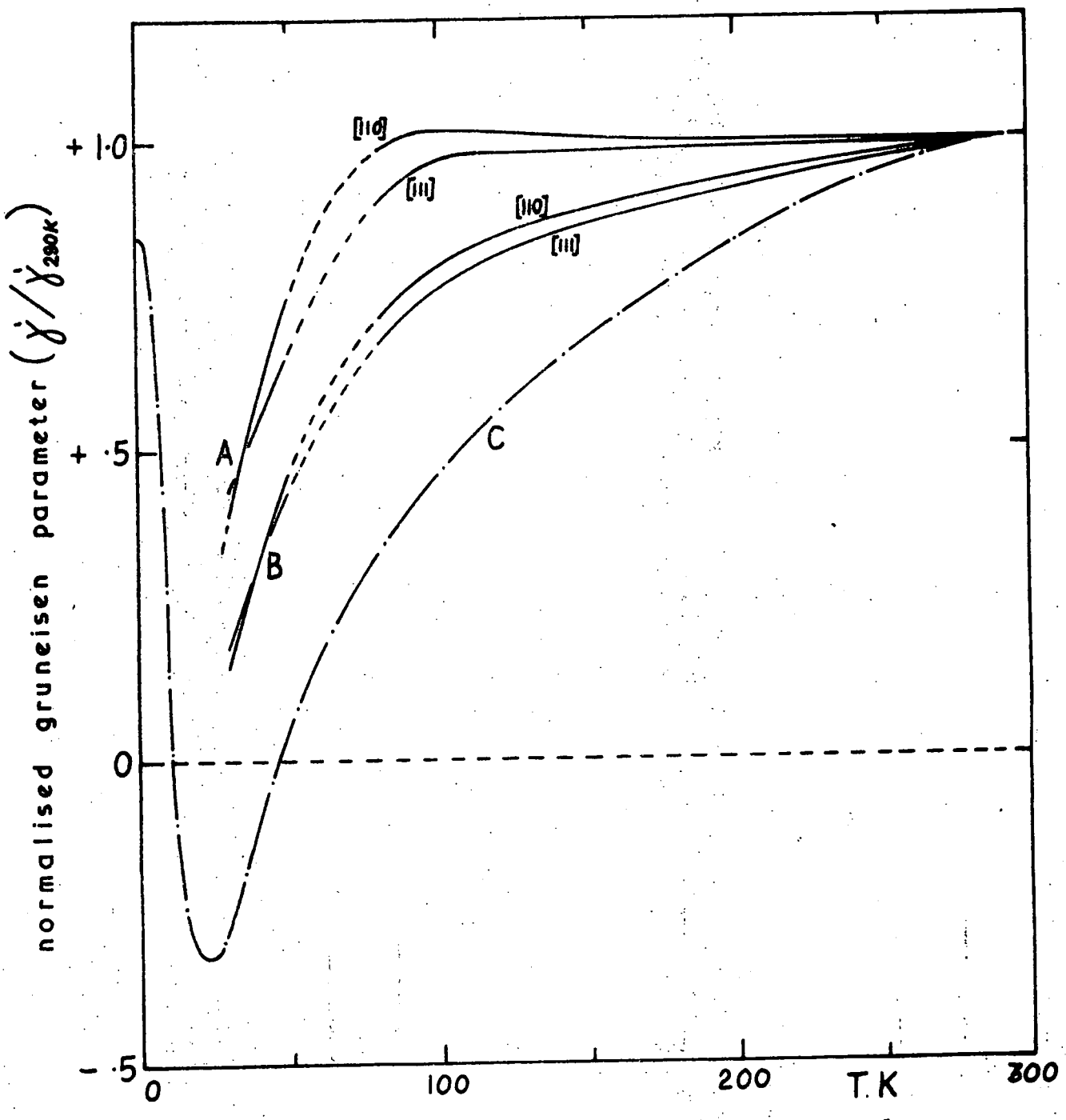

The normalised Grüneisen parameter of GaAs: curves A are calculated from the ultrasonic attenuation assuming the frequency exponents given in figures 8.15 and 8.16; curves B are calculated from the ultrasonic attenuation assuming the exponent is 2, independently of temperature; curve C is calculated from the Grüneisen Law.

FIGURE 8.17

1.7 at 40 MHz and 2.4 at 320 MHz), however, both the frequency dependence and temperature dependence of attenuation over this range can be accounted for by the inclusion of a frequency dependent term in the Grüneisen parameter:

$$\gamma'_{WE} = P\,\omega^{-m} + \gamma'_{R},$$

where P is a small constant, m is small and γ'_R is the frequency independent part of γ'_{WE}. This is consistent with the value of $\omega\tau$ between 100 K and 290 K (Figure 8.11): over the whole range $\omega\tau \ll 1$ and a strongly temperature dependent frequency exponent is not expected. Assuming, then, that ω^n follows a square law from 100 K to 290 K in the range 40 to 320 MHz, the Grüneisen parameter temperature dependences at 40 MHz and frequency dependences to first order in the range 40 to 320 MHz are as shown in Figures 8.18 and 8.19, respectively.

The temperature dependences of γ'_{WE} are similar in form to that of γ'_G derived from the Grüneisen law (see Figure 8.17) but the absolute values are larger. Interactions between thermal phonons and the ultrasonic phonons will be a function of the mode-Grüneisen parameters of both, and although the thermal phonon parameters have a range of values corresponding to different modes, the ultrasonic phonons will be characterised by a single mode-parameter, which will therefore have a dominating influence in the mode-parameter average relevant to ultrasonic attenuation. Vetelino, Mitra and Namjoshi (1970) have calculated the mode-Gruneisen parameter dispersion curves for the [111] and [110] directions of zinc telluride (which has the

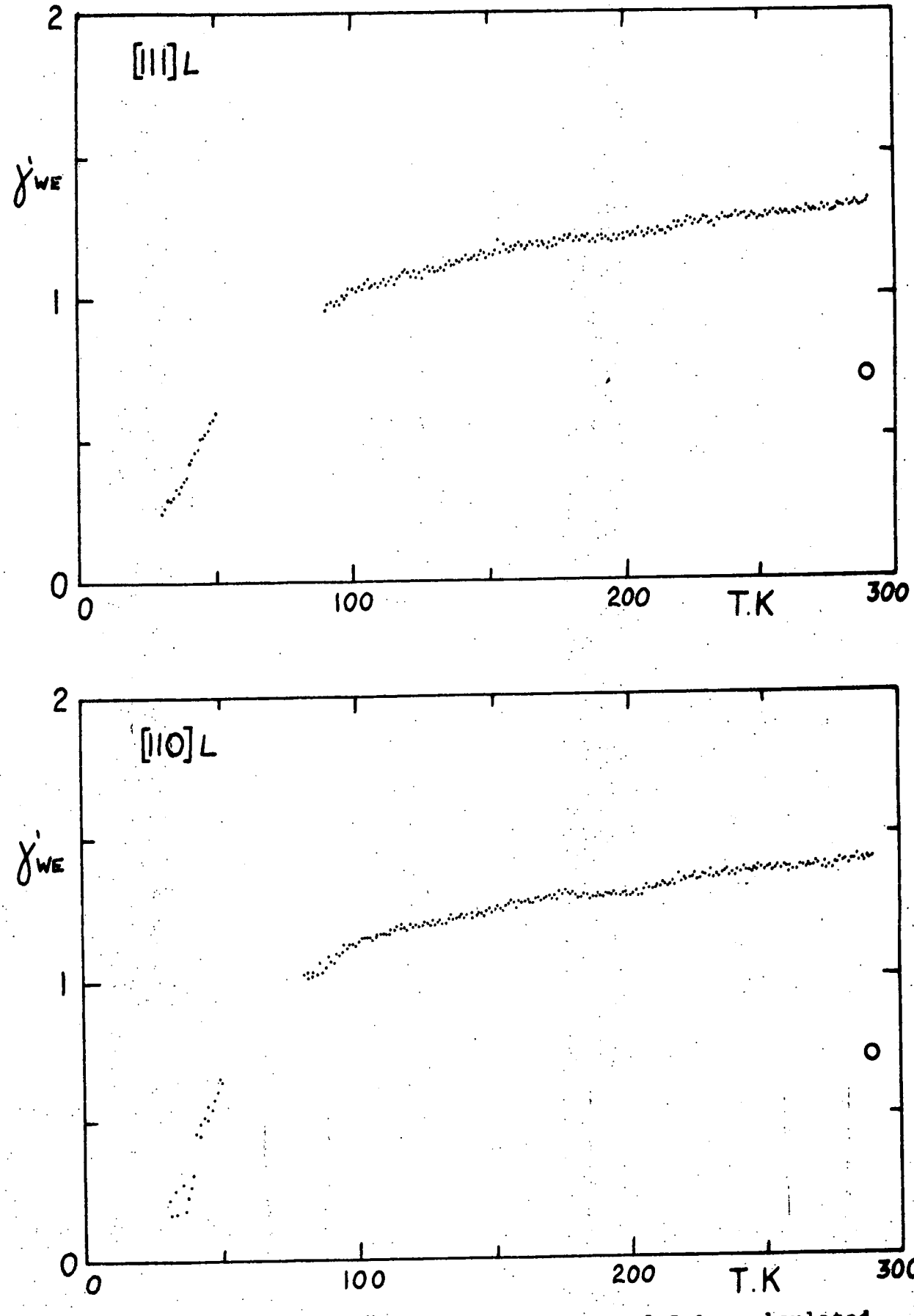

The phonon-phonon Grüneisen parameters of GaAs calculated from the [111] and [110] longitudinal ultrasonic attenuation measurements at 40 MHz, assuming a frequency exponent of 2 independent of temperature.

FIGURE 8.18

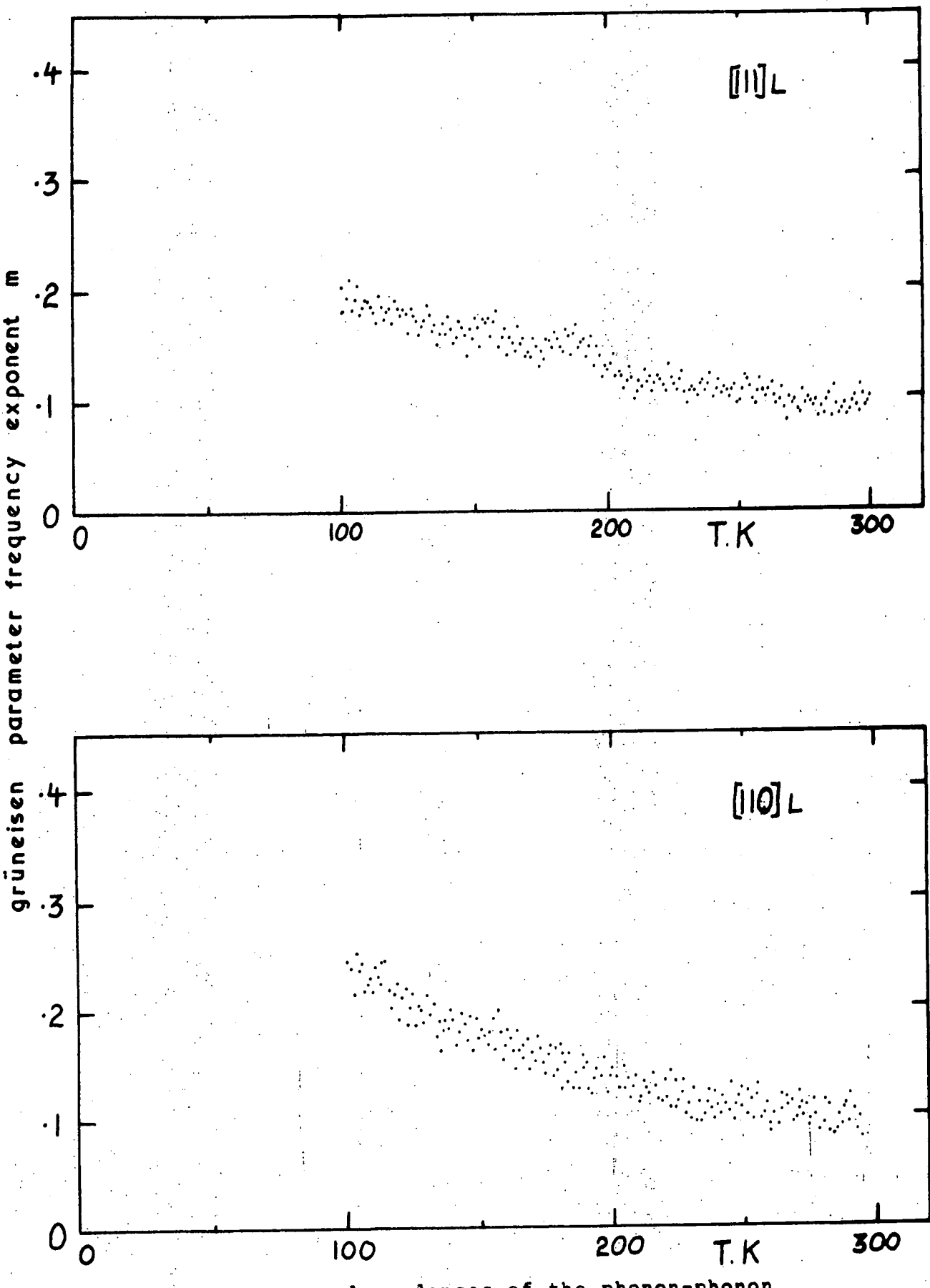

The temperature dependences of the phonon-phonon Grüneisen parameter frequency exponents in GaAs calculated from the [111] and [110] longitudinal ultrasonic attenuation measurements, assuming a frequency exponent of 2 independent of temperature.

FIGURE 8.19

same zinc-blende structure as GaAs) and also the average γ'_G, which is not susceptible to single-mode domination. They found room temperature values for longitudinal acoustic modes in the [111] and [110] directions of 1.33 and 1.45, respectively, while the room temperature average came out to be 0.97: we might expect the [111]L and [110]L values of the average γ'_{WE} to be larger than the value of γ'_G in this case, as is found for gallium arsenide. Unfortunately no information on phonon-phonon attenuation in ZnTe is reported in the literature. The frequency dependences of γ'_{WE} in GaAs (Figure 8.19) are consistent with the dispersion curves calculated by Vetelino, Mitra and Namjoshi (1970) for the [111] and [110] longitudinal acoustic mode - Grüneisen parameters, both of which are an inverse function of frequency.

It is not possible to carry out a complete analysis of the attenuation data below ∿100 K because of the impossibility of separating the temperature dependences of the frequency and Grüneisen parameter exponents in the region for which $\omega\tau=1$, and also the data is complicated by the small ratio of phonon-phonon attenuation to residual attenuation below 30 K and the anomalous peak between 50 K and 80 K.

8.5 THE NITROGEN PEAK

Measurements of attenuation in GaAs made by Bobylev and Kravchenko (1969) in the region 50 K to 80 K exhibit a similar anomaly to that found in this work. In a later publication (Bobylev and Kravchenko, 1970) they attributed

the peak to the condensation of air on the surface of the sample or evaporation of the coolant into the atmosphere. A similar phenomenon has also been observed for other III-V compounds (InSb, InAs, GaSb; Bobylev and Kravchenko, 1970), for glass (Maynell, 1973) and for indium (Gunton, 1973). Bobylev and Kravchenko's finding has been checked in this work by investigation of the anomaly in a number of different sample environments: the presence of nitrogen has been found to be the controlling factor. Figure 8.20 shows the attenuation temperature dependences (temperature rising) for GaAs in atmospheres of varying nitrogen content and in a vacuum. The effect was not observable on cooling the samples past 80 - 50 K, but only when the temperature was rising. The peak height is approximately proportional to the amount of nitrogen in the atmosphere: the inclusion of oxygen appears to be unimportant. The apparently small temperature dependence and lack of scatter outside the peak region in Figure 8.20 is due to the reduced scale required to display this enormous phenomenon: curve (a) is a replot of that given in Figure 8.1: all the measurements present in Figures 8.1 - 8.8 were made after carefully flushing the cryostat with pure helium gas at room temperature.

The majority of the observed peaks show a maximum in the region of 63 K - the melting temperature of solid nitrogen. The sharp rise in attenuation up to this point could be explained in terms of the melting of solid nitrogen which was frozen on to the sample or transducer during cooling from 77 K to 4.2 K. A very rapid rise in

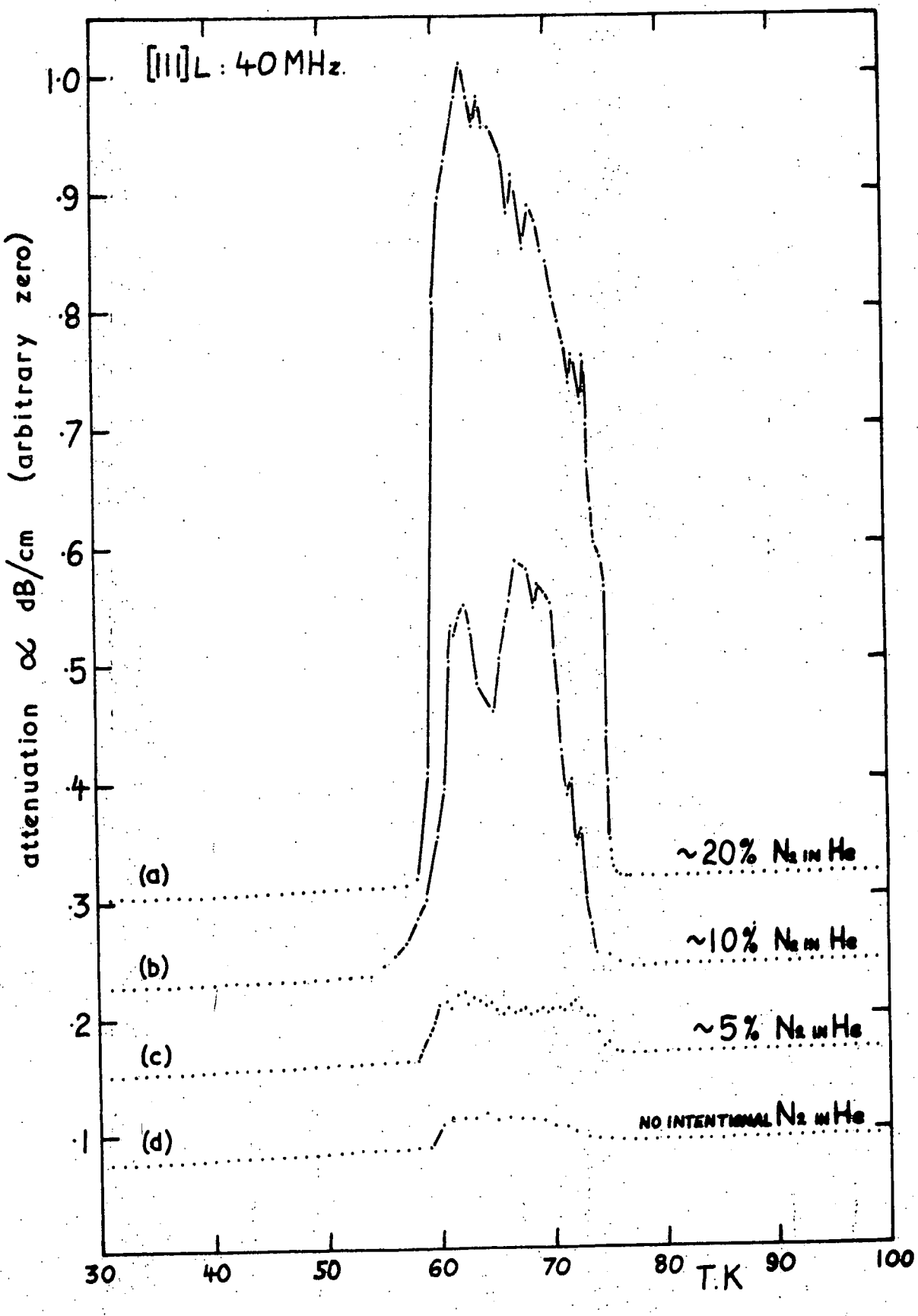

The low temperature ultrasonic attenuation anomally of GaAs in atmospheres of (a) ∿20% N_2 in He, (b) ∿10% N_2 in He, (c) ∿5% N_2 in He, (d) nominally pure He.

FIGURE 8.20

acoustic attenuation has been observed in many materials on approaching their melting temperatures from below (see, for example, Saunders et al, 1967). If the acoustic coupling between condensed nitrogen and GaAs/CdS were high enough to allow a substantial penetration of acoustic energy into the nitrogen on pulse-reflection at a coated surface, then absorption in the nitrogen could cause high apparent reflection losses from the ultrasonic pulses. This explanation is in qualitative agreement with the attenuation rise below 63 K:

(i) the peak rises to a maximum at 63 K, where the latent heat increases the total nitrogen energy-requirement greatly.

(ii) there are no anomalous acoustic losses on cooling past 63 K.

(iii) the peak height is roughly proportional to the atmospheric nitrogen content before cooling, and therefore to the thickness of a condensed nitrogen film formed on cooling past 63 K.

It is very difficult to make an accurate quantitative check of the agreement with experiments. A rough estimate has been made assuming:

(i) a nitrogen film thickness of 1 μm over an area of 1 cm^2.

(ii) the latent heat of fusion of nitrogen : 6.1 cal cm^{-1}.

(iii) total loss of the acoustic pulse energy to the nitrogen, as its latent heat; the apparent attenuation amplitude is much higher than that of the background attenuation.

(iv) the time over which melting takes place (calculated from Figure 5.30 and 8.20).

(v) an ultrasonic pulse duty cycle of 10^{-3} (measured).

The calculated pulse power required turns out to be of the order of 20 mW, which itself is of the order of magnitude of the ultrasonic pulse powers used in these measurements.

It is more difficult to ascribe a mechanism to the remainder of the peak above 63 K. The measured attenuation regains the background value at around 75 K: the complete peak width is approximately the range over which liquid nitrogen is stable at atmospheric pressure (under which these experiments were conducted). There is apparently no great abstraction of acoustic energy at the boiling temperature of nitrogen (77 K): it is possible that the nitrogen present after liquifaction is vapourised by a mechanism similar to that of the liquifaction: the time period between 63 K and 75 K is considerably longer than that between 58 K and 63 K and the latent heat of vapourisation is considerably larger than that of fusion.

CHAPTER 9

ULTRASONIC ATTENUATION IN MERCURY TELLURIDE

Alper (1968) investigated the temperature dependence of the attenuation of ultrasonic waves in HgTe between 4 K and room temperature at frequencies between 10 MHz and 75 MHz for some crystallographic directions, and the attenuation frequency dependence up to 300 MHz at 4.2 K and 77 K. His results for the temperature dependences of the [100] and [111] longitudinal attenuations in annealed and unannealed crystals are summarised in Figure 9.1 and 9.2, respectively. The main features are:

(i) a residual attenuation at temperatures below about 10 K.

(ii) a sharp rise between 20 K and 30 K to a peak at about 50 K, followed by a slow falling away.

(iii) an apparently rising background attenuation, particularly for the [100]L mode at 10 MHz above 200 K.

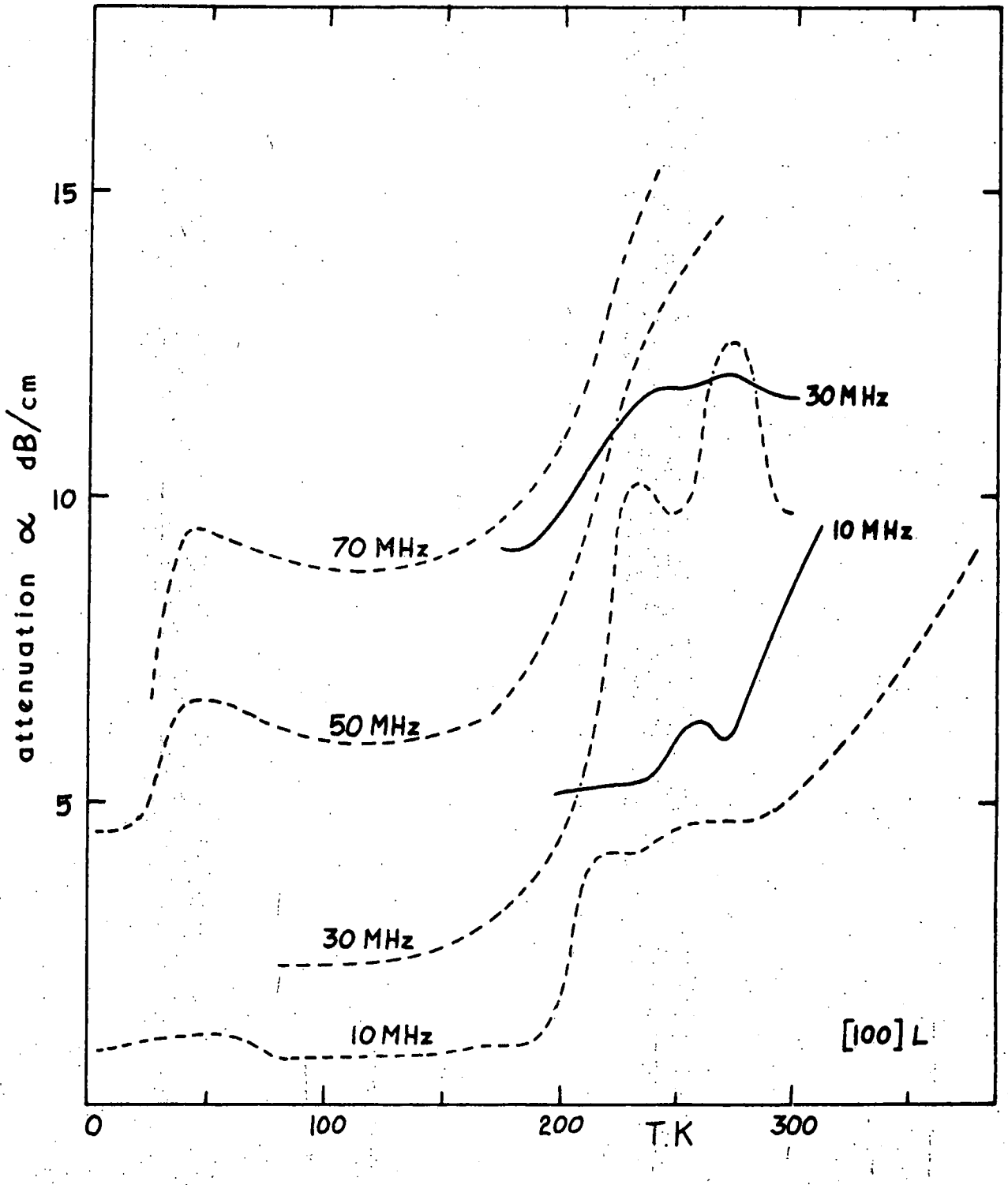

The longitudinal ultrasonic attenuation in the [100] direction of HgTe measured by Alper (1968).

FIGURE 9.1

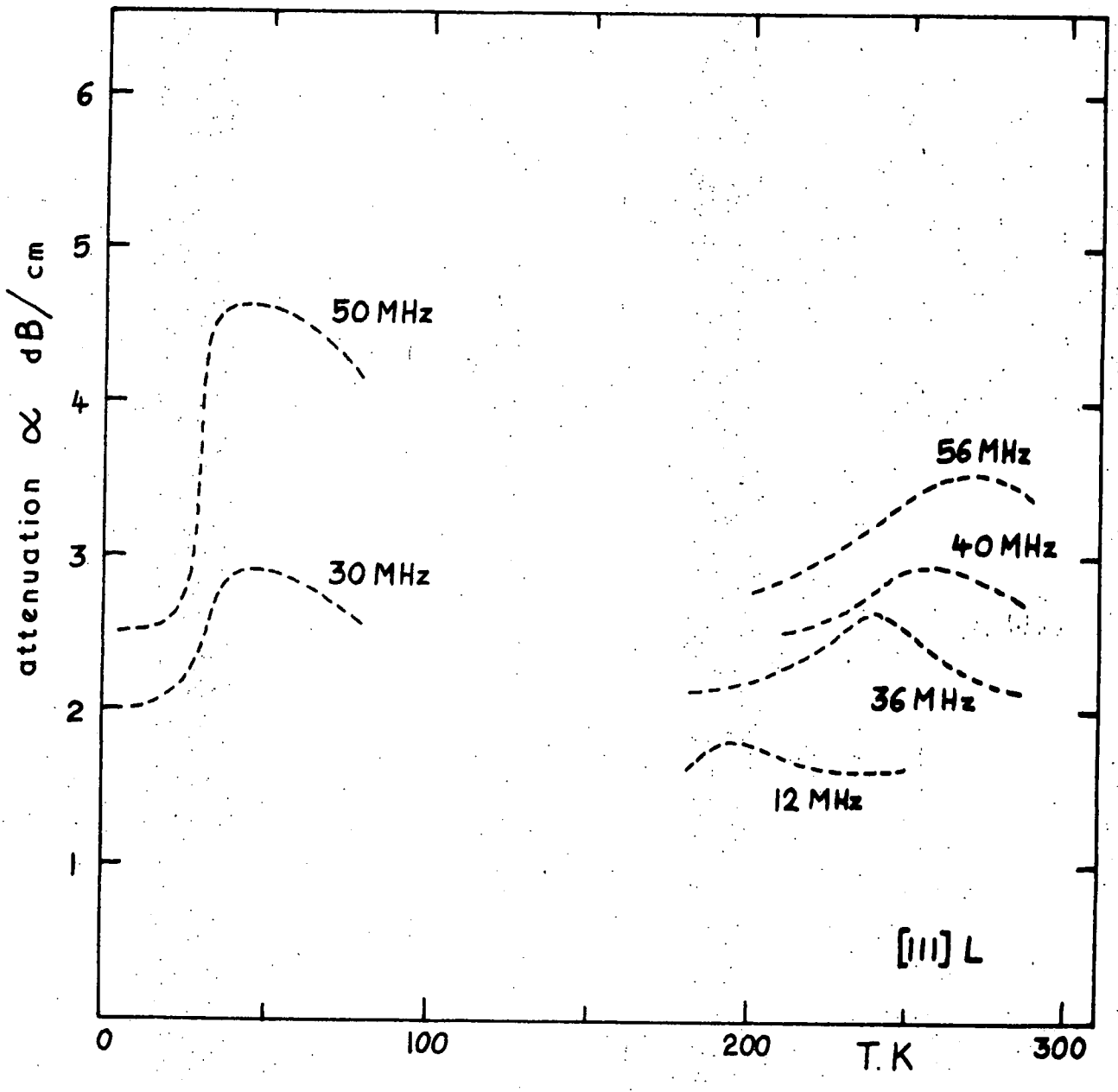

The longitudinal ultrasonic attenuation in the [111] direction of HgTe measured by Alper (1968).

FIGURE 9.2

(iv) a peak or set of peaks in attenuation between 200 K and 300 K whose position depends on frequency.

Alper (1968) attributed the residual attenuation at low temperatures to dislocation damping of the ultrasound, the sharp rise and peak at about 50 K to thermal phonon damping, and the high temperature peaks to forced dislocation-motion damping (Bordoni peaks). He observed that the background attenuation for the 10 MHz [100]L mode followed the relation

$$\alpha = 16.7 \exp(-0.063/kT) \qquad (9.1)$$

between 230 K and 388 K.

In this work, preliminary attenuation measurements made at above 300 MHz showed frequency dependences for the [100]L and [111]L modes in the region of the low temperature peak to be entirely uncharacteristic of thermal phonon damping, the attenuation falling away above 300 MHz rather than following a linear or square law dependence on frequency (see Section 8.1), suggesting that the controlling interaction in this temperature region is the same as that at 4.2 K, where Alper (1968) found a similar levelling-off above 200 MHz. To investigate this dislocation damping more fully, measurements of attenuation have been made over wide frequency and temperature ranges for longitudinal waves propagating in the two major crystallographic directions in HgTe: [100] and [111].

It has long been recognised that the effect of dislocations is important in mechanical damping in solids (Read, 1941). Koehler (1952) proposed a model for the

damping of sound waves by dislocations vibrating as strings, pinned at the ends by defects. This approach was developed by Granato and Lücke (1956), whose model forms the basis of present understanding of the interaction.

9.1 THE GRANATO-LÜCKE THEORY

In the Granato-Lücke (1956) model for dislocation damping of mechanical waves the dislocations are treated as "strings" through the crystal, pinned in position at various points along their length at dislocation nodes or by vacancies, impurities or other point defects. The distance between any two adjacent pinning points (L) will be a function of dislocation density, point defect density, and the spacial distribution of the pinning points. For a random distribution of pins there will be a distribution of loop lengths which is an inverse exponential of length (Granato and Lücke, 1966): in the following derivation it is assumed that the distribution can be approximated by a single loop length, L_c. If the stresses imposed on a pinned dislocation are sufficiently large, breakaway from some of the weaker pins can take place, causing emergy absorption on imposition of the stress and hysteresis on relief, as the subsequent collapse to the initial pinning condition will be elastic. The stresses involved in ultrasonic experiments of the kind performed in this work are too small to cause breakaway without the imposition of an external static stress (Alper and Saunders 1969), and it will be assumed that all the pins are equally infinitely resistant to unpinning by stress alone. However, it is possible for some of the pins to be thermally deactivated,

and this would give a temperature-dependent loop length distribution.

Under the above conditions, the dislocations may be represented by a set of extensible strings, all of length L_c and each with an effective mass per unit length A, acting under the influence of a line tension on displacement which imposes a force C per unit dislocation length. The equation of motion for a single dislocation may be written

$$A \frac{\partial^2 U}{\partial t^2} + B \frac{\partial U}{\partial t} - C \frac{\partial^2 U}{\partial y^2} = b\sigma \qquad (9.2)$$

where $U = U(x, y, t)$ is the displacement in the x direction from its equilibrium position: $U(x, y, t) = 0$ at the nodal points ($y = 0$, $y = 1$). Other parameters in equation (9.2) are defined as follows:

A is the effective mass per unit length, given approximately by

$$A = \rho b^2 \qquad (9.3)$$

ρ is the density

b is the Burger's vector

B is the damping coefficient, which is equal to the frictional force on unit length of a dislocation moving at unit velocity

C is the force per unit length imposed by the line tension, and is given by

$$C = \frac{2Gb^2}{\pi(1-\nu)} \qquad (9.4)$$

G is the shear modulus of the material in the slip plane

ν is Poisson's ratio

σ is the applied stress

$b\sigma$ is the driving force per unit length of the dislocation exerted by the applied stress.

In order to evaluate the mechanical damping an expression for the total strain is necessary:

$$\varepsilon = \varepsilon_{el} + \varepsilon_{dis} \tag{9.5}$$

The elastic strain (ε_{el}) equals (σ/G). The dislocation strain (ε_{dis}) for a single loop may be written

$$(\varepsilon_{dis}) \text{ one loop} = \bar{U} L_c b \tag{9.6}$$

where the average dislocation displacement $\bar{U}$ is given by

$$\bar{U} = \frac{1}{L_c} \int_o^{L_c} u(y)\, dy \tag{9.7}$$

for a dislocation-line density of Λ , the dislocation strain becomes

$$\varepsilon_{dis} = \frac{\Lambda b}{L_c} \int_o^{L_c} u(y)\, dy \tag{9.8}$$

The total strain expression (9.5) may now be inserted into Newton's equation of motion of the form

$$\frac{\partial^2 \sigma}{\partial x^2} = \rho \frac{\partial^2 \varepsilon}{\partial t^2} \tag{9.9}$$

to give

$$\frac{\partial^2 \sigma}{\partial x^2} - \frac{\rho}{G} \frac{\partial^2 \sigma}{\partial t^2} = \frac{\Lambda \rho b}{L_c} \frac{\partial}{\partial t^2} \int_o^{L_c} S\, dy \tag{9.10}$$

Granato and Lücke (1956) showed that equations (9.2) and (9.10) form a system of simultaneous equations. The displacement U may be derived from a trial solution of the form

$$\sigma = \sigma_o \exp(-\alpha x) \exp\left[i(\omega t - \frac{\omega x}{v})\right] \tag{9.11}$$

where ω is the mechanical wave angular frequency, and

expressions for the modulus change ($\Delta M/M$) and the decrement (α/ω) may be deduced:

$$\frac{\Delta M}{M} = \frac{\Omega\Delta\ \Lambda L_c^2}{\pi} \frac{1 - (\omega/\omega_o)^2}{\left[1-(\omega/\omega_o)^2\right]^2 + (\omega/\omega_o D)^2} \qquad (9.12)$$

$$\Delta = \Omega\Delta_o \Lambda L_c^2 \frac{(\omega/\omega_o D)}{\left[1-(\omega/\omega_o)^2\right]^2 + (\omega/\omega_o D)^2} \qquad (9.13)$$

where:

Ω is an orientation factor, which takes account of the propagation orientation with respect to the dislocation slip system.

Δ_o depends solely on material parameters:

$$\Delta_o = \frac{8\ G\ b^2}{\pi^3 C} \qquad (9.14)$$

ω_o is the dislocation resonant frequency in the absence of damping:

$$\omega_o^2 = \frac{\pi^2 C}{A\ L_c^2} \qquad (9.15)$$

D is the normalised inverse damping coefficient, indicating the freedom of dislocation movement:

$$D = \frac{\omega_o\ A}{B} \qquad (9.15)$$

The frequency dependence of the normalised decrement ($\Delta/\Omega\Delta_o\Lambda L_c^2$) calculated in this way is shown in Figure 9.3 as a function of the normalised frequency (ω/ω_o) (after Granato and Lücke, 1956). The form of the decrement depends greatly on the value of D. For $D>>1$ (low damping) the attenuation (α) and decrement pass through maxima at the resonant frequency ω_o; for $D<<1$ the loss follows a very broad peak, centred at ω_o but flat-topped, and the decrement

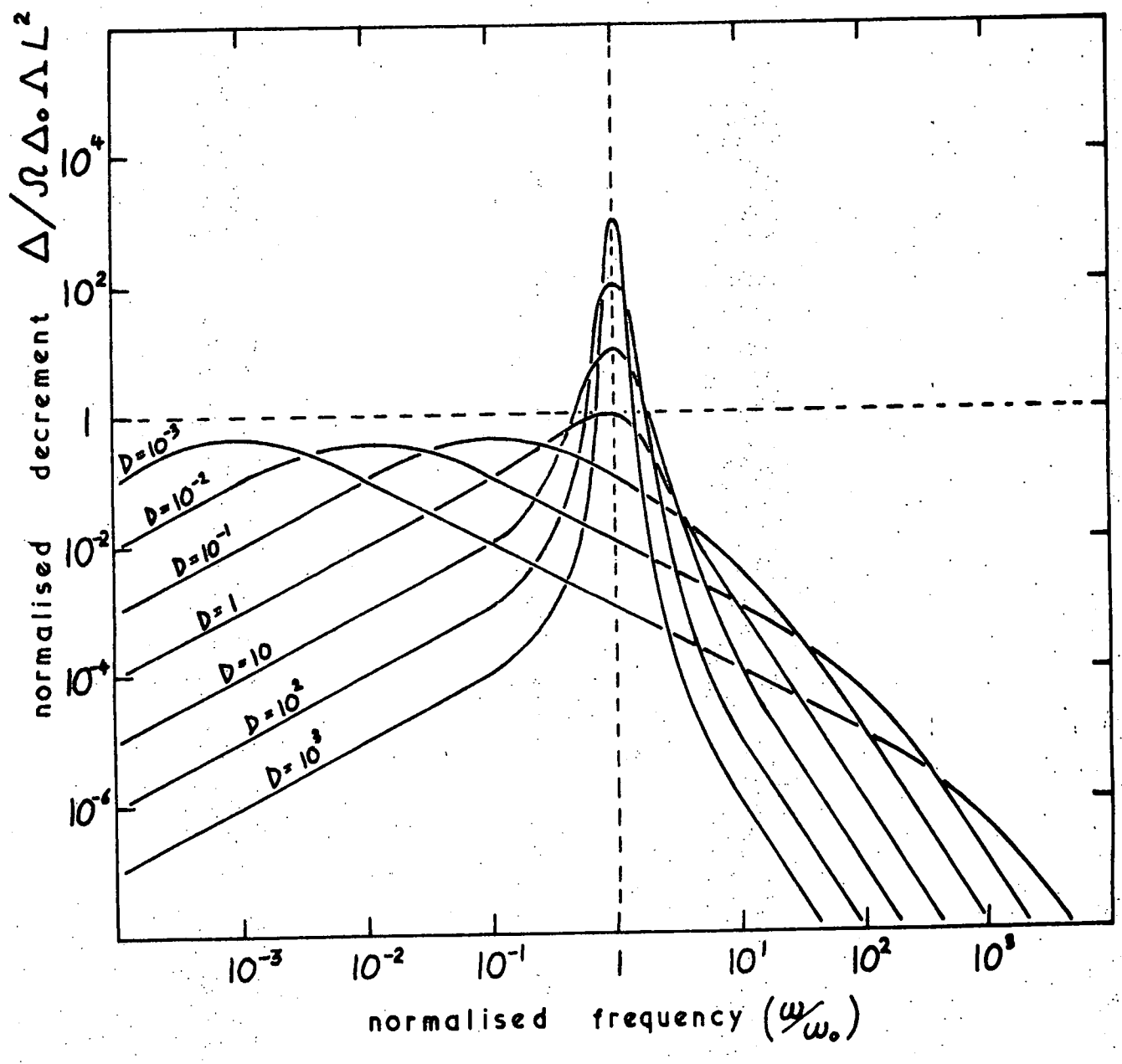

The damping of ultrasonic waves by dislocations : a plot of equation 9.13 as a function of frequency ω and damping coefficient D (after Granato and Lücke).

FIGURE 9.3

peaks at a frequency far below ω_o and then falls away as $(1/\omega)$ over the frequency range covered by the top of the peak in attenuation. In this latter condition ($D<<1$) the maximum in decrement is at frequencies far below ω_o (for example, at $\omega_o/100$ for $D = 10^{-2}$) and the region over which Δ is proportional to ω^{-1} extends up to frequencies above ω_o (for example, up to $10\ \omega_o$ for $D = 10^{-2}$); considerable simplification of expressions 9.12 and 9.13 may be effected in this region by putting $(\omega/\omega_o)^2<<1$. This approach was taken by Alper (1968) in analysing the dislocation damping of ultrasound in HgTe, and by Mason and Rosenberg (1966, 1967) in calculating the damping coefficients of aluminium and lead as a function of temperature. Unfortunately the approximation is not valid for mercury telluride over the frequency range of measurements made in this work, and the complete Granato-Lücke (1956) expressions 9.12 and 9.13 must be used.

Granato and Lücke (1966) have presented expressions for the decrement maximum Δ_M at frequency Δ_M in the approximation condition given above when an exponential distribution of loop lengths is included

$$\Delta_M = 2.2\ \Omega\Delta_o\ \Lambda\ L_E^2 \qquad (9.17)$$

$$\omega_M = \frac{0.084\ \pi^2\ C}{L_E^2\ B} \qquad (9.18)$$

where L_E is again a representative loop length. The main effect is to shift the attenuation maximum to a lower frequency, and thus to shift the decrement maximum to a lower frequency and a higher amplitude. Analysis of the effect of an exponential loop-length distribution on the

decrement for $D \sim 1$ yields very complicated results (see Truell et al, 1969) and in this region it is very difficult to calculate the experimental damping coefficient on such a basis.

9.2 EXPERIMENTAL RESULTS

The temperature dependences of longitudinal ultrasonic wave attenuation in HgTe from 2 K to 115 K in the [100] and [111] directions are presented in figure 9.4 to 9.11 and 9.12 to 9.19 respectively for frequencies at 100 MHz intervals between 50 MHz and 750 MHz. The results are summarised in Figures 9.20 and 9.21 along with the extension of the measurements up to 290 K: in regions where no curve is shown for a particular frequency the attenuation was found to be too high for measurements to be made using the equipment available. Three main features are discernable: a residual attenuation at the lowest temperature achieved (2 K); a sharp rise in attenuation up to a frequency-dependent peak between 40 K and 70 K; a slow frequency-dependent rise in background attenuation, all the way up to 290 K for the 50 MHz measurements. These will be discussed in turn.

(a) The residual attenuation

Figure 9.22 shows the residual attenuation at 4.2 K as a function of frequency for longitudinal wave propagation in the [100] and [111] directions of HgTe. The form of the frequency dependences in this region where only electronic and defect interactions are expected (Lewis, 1970) are consistent with Alper's (1968) discussion in

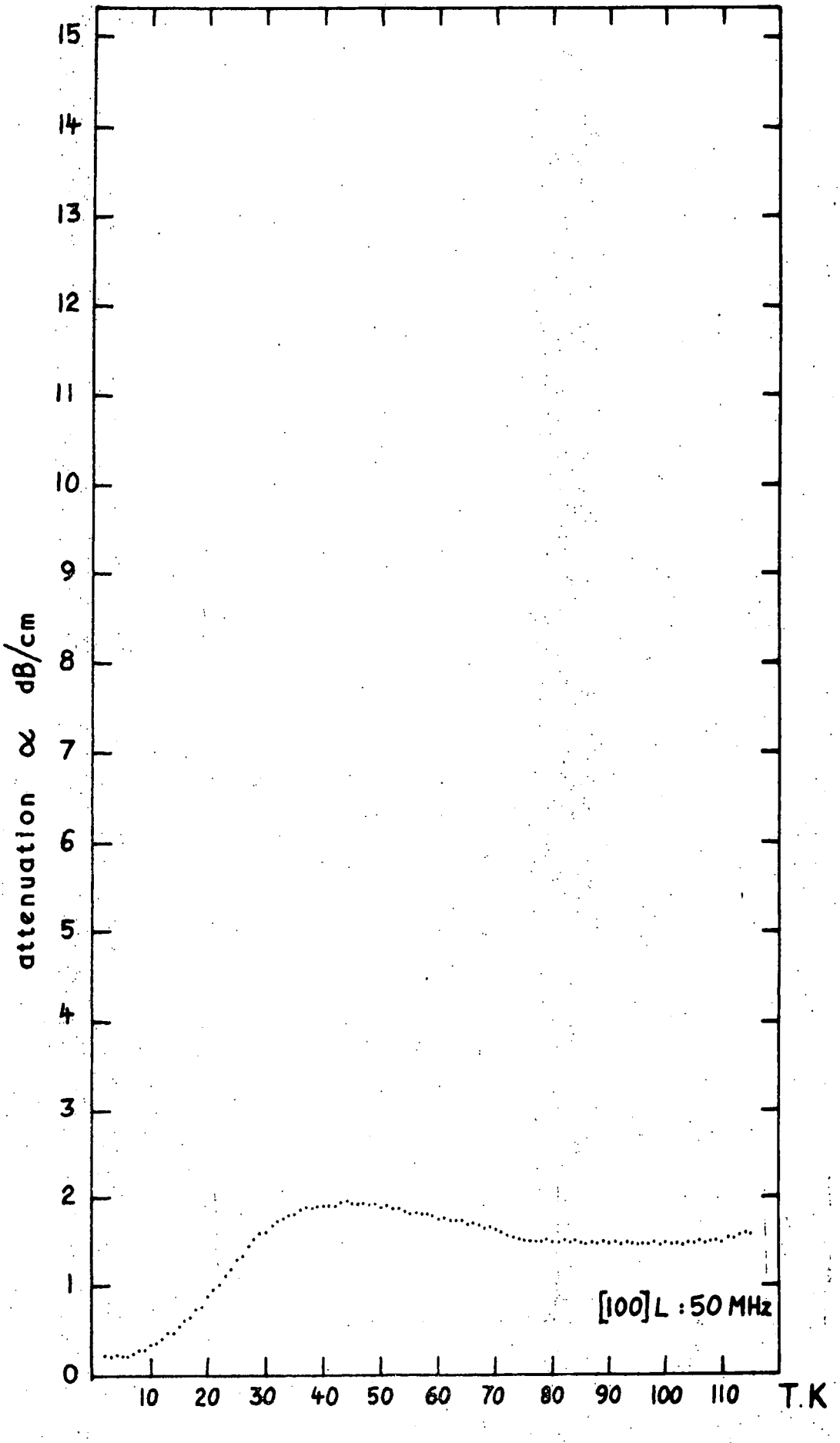

Longitudinal ultrasonic attenuation in the [100] direction of HgTe.

FIGURE 9.4

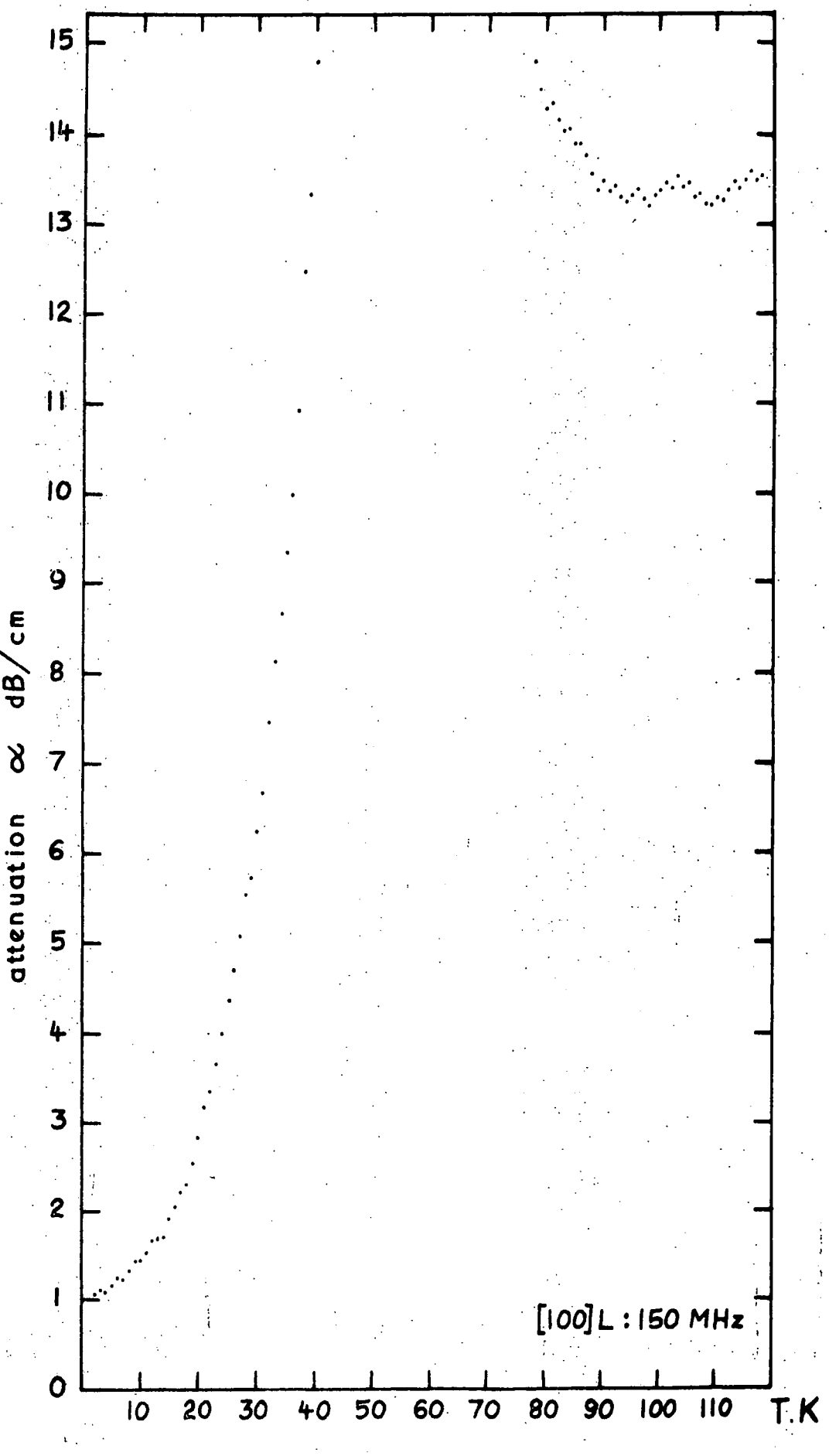

Longitudinal ultrasonic attenuation in the [100] direction of HgTe

FIGURE 9.5

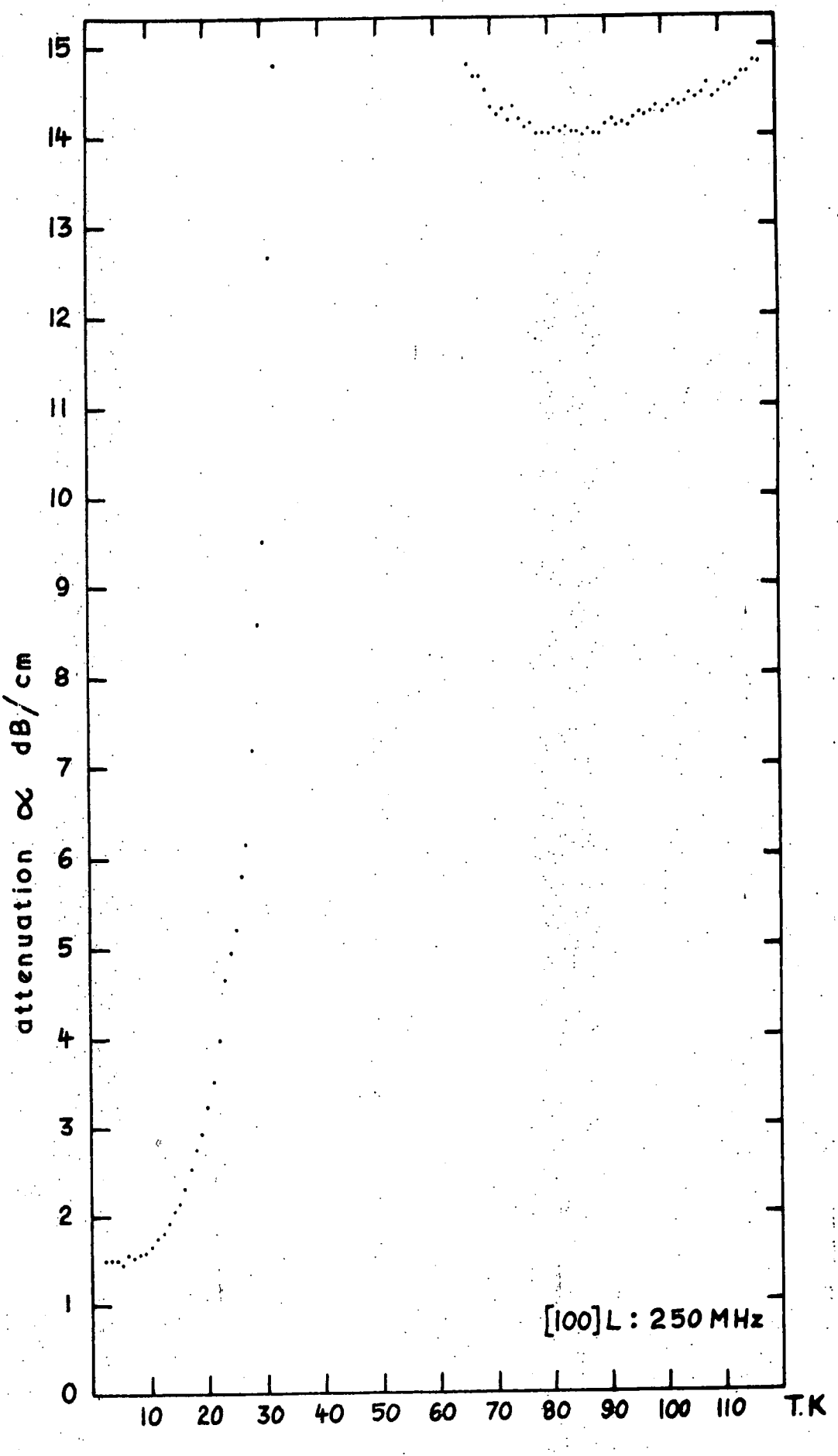

Longitudinal ultrasonic attenuation in the [100] direction of HgTe.

FIGURE 9.6

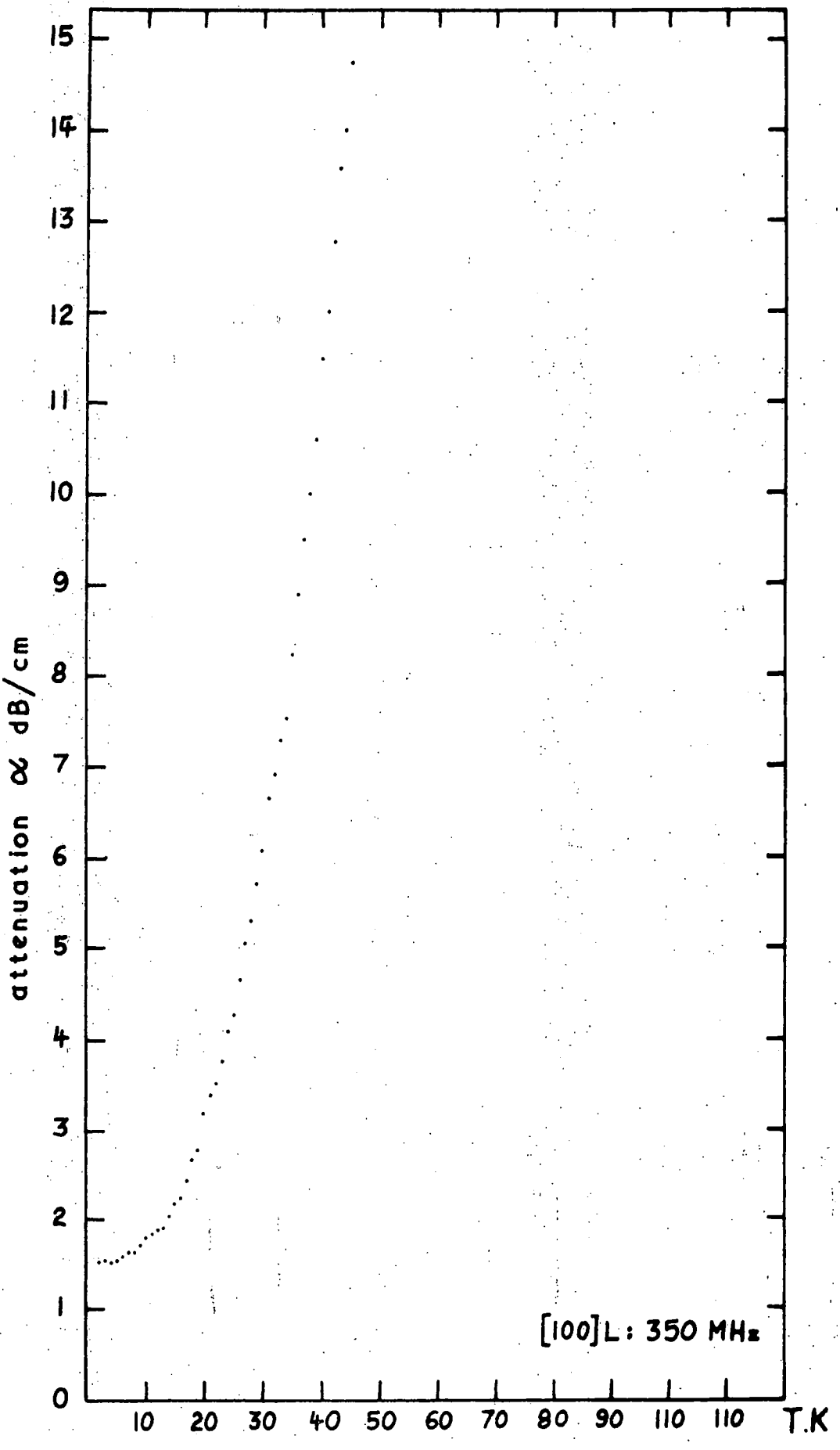

Longitudinal ultrasonic attenuation in the [100] direction of HgTe.

FIGURE 9.7

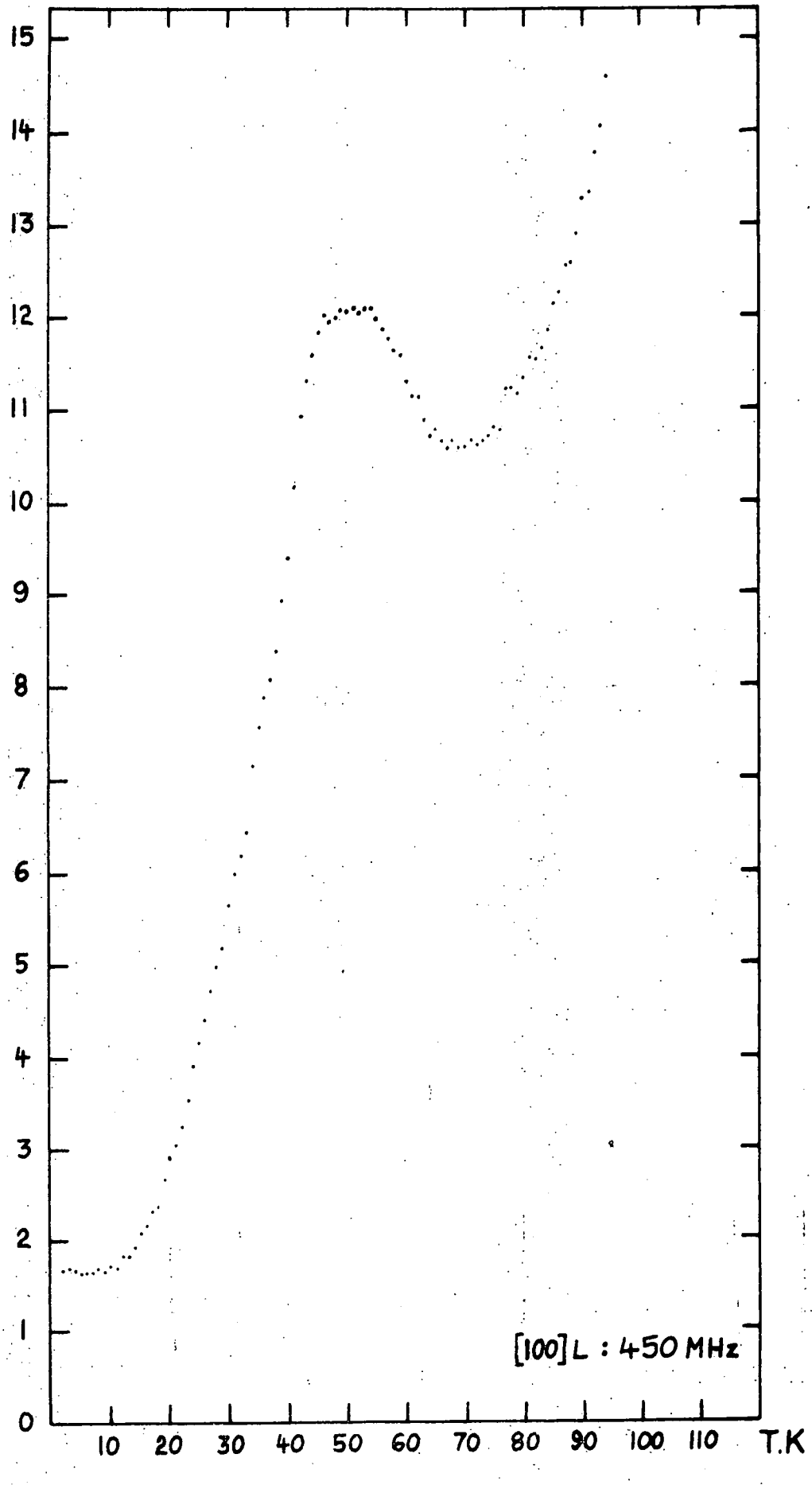

Longitudinal ultrasonic attenuation in the [100] direction of HgTe.

FIGURE 9.8

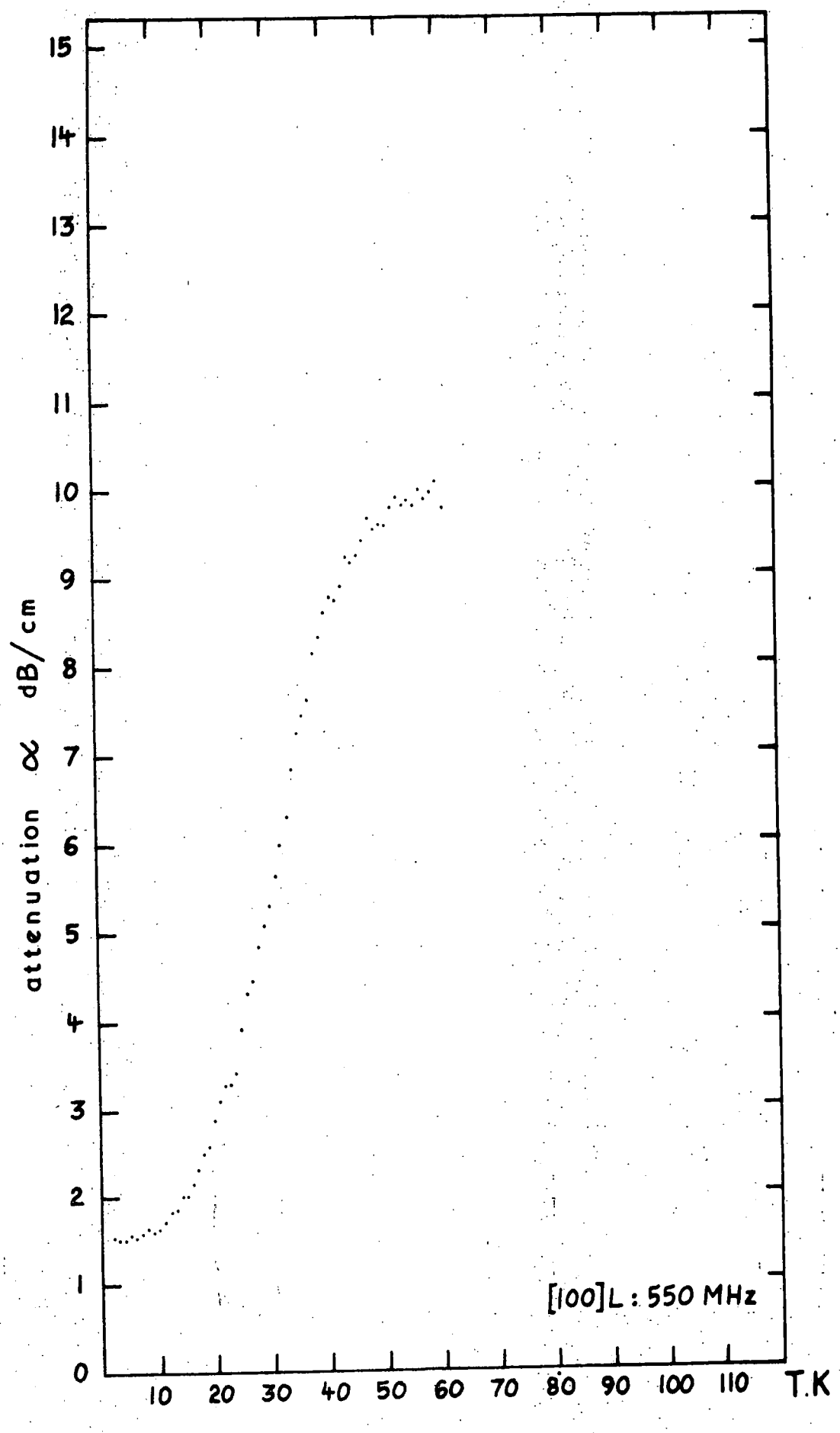

Longitudinal ultrasonic attenuation in the [100] direction of HgTe.

FIGURE 9.9

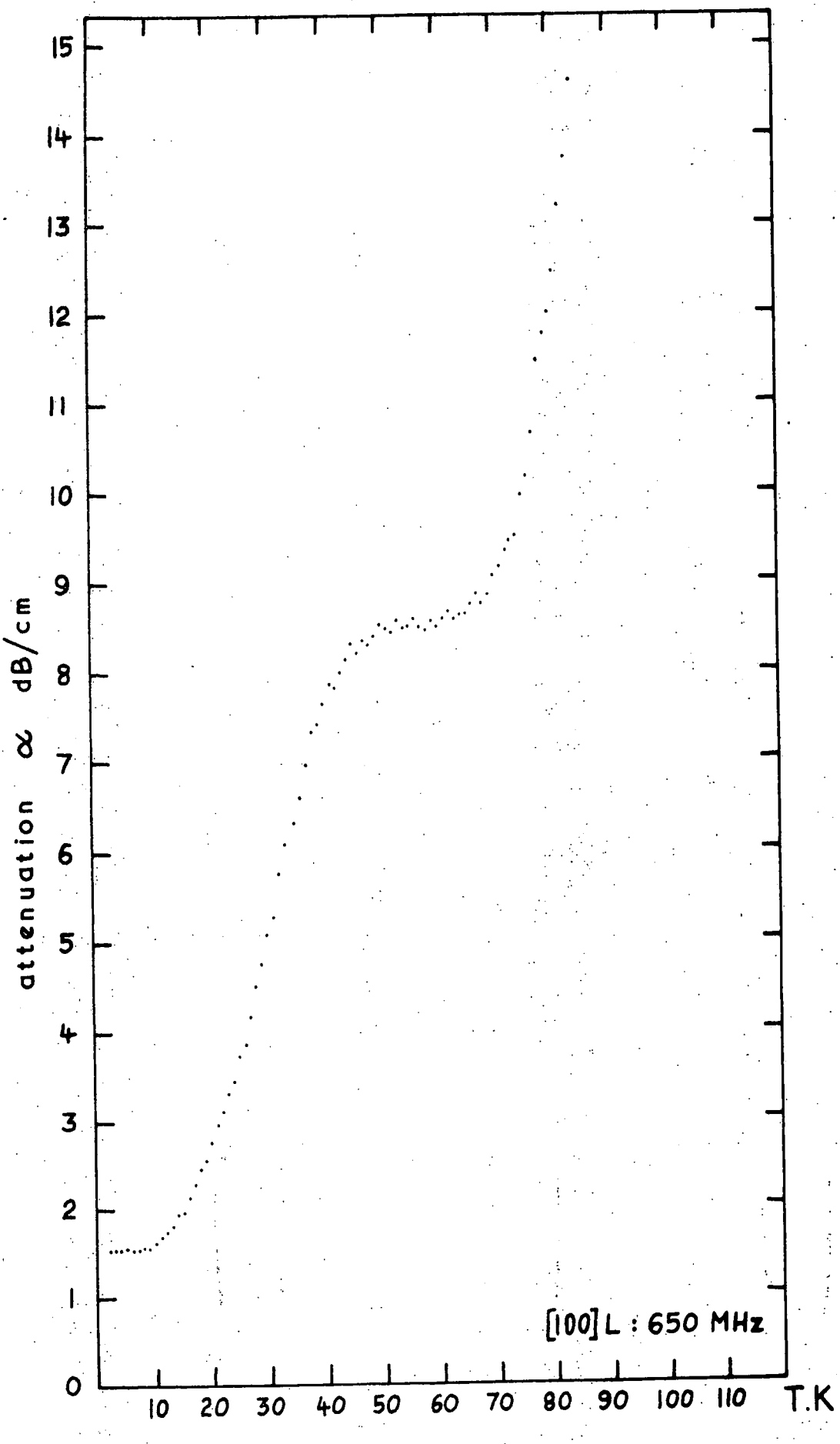

Longitudinal ultrasonic attenuation in the [100] direction of HgTe.

FIGURE 9.10

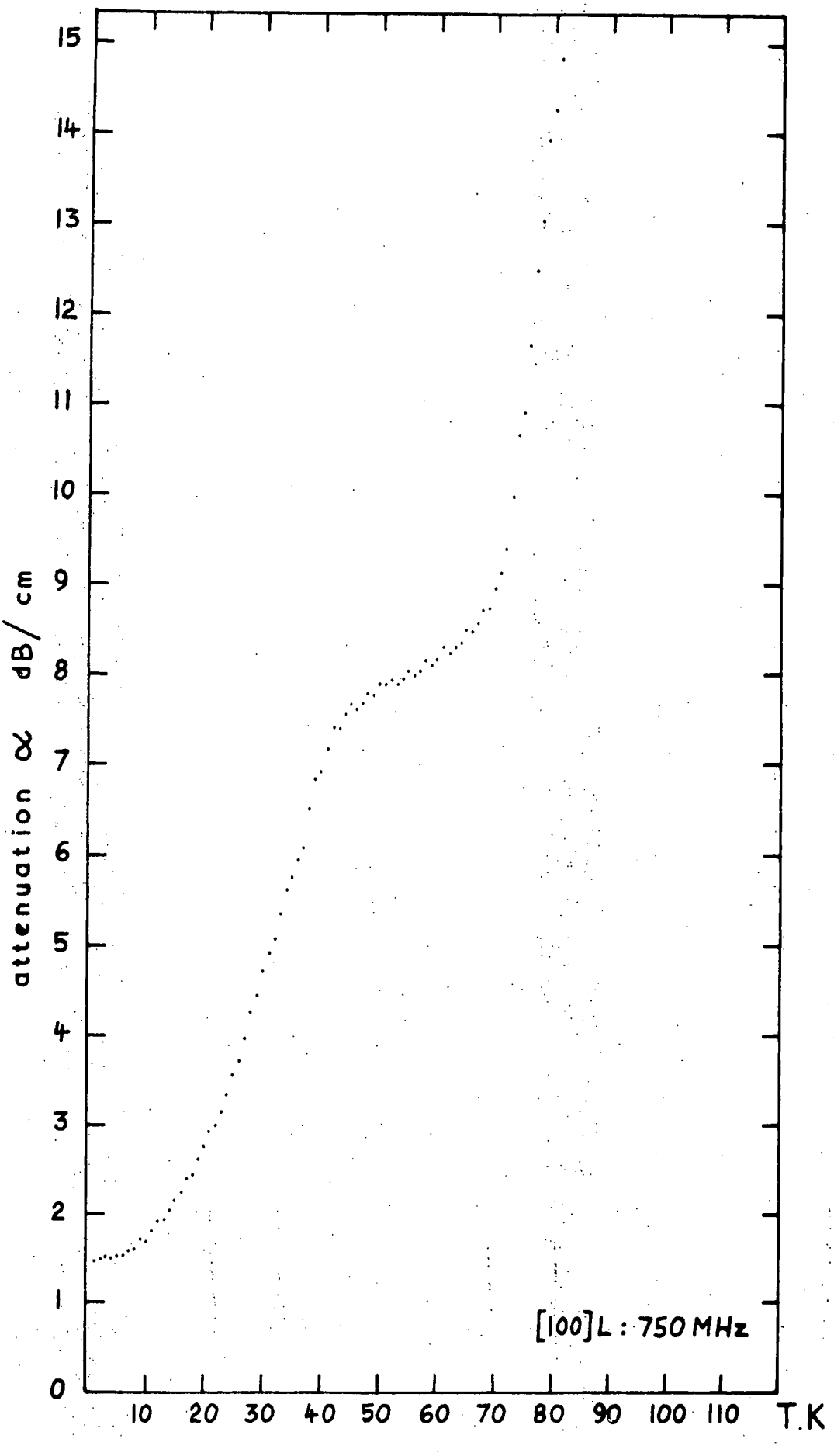

Longitudinal ultrasonic attenuation in the [100] direction of HgTe.

FIGURE 9.11

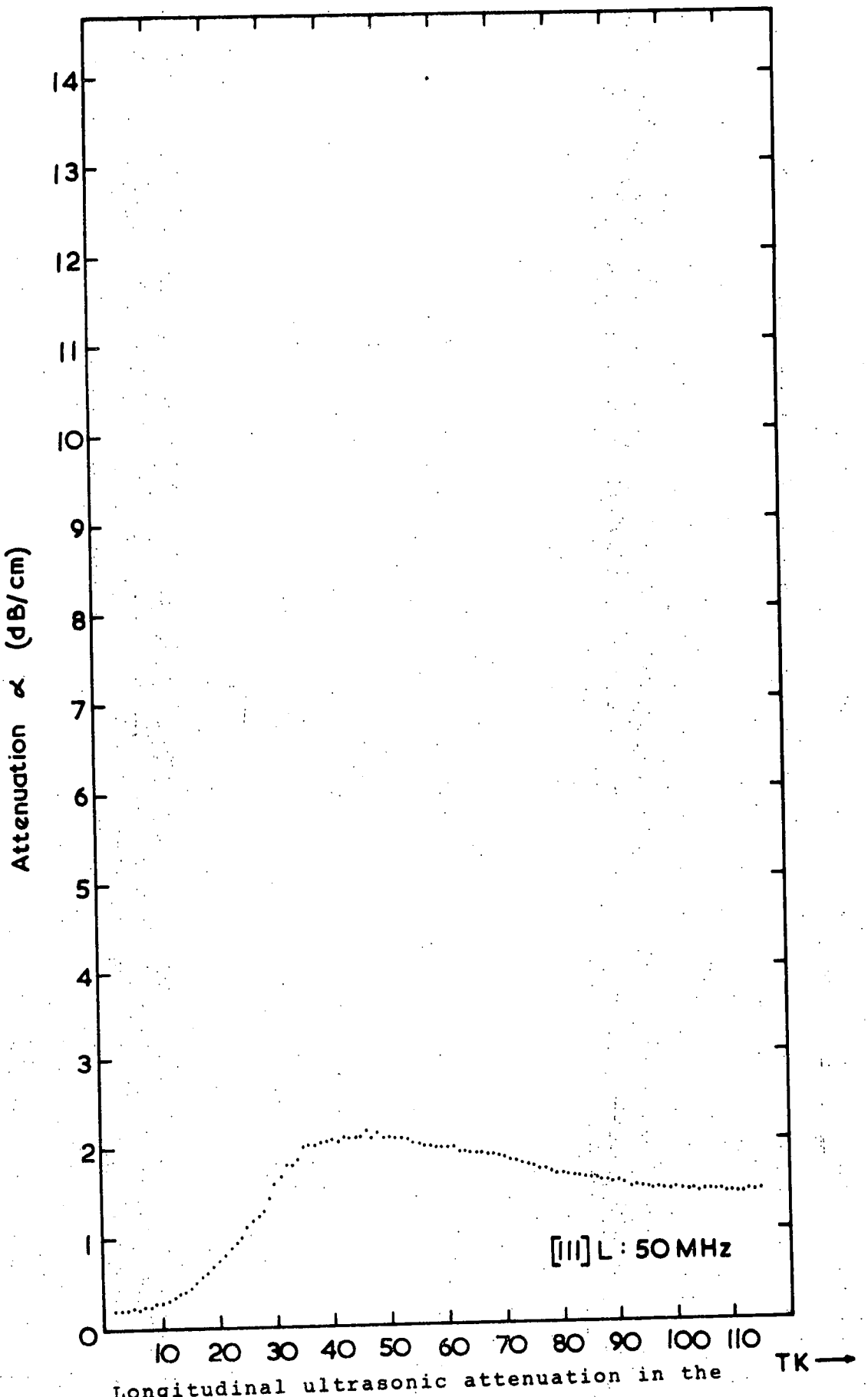

Longitudinal ultrasonic attenuation in the [111] direction of HgTe.

FIGURE 9.12

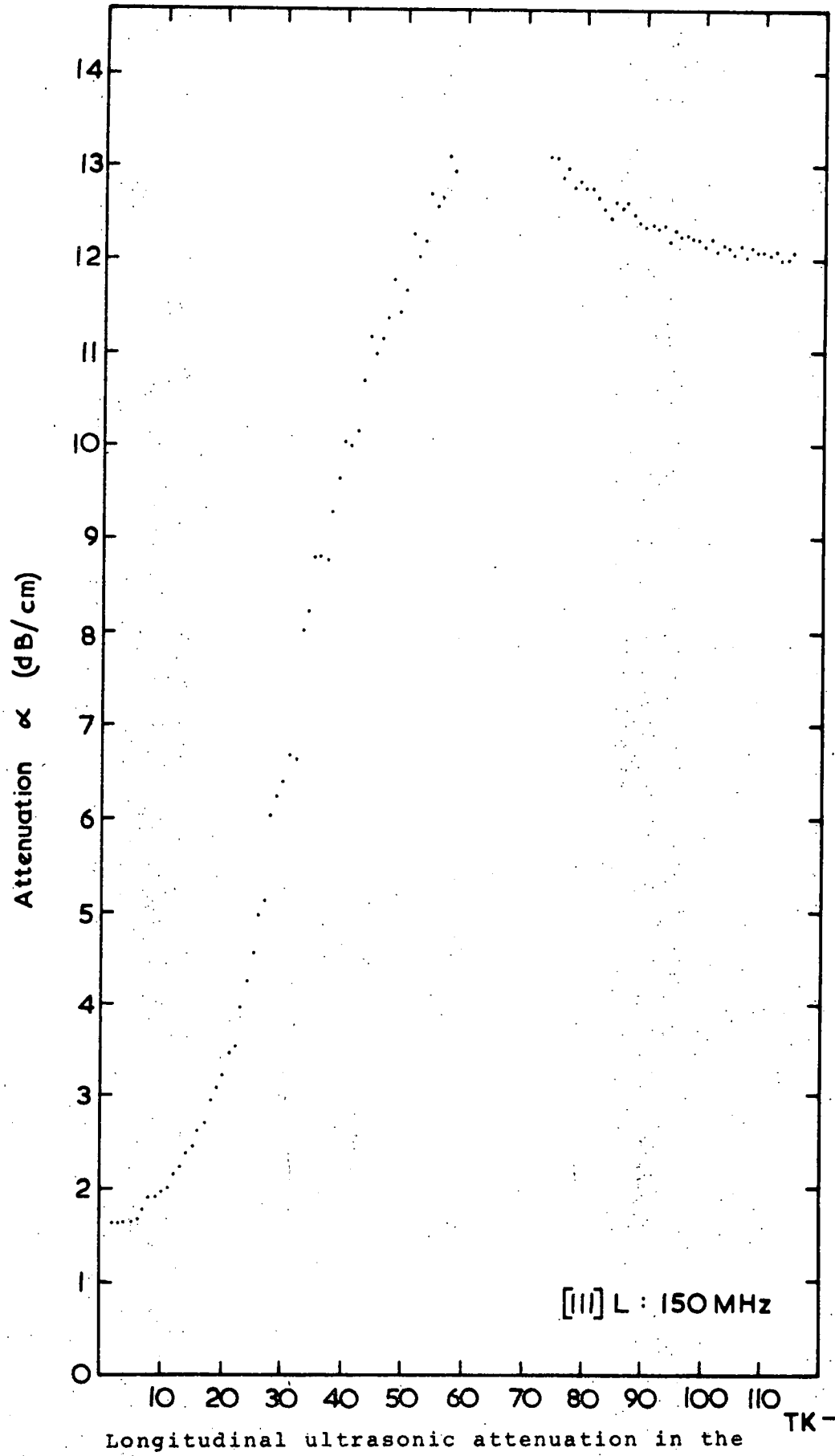

Longitudinal ultrasonic attenuation in the [111] direction of HgTe.

FIGURE 9.13

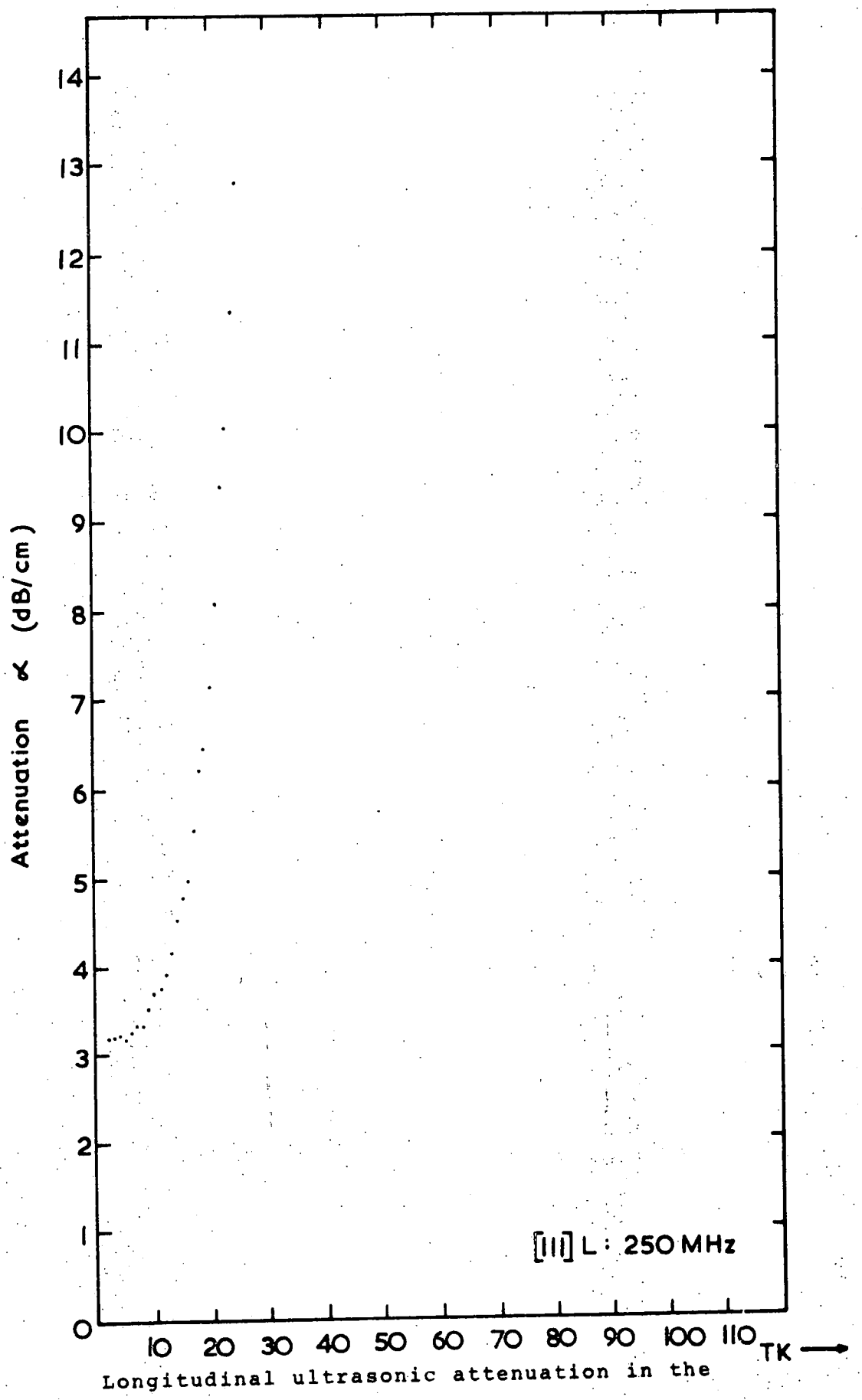

Longitudinal ultrasonic attenuation in the [111] direction of HgTe.

FIGURE 9.14

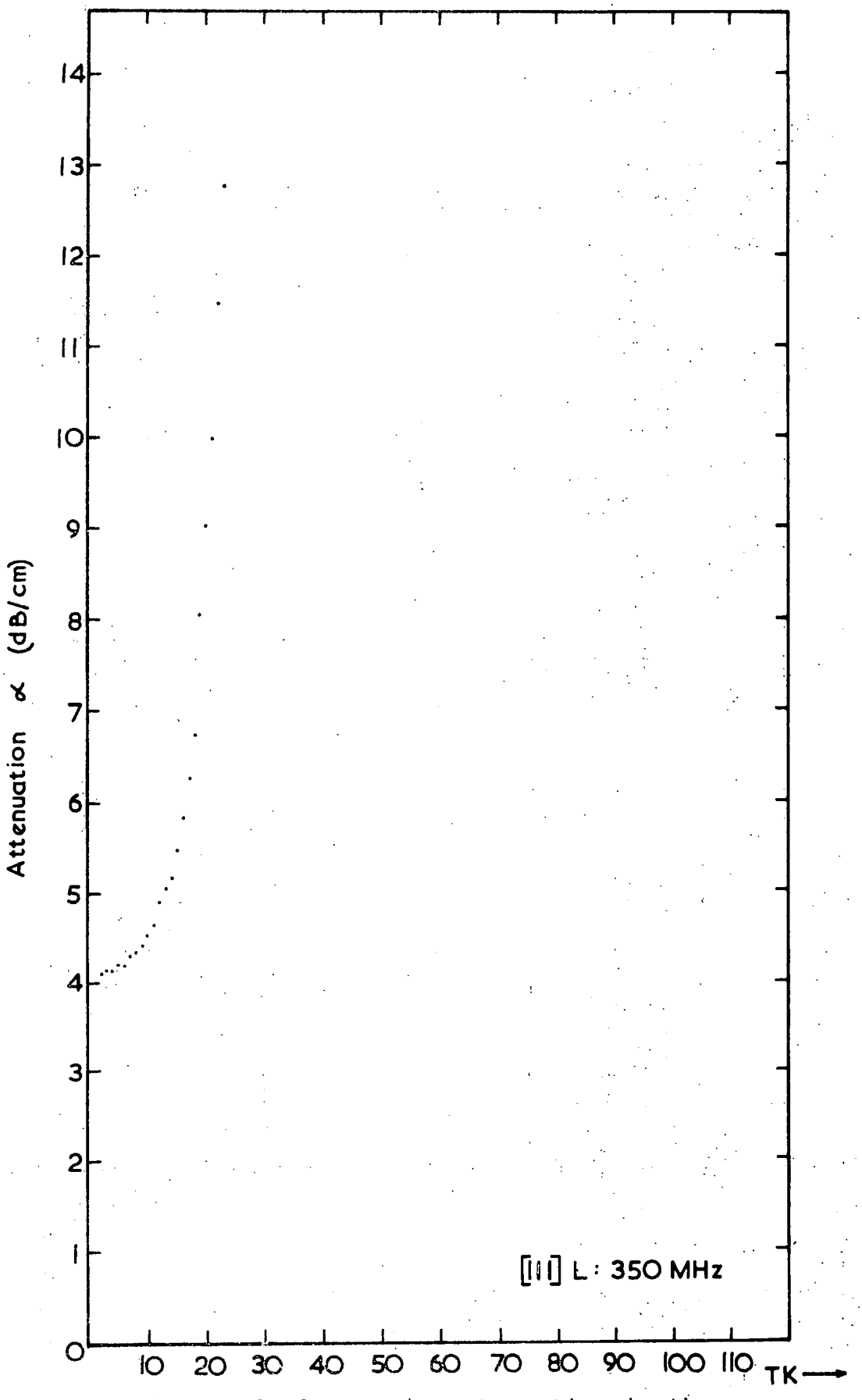

Longitudinal ultrasonic attenuation in the [111] direction of HgTe.

FIGURE 9.15

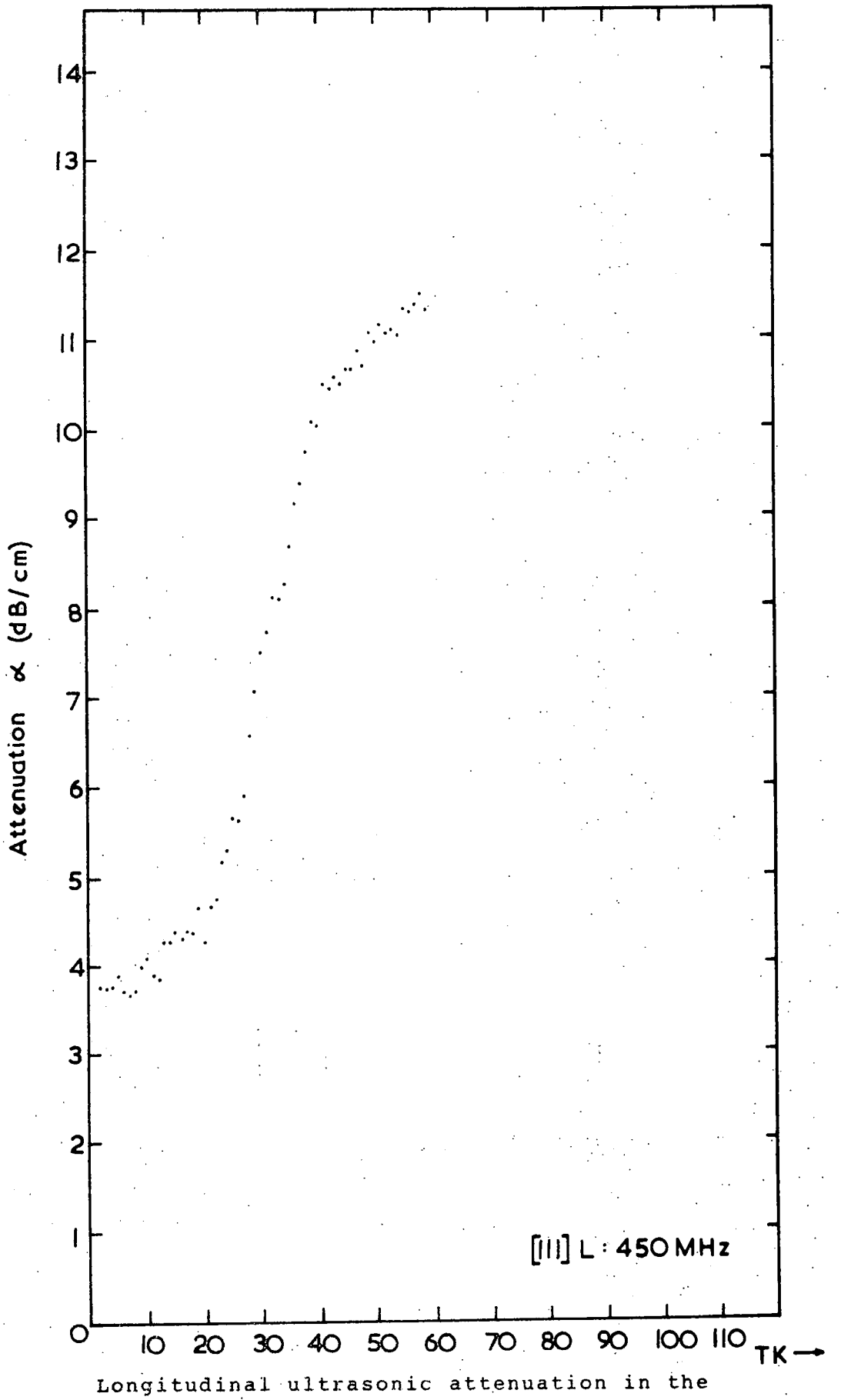

Longitudinal ultrasonic attenuation in the [111] direction of HgTe.

FIGURE 9.16

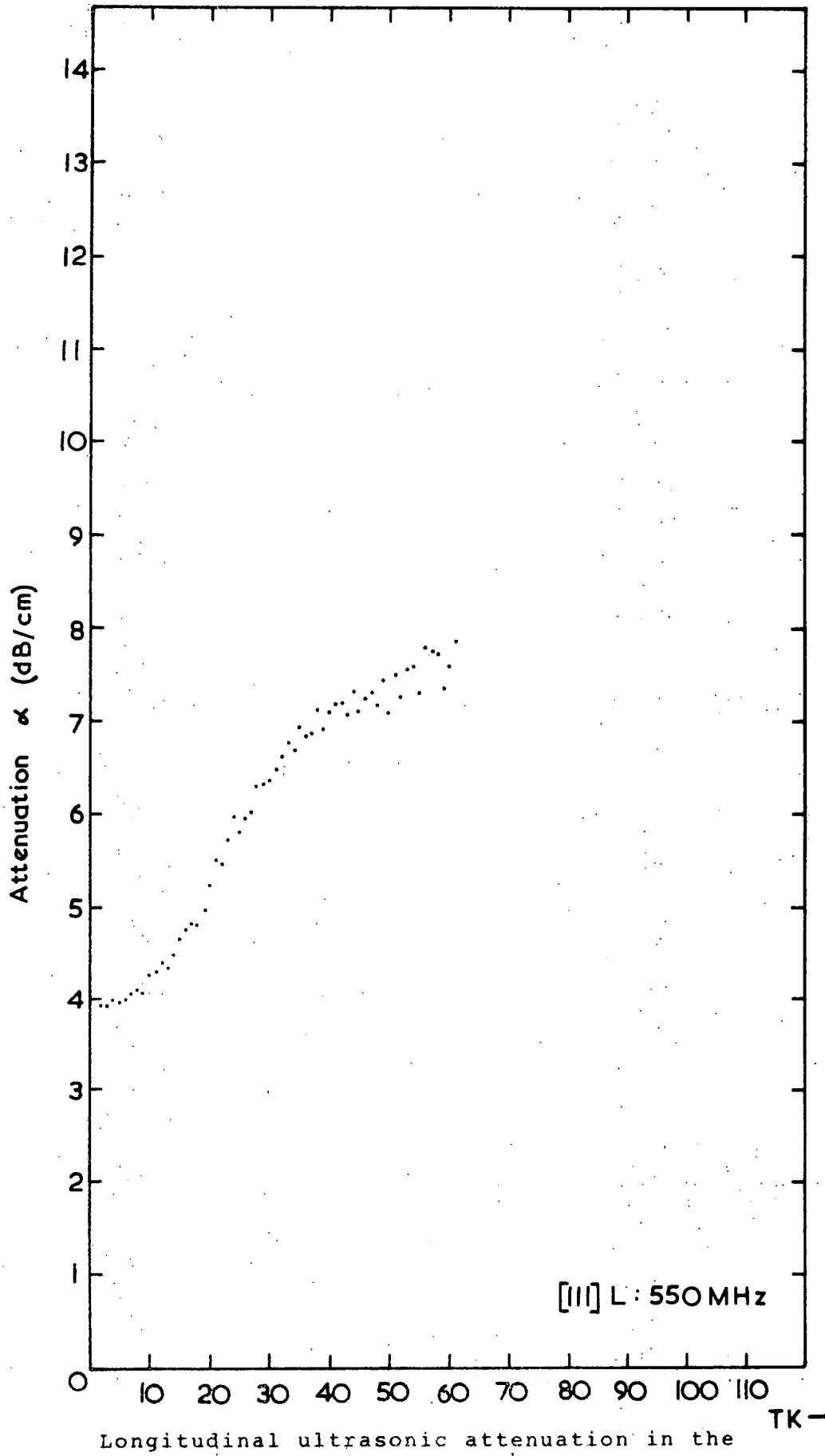

Longitudinal ultrasonic attenuation in the [111] direction of HgTe.

FIGURE 9.17

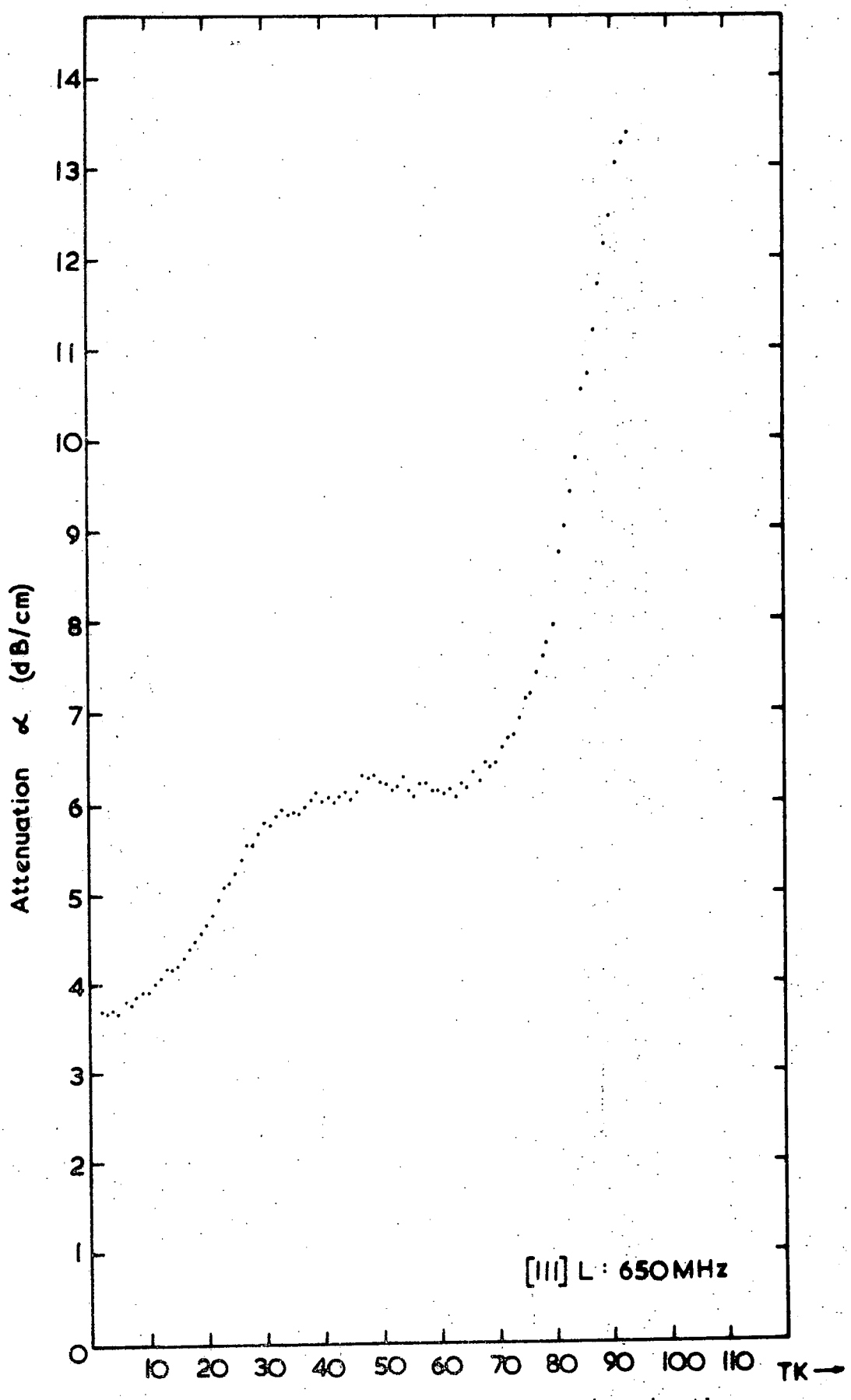

Longitudinal ultrasonic attenuation in the [111] direction of HgTe.

FIGURE 9.18

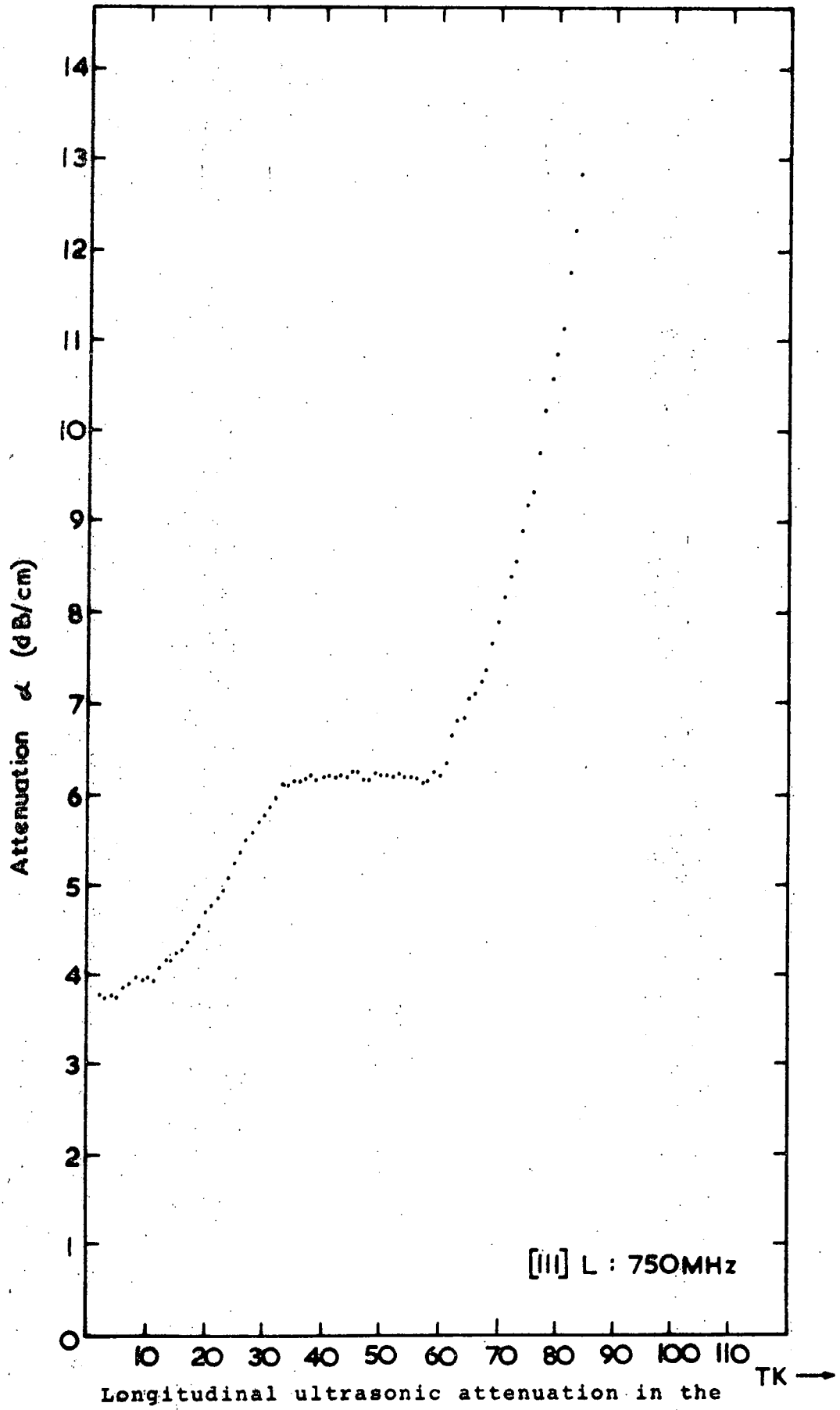

Longitudinal ultrasonic attenuation in the [111] direction of HgTe.

FIGURE 9.19

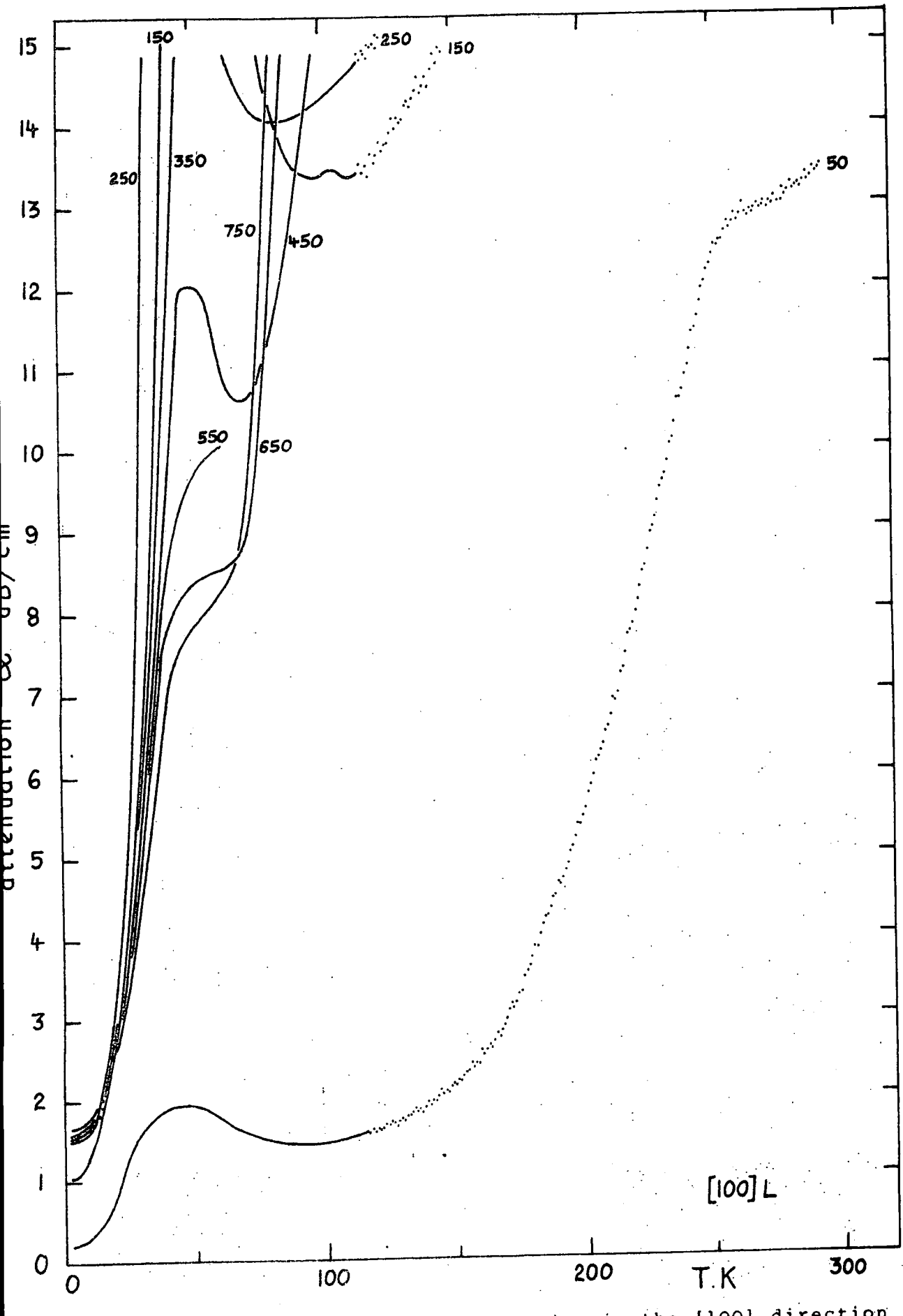

Longitudinal ultrasonic attenuation in the [100] direction of HgTe: A summary of figures 9.4-9.11 and data up to room temperature. Numbers refer to the ultrasonic frequencies associated with each line of measurements.

FIGURE 9.20

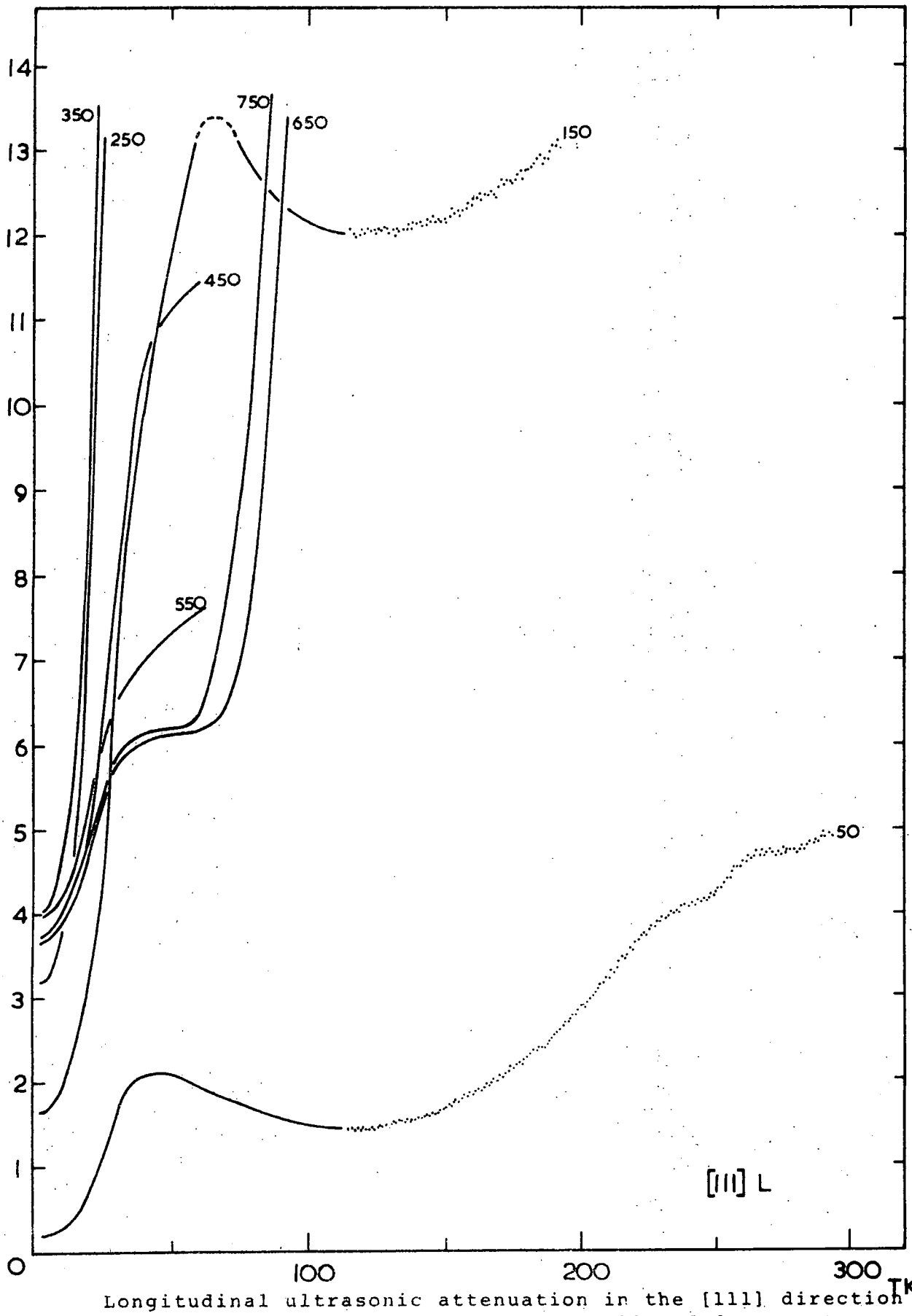

Longitudinal ultrasonic attenuation in the [111] direction of HgTe: a summary of figures 9.12-9.19 and data up to room temperature. Numbers refer to the ultrasonic frequencies associated with each line of measurements.

FIGURE 9.21

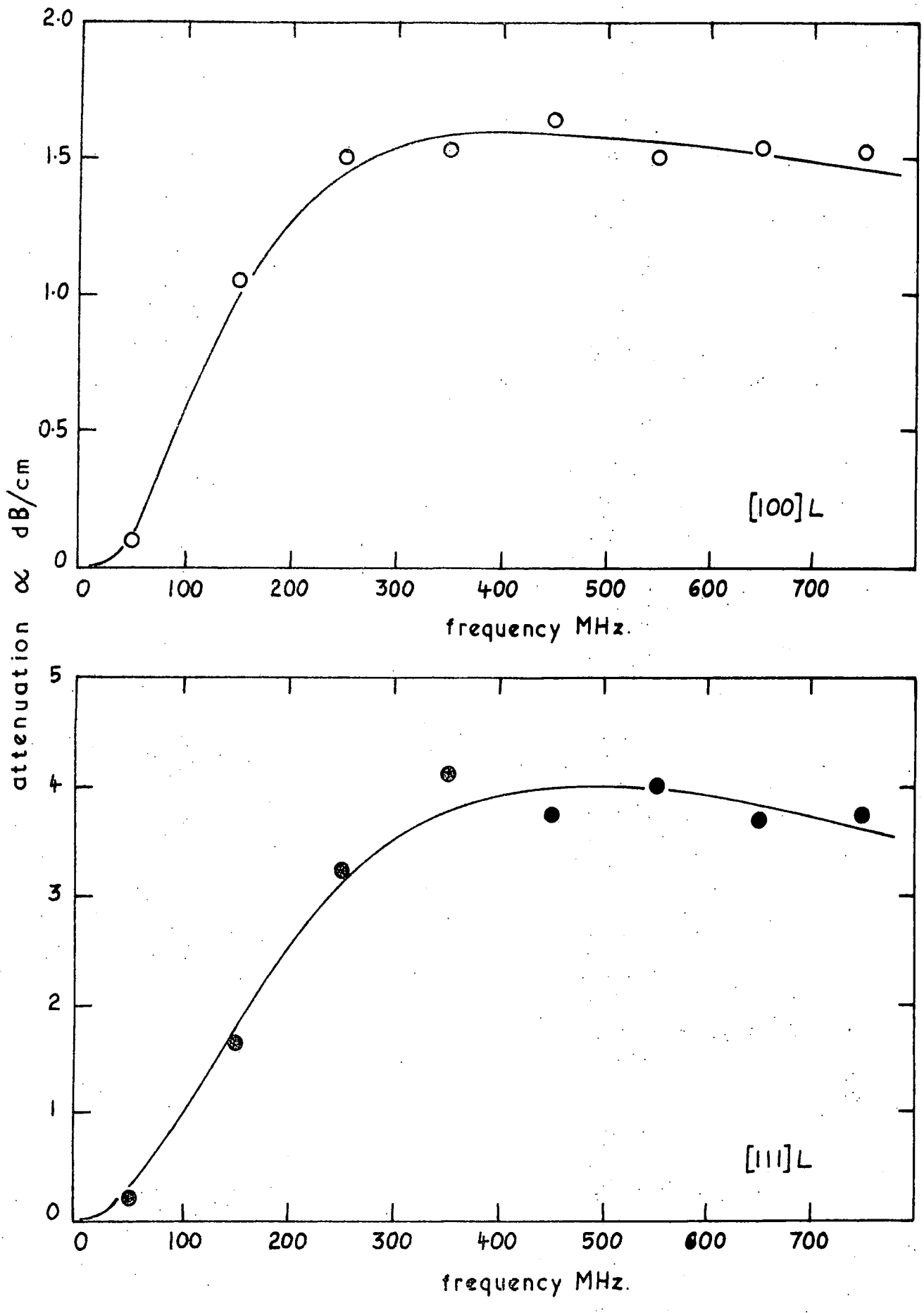

The 4 K residual longitudinal attenuations in the [100] and [111] directions of HgTe as a function of frequency. The lines are best fits to the data computed from equation 9.19.

FIGURE 9.22

terms of dislocation damping of the ultrasound. The full lines shown in Figure 9.22 are the computed best fits of the Granato-Lucke expression 9.13 to the experimental data: the fitting itself will be described later.

(b) The low temperature peak

The measurements of attenuation made by Alper (1968) in the temperature range 20 K to 70 K at frequencies up to 300 MHz are consistent with the form of the phonon-thermal phonon interaction described by Woodruff and Ehrenreich (1961) (see Section 8.1). The sharp rise is in the region where $\omega\tau = 1$. The temperature and frequency dependence of the $\omega\tau = 1$ condition has been computed here from the relation 8.7 for the thermal conductivity in terms of the phonon relaxation time using the data of Whitsett and Nelson (1972) (see Figure 9.23). However, the values of the Gruneisen parameter γ'_{WE} required to give a quantitative fit to the attenuation in this region are too high: between 2.7 and 4.8 for the [111]L, [100] L, [110]L and [111]S modes (calculated in this work). The frequency dependences of attenuation in the peak temperature range are in direct contradiction to the dependences associated with phonon-phonon interactions: the attenuation rises with frequency up to about 200 to 300 MHz, then falls away again (see Figure 9.24). It is possible that some of the attenuation above about 400 MHz can be accounted for by phonon-phonon interactions, but not the enormous peak below this frequency, which resembles a resonance - both in its frequency and temperature dependences. In view of the piezoelectric velocity coupling observed in propagation

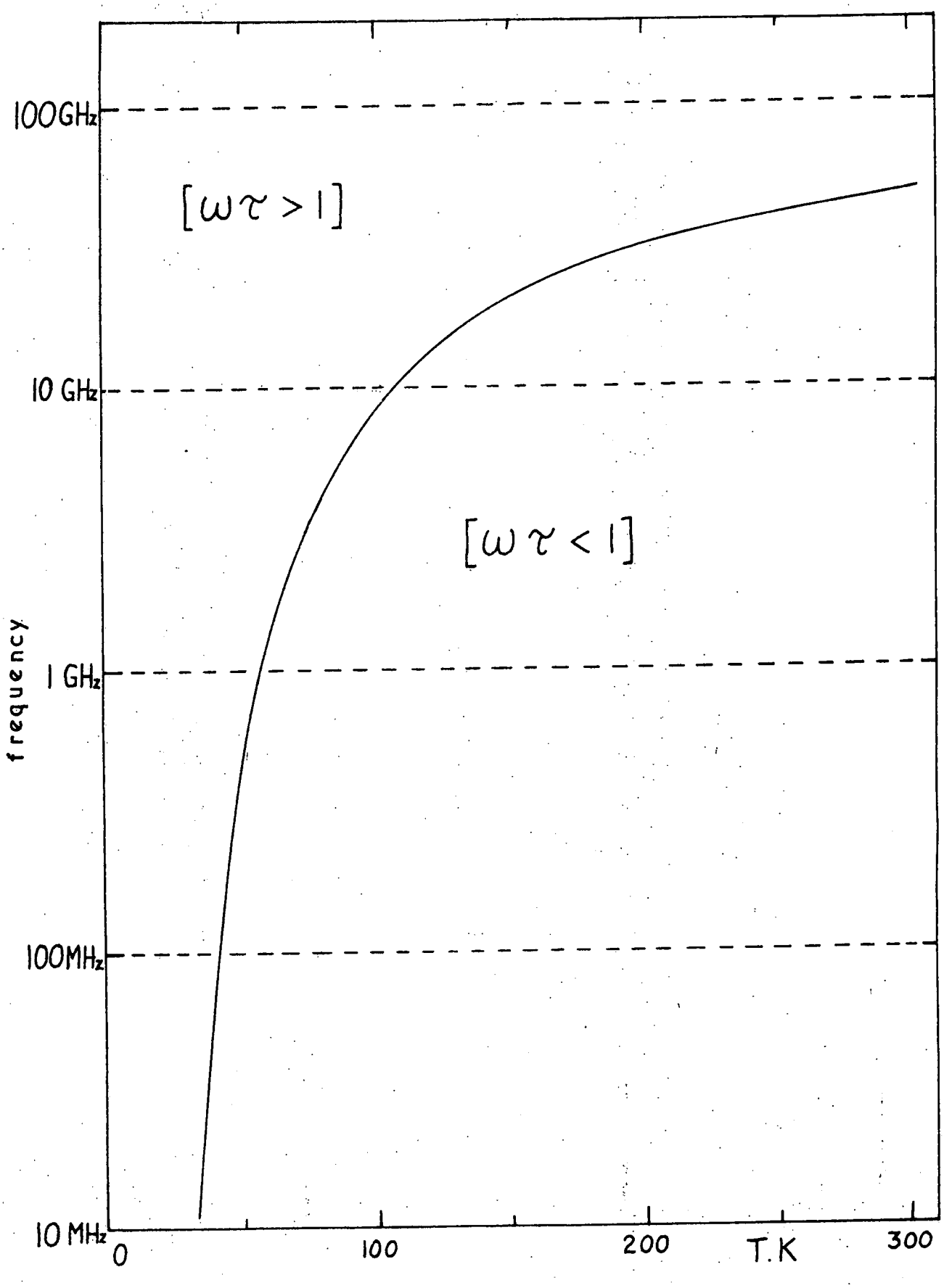

A plot of the condition $\omega\tau = 1$ for HgTe as a function of frequency and temperature.

FIGURE 9.23

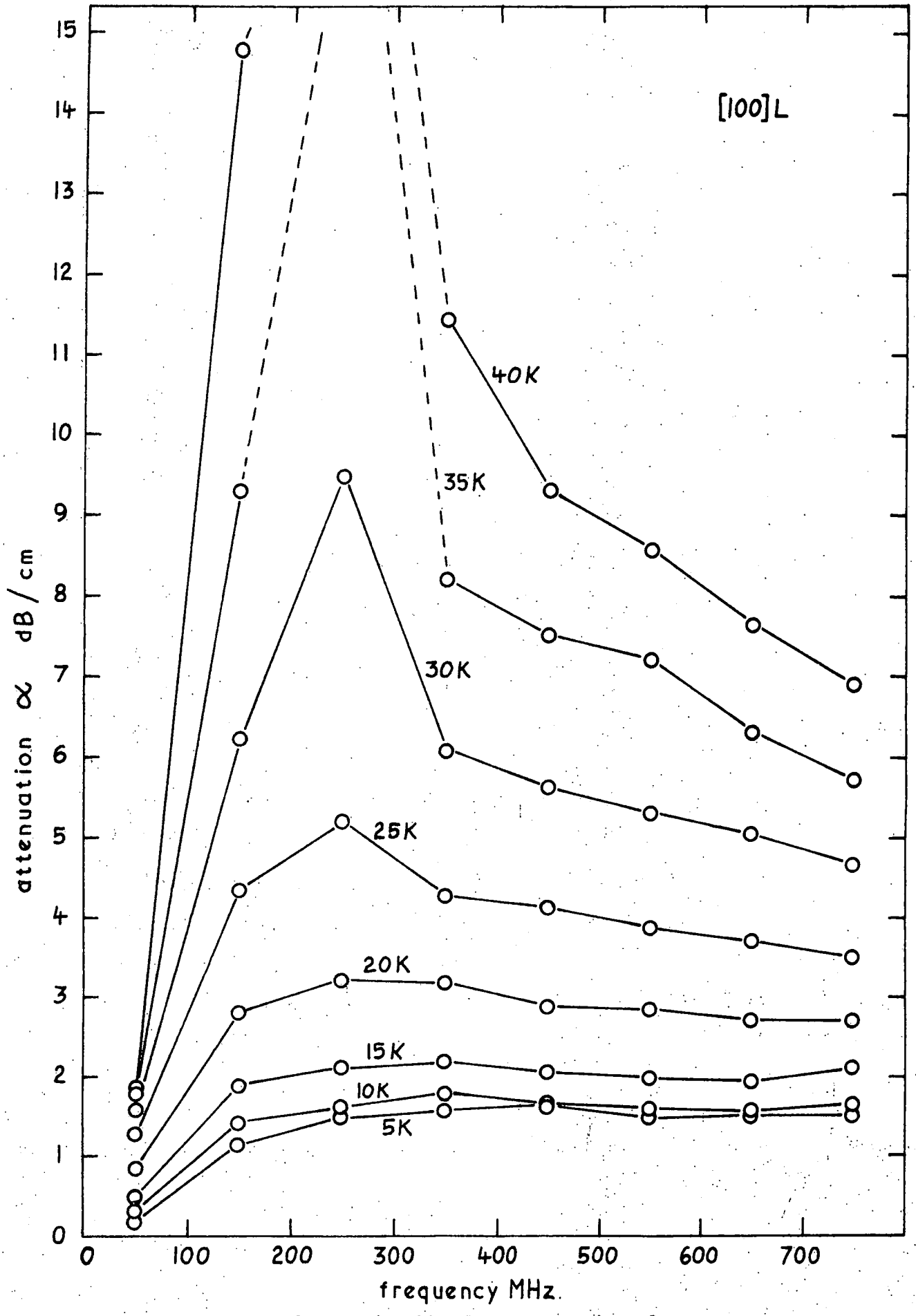

The [100] longitudinal attenuation frequency dependence in HgTe in the region of the low-temperature peak.

FIGURE 9.24.a

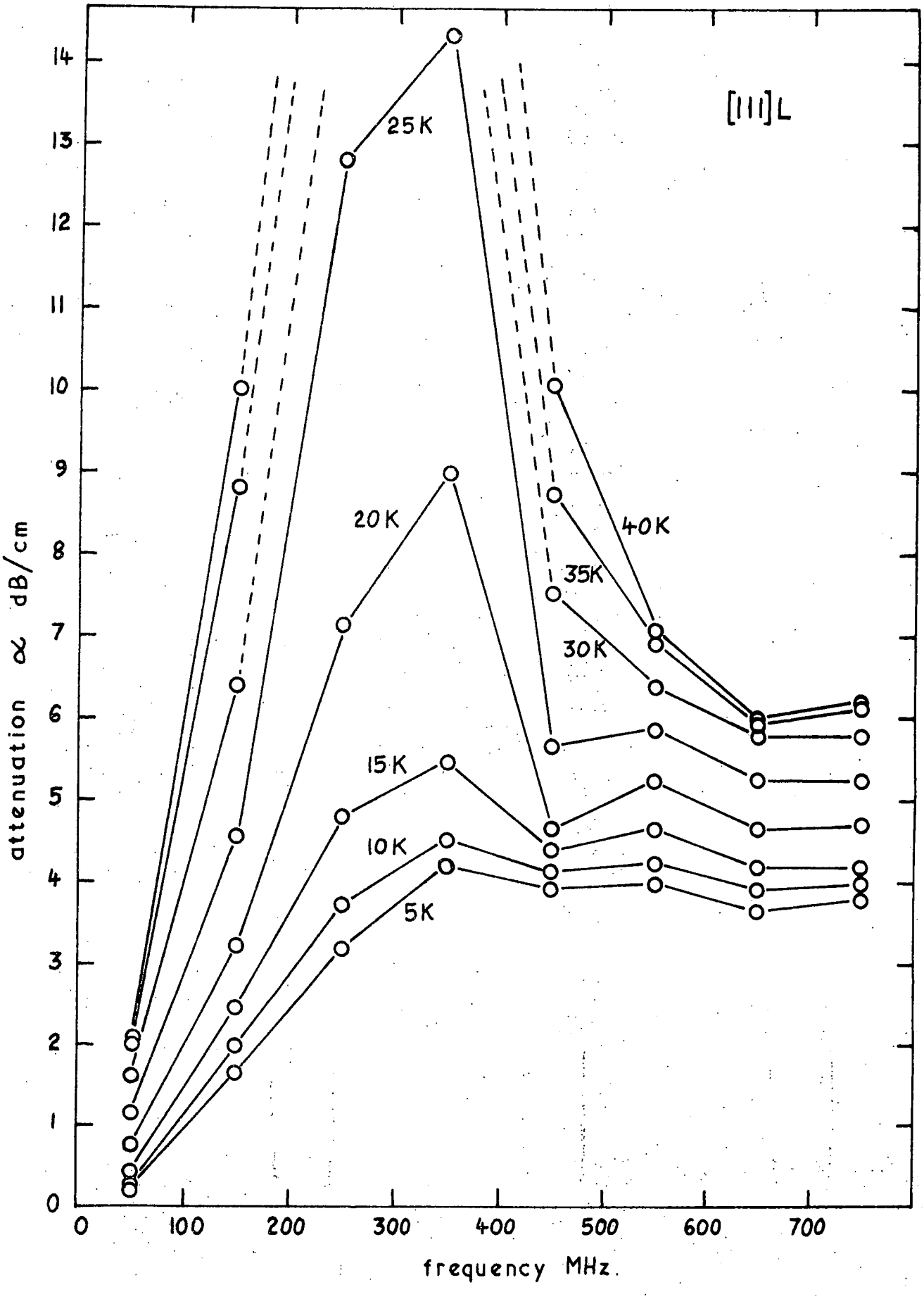

The [111] longitudinal attenuation frequency dependence in HgTe in the region of the low-temperature peak.

FIGURE 9.24.b

of the [111]L mode in HgTe (see Section 7.5) it must be considered whether this low temperature peak could be a related phenomenon. Examination of both Alper's (1968) work and these measurements indicate that this is not so: in this work entirely similar attenuation characteristics were found for both the [111]L piezoelectrically-coupled and the [100] piezoelectrically-inactive modes: in Alper's (1968) measurements below 100 K the largest peak was observed for the piezoelectrically-inactive [111]S mode, while the coupled [111]L mode showed only a small peak (Figure 9.25). It is concluded that the enormous effects in the region of 30 to 70 K in HgTe are due mainly to dislocation interactions with the ultrasonic waves: the frequency and directional dependences of the attenuation are inconsistent with any other mechanism.

(c) The back-ground attenuation

Above about 150 K Alper (1968) observed a background rise in attenuation at 10 MHz which he described by an Arhenius equation of activation energy 0.062 eV (Figure 9.1). It is tempting to attribute this to an interaction of the ultrasonic wave with point defects of formation or migration energy equal to the activation energy given by the Arhenius equation, but the consequent formation or migration energy (0.063 eV) is about an order of magnitude below that commonly found for the simplest point defects. Superimposed on this background attenuation Alper (1968) found high temperature peaks, which he attributed to forced dislocation motion. These are also observable in Figure 9.20 and 9.21 at similar

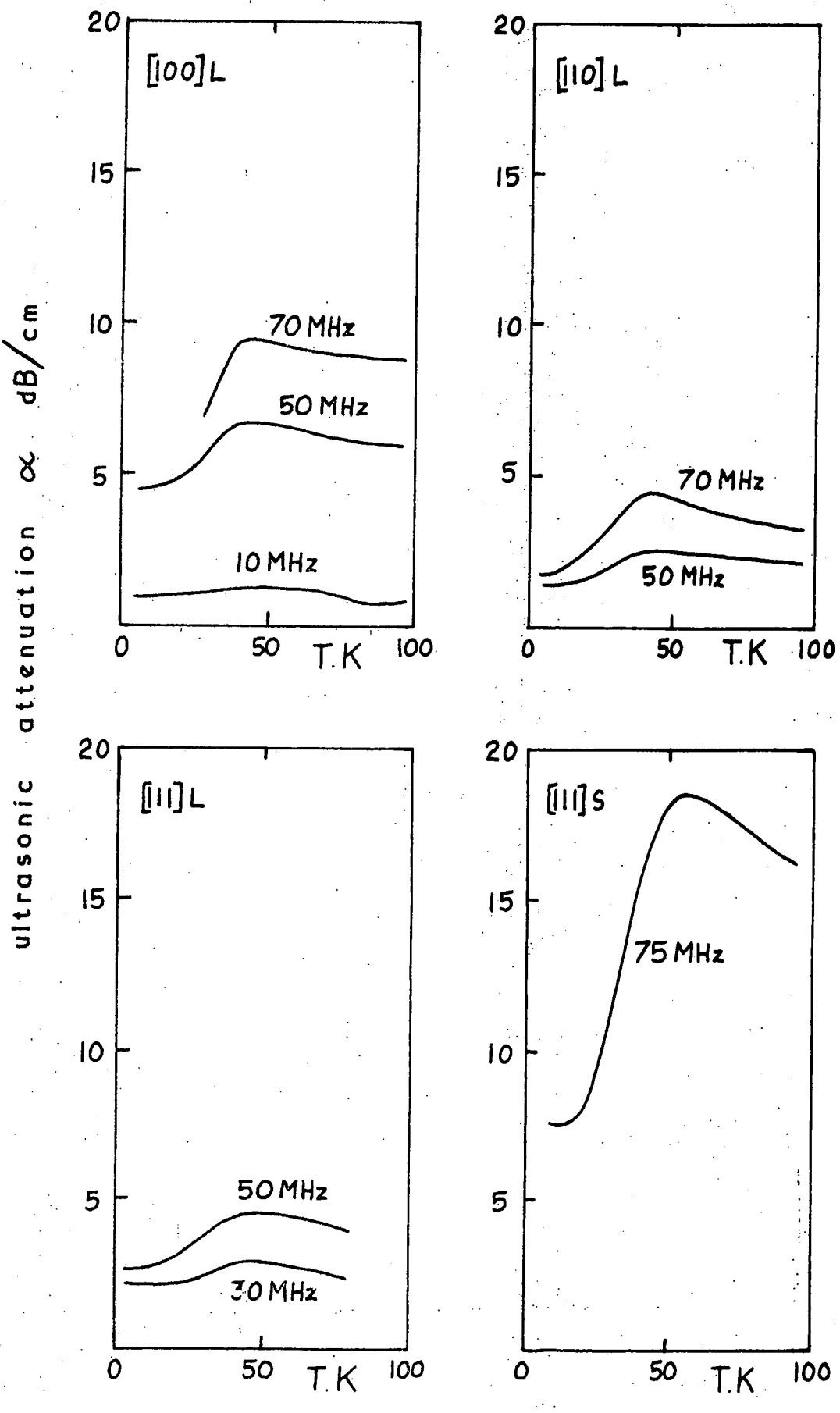

A summary of low-temperature attenuation measurements made in HgTe by Alper (1968): the only piezoelectrically active mode is that marked [111]L.

FIGURE 9.25

temperatures for 50 MHz ultrasonic waves, but have not been investigated further here. The attenuation measurements above 115 K are entirely consistent with the measurements and discussion presented by Alper and Saunders (1969). The sharp rises observed in the attenuation between 60 K and 90 K at frequencies above 150 MHz are attributed here to phonon-phonon coupling: this is discussed in Section 9.3.

9.3 PHONON-PHONON COUPLING IN HgTe

Mercury telluride has the same crystal structure as gallium arsenide, and very similar uncomplicated elastic behaviour as a function of temperature (see Chapters 6 and 7). In the absence of direct observations of the thermal phonon-ultrasonic phonon coupling in HgTe we may reasonably use the results of calculations of the coupling in GaAs (Chapter 8) to calculate the temperature and frequency dependences of the attenuation due to thermal-phonon damping in HgTe. On examination of Figure 8.11 and 9.23 it is apparent that for frequencies below 1 GHz the condition $\omega t = 1$ is fulfilled at higher temperatures in HgTe than in GaAs. Consequently the sharp rise in attenuation due to thermal-phonon coupling, which for GaAs is at temperatures slightly above those satisfying $\omega\tau=1$ and which shifts slightly to higher temperatures with frequency as does the $\omega\tau=1$ condition, should be at higher temperatures (50 K to 60 K) for HgTe than for GaAs. This is consistent with the steep rise in attenuation above 50 K observed in HgTe for propagation of the [100] and [111] longitudinal high

frequency waves (see Figures 9.20 and 9.21).

The attenuation due to thermal phonon damping expected in HgTe has been calculated using the W-E theory (see Section 8.1): the results are presented in Figure 9.26 for the [111] longitudinal mode. The thermal conductivity measured by Whitsett and Nelson (1972) has been used (Figure 9.27), along with the Debye velocity calculated from the elastic constant data presented in Chapter 7 (1.533×10^5 cm sec^{-1} at 0 K). The Grüneisen parameter γ'_{WE} for HgTe has been obtained from the calculated temperature dependence of γ'_G (Figure 7.6), the frequency exponent temperature dependence found for GaAs (Figure 8.19) and the temperature dependence differential between curves B and C presented for GaAs in Figure 8.17, related to the difference in absolute magnitudes between γ'_{WE} (Figure 8.18) and γ'_G (Figure 6.7) for GaAs. The curves presented in Figure 9.26 confirm that the sharp rise in attenuation between 50 K and 80 K at high frequencies in HgTe is due to thermal phonon-ultrasonic phonon coupling. Exact quantitative agreement is not to be expected owing to the large dislocation-phonon interactions in this region, and the approximations made in the derivation of γ'_{WE}.

9.4 DISLOCATION ULTRASOUND DAMPING IN HgTe

A computer program has been devised to give the best (least mean squares) fit of the Granato-Lucke dislocation damping equation 9.13 to the measured values of attenuation as a function of frequency at each temperature. The calculated phonon-phonon attenuation (see Figure 9.26)

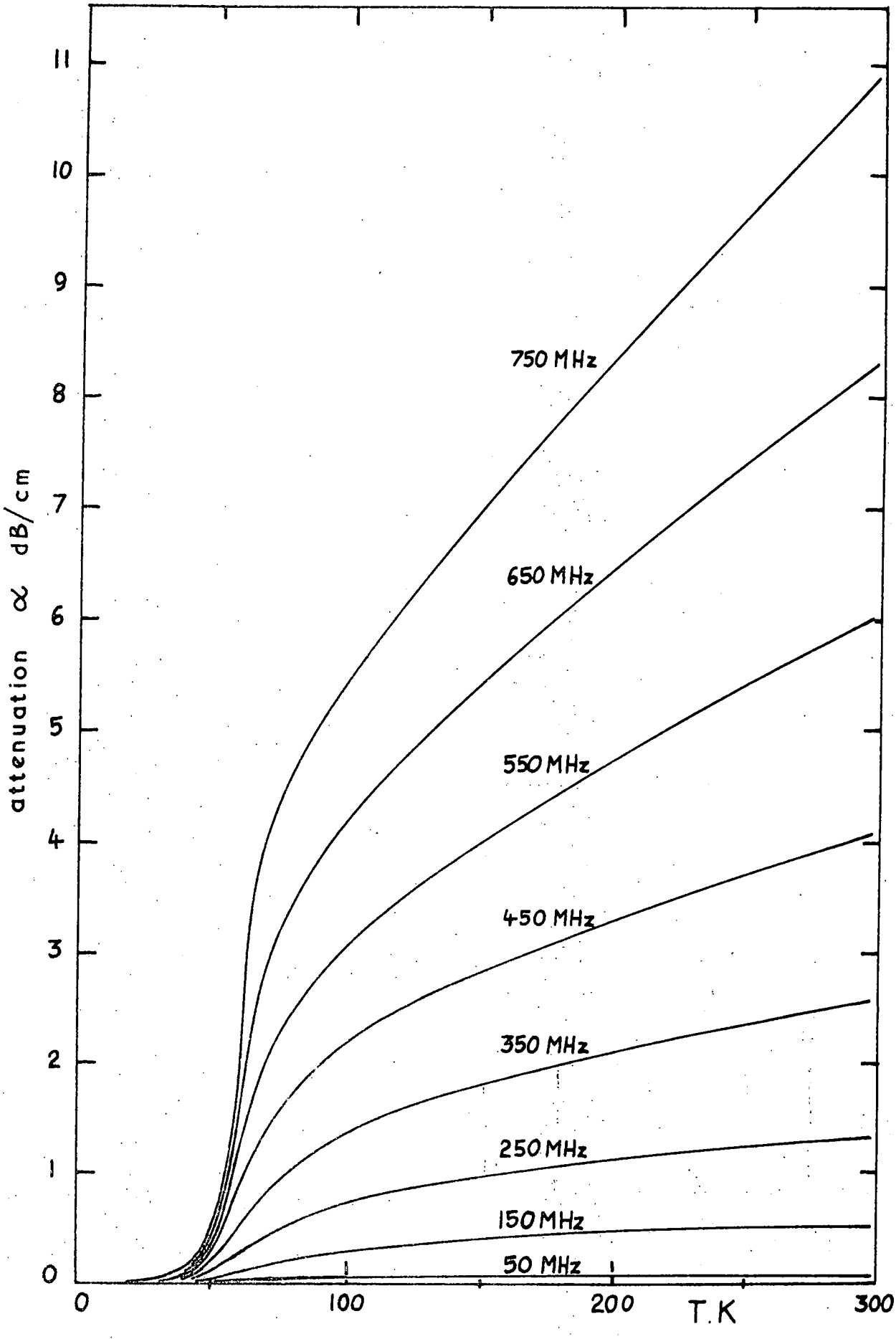

The calculated thermal phonon-ultrasonic phonon attenuation in HgTe as a function of temperature and ultrasonic frequency.

FIGURE 9.26

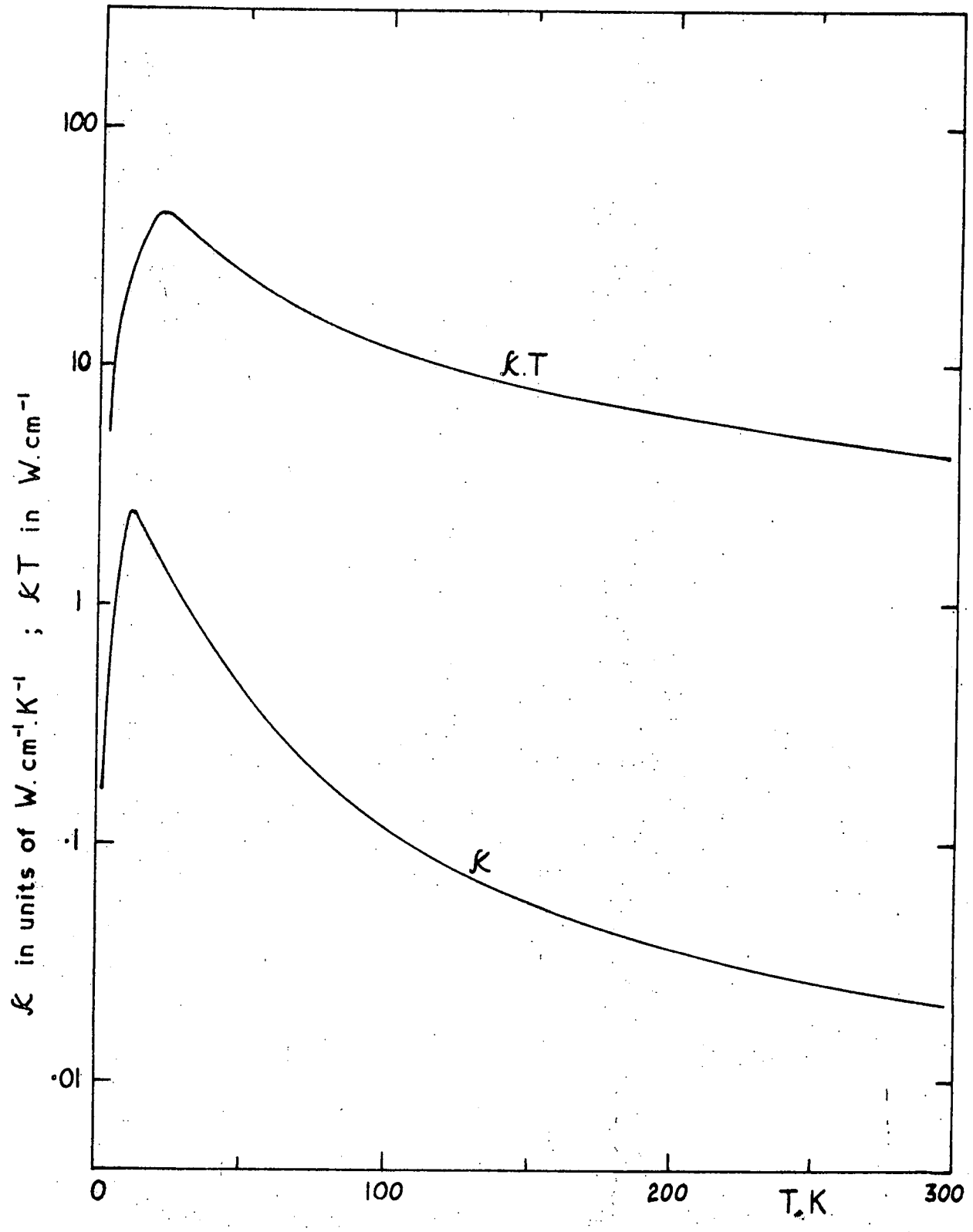

The thermal conductivity (κ) and the multiple (κT) for HgTe as functions of temperature (after Whitsett and Nelson).

FIGURE 9.27

is first subtracted, then the best fit computed from equation 9.13 formulated as

$$\Delta = \frac{W}{F_o^2 D} \quad \frac{\frac{F}{F_o}}{1 + \frac{1}{D^2} - 2\left(\frac{F}{F_o}\right)^2 + \left(\frac{F}{F_o}\right)^4} \tag{9.19}$$

where F is the ultrasonic frequency and F_o the damping-free dislocation loop resonant frequency. After substitution of equations 9.3, 9.4, 9.14 and 9.15 in 9.13 we find that

$$W = \frac{2\,\Omega\,G\,\Lambda}{\pi^3 \rho} \tag{9.20}$$

The three parameters W, F_o and D have been treated as independent variables in the computation. W is only a slight function of temperature (Equation 9.20) and its computed apparent temperature dependence serves as a guide to the validity of application of the Granato-Lücke model in this context.

The computed temperature dependences of W, F_o and D for the [100] and [111] longitudinal mode attenuations are shown in Figures 9.28 and 9.29, respectively. The parameter W is reasonably constant below about 80 K for both modes, a finding which indicates that the Granato-Lücke model is a good description of the ultrasonic attenuation in this region. Above 80 K the attenuation is complicated by other mechanisms, as found by Alper and Saunders (1969); the smooth changes in Fo and D in the region approaching 100 K support Alper and Saunders' (1969) conclusions that the attenuation above the low temperature peak is dominated by dislocation interactions.

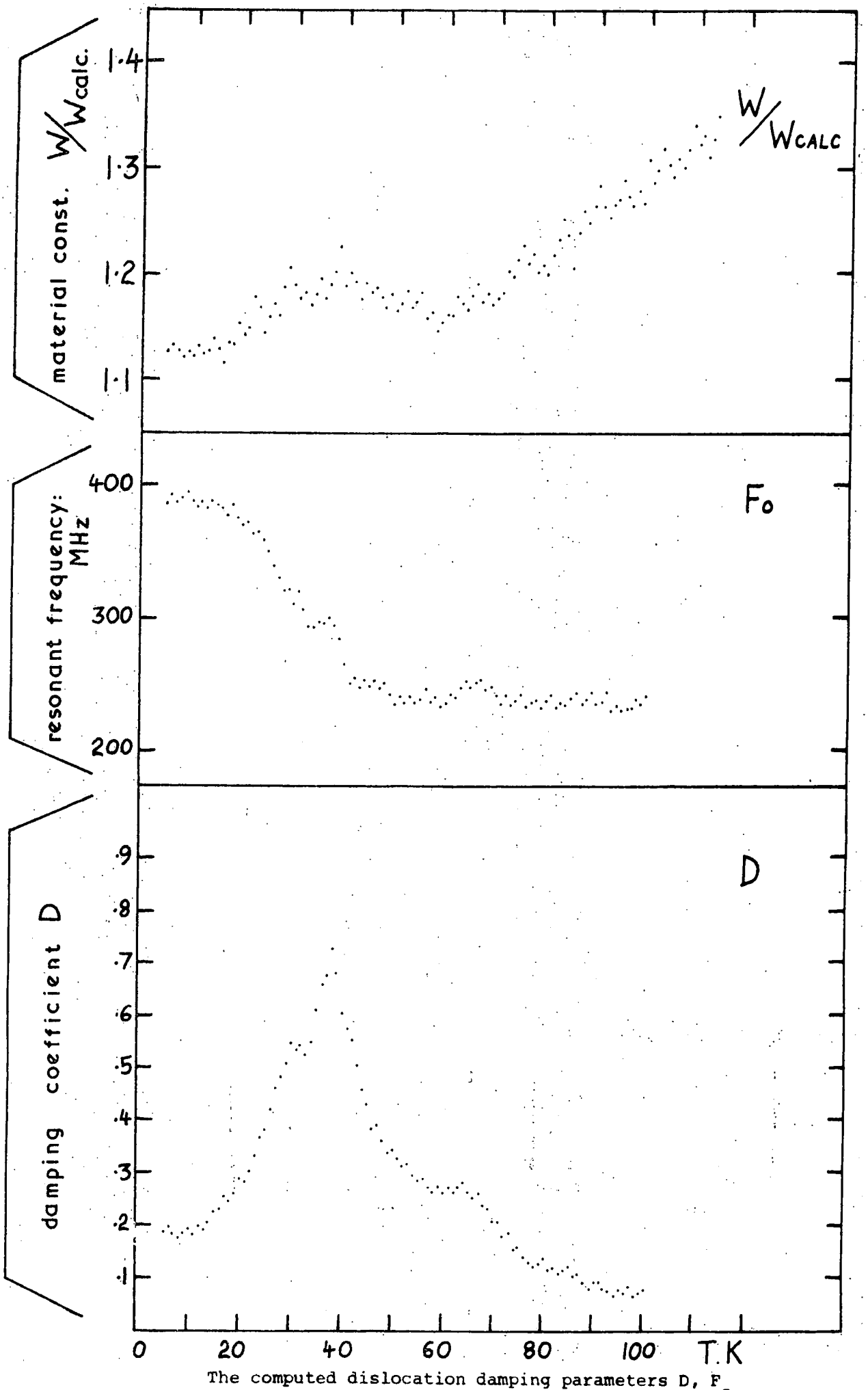

The computed dislocation damping parameters D, F_o and W/W_{calc} for the [100]L mode in HgTe

FIGURE 9.28

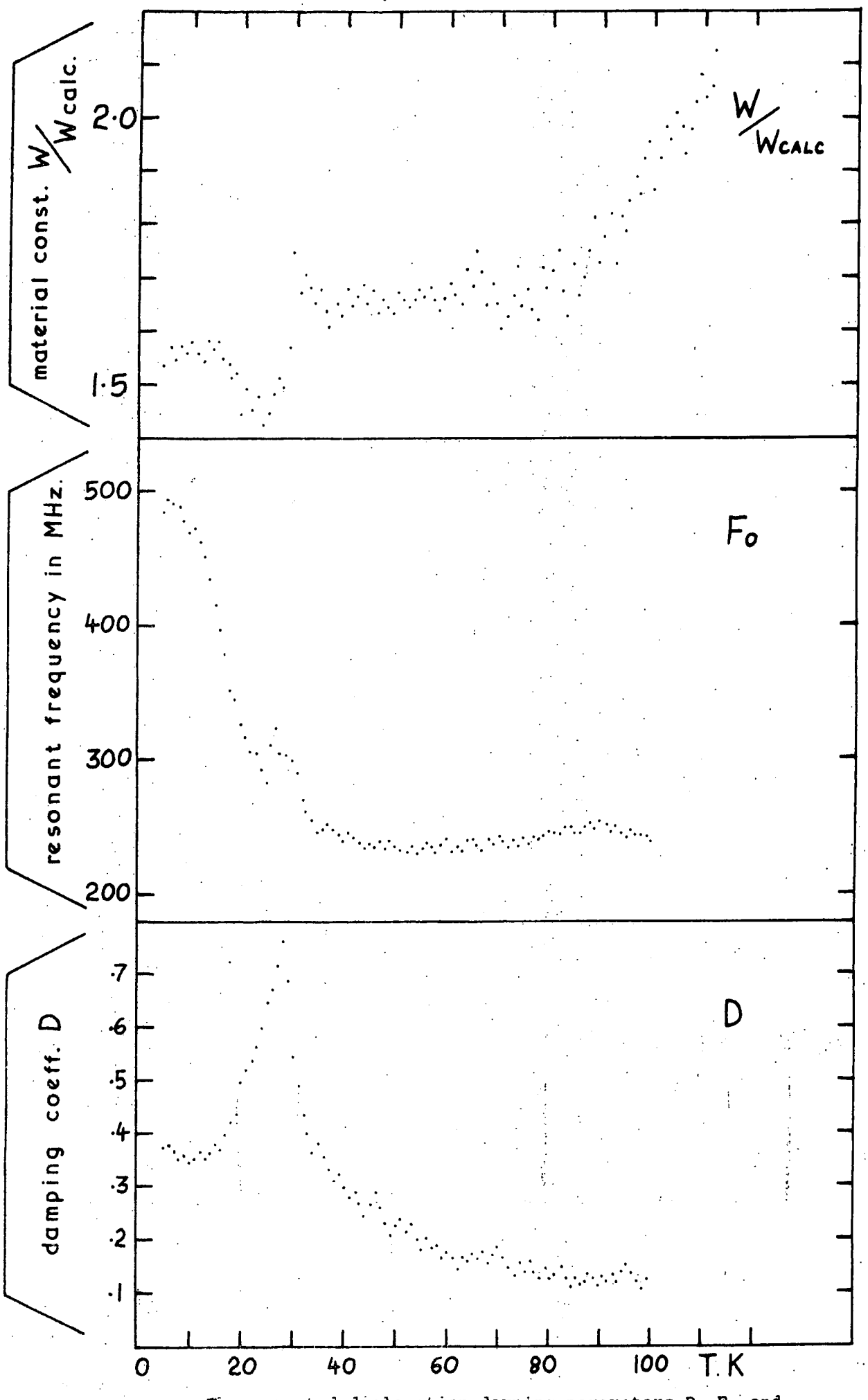

The computed dislocation damping parameters D, F_o and W/W_{calc} for the [111]L mode in HgTe

FIGURE 9.29

The behaviour of the resonant frequency Fo and the damping coefficient D at temperatures below 80 K is characteristic of thermal deactivation of some of the dislocation pins (thermal unpinning): the resonant frequency falls with increasing temperature, indicating an increasing dislocation loop length, and the damping coefficient exhibits a large peak (equivalent to a sharp drop in the damping) in the temperature range where the resonant frequency is changing most rapidly. Thermal unpinning of dislocations absorbs energy from the thermal phonon population and the phonon damping of the dislocations is consequently less in magnitude. Teuticono et al (1964) have treated the thermal unpinning of dislocations in detail, and they found that thermal breakaway would norm ally occur well below room temperature. Fo varies by a factor of about 2 across the unpinning temperature (Figures 9.28, 9.29): about half the total number of pins in the crystal are deactivated in the breakaway. Consequently, the model of Teutonico et al (1964) in terms of breakaway of alternate pins at equal spacings 2Lc is likely to apply. The equations resulting from their analysis are too complicated for application to a practical situation, but a qualitative comparison may be made by examination of their calculated curves of observed activation energy U_1 as a function of applied stress (see Figure 9.30). Quantitative comparison with these curves cannot be made as the activation energy is a strong function of applied stress, and it is not possible to assign accurate values to the stresses involved in the ultrasonic wave propagation in this work.

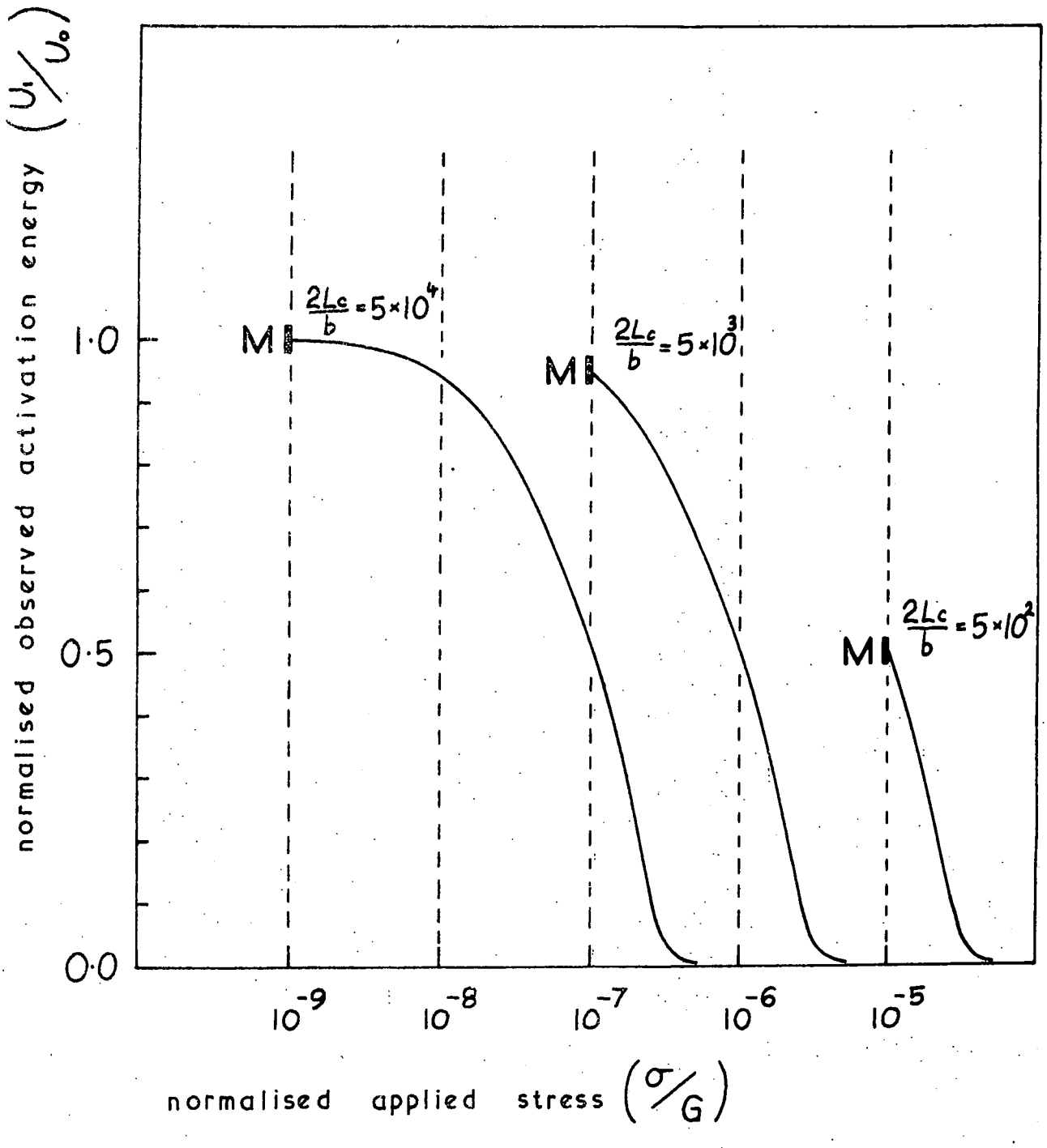

The dependence of the observed dislocation-unpinning activation energy U_1 on the applied stress σ in the Teutonico-Granato-Lücke model. U_o is the height of the unpinning barrier, G the shear stress in the glide plane and points M the critical stresses below which thermal unpinning cannot occur. Dislocation loop lengths are specified as multiples (2Lc/b) of the Burger's vector b.

FIGURE 9.30

The dislocation parameters effective at 5K can be calculated from equations 9.3, 9.4, 9.14, 9.15 and 9.16 using the data presented in Figures 9.28 and 9.29, and in Chapter 7. If the Burger's vector is taken as $\frac{1}{2}\langle 110\rangle$ (Holt, 1962) these parameters have values

Burger's vector $b = 4.569 \times 10^{-8}$ cm

Shear modulus $G = 0.1359 \times 10^{12}$ dyn cm^{-2}

Poisson's ratio $\nu = 0.3767$

Line tension $C = 2.898 \times 10^{-4}$ G. cm sec^{-3}

Line mass $A = 1.687 \times 10^{-14}$ G. cm^{-1}

Constant $\Delta_o = 0.2525$ dyn $G.^{-1}$ cm^{-1} sec^{-2}

For the [100] longitudinal mode:

Loop length $L_c = 1.70 \times 10^{-4}$ cm

Drag coefficient $B = 2.21 \times 10^{-4}$ dyn sec cm^{-2}

For the [111] longitudinal mode:

Loop length $L_c = 1.35 \times 10^{-4}$ cm

Drag coefficient $B = 1.39 \times 10^{-4}$ dyn sec cm^{-2}

The loop lengths as defined in Teutonico et als' (1964) work as a multiple of the Burger's vector are

$$\frac{2L_c}{b} = 7.4 \times 10^3 \text{ for the [100]L.}$$

$$\frac{2L_c}{b} = 5.9 \times 10^3 \text{ for the [111]L.}$$

The loop length L_c which appears in the Granato-Lücke theory is not corrected for the relative orientation of the ultrasonic wave in that the dislocation resonant frequency

is assumed independent of applied stress orientation. Consequently we may expect to find differences between values of L_c derived from modes where the average resonant frequency F_o is different: F_o itself depends on the orientational distribution of the dislocations in the glide plane relative to the propagation direction. This may also be seen in the differences in shape of the attenuation temperature dependences (Figures 9.28 and 9.29). If the derived values of 2Lc/b were the same for the [100] and [111] modes, we should expect to observe unpinning at the same temperature for both modes, according to the Teutonico-Granato-Lücke model (1964): for a single value of stress σ and a single value of 2Lc/b the value of the activation energy is uniquely defined in Figure 9.30. The stress distributions in conditions of ultrasonic wave propagation are too complicated for a direct comparison between the model and experiment to be made, but it is interesting to note that for the change in $2L_c/b$ found between the [100]L and [111]L modes, the observed unpinning temperature Tu (simply $Tu = U_1/k$, where k is Boltzmann's constant) should be greater for the [111]L mode than for the [100]L. If the unpinning temperature Tu is taken to be at the maximum in D, then the experimental situation is found to be the inverse of this:

Mode	Tu	U_1
[100]L	38 K	0.0033 eV
[111]L	28 K	0.0024 eV

The barrier height Uo restricting the unpinning is a multiple of U_1 depending on the value of σ: for an order

of magnitude change in σ the ratio (U_1/U_o) can change by an order of magnitude (see Figure 9.30).

Bailly (1968) has calculated the energy for formation of metal vacancies in mercury telluride on the assumption that covalent bonding occurs between Te neighbours. He found that this type of vacancy (called by him a "covalent" vacancy) has a negative formation energy (-0.13 eV), and consequently large concentrations can be expected to occur naturally. The bonds between Te neighbours may be broken at high temperatures, transforming these complex vacancies into normal ones: the calculated energy of transformation is in fair agreement with experiment (Rodot, 1964). Evidently Bailly's (1968) formation energy calculation is only valid for an isolated vacancy, and does not mean that HgTe cannot exist, as interactions between vacancies have not been considered, but it does indicate that a substantial number of these "covalent" vacancies of very low migration energy must be present in mercury telluride. This is confirmed by the studies of Rodot (1964).

For the dislocation density ($\sim 10^7$ cm^{-2}) and the density of the low-energy pinning points found in this ultrasonic work (between 2.9×10^3 and 3.7×10^3 per centimetre length of a dislocation) the volume density of low-energy pinning points below 20 K - 30 K is of the order of 3×10^{10} cm^{-3}: this would be consistent with identification of the pinning points with the low-energy "covalent" vacancies in HgTe discussed by Bailly (1968). It is evident that a great deal of further work on this point is required before a definite identification of the pinning mechanism can be made.

CHAPTER 10

SUMMARY AND CORRELATION : THE ELASTIC AND ANELASTIC PROPERTIES OF GaAs AND HgTe

The elastic and anelastic properties of gallium arsenide and mercury telluride have been studied through sound velocity and attenuation measurements in the temperature range 2 K to 320 K. Attention has been paid particularly to determination of the uncertainties involved in the velocity measurements in order to obtain the most accurate elasticity data possible, and the attenuation has been studied over a wide range of ultrasonic frequencies to enable accurate determination and separation of the various contributing damping mechanisms. On the basis of close similarities in the elastic behaviour of the two compounds it has been found possible to extract information from the ultrasonic attenuation in gallium arsenide which is vital to separation of the more complicated effects observed in the case of mercury telluride.

The absolute values of the measured elastic constants of GaAs and HgTe fit well into a general scheme of correlation between the elastic properties of the group IV, III-V and II-VI materials which has been devised in this work as a reformulation of the long established Keyes (1962) correlation. This will be described in the following section. The care taken in avoiding the use of piezoelectrically-coupling modes in the determination of the elastic constants has been justified by the finding of a temperature-dependent piezoelectric stiffening of the [111] longitudinal wave mode in both HgTe and GaAs. The quality of the experimental data is adequately demonstrated by the low temperature (2 K) agreement between the Debye temperature of GaAs derived from the specific heat (346.7 K) and the value calculated in this work from the measured elastic constants (346.8 K).

The temperature dependences of the elastic constants between 2 K and 320 K are well described by a phenomenological model devised by Lakkad (1971). On the basis of close examination of the small deviations of the model from the experimental data, a possible correlation in the temperature dependences of the mechanical properties of zinc-blende crystals is suggested in Section 10.2.

Whereas the ultrasonic attenuation observed in mercury telluride is very complicated in its frequency and temperature dependences, the attenuation in gallium arsenide is easily separable into individual components: it has proved possible to make a detailed comparison between the experimental results for GaAs and a theory of damping due to thermal phonon-ultrasonic phonon interaction. The

characteristics of the Grüneisen parameter appearing in the theory have been considered (see Section 10.3). A summary is presented in Section 10.4 of the separation of the dislocation damping of ultrasound from the HgTe attenuation data and the conclusions relevant to thermal dislocation unpinning in this material.

10.1 AN EXAMINATION OF THE KEYES-MARTIN CORRELATION

Keyes (1962) suggested a correlation between the elastic properties of the diamond structure group IV elements and the zinc-blende structure III-V and II-VI groups of compounds. Using dimensional analysis he produced a normalising constant C_o defined as

$$C_o = \frac{q^2}{r^4} \tag{10.1}$$

where q is the electronic charge and r the nearest-neighbour distance; the values of the normalised bulk modulus B^* and shear moduli C_{44}^* and C_S^*,

$$B^* = \frac{C_{11} + 2C_{12}}{3C_o} \tag{10.2}$$

$$C_{44}^* = \frac{C_{44}}{C_o} \tag{10.3}$$

$$C_S^* = \frac{C_{11} - C_{12}}{2C_o} , \tag{10.4}$$

were found to be approximately constant within each of the IV, III-V and II-VI groups. Martin (1970) extended the correlation by describing the deviations from constancy in B^*, C_{44}^* and C_S^* throughout the IV $\rightarrow$ III-V $\rightarrow$ II-VI series in terms of the bound character. He plotted the values of B^*, C_{44}^* and C_S^* against the bond ionicity f_i

defined by Phillips (1970), and found that the reduced moduli were approximate functions of $(1 - f_i)$.

For B^*, C^*_{44} and C^*_S to be constant inside a group including compounds P and Q, the ratios of the individual reduced moduli of P and Q must be equal:

$$\frac{B^{*P}}{B^{*Q}} = \left(\frac{C^{*P}_{44}}{C^{*Q}_{44}} \right) = \frac{C^{*P}_S}{C^{*Q}_S} \tag{10.5}$$

This is algebraically equivalent to the set of equalities

$$C^P_{11} = \left(\frac{C^P_o}{C^Q_o} \right) C^Q_{11}$$

$$C^P_{12} = \left(\frac{C^P_o}{C^Q_o} \right) C^Q_{12} \tag{10.6}$$

$$C^P_{44} = \left(\frac{C^P_o}{C^Q_o} \right) C^Q_{44}$$

which reduces to

$$C^P_{ij} = \left(\frac{C^P_o}{C^Q_o} \right) C^Q_{ij} \tag{10.7}$$

This relation has been tested here throughout the IV →III-V →II-VI series by defining first a standard material Q (GaAs) and calculating the spread of values of the constant (C^P_o/C^Q_o) required to satisfy equation (10.7) for a given material P. Keyes' (1962) correlation implies that for any material in the IV →III-V →II-VI series the spread should be zero. The principal problem is the choice of elastic constant values from the several sets of data available for many of the materials. A list of sources of data used in these calculations appears in Appendix I.

In all the correlations presented in this work both the best and worst fits have been calculated from all the data available, and these are referred to as such. Table 10.A lists the spreads R_C in values of (C_o^P/C_o^Q) for each material where R_C is defined as

$$R_C = \frac{(C_o^P / C_o^Q)_{max} - (C_o^P / C_o^Q)_{min}}{(C_o^P / C_o^Q)_{max}} \times 100\%$$

All percentages quoted in this section are defined in a similar manner.

The spread R_C is very large for most of the materials considered, excepting the gallium group of compounds: Keyes' relation does not hold in general, although the gallium group of compounds obey it reasonably well. If the elastic constants are normalised to a different material Q', local correlations between other small groups of compounds become apparent, but the general agreement remains similarly unsatisfactory. The spread in values of the reduced bulk modulus B^* inside one of the groups IV, III-V or II-VI is a lot smaller than would be expected from the table of R_C (Table 10.A); also the spread in values of C_{11}^* $(= C_{11}/C_o)$ is less than that for C_{12}^* $(= C_{12}/C_o)$ or C_{44}^*, and less than that for B^* in the III-V and II-VI groups (Table 10.A): it seems likely that the basis of a correlation may lie in elastic constant combinations other than those defined by Keyes. Martin (1970) indicated that an improved correlation could be found by relating the reduced elastic parameters to the bond character. There is certainly some degree of directionality in the bonding in the IV →II-VI series: the correlation should include

TABLE 10.A: Spread in the reduced elastic parameters of the group IV, III-V and II-VI materials

Group	Crystal	Minimum R_c (%)	C_o ($\times 10^{12}$ dyn.cm^{-2})	B^*	Minimum spread in B^* in group (%)	C_{11}^*	Minimum spread in C_{11}^* in group (%)
IV	$C_{(diamond)}$	76.36	4.0523	1.0916		2.6627	
	Si	14.77	0.7538	1.2984	17.14	2.1991	27.25
	Ge	33.37	0.6401	1.0759		1.9372	
III-V	AlSb	14.80	0.4630	1.2564		1.8940	
	GaP	2.21	0.7430	1.1945		1.9004	
	GaAs	-	0.6418	1.1977		1.8864	
	GaSb	2.88	0.4681	1.2382	8.87	1.9423	7.90
	InP	27.53	0.5529	1.3107		1.8484	
	InAs	27.61	0.4941	1.2902		1.8211	
	InSb	14.95	0.3723	1.1961		1.7889	
II-VI	ZnS	48.22	0.7660	1.0979		1.3905	
	ZnSe	28.72	0.6356	1.0184		1.3971	
	ZnTe	31.14	0.4765	1.1075	19.54	1.5467	12.44
	CdTe	50.76	0.3718	1.1961		1.5062	
	HgSe	58.64	0.4779	1.1793		1.4082	
	HgTe	50.65	0.3760	1.2657		1.5880	

TABLE 10.A

directional dependences of the elastic constant combinations.

Spread parameters similar to R_C have been calculated for ratios of all the longitudinal pure mode elastic constant combinations (see Table 10 B) in the IV →II-VI series using GaAs as the standard material. Both the minimum and maximum spreads in the ratios are quoted to give an idea of the wide range of measured elastic constant values found in the literature for some materials. Carefully measured values of elastic constants are commonly accurate to about 1%: the minimum spread in longitudinal pure mode ratios is less than, or of the order of, this value for all the IV, III-V and II-VI materials except $C_{(diamond)}$, S_i and ZnSe. It would be useful if further measurements could be made for ZnSe to ascertain the reason for the comparatively large spread (3.77%) in the elastic constant ratios for this one compound in the III-V and II-VI groups. With this exception there is an extremely good correlation between the elastic moduli defined in this way: it seems that in the III-V and II-VI zinc-blende materials this longitudinal pure-mode elastic constant combination ratio is independent of crystallographic direction. The value of the ratio itself is a measure of the magnitude of the directionally independent elastic constant combination, and it is directly proportional to C_{11}^* (the [100] longitudinal mode elastic constant equals C_{11}).

There is a general trend towards higher values of the longitudinal pure mode ratio through the series IV →III-V →II-VI, but no obvious correlation has been found between the ratio and any other parameter, except

TABLE 10.B The longitudinal pure mode elastic constant combination ratios in the IV →III-V →II-VI series.

Group	Crystal	Maximum Spread %	Minimum Spread %	Average value of ratio
IV	$C_{(diamond)}$	-	13.49	0.1225
	S_i	5.34	5.29	0.7547
	Ge	2.36	0.75	0.9808
III-V	AlSb	1.28	1.25	1.3919
	GaP	-	0.44	0.8597
	GaAs	-	-	1.0000
	GaSb	0.85	0.80	1.3384
	InP	-	0.73	1.1795
	InAs	2.24	0.58	1.3408
	InSb	10.70	0.18	1.8199
II-VI	ZnS	5.03	0.85	1.1671
	ZnSe	11.04	3.77	1.3325
	ZnTe	0.23	0.15	1.6450
	CdTe	5.79	0.40	2.1676
	HgSe	2.10	0.19	1.8010
	HgTe	0.21	0.09	2.0259

that the plot of C_{11}^* against f_i has a slightly better agreement with a function of $(1 - f_i)$ than does a plot of B^* against f_i (see Figure 10.1).

Exact agreement with Keyes' relation demands that the pure shear mode elastic constant combination ratios should also be equal, and also that the shear mode ratio for a pair of compounds should equal the longitudinal mode ratio. Table 10.C shows that this is not the case in general. The elastic constant combinations presented are normalised to those of three different compounds: GaAs, HgTe and ZnS. In general the ratio spreads are large and the ratio is not the same as the longitduinal one (column 2 of Table 10.C may be compared with column 3 of Table 10.B). A number of related groups of materials may be defined by examination of Tables 10.B and 10.C:

(a) Groups for which both the pure-longitudinal and pure-shear ratios are nearly directionally independent.

(b) Groups for which both ratios are nearly directionally independent and also are almost equal.

Groups falling into classification (a) are

(i) GaP, GaAs, GaSb, AlSb, and possibly InSb.

(ii) InSb, InAs, InP, ZnTe.

(iii) HgTe, CdTe.

(iv) ZnS, ZnSe.

Groups of class (b) are

(i) GaP, GaAs, GaSb.

(ii) HgTe, CdTe.

The spread in the pure shear mode ratios (Table 10.C) is not random. The [111] shear value falls almost exactly

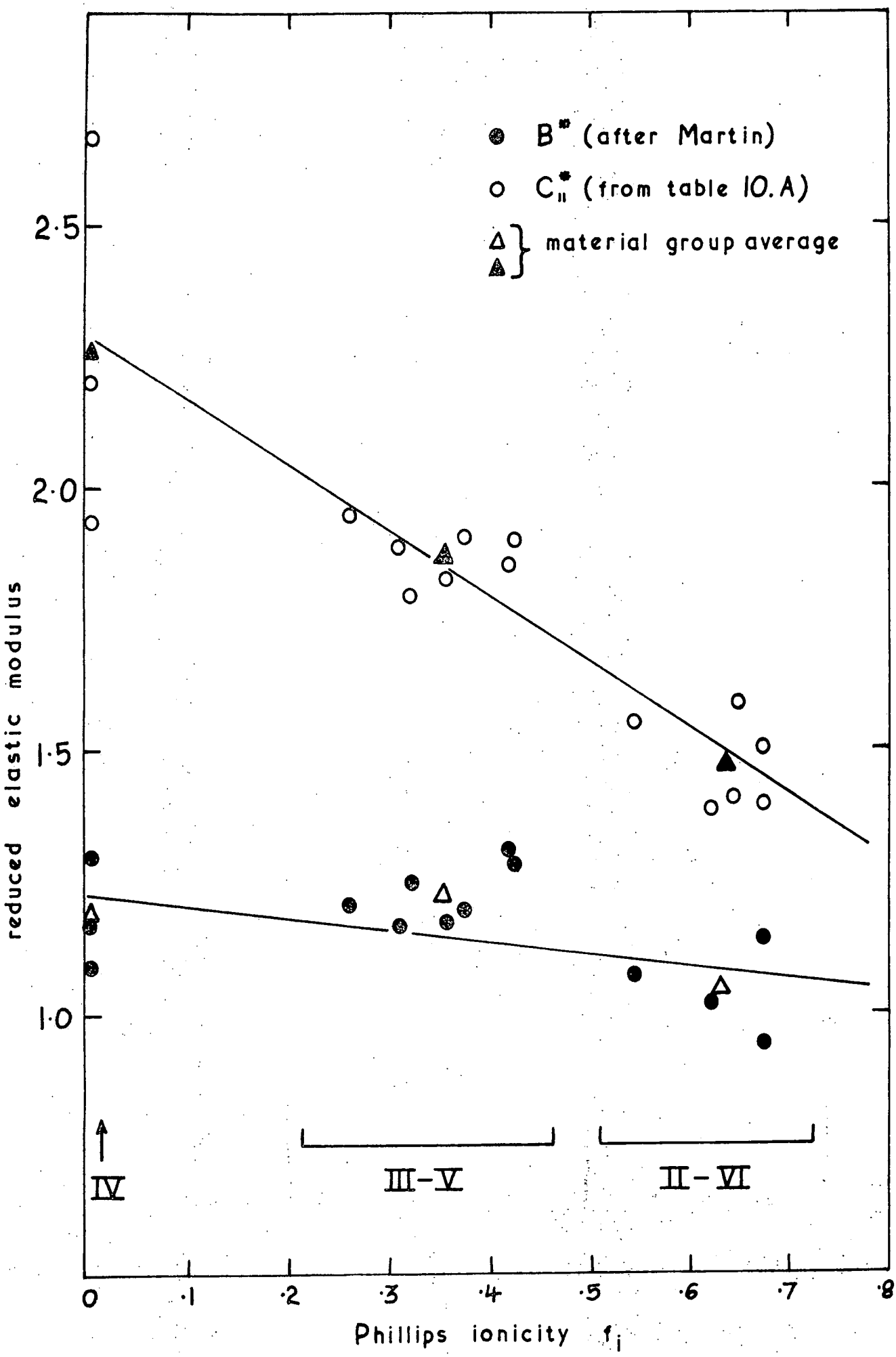

The reduced elastic moduli of the IV → III-V → II-V series as functions of the Phillips ionicity f_i : B^* the bulk modulus (after Martin) and C_{11}^* the longitudinal modulus (this work)

FIGURE 10.1

TABLE 10.C : The pure shear mode elastic constant combination ratios in the series IV— III-V— II-VI

Group	Crystal	GaAs normalised: % ratio spread	Average ratio	% Between average ratio & [111] S ratio	HgTe normalised: % ratio spread	Average ratio	% Between average ratio & [111] S ratio	Zns normalised: % ratio spread	Average ratio	% Between average ratio & [111] S ratio
IV	C (diamond)	33.52	0.0855	3.51	52.58	0.0282	6.17	47.56	0.0529	5.54
	Si	14.13	0.7024	0.63	37.12	0.2289	1.91	32.27	0.4306	1.60
	Ge	9.28	0.8414	0.31	33.56	0.2734	1.30	28.43	0.5147	1.06
III-V	AlSb	1.10	1.4892	0.01	25.97	0.4813	0.42	20.24	0.9071	0.31
	GaP	1.60	0.8495	0.02	27.95	0.2750	0.62	22.37	0.5180	0.47
	GaAs	-	-	-	26.77	0.3234	0.50	21.11	0.6094	0.38
	GaSb	1.36	1.3501	0.03	27.77	0.4369	0.58	22.18	0.8232	0.45
	InP	11.73	1.3989	0.06*	17.04	0.4495	0.09	10.64	0.8483	0.06
	InAs	11.35	1.5893	0.06*	17.40	0.5108	0.08	11.01	0.9639	0.05
	InSb	4.03	1.9630	0.04*	23.70	0.6334	0.22	17.80	1.1943	0.18
II-VI	ZnS	21.11	1.6564	0.56*	7.17	0.5291	0.19	-	-	-
	ZnSe	20.61	1.6430	0.53*	7.77	0.5250	0.19	0.63	0.9921	0.02
	ZnTe	10.94	1.9955	0.05*	17.76	0.6414	0.08	13.90	1.2228	0.97
	CdTe	25.00	3.3379	0.93*	2.36	1.0634	0.08	4.93	2.0111	0.16*
	HgSe	35.64	3.2810	2.58*	12.11	1.0370	0.75*	18.42	1.9649	0.18*
	HgTe	26.77	3.1428	1.14*	-	-	-	7.18	1.8917	0.27*

between the [100] and [110] shear values, irrespective of the normalising material chosen (see Table 10.C, columns 3,6,9). It is interesting to note that in general for materials above the normalising compounds in Table 10.C the ratios themselves decrease in the order [100]S → [111]S → [110]S, whereas for materials below the normalising compounds the order is reversed (indicated by * in Table 10.C).

10.2 THE ELASTIC CONSTANT TEMPERATURE DEPENDENCES

The measured elastic constant temperature dependences of GaAs and HgTe are described reasonably well by the Lakkad (1971) phenomenological model. The degree of misfit of the model has been computed as a function of temperature in terms of a variable Debye temperature (Figure 6.8 and 7.5) in a similar manner to that normally adopted in the case of specific heat data (see, for example, de Launay, 1956). The bases of the Lakkad elastic constant model and the Debye specific heat model are similar; the Lakkad model includes an anharmonic to harmonic force constant ratio, but its change with temperature is ignored: the temperature dependences of the Debye temperatures derived from the Lakkad fit to elastic constant data and the Debye fit to specific heat data should be similar: this is confirmed for GaAs (see Figure 6.8).

The temperature dependences of both the Debye temperature and the Grüneisen parameter are determined by the temperature dependence of the anharmonic to harmonic force constant ratio. The temperature variations of the Grüneisen parameters are very similar for GaAs (Figure 6.7)

and HgTe (Figure 7.6): the elastic constant Debye temperature variation should be as well. Figure 10.2 shows the Debye temperatures given in Figures 6.8 and 7.5 normalised to their respective O K calculated Debye temperatures: the two sets of values follow each other very closely. The implication is that although the anharmonic to harmonic force constant ratio may be determined at O K by the atom types present, the temperature dependence of this ratio is controlled more by the crystal structure.

10.3 PHONON-PHONON ATTENUATION AND THE GRÜNEISEN PARAMETER OF GaAs

The main features of the frequency and temperature dependences of ultrasonic attenuation in GaAs are well described by the theory developed by Woodruff and Ehrenreich (1961). A number of features of the model have been clarified in this work. It is possible to describe the temperature and frequency dependences of the phonon-phonon attenuation for $\omega\tau<<1$ with a frequency exponent of exactly 2, if the Grüneisen parameter is assumed to be of the form

$$\gamma'_{WE} = P\omega^{-m} + \gamma'_R$$

where P is a small constant, ω the ultrasonic frequency, m is small and γ'_R is frequency independent. The Grüneisen parameter frequency exponent m is then temperature dependent in a manner consistent with theoretical calculations for III-V compounds (see Vetelino, Mitra and Namjoshi, 1970). The value of γ'_R is about 1.9 times larger than that of the Grüneisen parameter derived from the thermal conductivity. The ultrasonic-attenuation parameter should be substantially dependent on a single mode-Grüneisen parameter (that of the

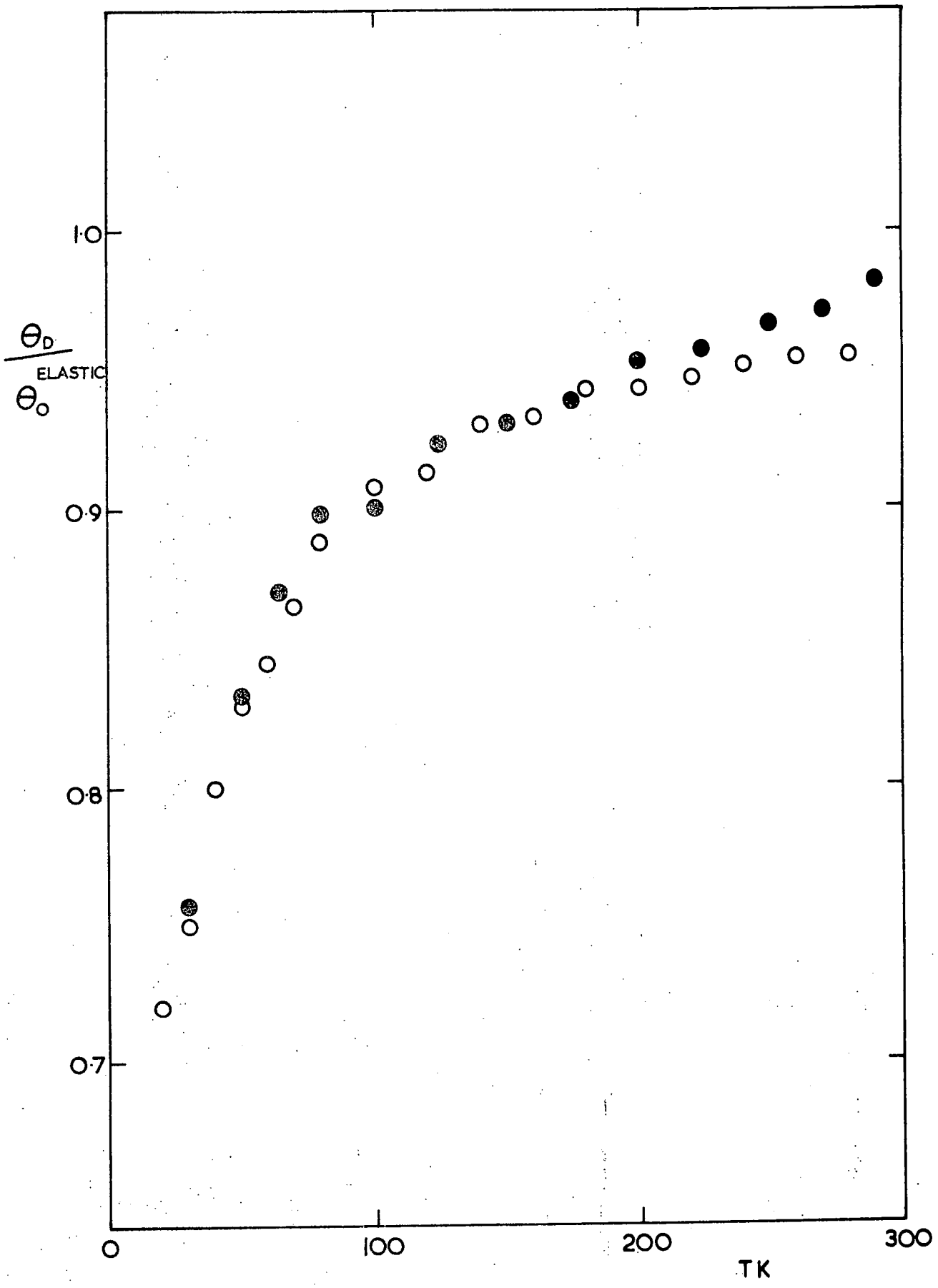

The normalised elastic constant Debye temperature (θ_D/θ_o elastic) derived from the Lakkad model for GaAs (o) and HgTe (●) as a function of temperature.

FIGURE 10.2

particular ultrasonic mode) whereas the thermal conductivity is mode-independent. In the similarly-structured ZnTe the Grüneisen parameter ratio based on this assumption is about 1.5 (Vetelino, Mitra and Namjoshi, 1970).

The frequency exponents predicted in the Woodruff-Ehrenreich (1961) model are 2 for $\omega\tau<<1$ and 1 for $\omega\tau>>1$: there is a sharp fall in the value of the exponent calculated from the measured attenuation (see Figures 8.15 and 8.16) in the region where $\omega\tau\sim1$ (Figure 8.11).

10.4 THE DISLOCATION DAMPING OF ULTRASOUND IN HgTe

The temperature and frequency dependences of ultrasonic attenuation in HgTe are extremely complicated (see Figures 9.20 and 9.21). In the region below about 80 K there are two major mechanisms contributing to the damping; dislocation loop resonance and phonon-phonon interactions. In order to evaluate the dislocation-damping the very large phonon-phonon attenuation must first be subtracted from the measured attenuation. This has been done using the Woodruff-Ehrenreich (1961) equations and a Grüneisen parameter derived from known data for HgTe and the Grüneisen parameter characteristics found for GaAs; the use of similar characteristics for the HgTe calculations is substantiated by the elasticity and Grüneisen parameter correlation described in Section 10.2. The remaining attenuation below 80 K has been found to be characteristic of dislocation damping, complicated by a dislocation unpinning mechanism at temperatures of about 28-38 K. It has not proved possible to identify positively the dislocation

pinning agent involved, but the results are consistent with unpinning through migration of a very low energy metal-ion vacancy. Rodot (1964) and Bailly (1968) have discussed the presence of enormous numbers of such vacancies in HgTe: the calculated number of dislocation pinning points deactivated between 28 and 38 K in HgTe is about 3×10^{10} cm^{-3}.

APPENDIX 1

The following is a list of sources of experimental data on the elastic constants of the group IV elements and the III-V and II-VI compounds. Wherever possible in Section 10.1 of this work the 0 K extrapolated values of the elastic constants have been used.

C (diamond):

McSkimin H.J., Andreatch (Jr.) P, Glynn P. JAP 43 3 985-7 1972

(includes a summary of previous work).

Si:

Beilin V M, Vekilov Yu Kh, Krasil'nikov O M Sov. Phys. Solid State 12 3 531-5 1970

McSkimin H J JAP 24 8 988-97 1953

McSkimin H J, Andreatch (Jr.) P. JAP 35 7 2161-5 1964

Ge:

Beilin V M, Vekilov Yu Kh, Krasil'nikov O M Sov. Phys. Solid State 12 3 531-5 1970

Burenkov Yu A, Nikanorov S P, Stepanov A V Sov. Phys. Solid State 12 8 1940-2 1971

McSkimin H J JAP 24 9 988-97 1953

AlSb:

Bolef D I, Menes M JAP 31 8 1426-7 1960

Weil R JAP 43 10 4271 1972

GaP:

Weil R, Groves W O JAP 39 9 4049-51 1968

GaAs:

See Chapter 6 for a summary.

GaSb

Lin J T, Wong C J. Phys. Chem. Solids 33 2 241-4 1972

McSkimin H J, Bond W L, Pearson G L, Hrostowski H J

Bull. Amer. Phys. Soc. SII 1 111 1956

InP:

Hickernell F S, Gayton W R JAP 37 1 462 1966

InAs:

Gerlich D JAP 34 9 2915 1963

Reifenberger R, Keck M J, Trivisonno J JAP 40, 13

5403-4 1969

InSb:

McSkimin H J, Bond W L, Pearson G L, Hrostowski H J

Bull. Amer. Phys. Soc. SII 1 111 1956

Potter R F Phys. Rev. 103 1 47-50 1956

de Vaux L H, Pizzarello F A Phys. Rev. 102 1 85 1956

ZnS:

Berlincourt D, Jaffe H, Shiozawa L R Phys. Rev. 129

3 1009-17 1963

Bhagavantam S, Suryanarayana J Proc. Ind. Acad. Science

A20 304-9 1944

Vekilov Yu Kh, Rusakov A P Sov. Phys. Solid State 13

4 956-60 1971

Zarembovitch A J. Physique 24 1097-1102 1963

ZnSe:

Berlincourt D, Jaffe H, Shiozawa L R Phys. Rev. 129

3 1009-17 1963

Lee B H JAP 41 7 2984-7 1970

ZnTe:

Berlincourt D, Jaffe H, Shiozawa L.R Phys. Rev. 129

3 1009-17 1963

Lee B H JAP 41 7 2984-7 1970

CdTe:

Berlincourt D, Jaffe H, Shiozawa L R Phys. Rev. 129 3 1009-17 1963

Greenough R D, Palmer S B J. Phys. (D) 6 587-92 1973

McSkimin H J, Thomas D G JAP 33 1 56-9 1962

Vekilov Yu Kh, Rusakov A P Sov. Phys. Solid State 13 4 956-60 1971

HgSe:

Krasil'nikov O M, Vekilov Yu Kh, Bezborodova V M, Yushin A V Sov. Phys. Semiconductors 4 11 1821-25 1971

Lehoczky A, Nelson D A, Whitsett C R Phys. Rev. 188 3 1069-73 1969

HgTe:

See Chapter 7 for a summary.

REFERENCES

Abrahams M S and Buiocchi C J 1965 JAP 36 2855-63

Akhieser A 1939 J Phys (USSR) 1 277

Alers G A 1965 : see Mason W P "Physical Acoustics" (Academic : New York)

Alper T 1968 Ph.D. Thesis Durham

Alper T and Saunders G A 1967 J Phys Chem Solids 28 1637-42

Alper T and Saunders G A 1969 Phil Mag 20 225-44

Anderson A C 1969 Rev Sci Insts 40 1502-3

Attard A E 1968 Brit JAP S2 1 390-1

Attard A E, Mifsud F A, Sant A K and Sultana J A 1969 J Phys (C) S2 2 816-23

Bailly F 1968 Phys Stat Sol 25 317-22

Balslev I 1968 Phys Rev 173 762-6

Banerjee R and Varshni Y P 1969 Can J Phys 47 451-62

Batchelder D N and Sidey G R 1969 J Phys (E) S2 2 533

Bateman T B, McSkimin H J and Whelan J M 1959 JAP 30 544-5

Beilin V M, Vekilov Yu Kh and Krasil'nikov O M 1969 Sov Phys Sol St 10 2443-6

Blanc J, Bube R H and Weisberg L E 1964 J Phys Chem Solids 25 225-40

Bobylev B A and Kravchenko A F 1967.a Sov Phys Acoust 12 315-7

Bobylev B A and Kravchenko A F 1967.b Sov Phys Acoust 13 242-3

Bobylev B A and Kravchenko A F 1969 Sov Phys Acoust 15 250-1

Bobylev B A and Kravchenko A F 1970 Sov Phys Acoust 16 13-16

Born M 1914 : see Born M and Huang K 1962 "Dynamical Theory of Crystal Lattices" (Oxford University)

Bouckaert L P, Smoluchowski R and Wigner E 1936 Phys Rev 50 58-67

Boyle W F and Sladek R J 1973 Sol St Commun 12 165-6

Bradfield G and Goodwin E T 1961 Phil Mag 6 1065-7

Braunstein R and Kane E O 1962 J Phys Chem Solids 23 1423-31

Brebrick R F and Strauss A J 1965 J Phys Chem Solids 26 989-1002

Brugger K 1965 JAP 36 759-68

Cardona M and Pollak F H 1966 Phys Rev 142 530-43

Cetas T C, Tilford C R and Swenson C A 1968 Phys Rev 174 835-44

Charlson E J and Mott G 1963 Proc IEEE 51 1239

Collins T C, Stukel D J and Euwema R N 1970 Phys Rev B1 724-30

Dahake L 1967 Ph.D. Thesis Durham

Delves R T 1965 Brit JAP 16 343-51

Delves R T and Lewis B 1963 J Phys Chem Solids 24 549-56

Dickey D H and Mavroides J G 1964 Sol St Commun 2 213

Dolling G and Cowley R A 1966 Proc Phys Soc 88 463-94

Dolling G and Waugh J L T 1964 Proc Int Conf Lattice Dynamics (Copenhagen 1963)

Drabble J R and Brammer A J 1966 Sol St Commun 4 467-8

Edmond J T 1960 JAP 31 1428-30

Ehrenreich H 1960 Phys Rev 120 1951-63

Elbaum C 1969 Ultrasonics April 113-16

Feder R and Light T 1968 JAP 39 4870-1

Foster N F, Coquin G A, Rozgonyi G A and Vannatta F A 1968 IEEE Trans Son Ult Son SU-15 28-41

Garland C W and Park K C 1962 JAP 33 759-60

Giriat W 1964 Brit JAP 15 151-6

Granato A and Lücke K 1956 JAP 27 583-90

Granato A and Lücke K 1966 : see Mason W P "Physical Acoustics" IVA (Academic : New York)

Groves S and Paul W 1963 Phys Rev Letts 11 194-6

Gunton D J 1973 Private communication

Hambleton K G, Hilsum C and Holeman B R 1961 Proc Phys Soc 77 1147-8

Harman T C 1967 : see Aven M and Prener J S "Physics and Chemistry of II-VI Compounds" (North Holland : Amsterdam)

Harman T C, Kleiner W H, Strauss A J, Wright G B, Mavroides J G, Honig J M and Dickey D H 1964 Sol St Commun 2 305

Hass M and Henvis B W 1962 J Phys Chem Solids 23 1099-1104

Herman F 1955 J Electronics 1 103

Hill M J and Holt D B 1968 J Mat Sci 3 244-58

Hill R 1952 Proc Phys Soc A65 349-54

Hilsum C 1966 : see Willardson R K and Beer A C "Physics of III-V Semiconductors" (Academic : New York)

Holland M G 1966 : see Willardson R K and Beer A C "Physics of III-V Semiconductors" (Academic : New York) page 17.

Hopfield J J 1961 JAP suppl 32 2277-8

Hutson A R and White D L 1962 JAP 33 40-7

Hwang C J 1968 JAP 39 5347-56

Hwang C J 1969.a JAP 40 4584-90

Hwang C J 1969.b JAP 40 1983-4

Ikoma H 1968 J Phys Soc Japan 25 1069-81

Ikoma H 1970 J Phys Soc Japan 28 1474-84

IRE Standards on Piezoelectric Crystals 1958 Proc IRE 46 764-78

Ivanov S N, Kotel'yanskii I M, Mansfel'd D and Khazanov E N 1971 Sov Phys Sol St 13 508-9

Ivanov-Omskii V I, Kolomiets B T, Mal'kova A A, Ogorodnikov V K and Smekalova K P 1965 Phys Stat Sol 8 613-18

Jaffe H and Berlincourt D A 1965 Proc IEEE 53 1372-86

Jeavons A P and Saunders G A 1968 Brit JAP S2 1 869-72

Jewell A J 1967 J Sci Insts 44 81-2

Johnson C J, Sherman G H and Weil R 1969 Applied Optics 8 1667-71

Kane E O 1957 J Phys Chem Solids 1 249-61

Keyes R W 1962 JAP 33 3371-2

King P J 1969 J Phys (D) S2 2 1349-52

King P J and Rosenberg H M 1970 Proc Roy Soc Lond A315 369-79

Koehler J S 1952 : see Shockley W, Holloman J H, Maurer R and Seitz F "Imperfections in Nearly Perfect Crystals" (Wiley : New York)

Kolosov E E and Sharavskii P V 1966 Sov Phys Sol St 7 2973-4

Kovár J and Hrivnák L 1969 Zborník Vysokey Školy Dopravnej V Žiline 11 45-50

Krasil'nikov O M, Vekilov Yu Kh and Kadyshevich A E 1969 Sov Phys Sol St 11 975-80

Ku H A 1966 J Res Nat Bur Stand 70c 263-73

Lakkad S C 1971 JAP 42 4277-81

Landau L and Rumer G 1937 Physik Z Sowjetunion 11 18

de Launay J 1956 : see Seitz F and Turnbull D "Solid State Physics" II (Academic : New York)

de Launay J 1959 J Chem Phys 30 91-2

Lehoczky A, Nelson D A and Whitsett C R 1969 Phys Rev 188 1069-73

Lewis M F 1968 J Acoust Soc Amer 43 852-8

Lewis M F 1970 Cryogenics 10 38-44

Love A E H 1944 "A Treatise on the Mathematical Theory of Elasticity" (Dover : New York)

McSkimin H J 1961 J Acoust Soc Amer 33 12-16

McSkimin H J and Andreatch P 1962 J Acoust Soc Amer 34 609-15

McSkimin H J and Andreatch P 1967 JAP 38 2610-11

McSkimin H J, Jayaraman A and Andreatch P 1967 JAP 38 2362-3

Mahan G D 1964 Phys Rev 135 A428-33

Maris H J 1969 Phys Rev 188 1303-7

Martin R M 1970 Phys Rev 1 B4005-11

Mason W P and Bateman T B 1966 J Acoust Soc Amer 40 852-62

Mason W P and Rosenberg A 1966 Phys Rev 151 434-41

Mason W P and Rosenberg A 1967 JAP 38 1929-36

Mavroides J G and Kolesar D F 1964 Sol St Commun 2 363

Maynell C A 1973 Private communication

Miller J G and Bolef D I 1969 Rev Sci Insts 40 915-20

Miller J G and Bolef D I 1970 JAP 41 2282-93

Musgrave M J P 1954.a Proc Roy Soc Lond A226 339-55

Musgrave M J P 1954.b Proc Roy Soc Lond A226 356-66

Musgrave M J P 1957 Proc Camb Phil Soc 53 897-906

Neighbours J R and Schacher G E 1967 JAP 33 690-6

Novikova S I 1961 Sov Phys Sol St 3 129-30

Novikova S I and Abrikosov N Kh 1963 Akad Nauk CCCP : Solid St Physics 5 2138-40

Nye J F 1957 "Physical Properties of Crystals and their Representation by Tensors and Matrices" (Oxford Clarendon)

Ožvold M 1969 Fyzikálny Časopis 19 1-12

Ožvold M 1970 Phys Stat Sol 37 79-89

Pauling L C 1960 "Nature of the Chemical Bond" (Cornell U P: Ithaca)

Phillips J C 1970 Rev Mod Physics 42 317-56

Pierron E D, Parker D L and McNeely J B 1967 JAP 38 4669-71

Piesbergen U 1963 Z Naturf 18a 141-7

Quilliet A, Rodot H and Rodot M 1962 Report of Int Conf on Phys of Semicond (Exeter 1962) page 711

Read T A 1941 Trans AIME 143 30

Reuss 1929 : see Huntington H B 1958 "The Elastic Constants of Crystals" Sol St Phys 7 Edited Seitz F and Turnbull D

Rodot H 1964 J Phys Chem Solids 25 85-93

Rodot M and Rodot H 1959 Compt Rendus 248 937-40

Ruppin R 1972 J Phys Chem Solids 33 945-9

Rusakov A P 1971 Sov Phys Sol St 13 510-11

Saunders G A, Pace N G and Alper T 1967 Nature 216 1298-9

Sparks P W and Swenson C A 1967 Phys Rev 163 779-90

Stillman G E, Wolfe C M and Dimmock J O 1970 J Phys Chem Solids 31 1199-1204

Straumanis M E and Kim C D 1965 Acta Cryst 19 256-9

Strauss A J and Brebrick R F 1965 : see Harman T C 1967

Suchet J P 1965 "Chemical Physics of Semiconductors" (Van Nostrand : London)

Szigeti B 1950 Proc Roy Soc Lond A204 51-62

Szymánska W, Śniadower L and Giriat W 1965 Phys Stat Sol 10 K11-13

Teutonico L J, Granato A V and Lücke K 1964 JAP 35 220-34

Truell R, Elbaum C and Chick B B 1969 "Ultrasonic Methods in Solid State Physics" (Academic : New York)

Vecht A 1966 : see Hass G and Thun R E "The Physics of Thin Film" III (Academic : New York)

Vetelino J F and Mitra S S 1969 Sol St Commun 7 1181-6

Vetelino J F, Mitra S S and Namjoshi K V 1970 Phys Rev B2 967-73

Vetelino J F, Namjoshi K V and Mitra S S 1970 JAP 41 1541-4

Voigt W 1892 Ann der Phys 47 671

Voigt W 1928 "Lehrbuch der Kristallphysik" (Teubner : Leipzig)

Warekois E P, Lavine M C, Mariano A N and Gatos H C 1962 JAP 33 690-6

Waterman P C 1959 Phys Rev 113 1240-53

Waugh J T L and Dolling G 1963 Phys Rev 132 2410-12

White G K 1959 "Experimental Techniques in Low Temperature Physics" (Oxford Clarendon)

White J G and Roth W C 1959 JAP 30 946-7

Whitsett C R and Nelson D A 1972 Phys Rev B5 3125-38

Wilson J I B 1971 Ph.D. Thesis Durham

Wolfe C M, Stillman G E and Dimmock J O 1970 JAP 41 504-7

Wolfe C M, Stillman G E and Lindley W T 1970 JAP 41 3088-91

Wolff G A and Broder J D 1959 Acta Cryst 12 313-23

Woodruff T O and Ehrenreich H 1961 Phys Rev 123 1553-9

Yamamoto M 1968 J Phys Soc Japan 24 73-81

Yamamoto M and Fukuroi T 1966 J Phys Soc Japan 21 2428

Zener C 1947 "Elasticity and Anelasticity of Metals" (Chicago U P)

Zerbst M and Boroffka H 1963 Z Naturf 18a 642

Zucker I J 1968 J Phys (C) S2 1 1456-9

PUBLICATIONS

Parts of the work presented in this thesis are the subjects of the following publications:

1. "The elastic constants of GaAs from 2 K to 320 K" R I Cottam and G A Saunders, J. Phys. (C) 6 2105-18 1973

2. "An investigation of the validity of ultrasonic pulse superposition measurements using thin-film transducers" R I Cottam and G A Saunders, J. Phys. (D) : in press.

3. "The elastic and anelastic properties of HgTe" R I Cottam and G A Saunders, Proc. Int. Conf. on the Physics of Semimetals and Narrow Gap Semiconductors (Nice-Cardiff 1973) : in press.